ABSTRACT

Title of Document: TOWARDS SINGLE SHOT MEASUREMENTS OF A COOPER PAIR BOX QUBIT USING AN RF-SET

Carlos A. Sanchez, Doctor of Philosophy, 2005

Directed By: Professor Frederick C. Wellstood, Department of Physics

I report an investigation into using an rf Single Electron Transistor (rf-SET) to implement single shot readout of the quantum state of a Cooper pair box.

I fabricated Al/AlO_x/Al SETs and Cooper pair boxes using e-beam lithography and double-angle evaporation. The devices had typical charging energies of about 1 K and were measured at 30 mK in a dilution refrigerator. I built rf-SETs with an *LC* resonant circuit integrated on the chip and operating frequencies of 650 MHz and 1.5 GHz. The rf-SETs had a typical bandwidth of 30 MHz and the best achieved charge sensitivity was $8\times10^{-6}\ e_{rms}/(Hz)^{1/2}$ at 1.5 GHz.

The rf-SETs were used to measure the Coulomb staircase on the Cooper pair box. Measurements of the staircase show features due to quasiparticle poisoning that are dependent on temperature and SET bias. The data was compared to a theory I developed to extend existing theories of quasiparticle poisoning. My model is based

on the calculation of tunneling rates to explain observations of parity effects in the Cooper pair box over a wide temperature range.

Quantum state control of the Cooper pair box was demonstrated by using fast voltage pulses applied to the gate. Temporal oscillations of charge states and spectroscopy measurements reveal a dephasing time $T_2 \approx 200$ ps at 30 mK, for a drive frequency of 30 GHz. The energy relaxation time $T_1 \approx 140$ ns was determined from time domain measurements of the decay of the Cooper pair box charge.

The fidelity of single shot measurements and the feasibility of this quantum readout scheme based on the results are discussed.

TOWARDS SINGLE SHOT MEASUREMENTS OF A COOPER PAIR BOX QUBIT USING AN RF SINGLE ELECTRON TRANSISTOR

By

Carlos A. Sanchez

Dissertation submitted to the Faculty of the Graduate School of the
University of Maryland, College Park, in partial fulfillment
of the requirements for the degree of
Doctor of Philosophy
2005

Advisory Committee:
Professor Frederick C. Wellstood, Chair/Advisor
Professor Christopher J. Lobb
Professor James R. Anderson
Associate Professor Romel del Rosario Gomez
Dr. Pierre M. Echternach

ACKNOWLEDGEMENTS

I have received help from many people during my time in graduate school. I want to thank Dr. Marc Manheimer for providing me with a research project and supporting me for many years. I am very grateful to my advisor, Dr. Fred Wellstood, for taking an interest in my research, for many illuminating discussions and for his dedication to teaching and advising students. I thank Dr. Chris Lobb for guiding me towards the PhD program at the University of Maryland. I am indebted to Dr. Pierre Echternach, who helped my research in a fundamental way, by providing me with samples and by sharing very useful information. I thank Dr. Keith Schwab for teaching me many experimental techniques, such as e-beam lithography, vacuum technology and cryogenics. I am very glad to have collaborated with Dr. Ben Palmer. I express my gratitude to Dr. Nick Chant, my professors and the very nice staff of the Physics Department and the Laboratory for Physical Sciences. I am grateful to friends and colleagues for their support and assistance during this time, in particular to Dan Sullivan, Breno Imbiriba, Matt LaHaye and Kenton Brown, for making my time here more enjoyable. Finally, I acknowledge financial support from the Mexican National Center of Metrology (CENAM) and the Mexican National Council of Science and Technology (CONACYT).

Table of Contents

List of Symbols

A	attenuation
B	magnetic field
C	capacitance
C_c	coupling capacitance
C_g	gate capacitance
C_Σ	total capacitance
CPB	Cooper pair box
Δ	superconducting energy gap
Δ_I	superconducting energy gap of the island
Δ_L	superconducting energy gap of the leads
E	energy
E_c	charging energy
E_J	Josephson energy
ΔE_{10}	energy difference between the ground state and the excited state
e	magnitude of the electron charge (1.602×10^{-19} C)
f	frequency
ϕ	phase difference of the superconducting wave functions
Φ	magnetic flux
Φ_o	flux quantum ($h/2e = 2.07 \times 10^{-15}$ Wb)
Γ	transition rate
$\Gamma\uparrow$	transition rate from the ground state to the excited state
$\Gamma\downarrow$	transition rate from the excited state to the ground state
Γ_{oe}	transition rate from the odd state to the even state
Γ_{eo}	transition rate from the even state to the odd state
Γ_{LI}	tunneling rate from leads to island from thermal quasiparticles
Γ_{IL}	tunneling rate from island to leads from thermal quasiparticles
Γ^*_{LI}	tunneling rate from leads to island from non-equilibrium quasiparticles
Γ^*_{IL}	tunneling rate from island to leads from non-equilibrium quasiparticles

γ	escape rate of the un-paired electron on the island
h	Planck's constant (6.63×10^{-34} J·s)
$\hbar$	reduced Planck's constant (1.05×10^{-34} J·s)
I	current
I_c	critical current
κ	coupling factor
k_B	Boltzmann's constant (1.38×10^{-23} J/K)
L	inductance
n	number of excess electrons on the island
n_g	gate charge
N^*_I	number of non-equilibrium quasiparticles in the island
N^*_L	number of non-equilibrium quasiparticles in the leads
P	probability
P_e	probability of the even state
P_o	probability of the odd state
Q	charge
Q	resonator quality factor
Q_L	resonator loaded quality factor
R	resistance
R_S	dynamic resistance of the SET
R_Σ	total resistance of the SET
R_Q	resistance quantum (h/e2 = 25.9 kΩ)
rms	root mean square
S_V	power spectral density of voltage fluctuations
S_I	power spectral density of current fluctuations
S_q	power spectral density of charge fluctuations
SET	single electron transistor
T	temperature
T_1	energy relaxation time
T_2	dephasing time
t_{mix}	mixing time

t_m	measurement time
t_d	decay time
V_{DS}	drain-source voltage
V_g	gate voltage
Z	impedance

List of Tables

List of Figures

Chapter 1: Introduction

1.1 Motivation

In recent years, quantum computing [1] has become a very active field of research due to the realization that quantum computers have the potential to solve problems that are impossible or impractical to solve with a classical computer. A quantum computer employs quantum bits or *qubits* to store information. *Qubits* are quantum two-level systems, with the ground state $|0\rangle$ representing a logical "0" and the excited state $|1\rangle$ a logical "1". The novelty of quantum computing is that it relies on the principles of superposition and entanglement. A qubit can be prepared in a superposition state $|\psi\rangle = a|0\rangle + b|0\rangle$ and two qubits can be described by an entangled state $|\psi\rangle = a|00\rangle + b|01\rangle + c|10\rangle + d|11\rangle$. Neither of these states would exist in a classical computer. These two properties make it possible to process information in new and more efficient ways [2].

Significant progress has been made in the theory of quantum computing over the past ten years. The most remarkable advances include Shor's algorithm, which allows for the fast factorization of large numbers [3], Grover's Quantum search algorithm [4] and quantum cryptography [5]. Moreover, quantum error correction techniques have been proposed [6] that would allow a practical quantum computer to operate with some level of noise if the coherence time can be made significantly long compared to the gating time [7]. Much of the present work on quantum computing consists in investigating physical systems that can function as qubits. According to DiVincenzo, a system suitable for the implementation of a quantum computer should meet the following criteria [7]:

1. Scalability

2. Capable of being initialized in a well-defined state

3. Long coherence times

4. A universal set of quantum gates

5. Qubit-specific readout capability.

Many different systems have been proposed for the implementation of qubits, among them ion traps [8], nuclear magnetic resonance (NMR) [9], cavity quantum electro-dynamics (QED) [10] and solid state qubits [11]. All of these approaches have advantages and disadvantages. Ion traps and NMR systems have very long coherence times and very encouraging results have been obtained in systems with a small number of qubits [12,13]. However, it is not clear whether these schemes can be implemented on a large scale (thousands or millions). On the other hand, nanofabrication techniques are very common in the semiconductor industry and could be used to integrate a large number of solid state qubits in a single chip. Superconductors are systems with inherently low dissipation and therefore one of the most promising technologies for the realization of solid state qubits. Their disadvantage is that they have had relatively short coherence times. Exploiting the advantages and overcoming the disadvantages is a subject of active research.

1.2 Superconducting qubits

Superconducting qubits are very promising candidates for quantum computing. Unlike other proposed technologies which are based on microscopic degrees of freedom, superconducting qubits exploit the macroscopic wave function of the superconducting

state formed by the condensate of Cooper pairs. The Josephson junction [14] is the basic element in all superconducting qubits. Its quantum behavior is characterized by two physical variables; the charge Q on the junction's capacitance and the gauge invariant phase difference across the junction ϕ (see Fig. 1.1). These are canonically conjugate variables that obey the commutation relation $[\phi,Q]=ie$ [15]. The three basic types of superconducting qubits (flux, phase and charge) are shown schematically in Fig. 1.1.

The flux qubit is basically an rf-SQUID, consisting of one or more Josephson junctions inserted in a superconducting loop (see Fig. 1.1a). This scheme utilizes the phenomenon of flux quantization in a superconducting ring. A supercurrent is induced in the loop when the SQUID is biased with a magnetic flux. The logical "0" and "1" of the qubit correspond to states of the system with the supercurrent circulating clockwise or counterclockwise. The single junction rf-SQUID Hamiltonian is given by [16]:

$$H = \frac{Q^2}{2C_J} + \frac{(\Phi - \Phi_{ext})^2}{2L} - E_J \cos\left[\frac{2e}{\hbar}(\Phi - \Phi_{ext})\right] \tag{1.1}$$

Where C_J is the capacitance of the Josephson junction, Q is the charge in C_J, L is the total inductance of the SQUID, Φ_{ext} is the bias flux and Φ is the total flux through the loop. A close variation of this has been demonstrated in a three junction loop by Chiorescu *et al.* [17] who observed Rabi oscillations with an energy relaxation time $T_1=900$ ns and dephasing time $T_2=20$ ns.

The phase qubit consists of a current biased Josephson junction. If the bias current I is less than the critical current I_c of the junction, the dynamics of the phase difference ϕ is analogous to the position of a particle trapped in an anharmonic potential well [18]. The energy levels of the well can be found by solving the Hamiltonian for this system:

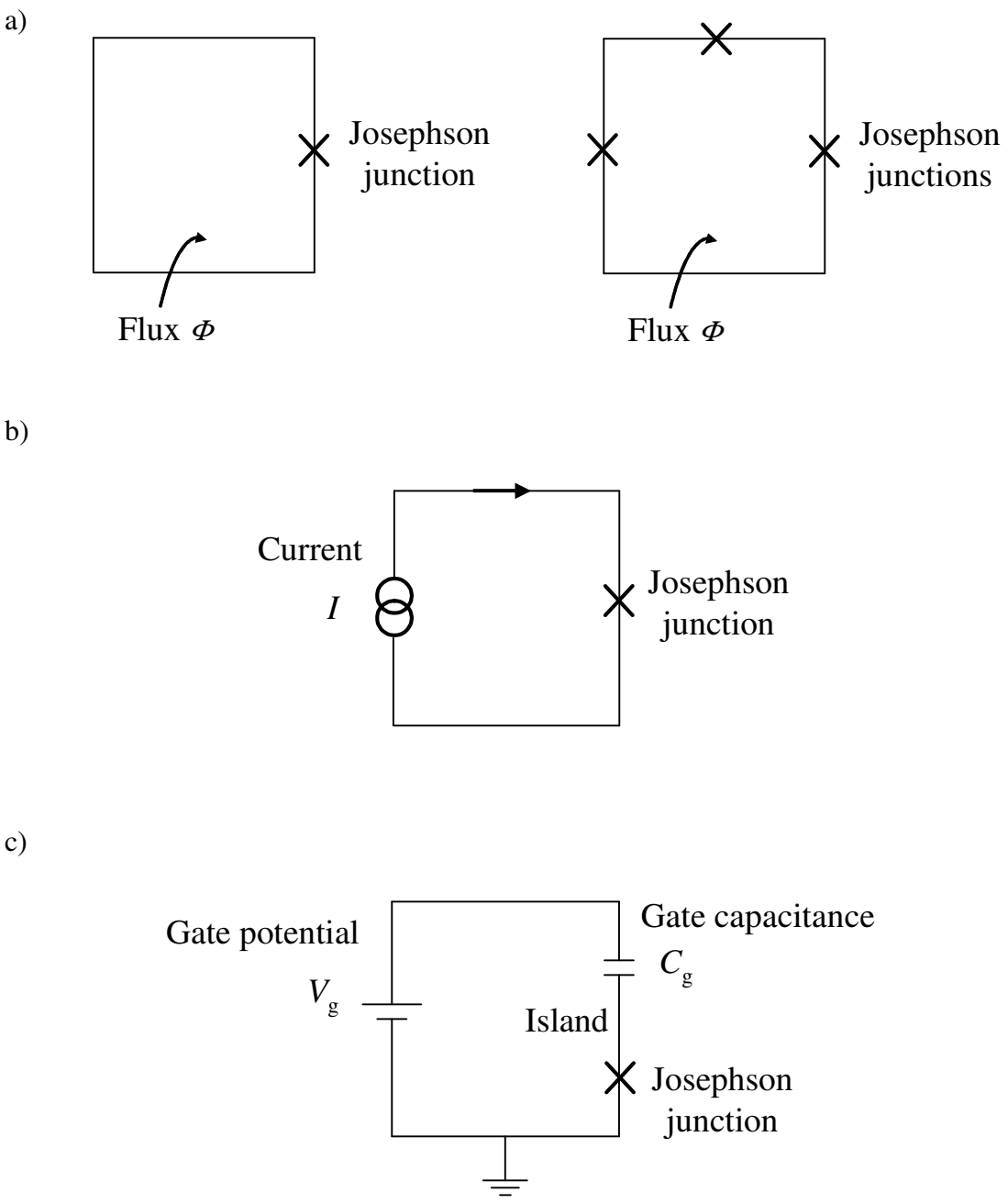

Fig. 1.1: Schematic illustration of the three basic types of superconducting qubits: (a) single junction and three junction flux qubits, (b) phase qubit, (c) charge qubit (Cooper pair box).

$$H = \frac{Q^2}{2C_J} - \frac{\Phi_0}{2\pi}\left[I_c \cos(\phi) + I\phi\right] \tag{1.2}$$

Even though $I<I_c$, there is a finite probability that the fictitious particle will escape the potential well and drive the junction into a dissipative state with a non-zero dc voltage across the junction. The escape rate depends on the quantum state of the system and thus one can determine the state by measuring the bias current at which a dc voltage appears. Promising results have been achieved with phase qubits, such as single qubit manipulations with long coherence times (T_1=500 ns and T_2=150 ns), by Martinis *et al*. [19] and spectroscopy measurements of two-qubit and three-qubit entangled states by Berkley *et al*. [20] and Xu *et al.* [21].

The superconducting charge qubit or Cooper pair box consists of a superconducting island with small total capacitance C coupled to a charge reservoir through an ultra-small Josephson junction. If the charging energy $E_c \equiv e^2/2C$ is larger than the Josephson energy E_J then the charge on the island is a well-defined quantity and the number of excess Cooper pairs on the island n can be used to represent the states of the qubit. The Cooper pair box Hamiltonian is given by [22]:

$$H = 4E_c\left(n - \frac{C_g V_g}{e}\right)^2 - E_J \cos(\phi) \tag{1.3}$$

The Cooper pair box qubit is the focus of this thesis. In the next section I present a brief review of the most significant prior results on this qubit.

1.3 Previous work on the Cooper pair box.

The theory of the Cooper Pair Box (CPB) was first developed by Büttiker [23] and latter proposed as a qubit by Shnirman *et al.* [24]. The first experimental work on the CPB was realized by Bouchiat *et al*. [25], who measured the charge on the CPB island in the ground state using an SET and found evidence for the coherent superposition of charge states. Quantum state manipulation was first achieved by Nakamura *et al*. [26]. They used fast voltage pulses to prepare the state of the CPB in a superposition of the ground and excited states and observed temporal oscillations of charge states with a coherence time of about 2 ns. An ensemble measurement of the state of the CPB was done in this experiment by measuring the dc current through a highly resistive probing junction attached to the CPB island.

The invention of the rf-SET [27] opened up the possibility of single shot measurements of the CPB state via fast charge measurements. Several groups have pursued this kind of measurements. Lehnert *et al*. [28] performed spectroscopy measurements and determined a relaxation time $T_1 = 1.3$ μs by observing the decay of the charge signal coupled to the rf-SET. Coherent oscillations were demonstrated by Duty *et al*. [29] and Guillaume *et al*. [30] by average measurements of the CPB charge. Although a lot of progress has been made, single shot measurements using an rf-SET have not been demonstrated at the time of this writing. In Chapters 4 and 8 I examine some of the issues and limitations concerning single shot measurements using an rf-SET.

Other read-out schemes have been used successfully to achieve single shot measurements of a CPB qubit. Vion *et al*. [31] designed a circuit consisting of a split

CPB shunted by a large Josephson junction. This arrangement allows the state of the CPB to be determined by measuring the switching current of the large junction. A different idea was demonstrated by Ostafiev *et al*. [32]. Their scheme circumvented the short relaxation times by quickly transferring the CPB charge to a trap with a long retention time and then measuring the charge on the trap with an SET.

1.4 Overview of the thesis

The rest of the thesis is organized as follows. Chapter 2 introduces the basic theory of the CPB. Chapter 3 explains the physical limitations affecting quantum coherence in the CPB. Chapter 4 covers the theory and operating principles of the rf-SET. Chapter 5 deals with engineering aspects of the experiments such as microwave design, sample fabrication, cryogenics and electronics. Chapter 6 shows the basic measurements I used to characterize devices. Chapter 7 discusses the problem of quasiparticle poisoning and compares theory with measurements. Chapter 8 presents measurements involving the excited state of the CPB and discusses the fidelity of single shot measurements. Finally, Chapter 9 contains a summary of results and suggestions for future research.

Chapter 2: Theory of the Cooper pair box

2.1 Introduction

The Cooper pair box (CPB) is a type of ultra-small superconducting circuit that exhibits charge quantization with a fundamental charge of $2e$, i.e. the charge of a Cooper pair. The CPB is a very close relative of the single electron box, first developed at Saclay. However, superconductivity produces additional effects not seen in the normal state. In particular, macroscopic quantum coherence can be observed in the CPB due to the low dissipation inherent to the superconducting state. The possibility that the two lowest energy states of a CPB could be used to realize a qubit for quantum computation was first proposed by Shnirman *et al.* [24]. The ground state of the CPB was first observed by Bouchiat *et al.* [25] and quantum state control using the charge states of the CPB was first demonstrated by Nakamura *et al.* [26]. In this chapter I present the theory of the CPB and explain the conditions that need to be satisfied to use it as a qubit.

2.2 The normal single electron box

A single electron box consists of a very small non-superconducting island that is connected electrically to the rest of a circuit by an ultra-small tunnel junction and a small gate capacitance. The device is controlled by means of a gate voltage source V_g that is connected to the gate capacitance (see Fig. 2.1). The box is characterized electrically by the tunneling resistance R [33] and the total capacitance of the island $C_\Sigma = C_J + C_g$, where C_J is the capacitance of the ultra-small junction and C_g is the gate capacitance. The number n of electrons on the island is generally not a sharply defined physical quantity

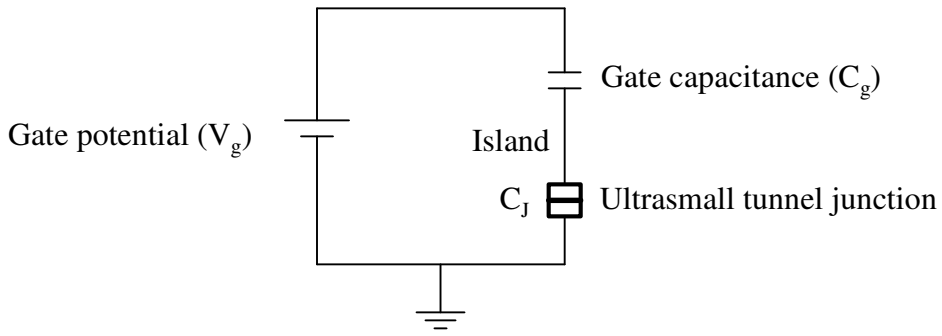

Fig. 2.1: Schematic diagram of a single electron box consisting of a small-capacitance normal metal island that is capacitively coupled to a gate electrode and gate voltage source. Electrons can tunnel on and off the island through a tunnel junction with tunnel resistance R and capacitance C_J. The total capacitance of the island is $C_\Sigma = C_g + C_J$.

due to the uncertainty principle of quantum mechanics and thermal fluctuations. However, for sufficiently small C_Σ and temperature T, n can be well-defined at most values of V_g. Thermal fluctuations are suppressed if the thermal energy $k_B T$ is much less than the charging energy $E_c \equiv e^2/2C_\Sigma$. I note that E_c is just the electrostatic energy of the box when there is one extra electron on the island and $V_g = 0$.

The island capacitance and the tunneling resistance can be used to define a characteristic tunneling time $\Delta t = RC_\Sigma$. This can be thought of as the typical time scale for an added electron to tunnel off the island. The energy-time uncertainty relation $\Delta E \Delta t > \hbar/2$, with $\Delta E \leq E_c = e^2/2C_\Sigma$, suggests (but does not prove) that the tunneling resistance must be larger than the resistance quantum $R_Q \equiv h/e^2 = 25.9\ \text{k}\Omega$ for the charge number n to be well-defined. The two conditions, $R > R_Q$ and $E_c > k_B T$, can be satisfied in devices with ultra-small (i.e. submicron) junctions. The devices I used here typically have a total capacitance of about 1 fF or $E_c \lesssim 1\text{K}$, so they must be operated at temperatures well below 1K for charging effects to be observable.

The electrostatic charging energy U of the box can be varied by applying a voltage V_g to the gate electrode:

$$U = E_c (n - n_g)^2 \tag{2.1}$$

where $n_g = C_g V_g / e$, n is the number of electrons on the island and $e = 1.602 \times 10^{-19}$ C is the magnitude of the electron charge. Note that a positive gate voltage will tend to attract electrons (negatively charged) to the island, so that n_g and V_g will have the same sign. Also note that n_g is an external control parameter that can be varied continuously, while n is an internal, quantized variable. Equation 2.1 defines a series of parabolas as a function of n_g (see Fig. 2.2a) with the charge number n as a parameter. For $k_B T \ll E_c$ and $R \gg R_Q$

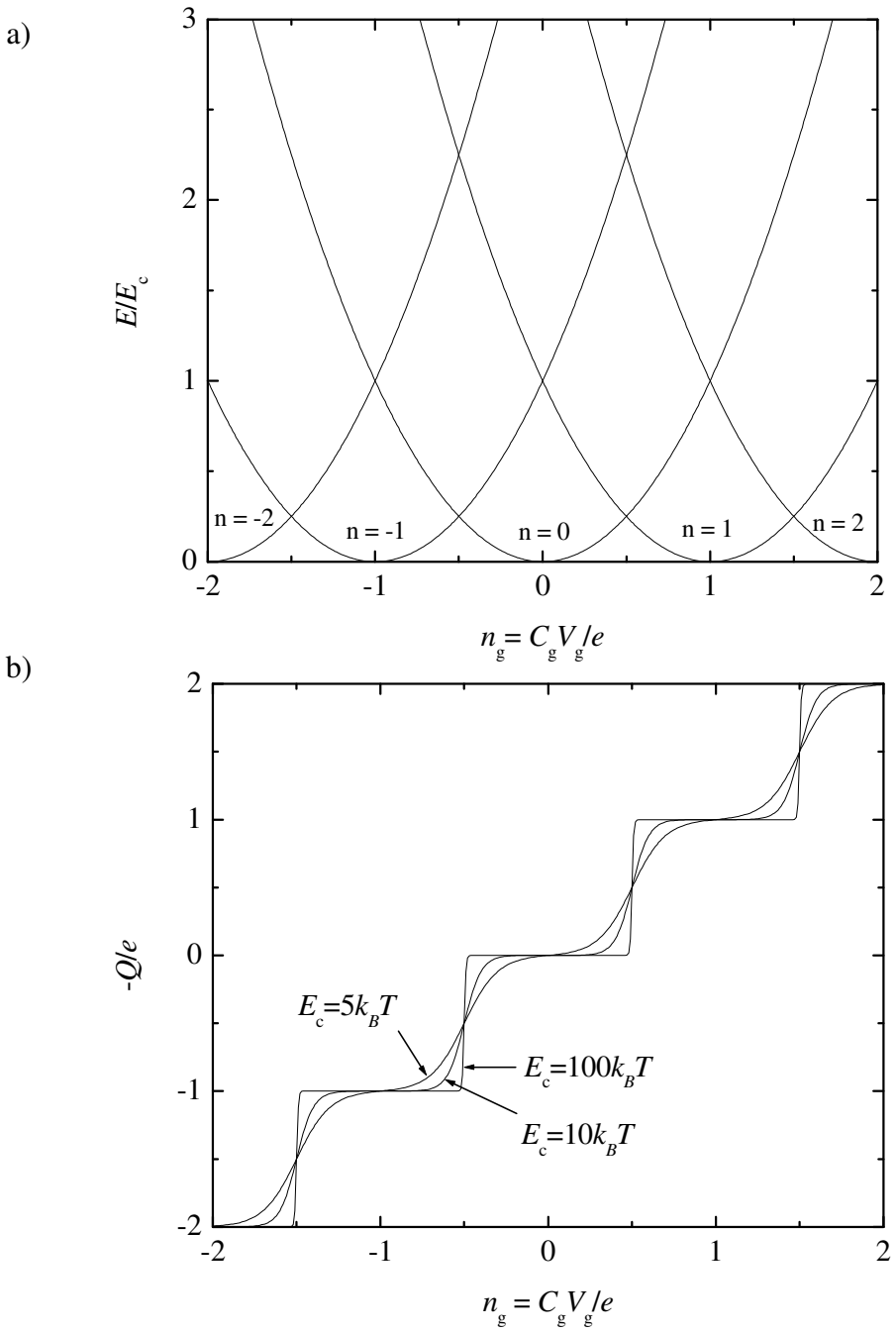

Fig. 2.2: (a) Electrostatic energy of the single electron box as a function of gate charge $n_g = C_g V_g$ for different number of excess electrons n. (b) Charge on the box as a function of gate charge for $k_B T / E_c = 0.01$, 0.1 and 0.2.

there is a high probability for the box to be found in the charge state that minimizes the electrostatic energy.

In thermal equilibrium the average charge Q on the island can be found from elementary statistical mechanics:

$$Q = \frac{-\sum_{-\infty}^{\infty} P_n ne}{\sum_{-\infty}^{\infty} P_n} = \frac{-e\sum_{-\infty}^{\infty} n \exp\left(\frac{-E_c\left(n-n_g\right)^2}{K_B T}\right)}{\sum_{-\infty}^{\infty} \exp\left(\frac{-E_c\left(n-n_g\right)^2}{K_B T}\right)} \tag{2.2}$$

where P_n is the probability of finding n electrons on the island and we have assumed that $n=0, \pm 1, \pm 2, \ldots$ is quantized and that each specific n has one state.

Figure 2.2b shows an example of Q vs n_g found from Eq. 2.2. One sees a series of steps at charge $Q=ne$ and the resulting curve is called the "Coulomb staircase". The charge on the box changes at the degeneracy points ($n_g = \pm 1/2, \pm 3/2$, etc.) where the two lowest energy parabolas cross (see Fig. 2.2b). The staircase is rounded in the vicinity of these points since the electrostatic energy (equation 2.2) becomes comparable to the thermal energy, and the roundup becomes more pronounced as the temperature increases, until the staircase is washed out at $k_B T \sim E_c$.

2.3 The superconducting box or Cooper pair box

New phenomena arise when the electrodes and island of the box are superconducting. In a conventional s-wave superconductor at $T=0$ with no field or currents applied, all electrons are bound in Cooper pairs [15]. This assumes that there are an even number of electrons, a point to which we will return later. A minimum energy 2Δ is necessary to

break a Cooper pair, where Δ is the superconducting energy gap. At finite temperatures, the excited states or quasiparticle excitations are occupied in thermal equilibrium according to the Fermi distribution function $f=1/\{1+\exp[(E-\mu_F)/k_BT]\} \approx e^{-(\Delta/k_BT)}$ for $k_BT \ll \Delta$. As we will see, the presence of paired electrons and the superconducting energy gap produces dramatic changes in the Coulomb staircase [34].

Figure 2.3 illustrates the situation when $\Delta < E_c$ while Fig. 2.4 shows the case for $\Delta > E_c$. States with odd-n, i.e. when at least one quasiparticle is present, have an additional energy Δ for each quasiparticle besides the electrostatic energy (see Eq. 2.1) and the corresponding parabolas are shifted vertically. For $\Delta < E_c$ the crossings between parabolas occur now closer to $n_g = \pm 1, \pm 3$, etc. This produces shorter steps in the charge staircase for odd-n states and longer steps for even-n states.

In addition, I note that for $\Delta < E_c$, for example, for the $n=2$ charge state it is possible to have two quasiparticles or one Cooper pair. The two quasiparticle state would lie 2Δ above the one Cooper pair state.

The gray areas in Figs. 2.3 and 2.4 illustrate the fact that the quasiparticle can have momentum and any energy above the gap. In contrast, unless there is a net current, the Cooper pairs have a single well-defined energy at each gate voltage.

I note that in Fig. 2.4 the state with minimum energy is always even, so the staircase displays no odd steps. In this limit, we expect to see full $2e$ periodicity due to $2e$ charge of the Cooper pairs.

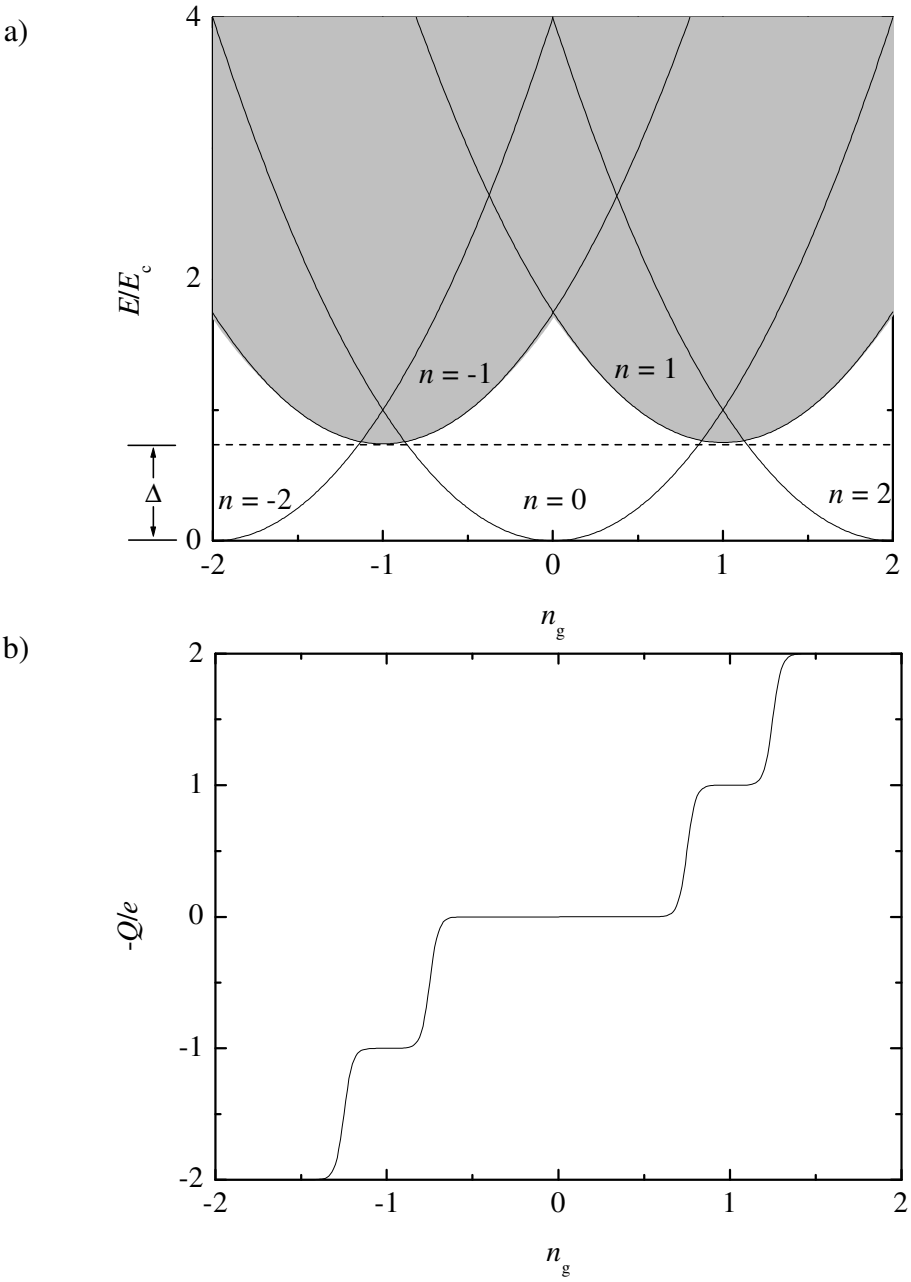

Fig. 2.3: (a) Electrostatic charging energy in a superconducting box with $E_c > \Delta$. Charge states with odd-n are displaced vertically to reflect the energy cost of creating one quasiparticle. The grey areas are allowed quasiparticle energies, including their kinetic energy. (b) Average charge on the island for the energy diagram shown in (a). The odd-n steps are shorter than the even-n states as a consequence of the superconducting energy gap.

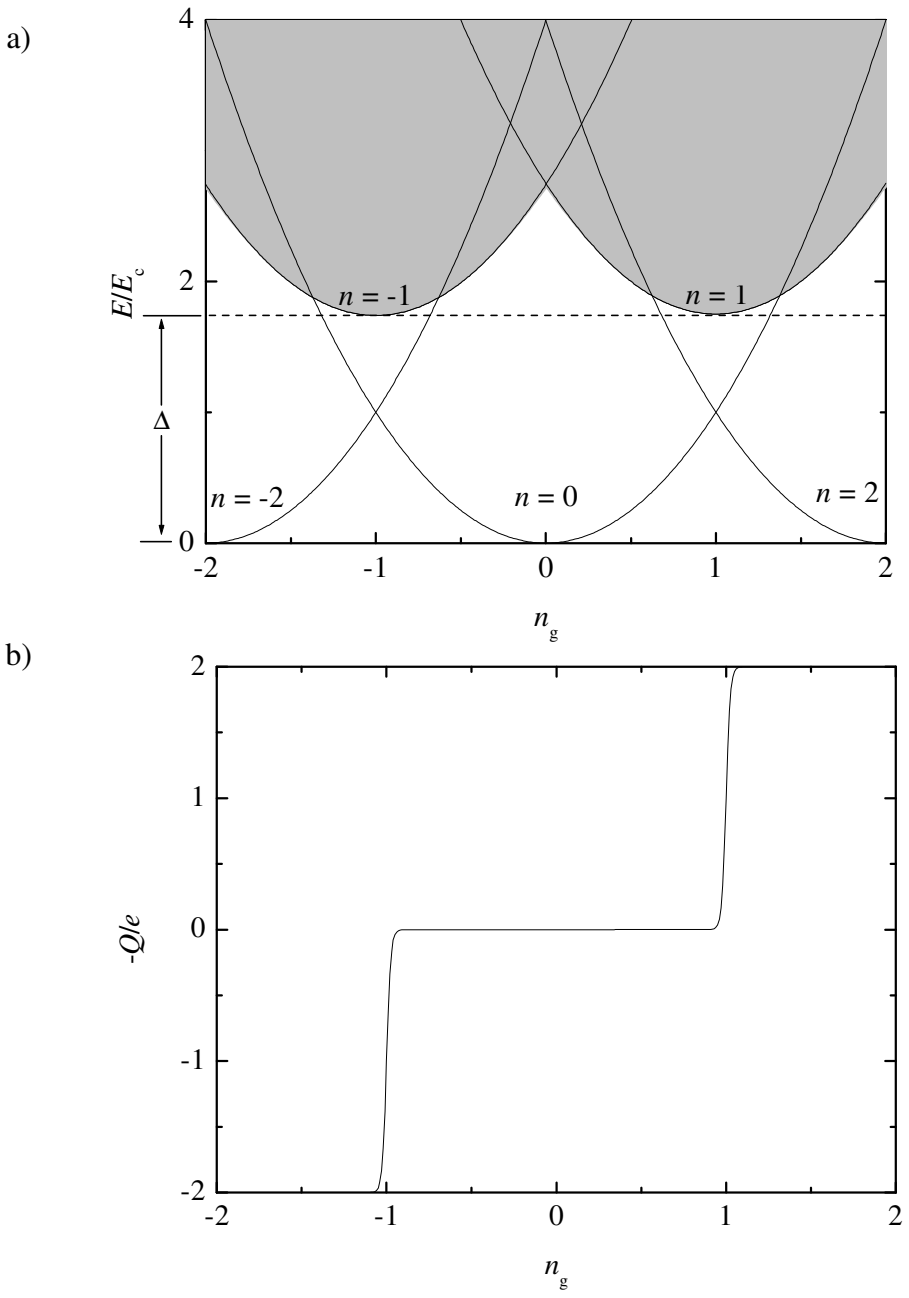

Fig. 2.4: (a) Electrostatic energy in a superconducting box with $E_c<\Delta$. Charge states with odd-n are displaced vertically to reflect the energy cost of creating a quasiparticle. The gray areas show allowed quasiparticle energies, including their kinetic energy. (b) Average charge on the island for the energy diagram shown in (a). In this case the state with the minimum energy is always an even-n state and no steps appear at $n_g = \pm 1, \pm 3$, etc.

2.4 Quantum mechanical description of the CPB

In the above description, I implicitly assumed that quantum fluctuations of the charge were negligible and that therefore n was precisely defined. In fact, this need not be true. In particular, one must take into account the effect of Cooper pair tunneling.

Neglecting dissipation and the environmental impedance and in the absence of quasiparticles (even n only) the Hamiltonian of the box is given by [22]:

$$H = E_c\left(n - n_g\right)^2 - E_J\cos(\phi) \tag{2.3}$$

where ϕ is the difference in the gauge-invariant phase difference of the superconducting macroscopic wave functions of the lead and island electrodes [15] and E_J is the Josephson energy of the junction. E_J is related to the energy gap and to the junction's critical current I_o according to [35]:

$$E_J = \frac{R_Q}{R}\frac{\Delta}{8} = \frac{I_o\Phi_o}{2\pi} \tag{2.4}$$

where $R_Q \equiv h/e^2 = 25.9\ \mathrm{k}\Omega$ is the resistance quantum and R is the normal state tunnel resistance. The excess number of Cooper pairs $n_p = n/2$ and the phase difference ϕ are canonical conjugate variables obeying the commutation relation $[\phi, n_p] = i$ [36].

The competition between charge and phase degrees of freedom is quantified by the ratio E_c/E_J. In the limit where $E_J \gg E_c$ the superconducting phase is well defined and charging effects are not significant. On the other hand, if $E_J \ll E_c$, charging effects dominate and the phase is not sharply defined. A CPB typically has parameters in the range $E_c \gtrsim E_J$ where charging effects are important but E_J is not completely negligible compared to E_c. Using charge states as a basis Eq. 2.3 can be written as [36]:

$$H = E_c\sum_{even-n}\left(n - n_g\right)^2\left|n\right\rangle\left\langle n\right| - \frac{E_J}{2}\sum_{even-n}\left(\left|n\right\rangle\left\langle n+2\right| + \left|n+2\right\rangle\left\langle n\right|\right) \tag{2.5}$$

In the subspace spanned by the five charge states n=−4,−2,0,2 and 4, the Hamiltonian takes the form:

$$H = \begin{pmatrix} E_c(4+n_g)^2 & -\frac{E_J}{2} & 0 & 0 & 0 \\ -\frac{E_J}{2} & E_c(2+n_g)^2 & -\frac{E_J}{2} & 0 & 0 \\ 0 & -\frac{E_J}{2} & E_c(n_g)^2 & -\frac{E_J}{2} & 0 \\ 0 & 0 & -\frac{E_J}{2} & E_c(2-n_g)^2 & -\frac{E_J}{2} \\ 0 & 0 & 0 & -\frac{E_J}{2} & E_c(4-n_g)^2 \end{pmatrix} \quad (2.6)$$

Figure 2.5a shows the two lowest eigen-energies obtained by numerically solving the Hamiltonian (2.6) with $E_c/E_J=2$. I obtained the eigen-values and eigenvectors using MatLab (see Apendix A). I note that the energy bands are reminiscent of the parabolas of Fig. 2.4 except near the degeneracy points ($n_g=\pm 1$) where the parabolas are now split apart rather than crossing. At the degeneracy point the energy splitting is equal to E_J in the limit $E_J \ll E_c$. Figure 2.5b shows the expectation value of the charge in the ground state and first excited state for the same parameters used in Fig. 2.5a.

Shnirman *et al*. [24] first proposed that the two lowest energy states can be used as the basis for a qubit. The state of the qubit can be determined, for example, by measuring the charge on the box with a single electron transistor. The realization of this qubit requires the CPB to have $\Delta > E_c$, $E_c \gtrsim E_J$ and $\Delta, E_c, E_J \gg k_B T$. The first condition makes the energy of the odd-n states (i.e. states with one quasiparticle on the island) larger than the energy of the even-n states. The second condition leads to well-defined charge states and

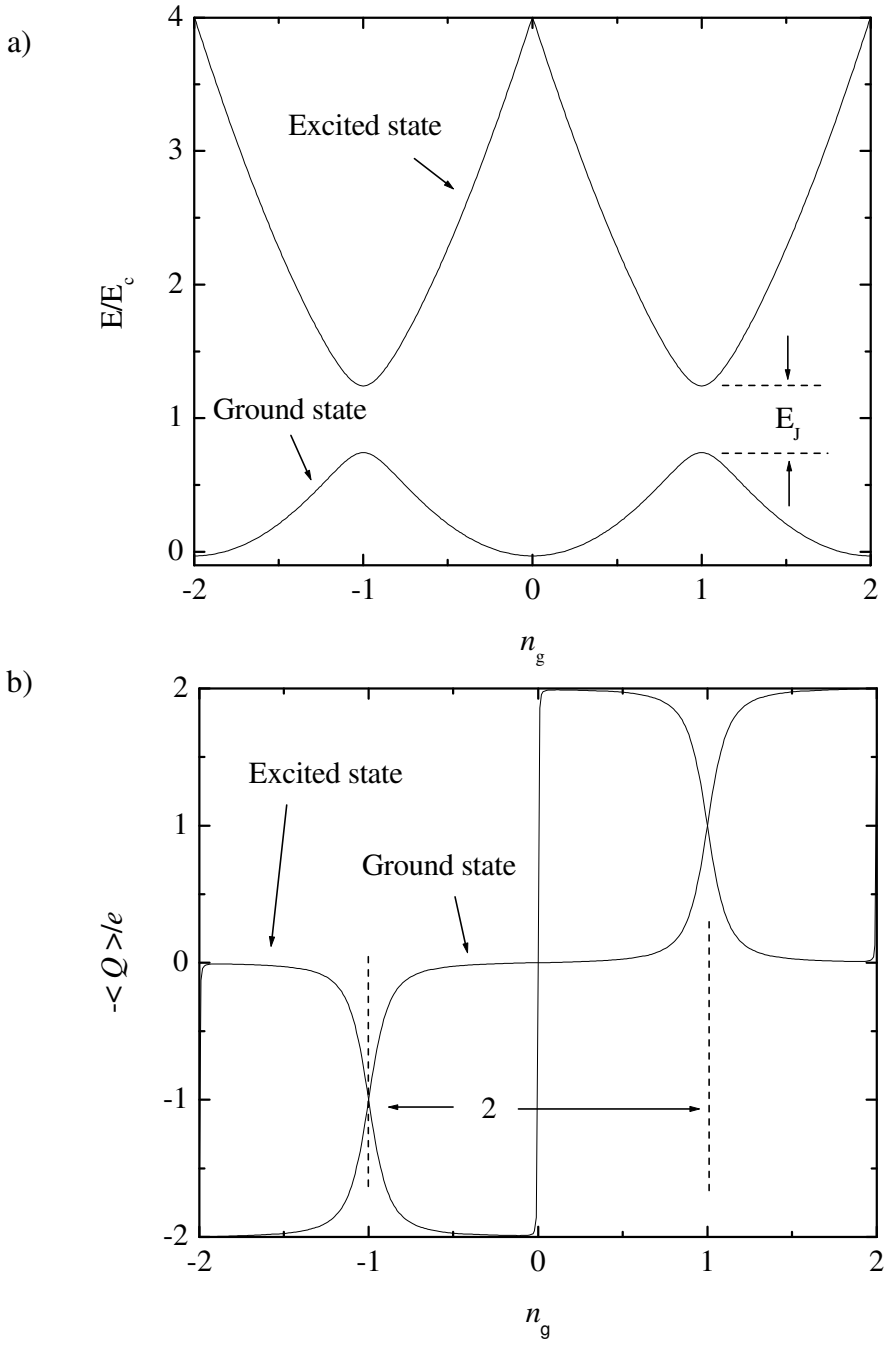

Fig. 2.5: (a) Ground state and first excited state energies of the CPB as a function of n_g with $E_c/E_J=2$ and $T=0$ and no quasiparticles. (b) Expectation value of the charge in the ground state and first excited state for the same parameters.

allows for the state of the qubit to be determined by a charge measurement. The last condition is necessary to prevent thermal excitations.

If the gate voltage is limited to the range $0 \le n_g \le 2$ the state of the box can be described approximately using just the $n=0$ and $n=2$ charge states.

In this case, the Hamiltonian can be represented by a 2×2 matrix:

$$H = \frac{1}{2}\begin{pmatrix} 4E_c(1-n_g) & -E_J \\ -E_J & -4E_c(1-n_g) \end{pmatrix} \tag{2.7}$$

The eigen-energies and eigen-states can be written as:

$$E_o = -\frac{1}{2}\sqrt{[4E_c(1-n_g)]^2 + [E_J]^2} \tag{2.8}$$

$$E_1 = +\frac{1}{2}\sqrt{[4E_c(1-n_g)]^2 + [E_J]^2} \tag{2.9}$$

$$|\psi_o\rangle = \cos\left(\frac{\theta}{2}\right)|0\rangle + \sin\left(\frac{\theta}{2}\right)|2\rangle \tag{2.10}$$

$$|\psi_1\rangle = -\sin\left(\frac{\theta}{2}\right)|0\rangle + \cos\left(\frac{\theta}{2}\right)|2\rangle \tag{2.11}$$

where

$$\theta = \arctan\left(\frac{E_J}{4E_c(1-n_g)}\right) \tag{2.12}$$

I note that θ goes from 0 at $n_g=0$, to $\theta=\pi/2$ at the degeneracy point ($n_g=1$), to $\theta \approx \pi$ at $n_g=2$. We can also write the energy splitting between the ground state and the excited state as:

$$\Delta E_{10} = \sqrt{[4E_c(1-n_g)]^2 + [E_J]^2} \tag{2.13}$$

which has a minimum of E_J at $n_g=1$, as expected.

Finally, I note that in many experiments the CPB has two Josephson junctions in parallel connecting the island to ground (see Fig. 2.6). The idea is that the two parallel junctions act like a single junction with a Josephson energy that can be tuned by an applied magnetic field, according to [37]:

$$E_J = \frac{R_Q}{R}\frac{\Delta}{8}\cos\left(\frac{\pi\Phi}{\Phi_o}\right). \tag{2.14}$$

Here Φ is the magnetic flux through the SQUID loop, $R=R_1R_2/(R_1+R_2)$ is the parallel tunnel resistance of the junctions and $\Phi_o=h/2e$ is the flux quantum. This is particularly useful, for example, to characterize the behavior of a system in E_J, since it allows results to be obtained on the same device, with identical parameters except for E_J. In this configuration the total capacitance of the CPB is given by $C_\Sigma=C_1+C_2+C_g$, where C_1 and C_2 are the capacitances of the Josephson junctions.

2.5 Concluding remarks

In this chapter I reviewed the theory of the normal metal single electron box and the superconducting Cooper pair box. Under appropriate conditions, the CPB can be used as a qubit for quantum computing. I presented expressions to compute the energy levels and eigenstates of the qubit as a function of device parameters and gate voltage bias.

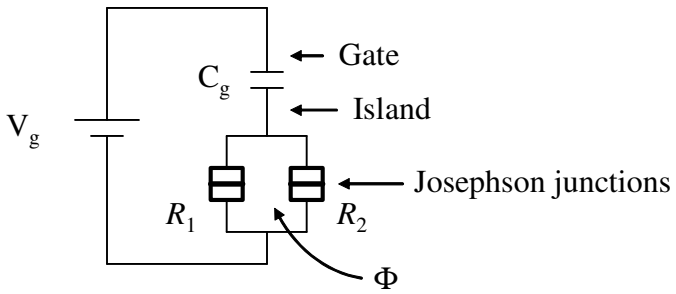

Fig. 2.6: Schematic of a CPB with a double junction. The Josephson energy can be tuned by applying a magnetic flux Φ through the loop.

Chapter 3: Energy relaxation and dephasing in the CPB

3.1 Introduction

The Hamiltonians discussed in Chapter 2 did not include fluctuations in the controlling variables, *i.e*. the gate voltage and the magnetic flux. Charge noise coming from any motion of charges in the substrate and the tunnel barriers also changes the electrostatic energy of the box. Under certain circumstances these can be approximated as random terms in the Hamiltonian and will cause the quantum state of the box to evolve in an uncontrolled way, degrading the performance as a qubit. In addition, I have not included energy loss caused by the leads attached to the box, or from dielectric loss in the insulators. Ultimately, if the CPB is to be useful as a qubit, it is essential to understand and minimize all sources of loss and decoherence. In this chapter, I review the relevant theory.

3.2 Excitation and relaxation rates

Charge motion affects the CPB in two different ways. A fluctuating quantity can always be decomposed into a part that commutes with the Hamiltonian and a part that does not. For example, voltage and charge noise commute with the electrostatic part of the Hamiltonian but not with the Josephson term. The opposite is true for flux noise. If the part that does not commute is at high enough frequency, it can cause transitions between eigenstates (excitation or relaxation). On the other hand, the part that commutes causes the eigenstates to acquire random phases, therefore destroying coherent

superpositions. The CPB tends to be relatively more sensitive to voltage and charge noise due to its large ratio of E_c/E_J.

The effects of gate voltage noise on the CPB can be calculated for certain specific situations. For example, Schoelkopf *et al.* [38] found the transition rates between the CPB eigenstates using Fermi's golden rule. For this calculation, they used the fluctuations of the gate voltage about its mean value as the perturbation and defined the power spectrum of voltage fluctuations S_V as:

$$S_V(\omega) = \frac{1}{2\pi}\int_{-\infty}^{\infty} d\tau\, e^{i\omega\tau}\langle V(t+\tau)V(t)\rangle \tag{3.1}$$

where $V(t)$ is the voltage at time t and $\langle\rangle$ denote an ensemble average over time t. I note that power spectra are conventionally defined only for positive frequencies, *i.e.* $\omega>0$. If the gate voltage is treated as a classical variable, the autocorrelation function $\langle V(t+\tau)V(t)\rangle$ is real and $S_V(\omega)=S_V(-\omega)$. However, with a full quantum mechanical treatment $S_V(\omega)$and $S_V(-\omega)$ are generally different and the distinction between positive and negative frequencies has a physical meaning; Noise at negative frequency is responsible for excitation of the qubit whereas noise at positive frequency causes relaxation [38].

At the typical low powers of interest, only the noise in the neighborhood of frequency $\omega_{10}=\Delta E_{10}/\hbar$ generates transitions. The excitation rate is given by [38]:

$$\Gamma_{\uparrow} = 2\pi\left(\frac{e}{\hbar}\right)^2 \kappa^2 \frac{E_J^2}{\left[4E_c(1-n_g)\right]^2 + E_J^2} S_V(-\omega_{10}) \tag{3.2}$$

while the relaxation rate is equal to [38]

$$\Gamma_{\downarrow} = 2\pi\left(\frac{e}{\hbar}\right)^2 \kappa^2 \frac{E_J^2}{\left[4E_c(1-n_g)\right]^2 + E_J^2} S_V(\omega_{10}) \tag{3.3}$$

The factor κ is the coupling strength between the noise source and the island and is equal to C_g/C_Σ for voltage noise applied to the gate (see Fig. 2.6).

If the gate voltage fluctuations are generated by the impedance of the leads at temperature T, the spectral density S_V is given by [38]:

$$S_V(\omega) = \frac{1}{\pi}\left\{\frac{R\hbar\omega}{1-\exp\left(-\frac{\hbar\omega}{k_B T}\right)}\right\} \tag{3.4}$$

where R is the lead impedance. I note that this is essentially just the fluctuation dissipation theorem. Figure 3.1a shows a plot of the spectral density (Eq. 3.4) for a 50 Ω resistor at T=0 and 1K. At T>0 the resistor generates noise of positive and negative frequencies so it causes excitation and relaxation of the qubit. At T=0 the box is not excited but the relaxation rate is still limited by quantum fluctuations due to a finite environment impedance. This is just spontaneous emission.

I note that the inverse of the total transition rate $(\Gamma\uparrow+\Gamma\downarrow)^{-1}$ is usually called T_1. If $\Gamma\uparrow$=0 (*i.e.* at T=0 and in the absence of non-equilibrium noise sources) this is just the lifetime of the excited state. Figure 3.1b shows T_1 calculated for a CPB at T=0 with E_c=1K, E_J=0.5K and coupled to a 50 Ω impedance with a coupling factor κ=0.01. I note that the minimum lifetime occurs at n_g=1. At this point the unperturbed Hamiltonian is proportional to σ_x and becomes orthogonal with the perturbation, which is proportional to σ_z.

The functional dependence of T_1 vs n_g shown in Fig. 3.1b has been observed in recent experiments [39], confirming that noise coupled to charge degrees of freedom is the

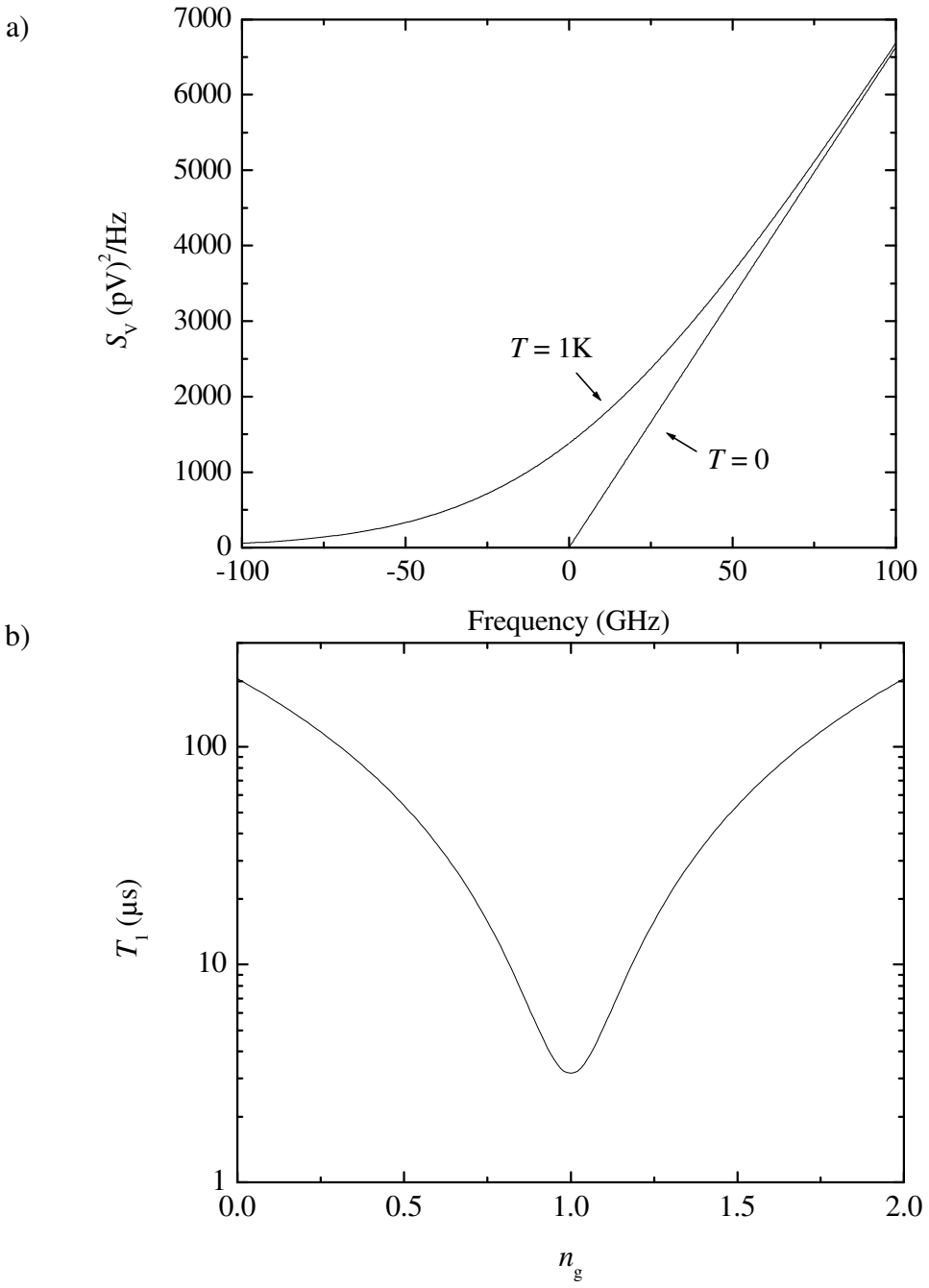

Fig. 3.1: (a) Spectral density S_V for a 50 Ω resistor at T=1 K and T=0. (b) Lifetime of the excited state T_1 of a CPB at T=0 with E_c=1K, E_J=0.5K with the gate coupled to a 50 Ω impedance with a coupling factor $\kappa \equiv C_g/C_\Sigma$=0.01.

dominant mechanism for relaxation in the CPB. However, the measured lifetimes (about 100 ns) in that and other experiments [29,30] are much smaller that the μs values predicted by Fig. 3.1 and thus they cannot be accounted for by relaxation onto a 50 Ω impedance.

Astafiev *et al.* [39] postulated that relaxation in his device was caused by charge fluctuators coupled to the CPB. In single electron devices, one normally finds excess low frequency noise with a spectral density $S_q=\alpha/f$, where α is typically on the order of $(10^{-3}e)^2$ [40]. Low frequency noise in SETs is believed to be generated by a large number of two level fluctuators with an electric dipole moment and energy splitting ε [40]. In thermal equilibrium, only fluctuators with energies $\varepsilon \lesssim k_B T$ are activated. Superposition of the noise coming from individual fluctuators has been found to produce a $1/f$ spectrum with a T^2 temperature dependence [41]. Astafiev's hypothesis is that, fluctuators with $\varepsilon > k_B T$ can absorb energy from the CPB and therefore, provide a relaxation channel.

This assumption is supported by calculations by Schnirman *et al.* [42], showing that an ensemble of coherent two level systems with a specific distribution of parameters produces high frequency noise proportional to f and $1/f$ low frequency noise with a T^2 temperature dependence. Martinis *et al.* [19] also reports that dielectric loss (which is caused by absorption of energy by two level systems [43]) in amorphous insulators such as SiO_2 and Al_2O_3 can be an important decoherence mechanism in superconducting phase qubits. In view of these findings, it cannot be ruled out that relaxation in the CPB can be affected by materials issues. Another possible source of relaxation, SET back-action [44], will be discussed in Chapter 4.

3.3 Dephasing

Dephasing effects can be understood by looking at the evolution of states formed from superpositions of eigenstates. For instance, if the box is in the state $a|0\rangle+b|1\rangle$ at $t=0$ after a time τ it will evolve to the state $a|0\rangle+e^{-i\phi}b|1\rangle$ with the phase $\phi=\Delta E_{10}\tau/\hbar$. Charge noise q_n for example, changes the energy difference ΔE_{10} depending on the slope of the energy bands ($\partial\Delta E_{10}/\partial q$) at the operating point (see Fig. 2.5a). From Eq. 2.13 we obtain:

$$\frac{\partial \Delta E_{10}}{\partial q}=\frac{\partial \Delta E_{10}}{\partial n_g}\frac{\partial n_g}{\partial q}=-\frac{1}{e}\frac{(4E_c)^2(1-n_g)}{\sqrt{\left[4E_c(1-n_g)\right]^2+E_J^2}} \tag{3.5}$$

For a pure dephasing mechanism, the mean squared phase noise is given approximately by [45]:

$$\left\langle \phi_n^2(t)\right\rangle \cong \frac{1}{\hbar^2}\left(\frac{\partial \Delta E_{10}}{\partial q}\right)^2\int_0^\infty S_q(f)\frac{\sin^2(\pi f t)}{(\pi f)^2}df \tag{3.6}$$

Dephasing in the CPB appears to be caused predominantly by low frequency charge noise [46]. The dephasing time T_2 resulting from $1/f$ noise can be estimated from Eq. 3.6, using:

$$\int_0^\infty S_q(f)\frac{\sin^2(\pi f t)}{(\pi f)^2}df=\int_0^\infty \frac{\alpha}{f}\frac{\sin^2(\pi f t)}{(\pi f)^2}df\approx\int_{1/tm}^{1/t}\frac{\alpha}{f}t^2df=\alpha t^2\ln\left(\frac{t_m}{t}\right) \tag{3.7}$$

where t_m is the measurement time. Combining Eqs. 3.5, 3.6 and 3.7 gives for $1/f$ noise:

$$\left\langle \phi_n^2(t)\right\rangle \approx\left(\frac{1}{\hbar e}\right)^2\frac{\left[(4E_c)^2(1-n_g)\right]^2}{\left[4E_c(1-n_g)\right]^2+E_J^2}t^2\alpha\ln\left(\frac{t_m}{t}\right) \tag{3.8}$$

I can define T_2 as the time when the accumulated phase $\langle\phi^2(t)\rangle\approx 1$. Thus:

$$T_2 \approx \sqrt{\frac{(\hbar e)^2}{\alpha}\frac{\left[4E_c\left(1-n_g\right)\right]^2 + E_J^2}{\left[\left(4E_c\right)^2\left(1-n_g\right)\right]^2}\ln\left(\frac{t_m}{T_2}\right)} \tag{3.9}$$

I note that the first order expansion (Eq. 3.6) fails close to the degeneracy point where the slope $\partial\Delta E_{10}/\partial n_g$ is zero. This means that charge noise should have much less effect at that point, as has been emphasized by Vion *et al.* [14]. An estimate of T_2 at n_g=1 can be obtained by making a few additional approximations. To second order, the rms fluctuations in energy $\delta(\Delta E_{10})$ are given by:

$$\delta\left(\Delta E_{10}\right) = \frac{1}{2}\frac{\partial^2 \Delta E_{10}}{\partial q^2}\delta q^2 \tag{3.10}$$

The coefficient $\partial^2\Delta E_{10}/\partial q^2$ can be found by differentiating Eq. 3.5. At n_g=1, I find:

$$\left.\frac{\partial^2 \Delta E_{10}}{\partial q^2}\right|_{ng=1} = \frac{1}{e^2}\frac{\left(4E_c\right)^2}{E_J} \tag{3.11}$$

and the rms charge noise δq can be estimated from:

$$\left(\delta q\right)^2 = \int_0^\infty S_q df \approx \int_{fm}^{fc}\frac{\alpha}{f}df = \alpha\ln\left(\frac{f_c}{f_m}\right) \tag{3.12}$$

where f_m=1/t_m is the inverse of the measurement time and f_c is a higher cut-off frequency of order $\Delta E_{10}/h$.

We can now write the rms phase noise at the degeneracy point as:

$$\delta\phi \approx \frac{1}{\hbar}\int_0^t \delta\left(\Delta E_{10}\right)dt = \frac{1}{2\hbar e^2}\frac{\left(4E_c\right)^2}{E_J}t\alpha\ln\left(\frac{f_c}{f_m}\right) \tag{3.13}$$

Setting $\delta\phi$=1, we find T_2 at the degeneracy point :

$$T_2\big|_{ng=1} \approx \frac{2\hbar e^2}{\alpha \ln\left(\frac{f_c}{f_m}\right)} \frac{E_J}{(4E_c)^2} \tag{3.14}$$

Figure 3.2 shows T_2 found from Eqs. 3.8 and 3.13 for a box with the same parameters used in Fig. 3.1, with $\alpha=(10^{-3}e)^2$ and t_m=1s. Here $(T_2)^{-1}=(T_{2\ \text{Eq. 3.9}})^{-1}+(T_{2\ \text{Eq. 3.14}})^{-1}$. Note that the dephasing is smallest and T_2 largest at n_g=1, as expected, and that T_2 reaches ~0.4 ns away from n_g=1. Finally, I note that in principle dephasing from low frequency noise can be greatly reduced by using spin echo refocusing techniques [45,46].

3.4 Discussion

The theoretical estimates for T_1 and T_2 from charge noise (see Figs. 3.1a and 3.2) suggest some guidelines for the optimization of the CPB qubit. For example, quantum operations should take place at the degeneracy point, where dephasing is minimized. However, the qubit eigenstates cannot be discriminated by a charge measurement at this point so the V_g bias will apparently need to be shifted away from degeneracy if an rf-SET is to be used for the state readout. It is also desirable to readout the state close to n_g=0 where T_1 is maximum, rather than at n_g=1, where T_1 is minimal. However, I note that the states n=2 and n=−2 are degenerate at n_g=0 so one should not get too close to this point during state read-out.

Both T_1 and T_2 could be increased either by parameter optimization or by reducing the noise coupled to the CPB. A large ratio of E_J/E_c would be beneficial to obtain a long dephasing time (see Eq. 3.13). However, this might conflict with other aspects of the qubit. For instance, Eqs. 3.2 and 3.3 show that T_1 scales as $(E_c/E_J)^2$ away from the degeneracy point. If a long T_1 is required to achieve single shot readout an increase of the

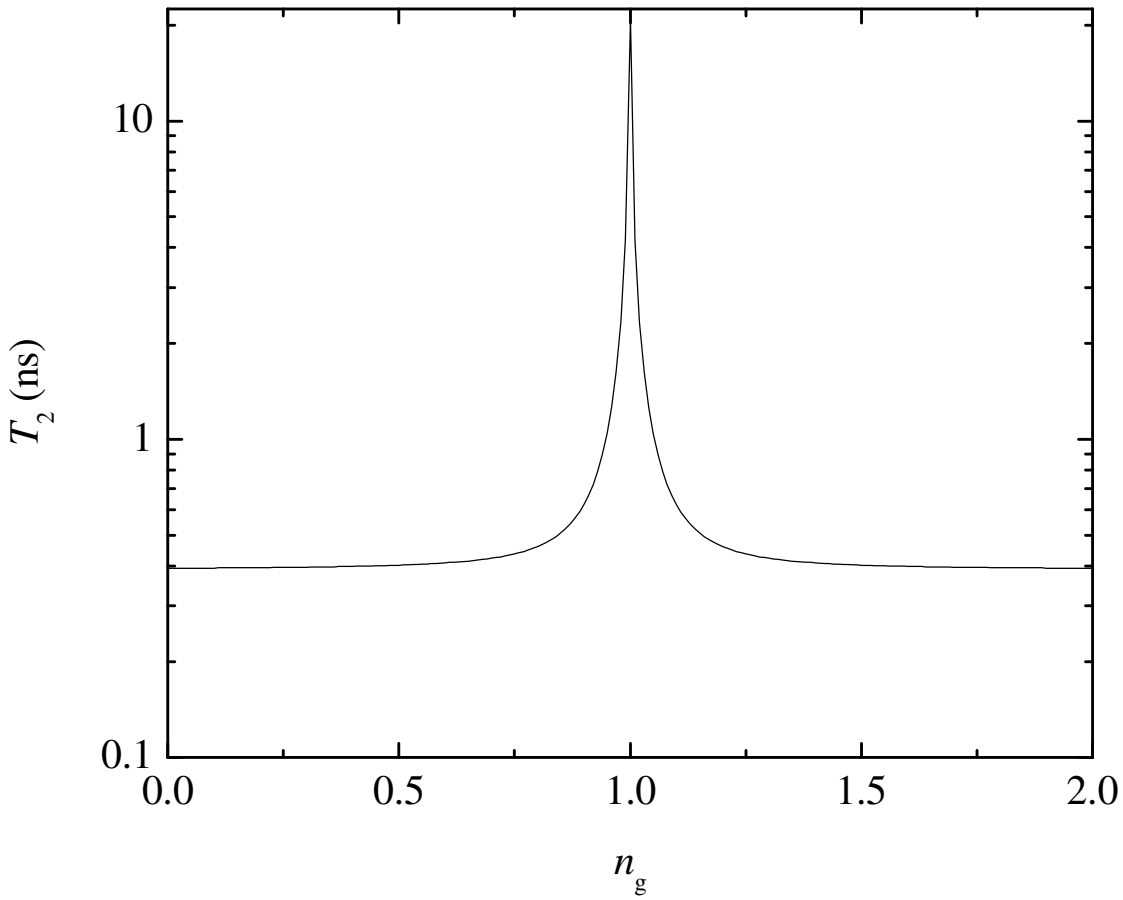

Fig. 3.2: Estimated dephasing time T_2 for a CPB with E_c=1K, E_J=0.5K resulting from 1/*f* charge noise with a power spectrum $S_q = (10^{-3}e)^2/f$ and a measurement time of 1s.

ratio E_c/E_J could result in T_2 being too short. Regardless of T_1 requirements, $E_c \gtrsim E_J$ is a necessary condition to be able to readout the state by a charge measurement.

On the other hand, one could try to decrease low frequency noise to improve dephasing times. 1/*f* charge noise is caused at least in part by the capacitive coupling of the CPB island to local charge fluctuators [40]. A reduction in 1/f noise has been demonstrated on SETs with very small islands [48], where charge noise as low as 10^{-5} $e/(\mathrm{Hz})^{1/2}$ was achieved at 10 Hz. However, reducing the size of the CPB island is in conflict with a measurement of its charge. The coupling $\kappa = C_c/C_\Sigma$ between the box and the electrometer cannot be made arbitrarily small since the SET sensitivity is at best on the order of 10^{-6} $e/(\mathrm{Hz})^{1/2}$ if it is limited by shot noise [49]. At the same time, C_Σ should be made large enough to keep $\Delta > E_c = e^2/2C_\Sigma$, which sets a lower limit on the coupling capacitance C_c and therefore on the size of the island. I note that Astafiev *et al.* [39] proposed that charge fluctuators are responsible not only for T_2 but also for T_1. The implication of this is that single shot charge measurements would not be affected by a reduction in κ as long as T_1 increases in the same proportion.

Given the wide range of design possibilities, an optimization of a CPB qubit will require a full understanding of the different decoherence mechanisms, and this is not available at present.

3.5 Conclusions

I presented the theoretical background for calculating energy relaxation and dephasing in the CPB. Estimates of T_1 considering only the electromagnetic environment yield relaxation times that are much longer than measured ones. I discussed the possibility that

relaxation and dephasing could be caused by two-level fluctuators. This decoherence mechanism might originate in lossy insulators surrounding the qubit and hopefully could be minimized by better materials and/or processing technology.

Chapter 4 : The rf-SET

4.1 Normal SET

The single electron transistor (SET) is a very sensitive electrometer, capable of detecting a charge much smaller than $e=1.602\times10^{-19}$ C. Figure 4.1 shows a schematic of a normal metal SET. The SET consists of two ultra small tunnel junctions that are connected in series. The junctions can be characterized by resistors R_1 and R_2 and capacitors C_1 and C_2. The middle electrode or island is isolated from the rest of the circuit by the junctions. The number of electrons n on the island can only change by tunneling through the junctions. As discussed in Chapter 2, n becomes a well defined integer quantity if the transistor is cooled down to a temperature $k_BT \ll E_c \equiv e^2/2C_\Sigma$ and if $R_\Sigma \equiv R_1+R_2 \gg R_Q$, where $C_\Sigma=C_1+C_2+C_g$ is the total capacitance of the SET.

When a single tunnel junction with non-superconducting electrodes is voltage biased, an average current I flows. This current is equal to the average charge per unit time that tunnels from the source to the drain. The IV characteristic is linear at low applied voltage and therefore the junction can be characterized by a resistance R, which will generally be a non-linear function of the voltage [15].

In an SET, current flow is produced by transitions between charge states. For the above assumptions, the current I can be calculated using the orthodox theory [50], and we find:

$$I = -e\sum_n P(n)\left[\Gamma_1^+(n)-\Gamma_1^-(n)\right] = -e\sum_n P(n)\left[\Gamma_2^-(n)-\Gamma_2^+(n)\right] \qquad (4.1)$$

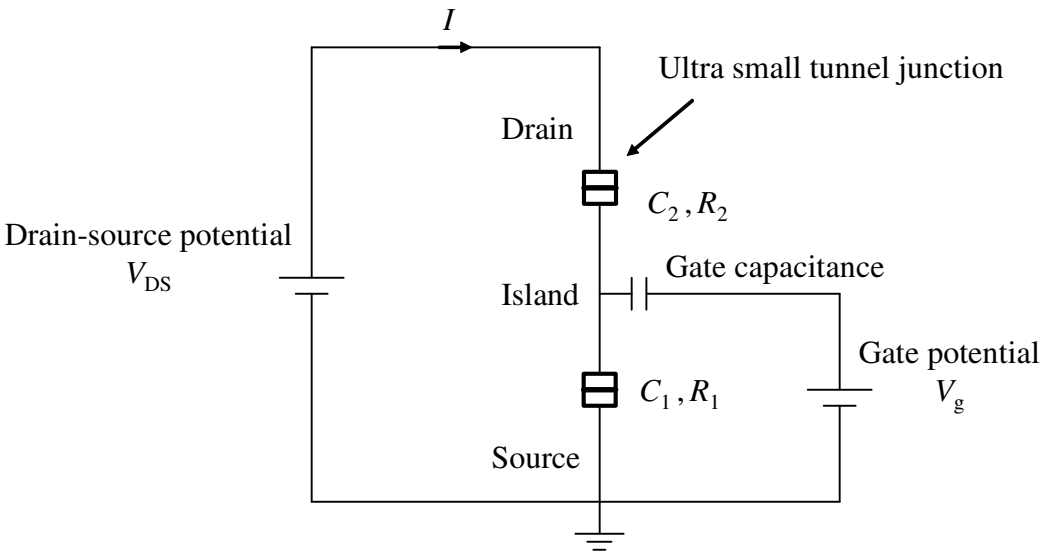

Fig. 4.1: Schematic of a single electron transistor (SET).

where $\Gamma_1^+(n)$ and $\Gamma_2^+(n)$ are the transition rates $|n\rangle \rightarrow |n+1\rangle$ through junctions 1 and 2 respectively, $\Gamma_1^-(n)$ and $\Gamma_2^-(n)$ are the corresponding rates $|n\rangle \rightarrow |n-1\rangle$ through junctions 1 and 2 and $P(n)$ is the probability for the SET to be in the state $|n\rangle$.

In the steady state, the probabilities $P(n)$ are found from the detailed balance condition:

$$P(n+1)\left[\Gamma_1^-(n+1)+\Gamma_2^-(n+1)\right] = P(n)\left[\Gamma_1^+(n)+\Gamma_2^+(n)\right] \tag{4.2}$$

The tunneling rates are given by [33]:

$$\Gamma_{1,2}^{\pm}(n+1) = \frac{-\Delta G_{1,2}^{\pm}(n+1)}{e^2 R_{1,2}} \frac{1}{1-\exp\left(\frac{\Delta G_{1,2}^{\pm}(n+1)}{K_B T}\right)} \tag{4.3}$$

Here, $\Delta G_1^+(n)$ and $\Delta G_2^+(n)$ are the change in the free energy of the system after a transition $|n\rangle \rightarrow |n+1\rangle$ through junctions 1 and 2, respectively, and $\Delta G_1^-(n)$ and $\Delta G_2^-(n)$ are the change in the free energy of the system after a transition $|n\rangle \rightarrow |n-1\rangle$ through junctions 1 and 2, respectively. The free energy includes the electrostatic energy stored in the capacitors and the work done by the voltage sources [15]. The free energy changes are:

$$\Delta G_1^-(n+1) = -E_c\left[2(n-n_g)+1\right] - \frac{C_2+C_g}{C_\Sigma} eV_{DS} \tag{4.4a}$$

$$\Delta G_1^+(n) = E_c\left[2(n-n_g)+1\right] + \frac{C_2+C_g}{C_\Sigma} eV_{DS} \tag{4.4b}$$

$$\Delta G_2^-(n+1) = -E_c\left[2\left(n-n_g\right)+1\right]+\frac{C_1}{C_\Sigma}eV_{DS} \tag{4.4c}$$

$$\Delta G_2^+(n) = E_c\left[2\left(n-n_g\right)+1\right]-\frac{C_1}{C_\Sigma}eV_{DS} \tag{4.4d}$$

Figure 4.2 shows *IV* characteristics calculated from these formulas with SET parameters R_Σ=100 kΩ, C_Σ=1 fF, R_1=R_2, C_1=C_2 and T=100 mK. The details of the calculation are provided in Appendix A. The plateau in Fig. 4.2a in the range $0<V_{DS}<2E_c/e$ is known as the Coulomb blockade. In this range, current through the SET is largely suppressed because of the high energy cost of charging the island. This energy changes from a maximum of E_c at n_g=0, ±1, *etc*, to zero at the degeneracy points n_g=±1/2, ±3/2, *etc*. At fixed voltage across the SET, the current is modulated by the gate voltage as a consequence of tuning the charging energy of the SET. This modulation is shown in Fig. 4.2b for a fixed drain-source voltage V_{DS} = 100 μV. Each period in the modulation curve corresponds to the average charge in the island changing by one electron.

I note that, if $R \lesssim R_Q$ or the material is not a normal metal, or the island becomes so small that internal states are evident, the orthodox theory will fail. The next section discusses one such system.

4.2 Superconducting SET

The *IV* characteristics of a superconducting SET are more complex than the characteristics of a normal SET. To understand why they behave so differently, I first

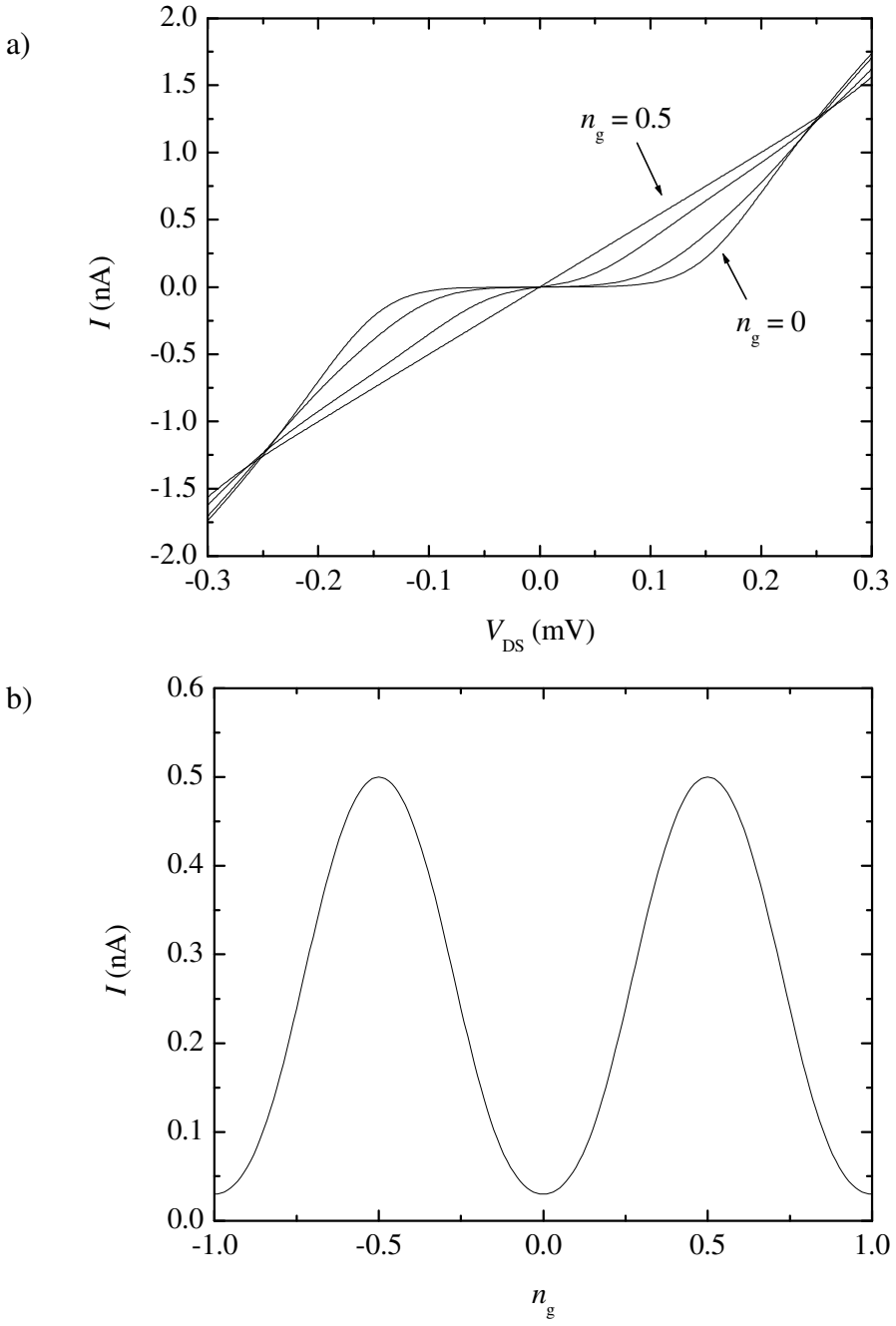

Fig. 4.2: Simulated *IV* characteristics of a normal SET with R_Σ = 100 kΩ, C_Σ = 1fF, R_1=R_2=50 kΩ, C_1=C_2= 0.5 fF and T=100 mK. (a) Current as a function of drain-source voltage V_{DS} for n_g from 0 to 0.5 (b) Current versus n_g voltage at fixed V_{DS}=100 μV.

consider the theoretical *IV* curve of an ideal, unshunted single Josephson junction without charging effects (see Fig. 4.3). A current spike or supercurrent is produced at $V=0$ due to the Josephson tunnel current, as given by the dc Josephson effect [14]. For $V>0$, a dc current flow implies power dissipation and this is only possible at energies that allow quasiparticle tunneling. Quasiparticles can be created if eV, the work done by the voltage source in transferring an electron across the junction, is larger than 2Δ. This process is known as Giaever tunneling [52]. The sharp rise of the current at $V=2\Delta/e$ arises from the discontinuity in the BCS density of states ($D(E)$) and corresponds to pair breaking. For an s-wave, BCS superconductor:

$$D(E)=\begin{cases} N(E_F)\dfrac{E}{\sqrt{E^2-\Delta^2}} & for\ E>\Delta \\ 0 & otherwise \end{cases} \tag{4.5}$$

where $N(E_F)$ is the normal density of states at the Fermi level. For $0<V<2\Delta/e$ the current is due to thermally excited quasiparticles and is strongly suppressed for temperatures $k_BT<<\Delta$.

In a superconducting SET, charging effects bring about new features in the *IV* characteristics. To illustrate these effects, Fig. 4.4 shows measured *IV* curves of a superconducting SET for different gate voltages. We first notice the apparent disappearance of the Josephson supercurrent at $V=0$. Second, there is a large quasiparticle current at $V_{DS}>4\Delta/e=876\mu V$, *i.e.* when the voltage across each junction is larger than 2Δ. The current in this range can be found using the orthodox theory by modifying the transition rates to include the superconducting gap [53]:

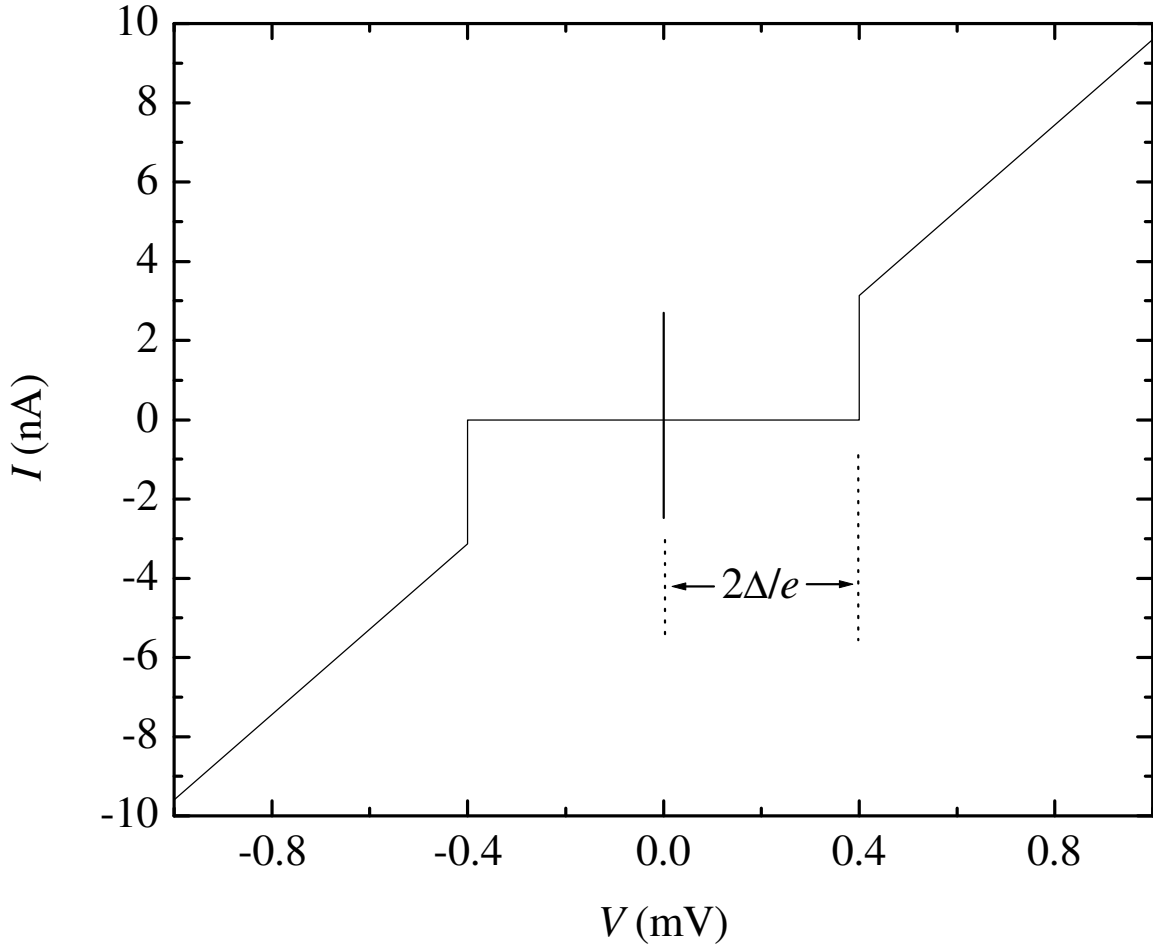

Fig. 4.3: Theoretical *IV* curve of an ideal single current-biased Josephson junction with a normal state resistance $R=100$ kΩ at $T=0$, neglecting charging effects ($E_c \ll E_J$). For clean Al thin films $\Delta/e=200\mu V$.

$$\Gamma(\Delta G) = \frac{1}{e^2 R} \int_{-\infty}^{\infty} \frac{D(E)}{N(E_F)} \frac{D(E+\Delta G)}{N(E_F)} f(E)[1 - f(E+\Delta G)]dE \tag{4.6}$$

where ΔG and $D(E)$ are given by Eqs. 4.4 and 4.5 respectively and $f(E)$ is the Fermi function:

$$f(E) = \frac{1}{1 + \exp\left(\frac{E-\mu}{k_B T}\right)} \tag{4.7}$$

where μ is the chemical potential.

The feature around V=574μV is known as the Josephson-quasiparticle peak (JQP) [54,55]. It results from a combination of Josephson tunneling through one junction followed by sequential tunneling of two quasiparticles through the other junction. Figure 4.5 shows a schematic of the JQP cycle. The source is kept at ground potential while the drain electrode is raised above ground by V_{DS}. The island potential depends on V_{DS}, n and V_g. For a particular n, the island potential can be made equal to V_{DS} by adjusting V_g (see Fig. 4.5). In this case, the states $|n+1\rangle$ and $|n-1\rangle$ are degenerate and Josephson tunneling can take place. In the range $2\Delta - E_c < V_{DS} < 2\Delta + E_c$ the state $|n+1\rangle$ is stable against quasiparticle tunneling but the states $|n\rangle$ and $|n-1\rangle$ are not. The result is that the $|n-1\rangle$ state transitions to $|n\rangle$ and then to $|n+1\rangle$ by sequential quasiparticle tunneling events. Thus the SET returns to the state $|n+1\rangle$ and the cycle starts again.

The two processes described above, Giaever tunneling and the JQP process, both show periodic current modulation by the gate voltage with e periodicity. In both situations V_{DS} is large enough to create quasiparticles. At very low V_{DS} (see Fig. 4.4b) a very small current can be seen that has $2e$ periodicity. This periodicity indicates that Cooper pairs

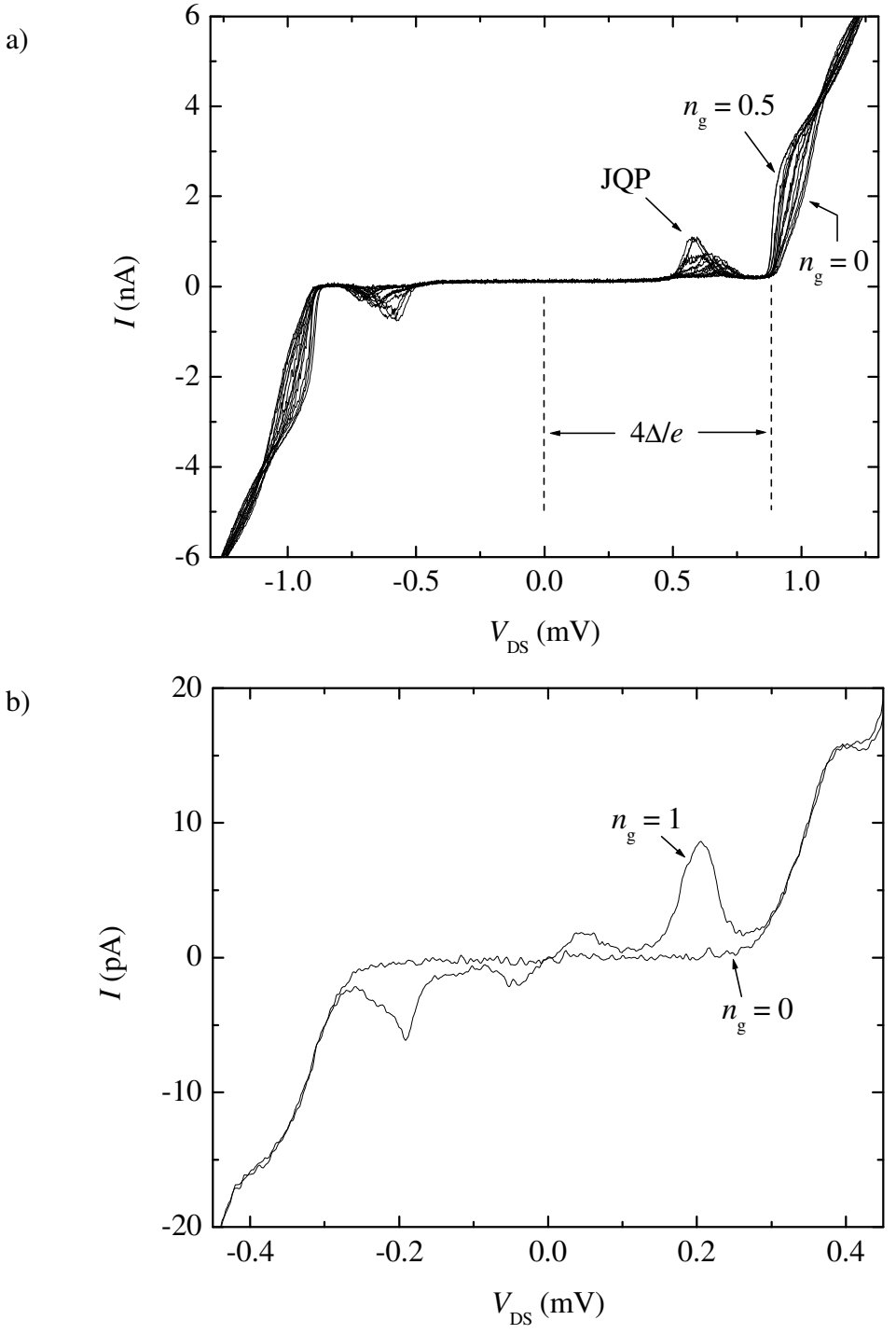

Fig. 4.4: (a) Measured I versus V_{DS} curves of an Al-AlO_x-Al superconducting SET (device CS1) at T=30 mK for a range of gate voltages. (b) IV characteristics at low V_{DS}.

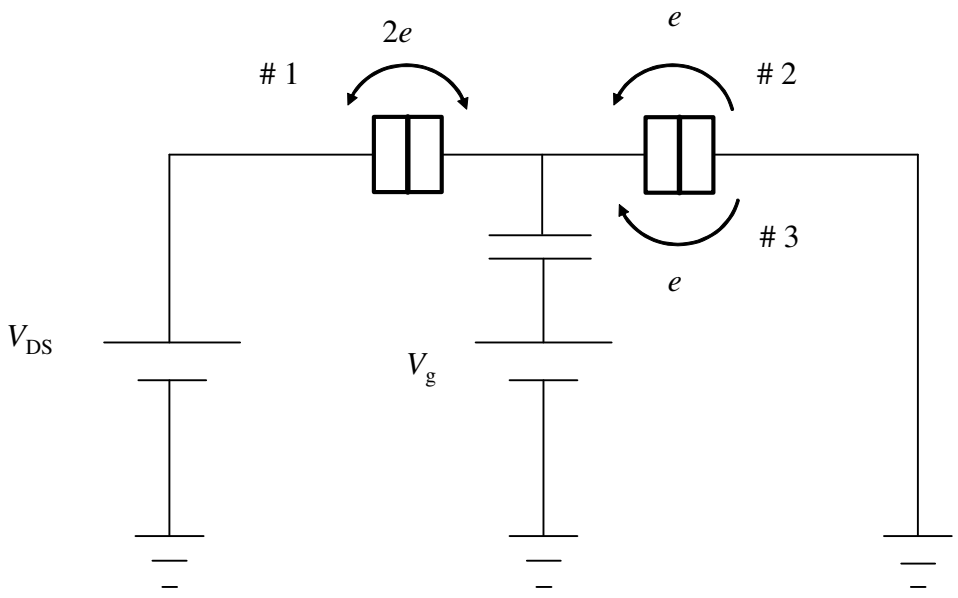

Fig. 4.5: Illustration of the JQP cycle. The SET undergoes transitions between the $|n+1\rangle$ and $|n-1\rangle$ states due to Josephson tunneling (# 1) between the drain and island electrodes. The island potential for the $|n\rangle$ and $|n-1\rangle$ states is larger than $2\Delta/e$ and therefore, these states decay quickly by successive quasiparticle tunneling events (# 2 and # 3).

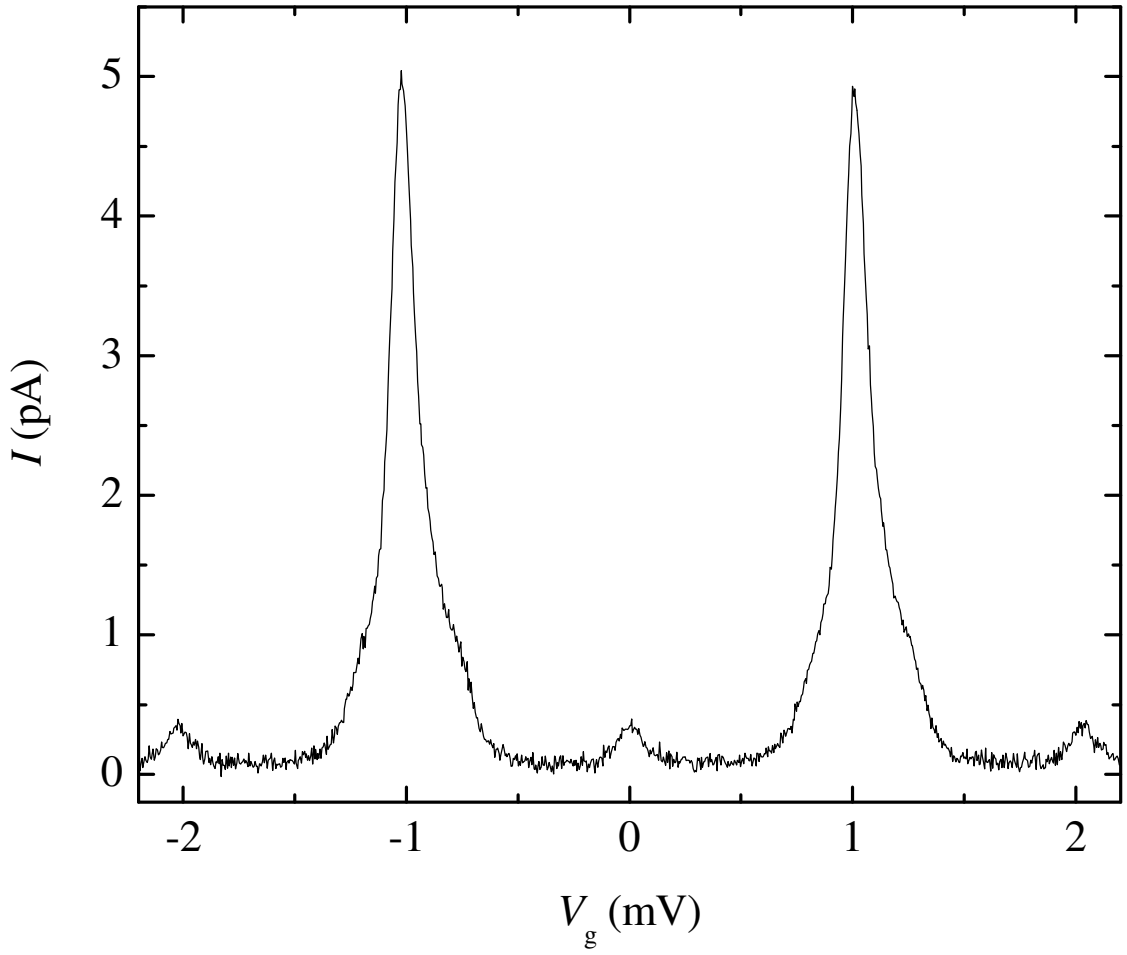

Fig. 4.6: 2*e* periodic current modulation for a superconducting SET (device CS1) biased at V_{DS}=30μV.

participate in the current but, since the power $V_{DS}I$ is being supplied by the voltage source, a dissipation mechanism must be present too, such as quasiparticle tunneling or absorption of energy by the electromagnetic environment [56,57].

4.3 Intrinsic SET Noise and charge sensitivity.

The SET can be used as an electrometer by biasing the device so that it converts a change in the charge applied to the gate into a change in current. The charge sensitivity is the key figure of merit for an electrometer. For an SET, the signal-to-noise ratio depends on the signal size $\Delta I=(\partial I/\partial Q)\Delta Q$ and the precision of the current measurement, which is ultimately limited by the intrinsic current noise of the SET. A large slope $\partial I/\partial Q$ in the modulation curve I vs n_g is desirable.

In the superconducting state the slope $\partial I/\partial Q$ can have a complicated dependence on the SET parameters and the choice of operating point. The slope tends to be largest near $V_{DS}=4\Delta/e$ and near the JQP. For example, at $T=0$ the JQP current for a symmetric SET ($R_1=R_2$, $C_1=C_2$) is approximately given by [55]:

$$I = 2e\frac{\Gamma_{qp}E_J^2}{4\delta^2 + \left(\hbar\Gamma_{qp}\right)^2} \tag{4.8}$$

where the quasiparticle generation rate is:

$$\Gamma_{qp} \approx \frac{2\left(eV_{DS} + E_c\right)}{e^2 R_\Sigma} \tag{4.9}$$

in the range $(2\Delta-E_c)/e<V_{DS}<(2\Delta+E_c)/e$ and

$$\delta = 4E_c\left(1 - n_g - \frac{C_\Sigma V_{DS}}{2e}\right) \tag{4.10}$$

evaluating $\partial I/\partial Q$ from Eqs. 4.8, 4.9 and 4.10 at $V_{DS}=2\Delta+E_c$ I find:

$$\left.\frac{\partial I}{\partial Q}\right|_{\max} = \frac{\pi^2}{8\hbar}\frac{\Delta^2 E_c}{(\Delta + E_c)^2} \tag{4.11}$$

At $T=0$ current fluctuations (shot noise) are present due to the random nature of tunneling events. The power spectral density of the current noise is:

$$S_I = (2eI)F \tag{4. 12}$$

where F is the Fano factor, which depends on correlations between tunneling events in the junctions and therefore on the mechanism producing the current. In the JQP region the Fano factor is $F\approx 2$ [58]. For a superconducting SET with $R_\Sigma=50\,\mathrm{k}\Omega$, $\Delta=200\,\mu\mathrm{V}$ (2.32 K), $E_c=100\,\mu\mathrm{V}$ (1.16 K) on the JQP biased near the maximum slope point, I find that the expected charge sensitivity is:

$q_n = (\partial I/\partial Q)^{-1}(S_I)^{1/2} = (14\ \mathrm{nA}/e)^{-1} \times 32\ \mathrm{fA/(Hz)^{1/2}} = 2.3\times 10^{-6} e/(\mathrm{Hz})^{1/2}$.

Unfortunately, at low frequency the charge sensitivity of SETs is not limited by shot noise but by the motion of charges in the substrate or in the tunnel junctions. This typically results in a charge spectral density of the form $S_q=\alpha/f$, with the constant $\alpha\sim 10^{-3}e^2$ [47,59]. With this level of $1/f$ noise, the predicted shot noise limited sensitivity would only be achieved at frequencies larger than ~ 1MHz.

The high intrinsic sensitivity of SETs makes them attractive for measurements on charge qubits. A single shot measurement of the state of the CPB is possible if the sensitivity is high enough and the measurement time can be made shorter than the relaxation time T_1 of the qubit. For measurements on a CPB, assuming $T_1\sim 1\,\mu\mathrm{s}$, the SET would require a bandwidth in excess of 1 MHz.

4.4 The rf-SET

The operation of the SET as discussed so far is not optimal at high frequencies. I note that, in contrast to the SET, many conventional current measurements make use of FET-based amplifiers to sense the voltage drop across a resistor R_s. Relatively high bandwidth measurements are possible by keeping the FET's input capacitance small and minimizing any capacitance from the connection between the FET and R_s. On the other hand, since an SET is run in a dilution refrigerator, a relatively long cable with capacitance $C \geqslant 100$ pF is necessary to connect the SET to a readout amplifier. This limits the measurement bandwidth to $f_c = 1/(2\pi R_s C)$. A trade off is evident, if R_s is decreased to get a larger bandwidth the signal becomes smaller and the sensitivity drops. High frequency operation and large bandwidth can be achieved while keeping a high sensitivity by using an rf readout scheme.

In order to optimize the readout of an SET at high frequencies it is necessary to transform the high impedance of the SET ($R_\Sigma \approx 50\text{k}\Omega$) down to $50\,\Omega$, the characteristic impedance of cables and rf instrumentation. This conversion can be implemented by means of the resonant circuit shown in Fig. 4.7 [27], where the dynamic impedance of the SET $(\partial I/\partial V_{DS})^{-1}$ is modeled by a resistor R_S. The impedance Z_t at the input of the resonant circuit is given by:

$$Z_t = \frac{R_S\left(1-\omega^2 LC\right)+i\omega L}{1+i\omega R_S C} \approx \frac{R_S\left(1-\omega^2 LC\right)+i\omega L}{i\omega R_S C} \tag{4.13}$$

The last approximation is justified for circuits designed to have $\omega RCs \gg 1$ in the frequency range of interest. At the resonant frequency:

$$\omega_0 \approx \frac{1}{\sqrt{LC}} \tag{4.14}$$

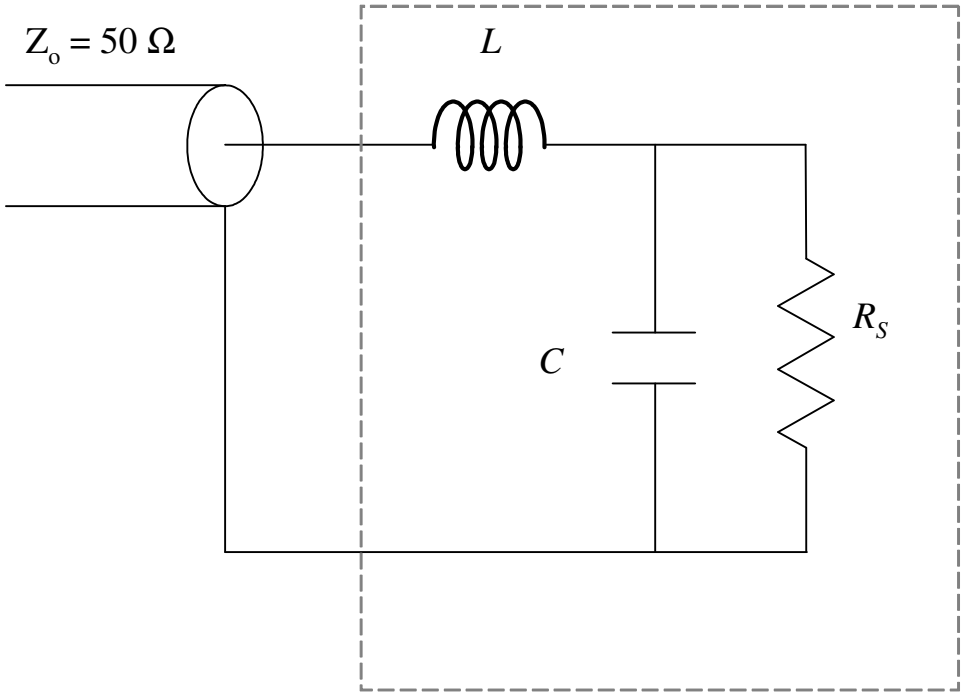

Fig. 4.7: LC resonant circuit used to match the impedance R_S of an SET to a Z_o=50Ω transmission line.

the impedance that the LCR circuit presents to the cable is equal to:

$$Z_t \cong \frac{L}{R_S C} = \frac{(\omega_0 L)^2}{R_S} = \frac{R_S}{Q^2} \tag{4.15}$$

where the unloaded quality factor is defined by:

$$Q = \frac{R_S}{\omega_0 L} \tag{4.16}$$

The technique for reading out the rf-SET is illustrated in Fig. 4.8. One sends an incident signal V_i to the resonant circuit at $\omega=\omega_o$ and measures the amplitude of the reflected wave $V_r=S_{11}V_i$ where the reflection coefficient S_{11} is given by:

$$S_{11} = \frac{Z_t - Z_0}{Z_t + Z_0} \tag{4.17}$$

where $Z_o=50\Omega$ is the characteristic impedance of the transmission lines. The reflected wave amplitude is modulated by the gate charge through the change in the SET resistance:

$$\frac{\partial V_r}{\partial n_g} = V_i \frac{\partial S_{11}}{\partial R_S}\frac{\partial R_S}{\partial n_g} = V_i \frac{2Q^2 Z_0}{\left(R_S + Q^2 Z_0\right)^2}\frac{\partial R_S}{\partial n_g} \tag{4.18}$$

Equation 4.18 indicates that the RF modulation $\partial V_r/\partial n_g$ increases with increasing V_i. However, the modulation of the SET resistance $\partial R_S/\partial n_g$ is large only on in a limited range $\Delta V_{DS} \sim E_c$. Therefore, the rf modulation is maximized when V_i produces an rf amplitude across the SET of about $V_{DS}^{RF} \sim E_c$. The voltage at the input of the resonant circuit V_{LC} and V_{DS}^{RF} are related through the unloaded Q:

$$V_S^{RF} \approx -iV_{LC}\,Q \tag{4.19}$$

The voltage V_{LC} is the sum of the incident wave and the reflected wave:

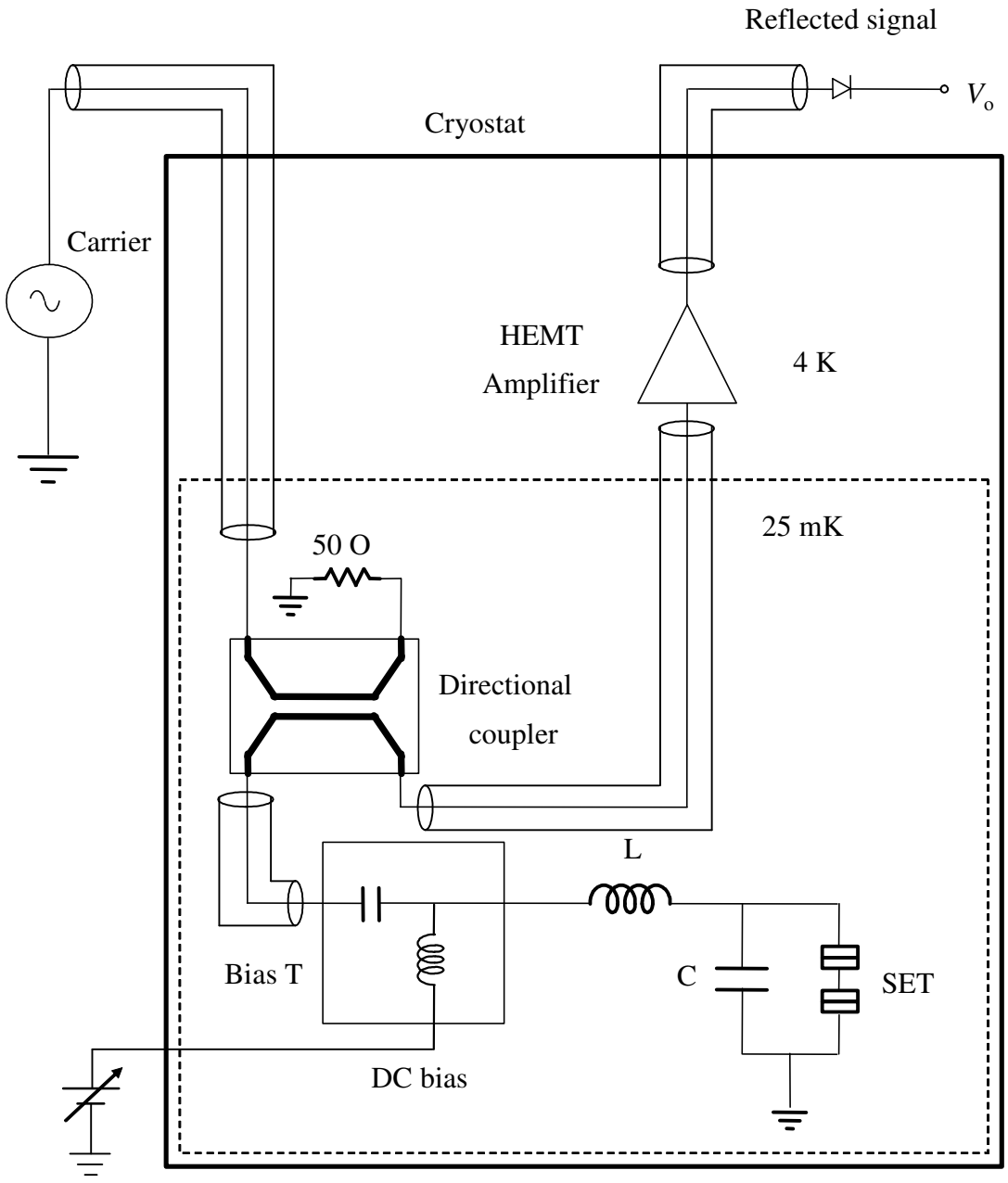

Fig. 4.8: Schematic diagram of an rf-SET. An rf signal V_i or carrier at frequency $\omega=1/(LC)^{1/2}$ is applied to a resonant circuit containing the SET. The reflected wave amplitude V_r depends on the impedance of the resonant circuit which is modulated by the gate charge n_g. The reflected wave is directed through a directional coupler to a low noise rf amplifier.

$$V_{LC} = V_i + V_r = V_i(1 + S_{11}) = V_{LC}\left(\frac{2R_S}{R_S + Q^2 Z_0}\right) \tag{4.20}$$

Combining Eqs. 4.18, 4.19 and 4.20 we get the optimum RF modulation:

$$\beta = \frac{\partial V_r}{\partial n_g} = V_{SET}\frac{QZ_0}{R_{SET}\left(R_{SET} + Q^2 Z_0\right)}\frac{\partial R_S}{\partial n_g} \tag{4.21}$$

I note that the modulation β is maximum when the resonant circuit impedance matches the cable impedance, i.e. $Q^2 Z_o = R_S$. For $R_S \approx 50$ kΩ and $Z_o = 50$ Ω, the impedance matching condition requires $Q = (R_S/Z_o)^{1/2} \approx 32$. Assuming an SET with $E_c = 1.16$K, $V_{DS}^{RF} \sim E_c = 100\mu$V, $R_S = 50$kΩ and $(1/e)\ \partial R_{SET}/\partial n_g = 50$kΩ $/e$, Eq. 4.21 yields an rf modulation of 1.5μV/e. Using an amplifier with a noise temperature $T_N = 2$K (a voltage noise of 74 pV/(Hz)$^{1/2}$), the charge sensitivity would be $q_n = 4.9 \times 10^{-5}\, e/(\text{Hz})^{1/2}$. Higher sensitivity is possible in superconducting SETs because some features in the IV can be very sharp and result in a larger slope $(1/e)\ \partial R_S/\partial n_g$ than the conservative figure used above. The best achieved sensitivity by any group at the time of this writing is $q_n = 3.2 \times 10^{-6}\, e/(\text{Hz})^{1/2}$ at a resonant frequency of 332 MHz [60].

The bandwidth of the rf-SET can be obtained by calculating the rf modulation as a function of frequency:

$$\frac{\partial V_r}{\partial n_g} = V_i \frac{\partial S_{11}}{\partial Z_t(\omega)}\frac{\partial Z_t(\omega)}{\partial R_S}\frac{\partial R_S}{\partial n_g} \tag{4.22}$$

with $Z_t(\omega)$ given by Eq. 4.13. Evaluating Eq. 4.22, substituting $\omega = \omega_o(1 + \delta\omega/\omega_o)$ and keeping the leading terms leads to the expression:

$$\frac{\frac{\partial V_r}{\partial n_g}(\omega_o + \delta\omega)}{\frac{\partial V_r}{\partial n_g}(\omega_o)} = \frac{1}{1+\left(Q_L \frac{2\delta\omega}{\omega_o}\right)^2} \tag{4.23}$$

where Q_L is the loaded quality factor determined by:

$$Q_L^{-1} = \frac{\omega_o L}{R_{SET}} + \frac{Z_o}{\omega_o L} \tag{4.24}$$

The bandwidth Δf, defined as the frequency δf where the modulation drops by half, is found from Eq. 4.23:

$$\Delta f = \frac{f_o}{2Q_L} \tag{4.25}$$

For an SET with R_S=50kΩ optimal impedance matching requires Q_L=16. A carrier frequency of f_o=650 MHz yields a bandwidth Δf=20.3 MHz.

I note that without the impedance matching network, the measurement bandwidth would be on the order of $\Delta f = 1/(2\pi R_S C) \sim 1/(2\pi \times 50\ \text{k}\Omega)(100\ \text{pF}) = 31.8$ kHz.

4.5 SET back-action and single shot considerations

Figure 4.9 illustrates a scheme for using an rf-SET to perform single shot measurements on a CPB qubit. A CPB is coupled to an SET electrometer through a small capacitance C_c. After qubit manipulations have been performed on the box by applying microwave voltages to its gate, the final state of the box can be determined by measuring the charge on the box with the electrometer. For example, if the CPB is in the state $|2\rangle$, the potential of the box island decreases by $\Delta V_i = 2e/C_{\Sigma b}$ and changes the SET bias by

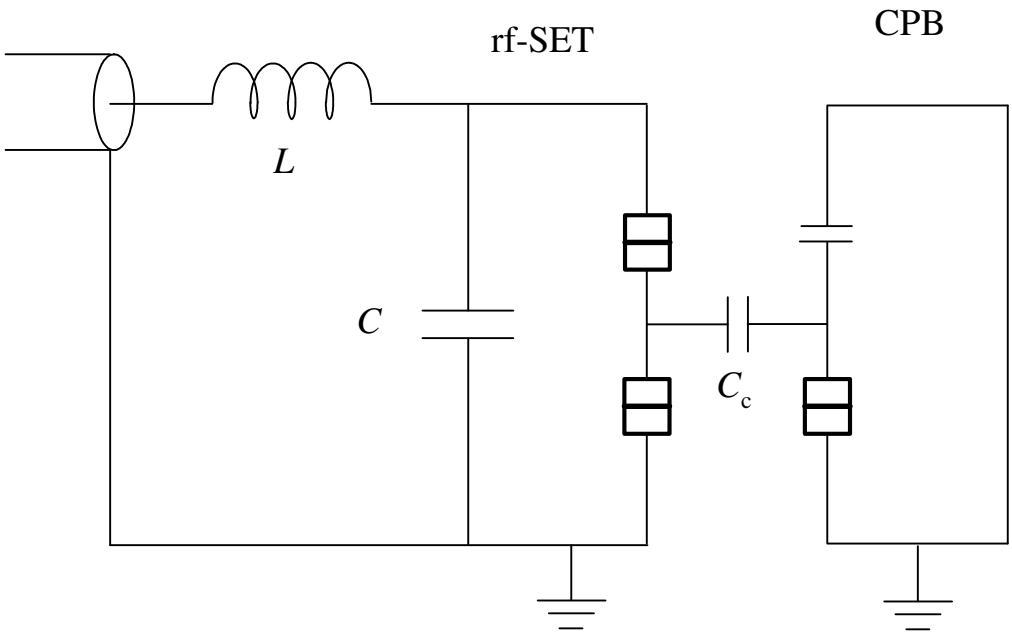

Fig. 4.9: Schematic for the measurement of the charge state of a Cooper pair box charge qubit using an rf-SET.

$\Delta n_g = \Delta V_i C_c / e = 2C_c / C_{\Sigma b} = 2\kappa$. In order to determine the charge state of the box the resolution of the measurement must be better than the induced SET charge $2e\kappa$. The rms fluctuations of the measured charge are given by:

$$\Delta Q = q_n \sqrt{B} = \frac{q_n}{\sqrt{t_m}} \tag{4.26}$$

where B is the measurement bandwidth and $t_m = 1/B$ is the measurement time and q_n is the charge sensitivity of the electrometer. Equation (4.26) means that the resolution of the measurement improves as the output signal is averaged for a longer time. However, t_m cannot be made arbitrarily large since it must be shorter than the lifetime of the qubit state. As discussed in Chapter 3, the rates of excitation $\Gamma\uparrow$ and relaxation $\Gamma\downarrow$ of the CPB depend on the voltage noise spectrum S_V coupled to the CPB island.

I note in particular that, charge fluctuations on the SET island lead to voltage noise that can perturb the state of the box through the coupling capacitor C_c. This is a form of "back-action". The voltage noise spectrum can be calculated for a normal state SET [61]. At low frequency, S_V can be calculated from Poisson statistics of the tunneling events using the orthodox theory [62,63]. If one assumes an SET bias $V_{DS} \approx 2E_c/e$, then S_V is given in this limit by:

$$S_V(\omega) \approx \frac{1}{2\pi}\left(\frac{4E_c}{e}\right)^2 \frac{I/e}{\omega^2 + 16(I/e)^2} \tag{4.27}$$

Needless to say, this does not include $1/f$ noise. At frequencies $f >> R_1C_1$ and $f >> R_2C_2$, the cut-off frequencies of the tunnel junctions, the SET looks like a passive resistor $R_{||} = R_1R_2/(R_1+R_2)$ shunted by a capacitor C_Σ. The voltage noise in this limit is given by:

$$S_V(\omega) = \frac{1}{2\pi} 2\hbar\omega \mathrm{Re}\left(\frac{R_{||}}{1 + i\omega R_{||} C_\Sigma}\right) \tag{4.28}$$

The estimated voltage noise for an SET with E_c=1K and R_Σ=50kΩ is shown in Fig. 4.10a. Equations 4.27 and 4.28 have been used for the limiting cases and then added in quadrature to interpolate between the two extremes. The exact solution [61] predicts a smaller noise in the intermediate frequency range.

As noted above, the perturbation of the qubit state by the electrometer is known as back-action. I recall that the transition rates $\Gamma_\downarrow$ and $\Gamma_\uparrow$ between the CPB eigenstates are proportional to $S_V(\omega)$ and $S_V(-\omega)$ respectively (see Eqs. 3.2 and 3.3). The effect of SET back-action can be characterized by a mixing time $t_{mix}=(\Gamma_\uparrow+\Gamma_\downarrow)^{-1}$ which characterizes the rate at which the charge state of the box changes. Figure 4.10b shows the estimated t_{mix} for a CPB with E_c=1K, E_J=0.5K and coupling κ=0.02 when the SET has the S_V shown in Fig. 4.10a. In this example a mixing time of ~1μs is obtained by operating the box at n_g=0.2. Equation 4.26 then reveals that the minimum sensitivity q_n required for a single shot measurement is $q_n=2e\kappa(t_{mix})^{1/2}=4\times10^{-5}e/(\text{Hz})^{1/2}$.

I note that the optimization of the readout can be made independent of the coupling κ to some extent since the transition rates are proportional to κ^2 and therefore $t_{mix} \propto \kappa^{-2}$. It is desirable to make κ large enough that T_1 is determined by the SET back-action but not so much that $(t_{mix})^{-1}$ is larger than the rf-SET bandwidth.

4.6 Summary

In this Chapter, I presented the theory of the rf-SET and I showed that the rf-SET is capable of performing fast and sensitive charge measurements. These characteristics are attractive for the quantum state readout of a CPB. I also examined the effect of

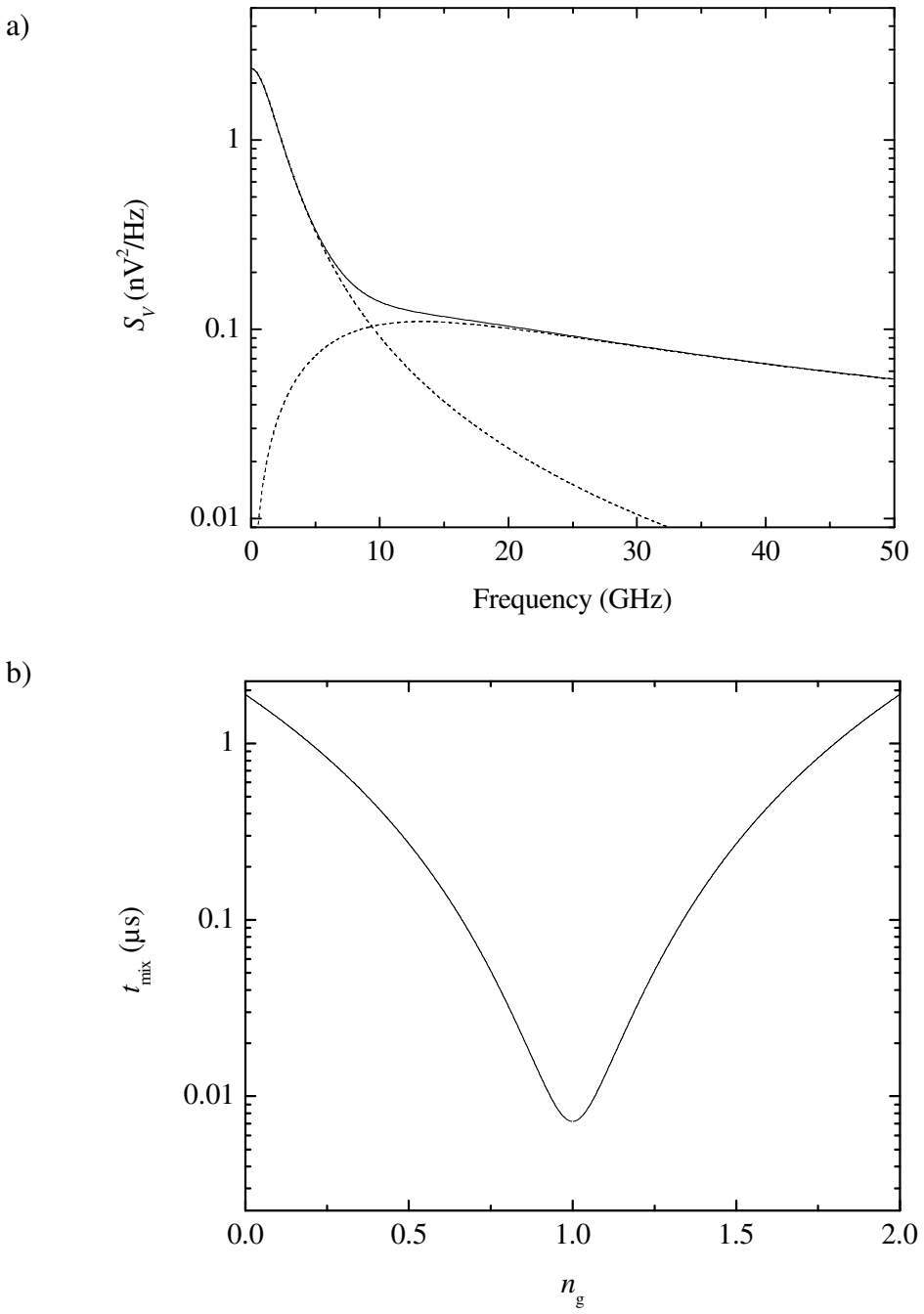

Fig. 4.10: (a) Voltage noise spectrum S_V of the island potential for a normal SET with E_c=1K and R_Σ=50kΩ. The solid line is the sum of the low frequency and high frequency limits (dotted lines). (b) Mixing time for a CPB plotted *vs*. n_g resulting from the SET voltage noise shown in (a) with CPB parameters E_c=1K, E_J=0.5K and coupling κ=0.02.

measurement back-action on a CPB and found the excitation and relaxation rates for typical device parameters. The calculations suggest that a single shot measurement is possible for $T_1 \gtrsim 1\ \mu s$.

Chapter 5 : Experimental Techniques: Fabrication, Cryogenics and Electronics

This Chapter presents some of the techniques I used in my experiments on the CPB. I start with a discussion of the design of microwave components that I integrated in the devices. I then describe the fabrication of my devices and the cryogenic techniques I used to bring electrical lines to the low temperature portions of the apparatus. I next discuss the effect of high frequency noise in my experiments, considering the filtering characteristics of the setup. Finally, I describe the electronics and instrumentation I used for dc and rf measurements.

5.1 Microwave design of the rf-SET

The devices I used in my experiments required the design of on-chip rf components such as the inductor and capacitor for the rf-SET resonant circuit and a tapered coplanar waveguide that I used to send microwave signals to the CPB (see Fig. 5.1).

I designed and tested resonators with different resonant frequencies of 1.5 GHz and 650 MHz. The optimum impedance matching for a 50 kΩ SET is obtained with $Q=(50\times10^3/50)^{1/2} \approx 32$. The inductance value is obtained from $Q=R_S/\omega_o L$ and the capacitance from $LC=1/\omega_o^2$. The optimized values are $L=168$ nH, $C=67$ fF at $f_o=1.5$ GHz, and L=387 nH, $C=155$ fF at $f_o=650$ MHz.

The inductance for the planar square inductor shown in Fig. 5.2a can be estimated from [64]:

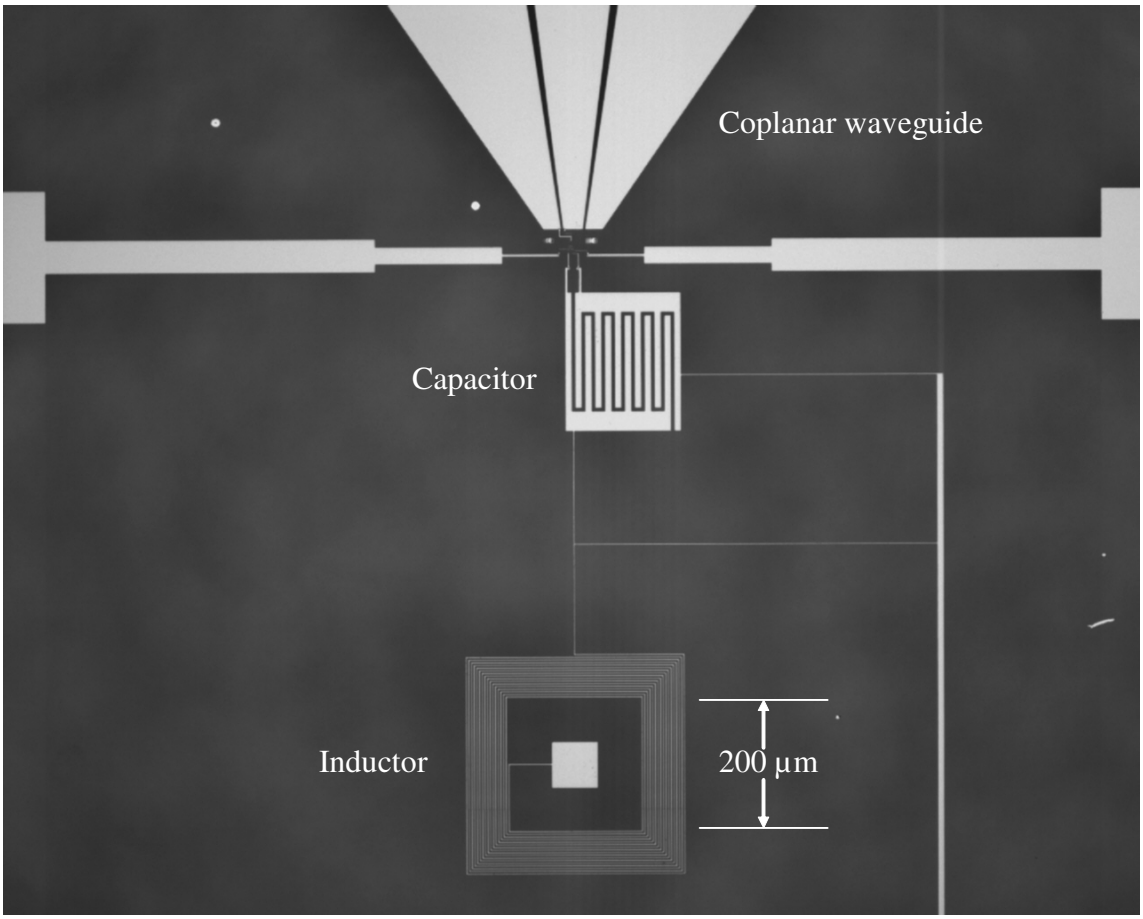

Fig. 5.1: Optical image of rf-SET device showing the larger features (inductor, interdigital capacitor, coplanar waveguides and bonding pads). This pattern was made using optical lithography and lift-off.

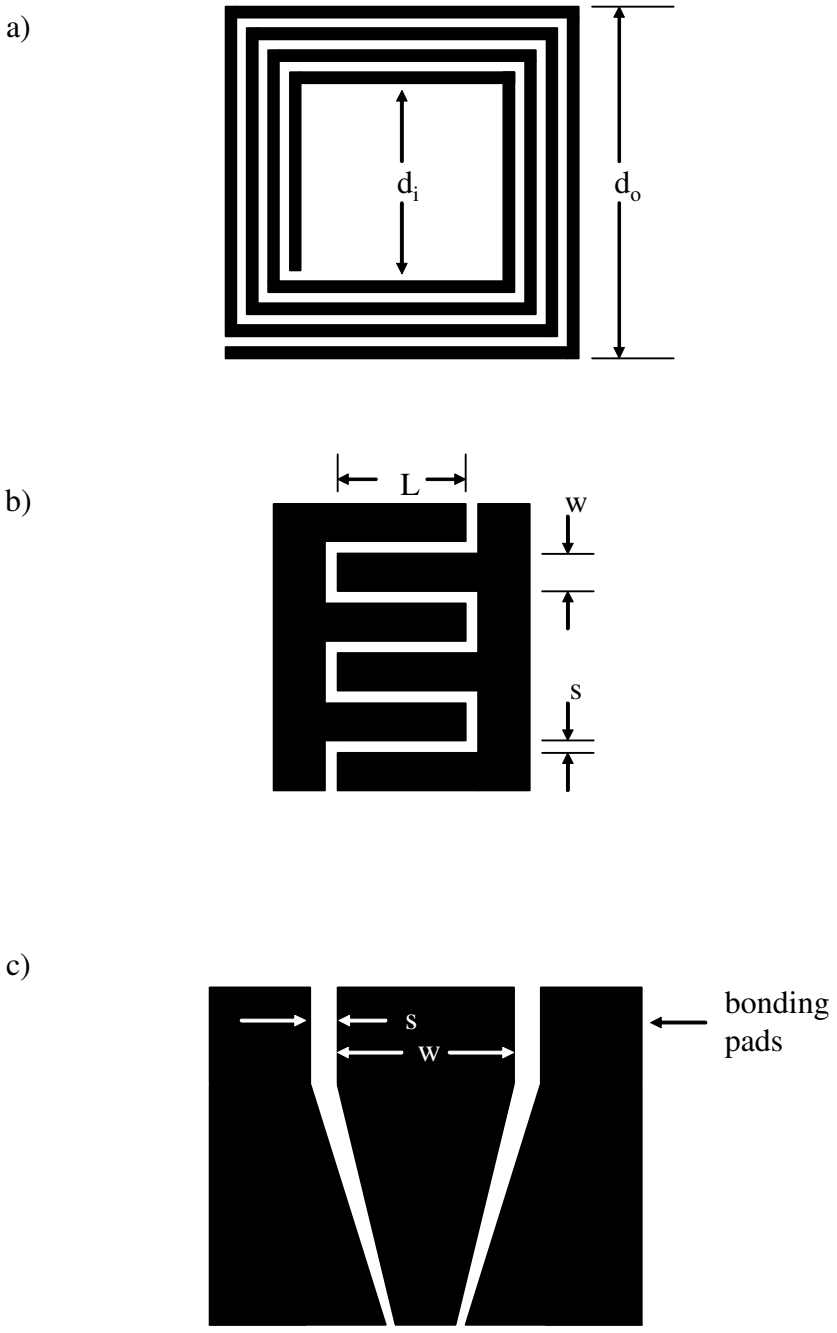

Fig. 5.2: Components used in the rf-SETs and CPBs. (a) Square inductor, (b) interdigitated capacitor and (c) tapered coplanar waveguide.

$$L = \frac{1.17\mu_o N_T^2 (d_i + d_o)^2}{d_i + d_o + 2.75(d_o - d_i)} \tag{5.1}$$

where N_T is the number of turns and d_i, d_o are the inner and outer diameters respectively. For my first design (f_o=1.5 GHz) I used N_T=17, d_i=200 μm and d_o=330 μm and for the second design (f_o=650 MHz) I used N_T=27, d_i=200 μm and d_o=522 μm. From Eq. 5.1, the estimated inductances were 134 nH and 348 nH, respectively. The total length of the inductor (18 mm and 39 mm respectively) should be small compared to λ/4 in order for the inductor to behave like an ideal lumped element and to minimize radiation loss. The wavelength λ depends on the dielectric constant of the substrate ϵ_r according to:

$$\lambda \approx \frac{c}{f}\sqrt{\frac{2}{\epsilon_r + 1}} \tag{5.2}$$

To keep λ large, I chose quartz for the substrate ($\epsilon_r \approx 3.8$), giving λ/4=32.3 mm at 1.5 GHz and 74.5 mm at 650 MHz.

The other micro component of the resonator is the interdigitated capacitor. The expression for the distributed capacitance of a coplanar waveguide [65] can be used to estimate the capacitance of the interdigitated capacitor (see Fig. 5.2b):

$$C = \epsilon_o(\epsilon_r + 1)[(N-1)L + N_F(W+S)]\frac{K(k)}{K(k')} \tag{5.3}$$

with the parameters:

$$k = \frac{W}{W + 2S} \tag{5.4}$$

and

$$k' = \sqrt{1 - k^2} \tag{5.5}$$

In these equations N_F is the number of fingers, L is the length of the fingers, W is the finger width, S is the gap between the fingers and K is the complete elliptic integral of the first kind. The ratio $K(k)/K(k')$ can be approximated by:

$$\frac{K(k)}{K(k')} \approx \begin{cases} \dfrac{\pi}{\ln\left(2\dfrac{1+\sqrt{k'}}{1-\sqrt{k'}}\right)} & for\ 0 \le k \le \dfrac{1}{\sqrt{2}} \\ \dfrac{\ln\left(2\dfrac{1+\sqrt{k}}{1-\sqrt{k}}\right)}{\pi} & for\ \dfrac{1}{\sqrt{2}} \le k \le 1 \end{cases} \tag{5.6}$$

I used N_F=12, L=145 μm, W=10 μm and S=5 μm for the 1.5 GHz design, which yielded C=59 fF. For the 650 MHz design I used N_F=16, L=209 μm, W=10 μm and S=5 μm, which yielded C=112 fF.

The tapered coplanar waveguide provides the transition from large bonding pads to a small gate that couples to the CPB (see Fig 5.2c), while keeping a 50 Ω characteristic impedance. The characteristic impedance of a coplanar waveguide on a substrate with thickness H and dielectric constant ϵ_r sitting above a ground plane is given by [65]:

$$Z = \frac{60\pi}{\sqrt{1+q(\epsilon_r - 1)}} \frac{1}{\dfrac{K(k_1)}{K(k_1')} + \dfrac{K(k_2)}{K(k_2')}} \tag{5.7}$$

where

$$k_1 = \frac{W}{W + 2S} \tag{5.8}$$

$$k_2 = \frac{\tanh\left(\frac{\pi W}{4H}\right)}{\tanh\left[\frac{\pi(W+2S)}{4H}\right]} \tag{5.9}$$

and

$$q = \frac{\frac{K(k_2)}{K(k_2')}}{\frac{K(k_1)}{K(k_1')} + \frac{K(k_2)}{K(k_2')}} \tag{5.10}$$

On both designs the dimensions on the wide side of the tapered line are W=500 μm, S=82.2 μm and on the narrow side W=30 μm, S=3 μm. These dimensions were chosen so that $Z \approx 50\ \Omega$.

5.2 Sample fabrication

I made my devices on 3-inch diameter, 0.5 mm thick, single-crystal quartz wafers [66]. I cleaned the wafers by first immersing them in piranha solution (1:4 H_2SO_4:H_2O_2) for 10 minutes and then spraying with pressurized acetone to wash particles off the surface. I then patterned thin films in two or three steps, depending on what features were incorporated in the device. I used photolithography to define large features (coplanar waveguides, inductors, capacitors and bonding pads) while the smaller features (SET, CPB, quasiparticle traps) were made with e-beam lithography.

5.2.1 Optical lithography

For photolithography, I used a trilayer resist system, with the process illustrated in Fig. 5.3. The bottom layer, PMGI SF8 (polymethylglutarimide) [67], is spun at 5000 rpm for

one minute and baked on a hot plate at 180 °C for five minutes. This produces a layer about 400 nm thick. The second layer, a 30 nm thick germanium film, is e-beam evaporated onto the PMGI. The top layer (NR7-1500 PY negative photoresist [68]) is spun at 4000 rpm for one minute and baked on a hot plate at 120 °C for one minute, producing a layer about 1.5 µm thick. I exposed the photoresist using a Karl-Suss contact aligner for 12 seconds with deep UV light of 15 mW/cm^2. Following exposure I baked the wafer again on a hot plate at 120 °C for one minute and then developed it in RD6 developer [68] for 12 seconds and rinsed in de-ionized (DI) water. At this point, the germanium layer is covered with photoresist on the areas that were exposed with UV light, but unprotected on the remaining areas. The pattern is transferred to the germanium layer by dry etching in a Plasmatherm RIE chamber (reactive ion etching) using SF_6 gas for 12 seconds at 10 mTorr pressure, 50 W rf power and 10 sccm (standard cubic centimeters per minute) flow rate. Then the bottom layer is dry etched in the same chamber using O_2 gas for 7 minutes (250 mTorr pressure, 19 sccm flow rate, 200 W rf power). The etch time and O_2 pressure are chosen to create an undercut below the germanium layer so that smooth edges are created during a subsequent lift-off stage.

I next deposited a superconducting film consisting of an Al-Ti-Au trilayer (60nm-20nm-20nm thickness, $T_c \approx 0.7$ K [69]) by e-beam evaporation. Superconductivity is essential to achieve a high Q inductor while the gold film provides an oxide-free surface that allows me to make electrical contact to subsequent metallic layers. The first layer is completed by a lift-off in NMP (N-Methyl-2-Pyrrolidone) at 90 °C for 30 minutes. Figure 5.1 shows a chip I built using this procedure.

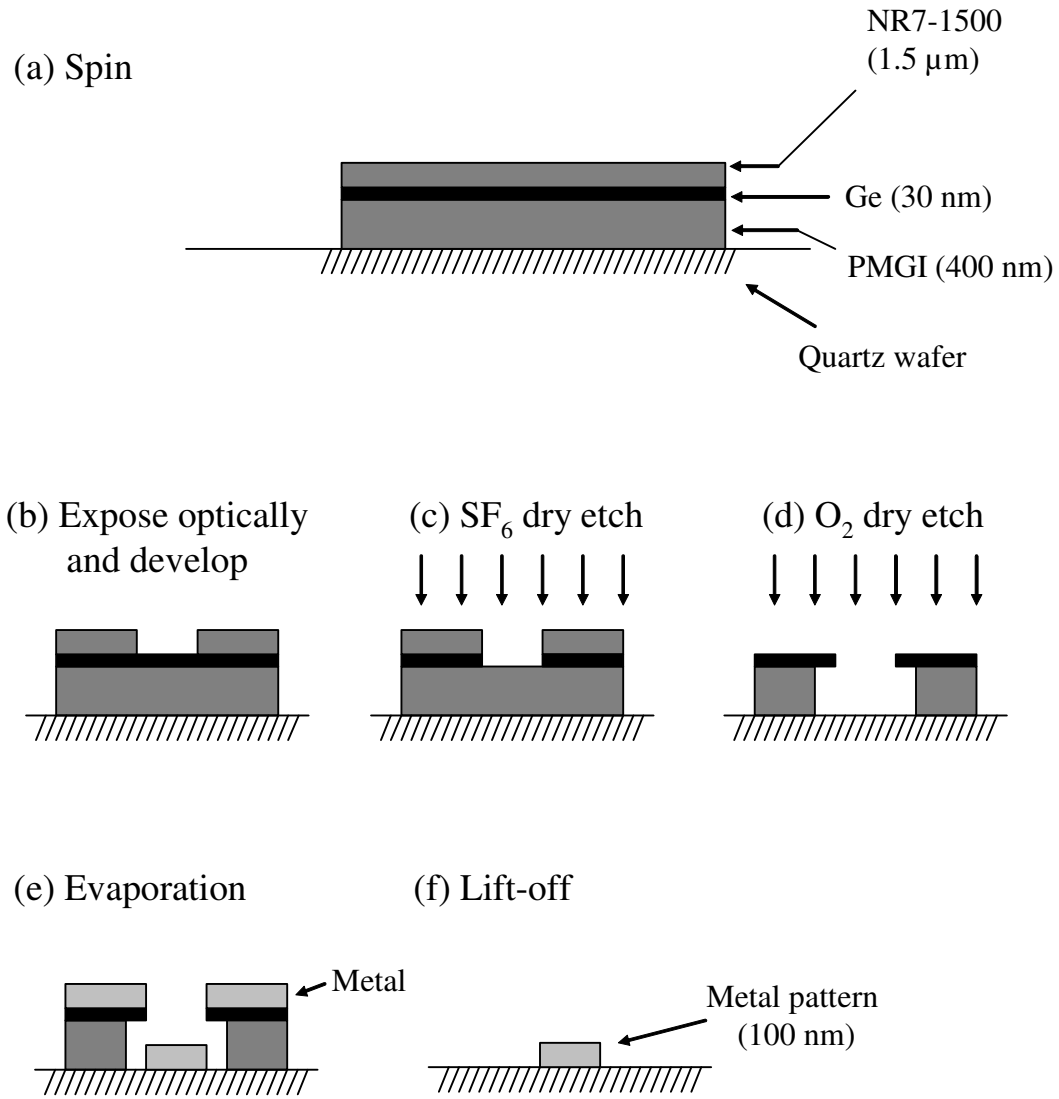

Fig. 5.3: Illustration of the trilayer photoresist system. (a) Deposition of the different layers. (b) The top layer (photoresist) is exposed and developed. (c) The pattern is transferred to the germanium layer using SF_6 dry etch. (d) The bottom layer is dry etched with O_2 gas (e) The metallic film is evaporated (f) Lift-off patterning is completed as material is removed by dissolving the PMGI layer in NMP.

5.2.2 E-beam lithography

The next step in the process is to add the SET and the CPB. I used a recipe developed by Dr. Pierre Echternach [70]. The first step is to coat the wafer with a bi-layer e-beam resist. The first layer (MMA(8.5)MAA EL11 or copolymer [67]) is spun at 5000 rpm for one minute and baked at 135 °C for 10 minutes on a hot plate. The second layer (2200 PMMA A1 [67]) is spun and baked using the same parameters as the copolymer. Before the devices can be patterned by e-beam lithography, they have to be coated with a thin metallic film or anti-charging layer, otherwise charge will build up on the quartz substrate and deflect the electron beam, distorting the pattern. I used a 10 nm thick Al film on top of the PMMA layer to prevent charging effects. I deposited this film by thermal evaporation since e-beam evaporation generates x-rays which can expose PMMA.

After this Al layer is deposited, I scribe and dice the wafer into 5 × 4 mm chips. Individual devices are exposed in a JEOL 6500 SEM using a commercially available e-beam lithography system developed by Joe Nabity [71]. The software allows me to align the e-beam exposure with the pre-existing pattern with an accuracy of about 100 nm. I do this by scanning specific areas that contain alignment marks and then guiding the software to correct for the offset of these marks with respect to their nominal position. I used a 30 kV accelerating voltage and a 45 pA beam current. The dose required to fully expose the PMMA-Copolymer bilayer is about 1.5 nC/cm for single pass lines and 350 $\mu C/cm^2$ for filled polygons. However, features requiring a large undercut, such as the leads and island of the SET and CPB, are exposed with a 10 times larger line dose or a 3 to 4 times larger area dose.

After exposure, I strip the anti-charging layer by immersing the chips in a TMAH (tetramethylammonium hydroxide) based positive photoresist developer for one minute. The devices are then developed in a 1:3 MIBK:IPA mixture [67] and rinsed in Isopropyl alcohol (IPA) for 30 seconds. The island and leads of the devices are defined by openings in the PMMA mask. The bottom layer (copolymer) is more sensitive than the top layer which allows for a large undercut to be created so the edges of the PMMA mask are free standing.

5.2.3 Double angle evaporation

I used the double angle evaporation technique [72] illustrated in Fig. 5.4 to make the tunnel junctions for the SETs and CPBs. I usually deposit Al on one or two chips at a time. The chips are loaded in an evaporation system assembled by Akshay Naik, with a rotating stage and a base pressure of 2×10^{-7} Torr. Aluminum films are evaporated either from a poco-graphite crucible or an intermetallic crucible [73] using an MDC e-beam evaporator. A 30 nm thick Al film is first evaporated at a rate of 0.3 to 0.4 nm/s, with the stage rotated to make an angle of 15° between the evaporation source and the axis perpendicular to the chip surface. I then admit O_2 gas into the chamber to grow an aluminum oxide insulating film that works as a potential barrier for the tunnel junctions. After an oxidation time of 3 minutes the O_2 gas is pumped out and a second Al film is deposited with the stage set to -15°, using the same deposition rate. Tunnel junctions are formed where the leads (island) from the first evaporation overlap the island (leads) from the second evaporation.

The oxidation pressure and the junction size are adjusted to achieve junctions with $C \sim 1$ fF and $R \sim 50$ kΩ. I typically used an oxidation pressure of 150 mTorr and a junction size of 100 nm × 100 nm to obtain the desired parameters. The last step in the process is a lift-off in acetone at room temperature for one hour.

Figures 5.5 and 5.6 show SEM pictures of two of my samples. The device shown in Fig. 5.6 included metallic films (10 nm Ti – 15 nm Au) in close proximity with the junctions, often referred to as quasiparticle traps. The purpose of the traps was to extract quasiparticles from the superconducting leads, to prevent them from entering the island. The quasiparticle traps in this sample were defined by e-beam lithography following the recipe described above. In this case the SET and Coooper pair box were made in a third step and deposited over the traps, using the same alignment marks for both exposures.

For measurements, individual chips were mounted in a microwave tight copper package using vacuum grease to ensure good thermal contact. The package has coplanar waveguides on the inside to facilitate wire bonding connections to the chip leads. The coplanar waveguides are soldered to wall-mount SMA connectors using indium solder. Connections to the devices are made using a wedge bounder with 1 mil diameter gold wire. Special care must be taken with the high speed gate of the CPB; the wiring is kept short (less than 1 mm long) and several parallel wires are used to reduce the parasitic inductance.

Also, in order to protect the SETs from electrostatic discharge, the interdigitated capacitor is shorted in the optical pattern. After the Source and Drain terminals of the SET are wire bonded, an SMA short is placed on the wall connector and the interdigitated capacitor is scratched open with a diamond-tip scriber. I then check the SET by

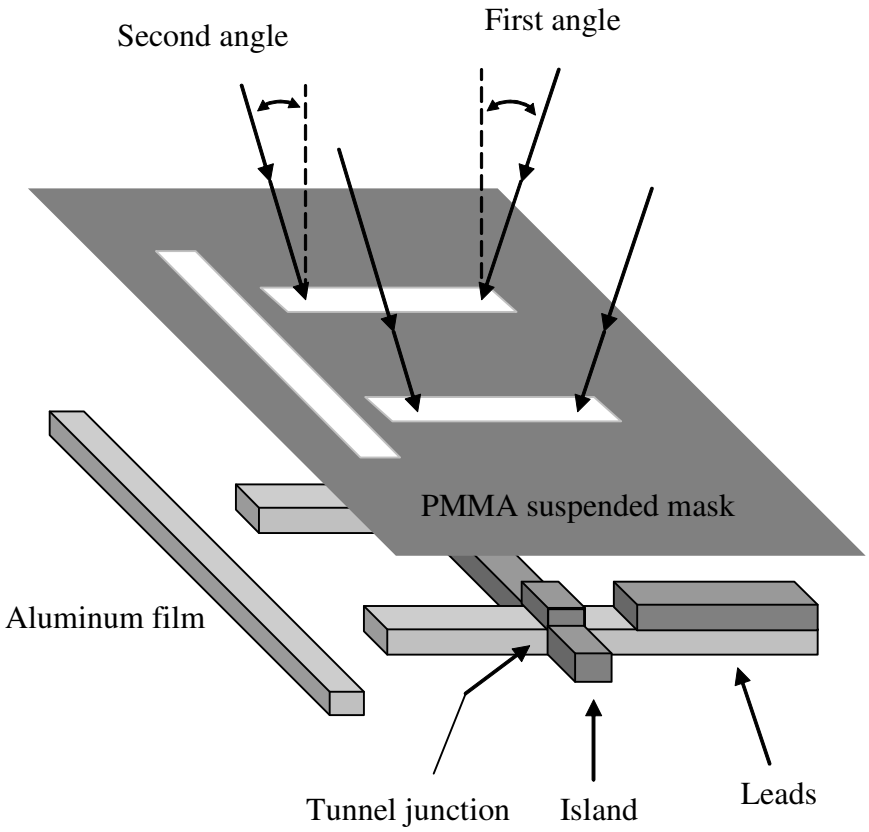

Fig. 5.4: Double angle evaporation technique. The bilayer resist system allows the definition of a suspended PMMA mask. A first Al film is evaporated from a 15° angle from the normal and then oxidized in O_2 gas to form a tunneling barrier. A second Al film is evaporated at a -15° angle and tunnel junctions are formed where the two films overlap.

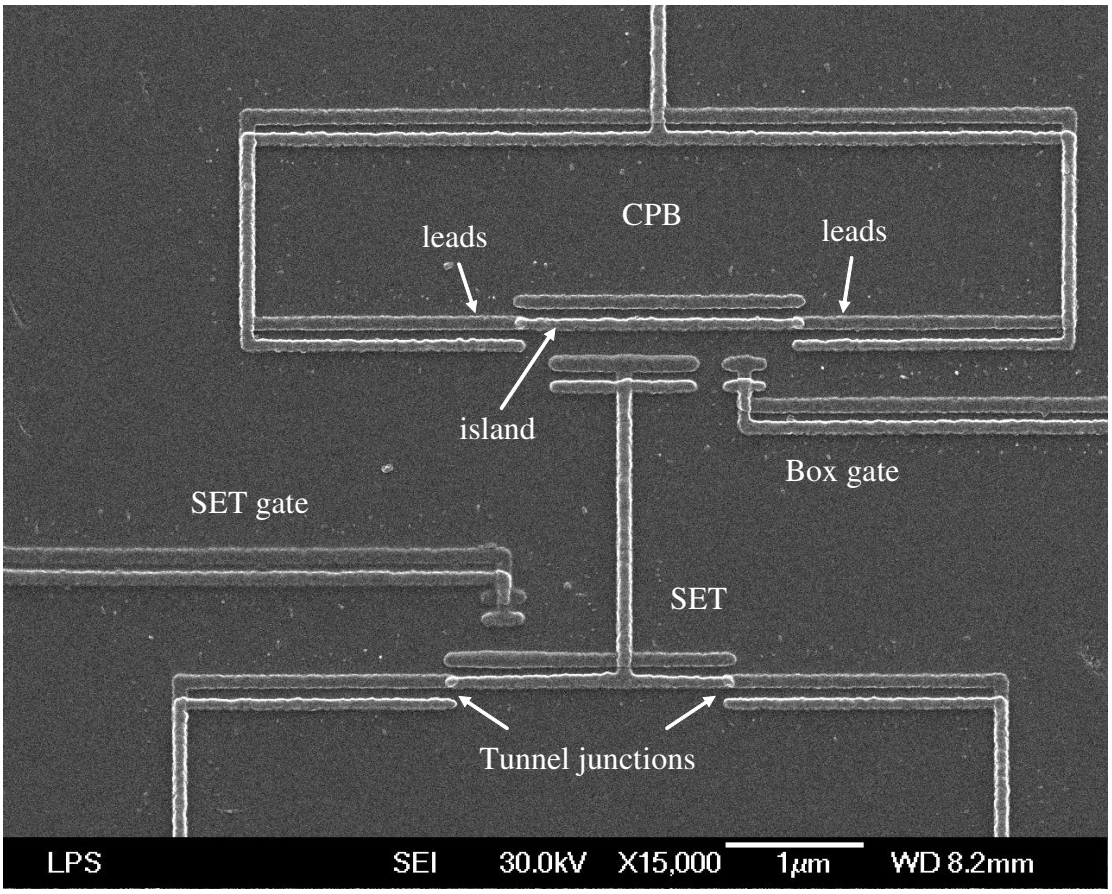

Fig. 5.5: SEM picture of coupled Cooper pair box and SET. I fabricated these devices using e-beam lithography and double-angle evaporation.

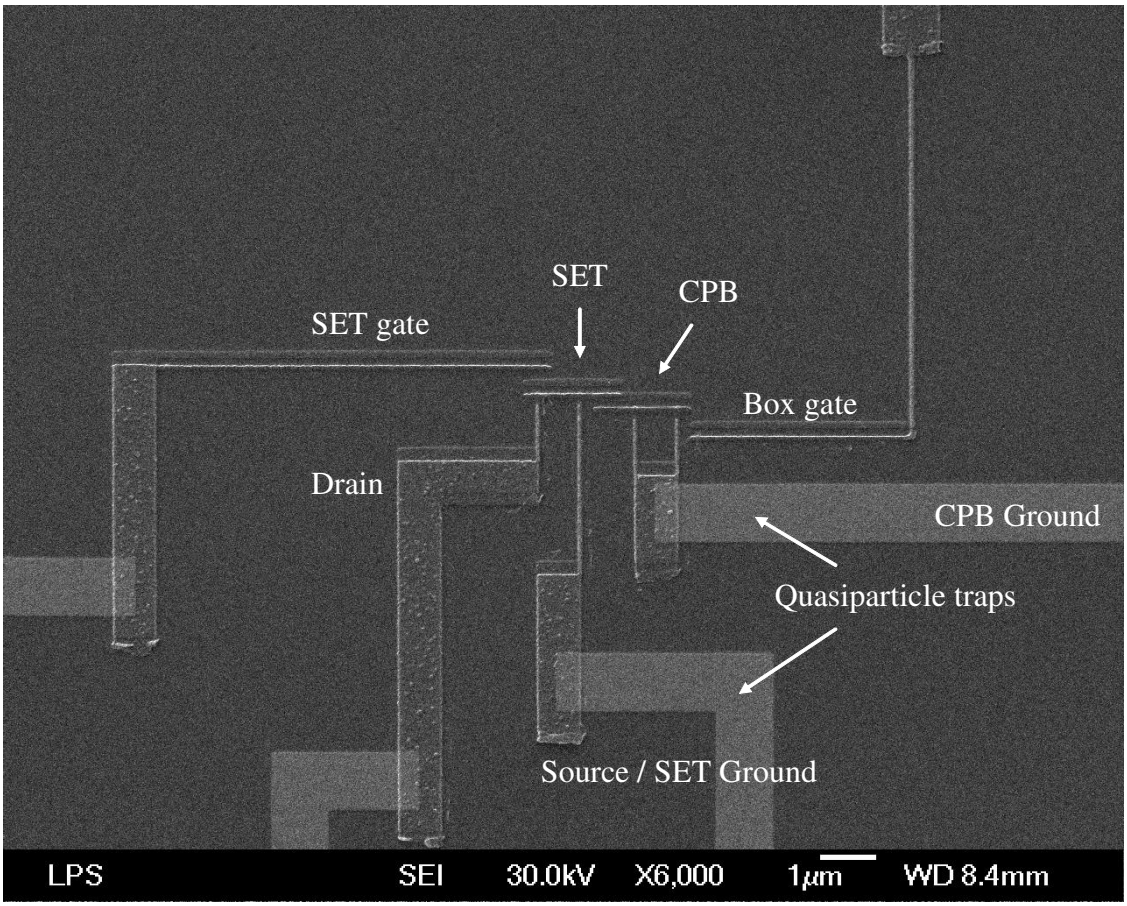

Fig. 5.6: SEM picture of coupled Cooper pair box and SET with quasiparticle traps.

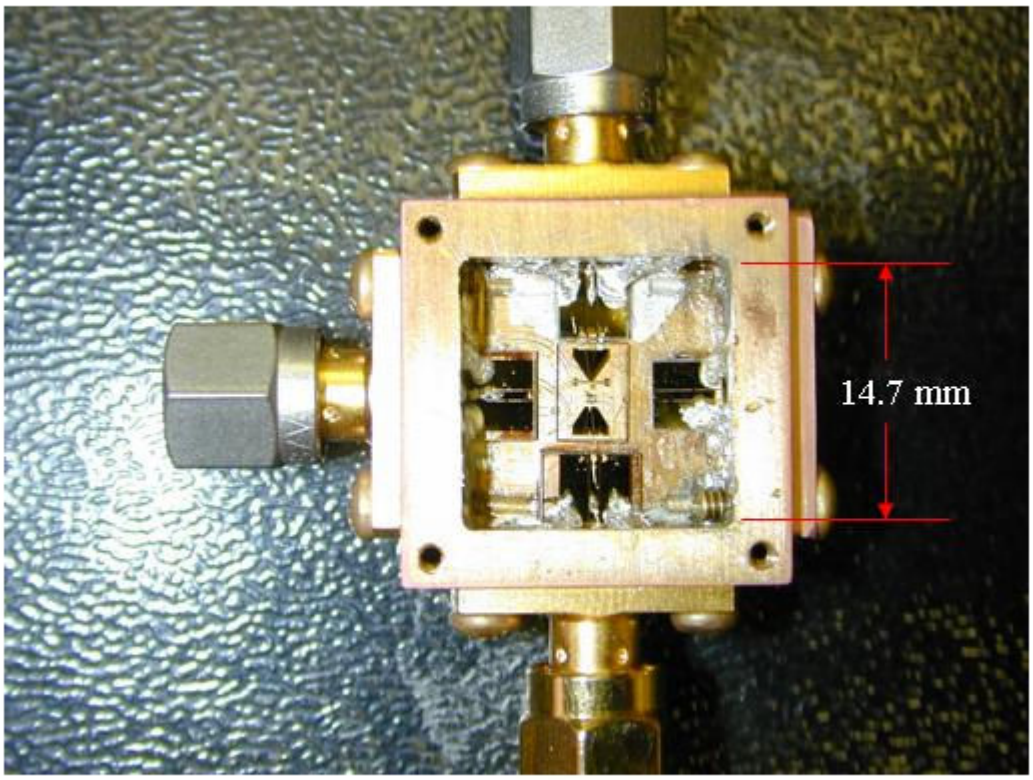

Fig. 5.7: Picture of a sample mounted in a microwave tight copper package.

measuring its resistance at room temperature with a battery-operated, hand-held multimeter set on the 4 MΩ range. This limits the current to a safe level of about 100 nA.

5.3 Cryogenics

To measure the samples, I first mount the package in a Kelvinox 100 ^{3}He-^{4}He dilution refrigerator from Oxford Instruments [51]. Samples are typically cooled down over a period of two days. After sealing the refrigerator, evacuating the inner vacuum chamber and introducing ^{3}He exchange gas into the vacuum space, the Dewar is raised until it encloses the refrigerator completely. The dewar is then pre-cooled with liquid nitrogen and left to thermalize overnight. The next day, the liquid nitrogen is pumped out of the dewar and liquid helium is transferred in. Once the mixing chamber temperature reaches 4.2 K, the exchange gas is pumped out and the ^{3}He-^{4}He mixture is circulated until the fridge reaches a base temperature of about 30 mK. The temperature of the mixing chamber is measured with a ruthenium oxide resistance thermometer that works in the range between 15 mK to 6.5 K.

The copper package was attached to a copper bracket which was in turn bolted to the mixing chamber. The bracket, designed by Dr. Benjamin Palmer, was annealed and gold plated to increase heat conduction to the mixing chamber and was attached to it using long brass screws with stainless steel spacers. Getting the fridge and the devices to 20-30 mK requires that the heat (coming down the electrical lines used in the experiment) be limited to less than 10 μW. Different techniques are used to thermally sink the lines at every stage depending on the physical and electrical characteristics of that particular line. Figure 5.8 shows a wiring diagram of the electrical lines used for these experiments. I

note that there were enough dc lines to run up to three SET/CPB chips but only one device could have rf lines attached to it.

I used low frequency lines with a bandwidth of tens of MHz to provide bias voltages (V_{DS}, V_g) for the SETs and CPBs. For these lines I used miniature cupro-nickel coaxial cable [74] (0.08 mm inner diameter, 0.33 mm outer diameter) from the mixing chamber to the 1K pot and flexible stainless steel coaxial cable [75] (0.203 mm inner diameter, 0.711 mm outer diameter) from the 1K pot to the top of the refrigerator. These cables provide both low thermal conductivity and high frequency filtering. I thermally grounded these lines by winding them tightly around copper posts attached to different spots on the refrigerator (mixing chamber, still, 1K pot and 4K flange) using long brass screws. The windings are coated with silver paint to fill in the voids and increase thermal contact to the posts. I used flexible coaxial cables with soldered SMA connectors to make electrical connections between these lines and the sample package.

Two rf lines are necessary for the operation of the rf-SET. The upper section of the input line (rf-SET carrier) is a stainless steel UT-85 semi-rigid coaxial cable that runs from the top of the fridge to the 1K pot (see Fig. 5.8). To filter out noise, this section is terminated in a 20 dB attenuator mounted on the 1K plate. I use SMA connectors and these provide a low thermal resistance path between the outer conductor of the coaxial cable and the 1K plate. The attenuator is useful in sinking some of the heat coming down the inner conductor through its 50 Ω resistance path to ground. The bottom section of the input line is a miniature stainless steel coaxial cable [75] (0.114 mm inner diameter, 0.51 mm outer diameter) that runs from the 1K pot to the base temperature bracket, where it is connected to a 20 dB attenuator and then teminated in a directional coupler (-20 dB

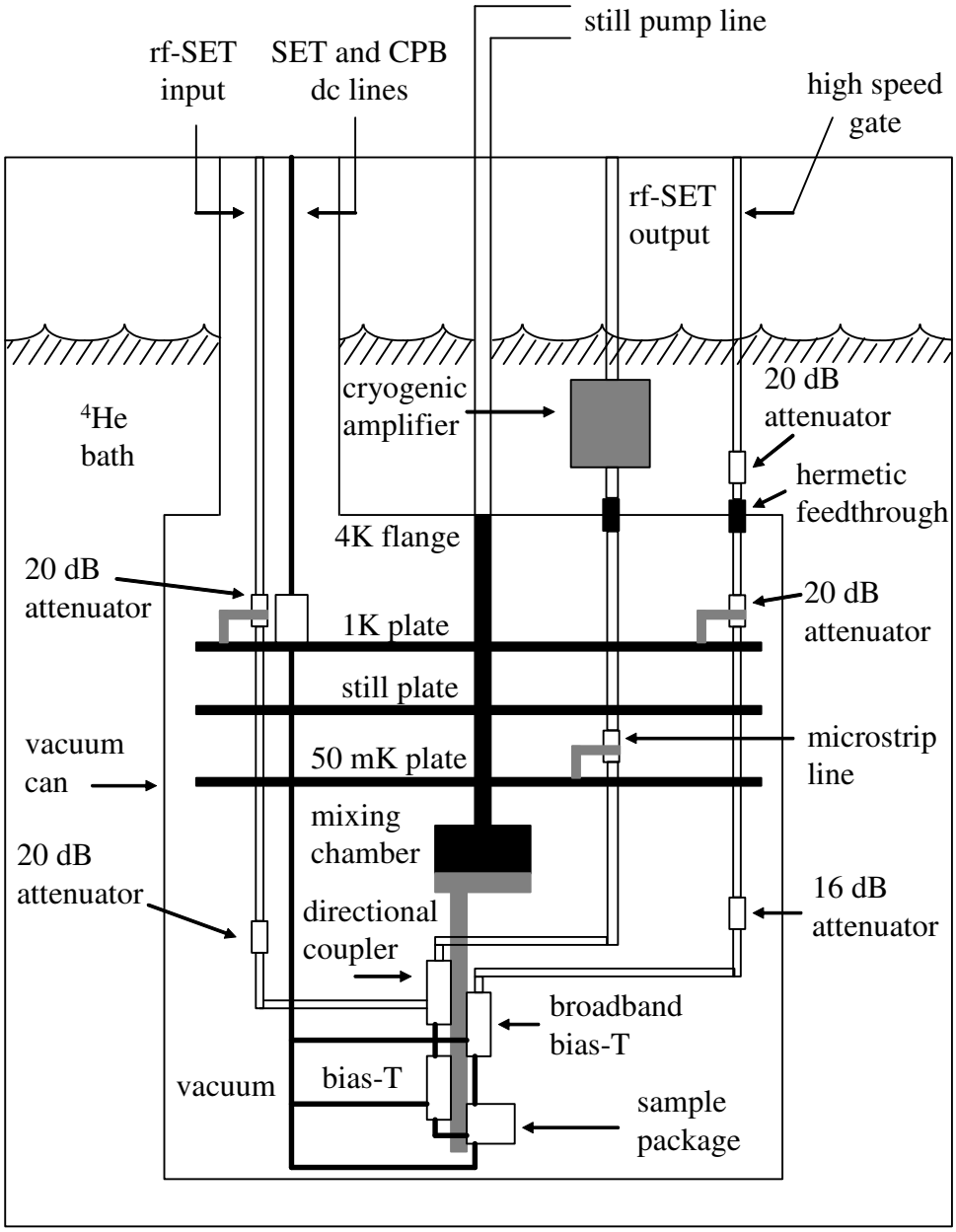

Fig. 5.8: Schematic of the wiring and heat sinks for measurement lines in the dilution refrigerator.

coupling) in good thermal contact with the bracket. The output conductor of this section is thermalized at the still by wrapping it in copper wire, coating with silver paint and then pressing the assembly against the still plate with a brass screw.

The output line carries the rf-SET reflected wave and should have negligible attenuation to prevent a reduced signal-to-noise ratio (S/N). Initially, I did rf-SET measurements at 1.5 GHz and chose a niobium UT-85 semi-rigid coaxial cable for the output signal. Thermal sinking of this line's output conductor was achieved by wrapping a copper wire around the cable, gluing it with Stycast and pressing the wire against the mixing chamber, still and 1K plates with brass screws. I used a thin film microstrip line inserted in this line at the 1K pot to thermally sink the inner conductor (in the last setup I used, this microstrip line was placed at the 50 mK plate, as shown in Fig. 5.8). The microstrip line was fixed with vacuum grease in a copper package that was attached to the still plate and soldered to wall-mount SMA connectors. This line ran from the base temperature bracket to a sealed feed-through on the 4K flange. On the other side of the feed-through, the signal is fed to a cryogenic amplifier [76] with a 2K noise temperature (75 $pV/(Hz)^{1/2}$ input voltage noise) sitting in the helium bath. I connected the output of the amplifier to the top of the fridge by a stainless steel semi-rigid UT-85 coaxial cable.

I note that for the last year (2005) I changed the design of the rf-SET resonator to 650 MHz. This was done to be able to test samples fabricated by Dr. Echternach at JPL [70], who designed his samples for this frequency. At about the same time, the feedthrough for the output line started leaking and Dr. Palmer and I had to replace the niobium coaxial cable when we repaired the leak. Since we were operating now at a lower frequency, we

decided to use the same kind of miniature stainless steel cable used for the input line. At this point I also moved the microstrip line to the 50 mK plate.

To produce the excited state of the CPB, a high-bandwidth (~40 GHz) line is required to apply microwave signals to the gate of the box. One common technique to control the quantum state of the box is to apply a fast-rising voltage pulse to the gate [26]. Since this pulse is not monochromatic, it requires a flat frequency response up to about 30 GHz. For this reason a coaxial line with low losses was desirable and the thermalization of this line posed a greater challenge than the other lines. For the upper section of this line, I used a silver-coated stainless steel UT-85 coaxial cable [77] with a measured attenuation of 6 dB at 40 GHz. This cable lies inside the helium bath and connects the top of the cryostat to a hermetic SMA feed-through on the 4K flange (see Fig. 5.8). The lower section is a niobium UT-85 coaxial cable with SMA crimp-on connectors at the ends, running from the 4K flange to the mixing chamber. Several matched attenuators are inserted along this line (20 dB in the helium bath, 20 dB at the still and 16 dB at the mixing chamber) to thermally sink the inner conductor and reduce high frequency noise generated at higher temperatures. Special copper clamps were designed by Dr. Palmer to ensure a good thermal contact between the attenuators and the fridge plates. A broad band bias-T attached to the base temperature bracket is used to add a dc bias to the microwave gate signals and provides further thermal isolation between the inner conductor of the high speed line and the sample (see Fig. 5.8). In addition to this, the outer conductor was directly connected to the refrigerator plates by wrapping copper wires around them. The wires were then glued with Stycast and then pressed to the plates by brass screws.

5.4 High frequency filtering

All of the high frequency lines are heavily filtered. First, the filters need to prevent broadband thermal energy from high temperature stages from reaching the SET and CPB. Second, the filters, need to reduce the amount of high frequency noise ($\hbar\omega \gtrsim E_c, E_J, \Delta$) reaching them to suppress unwanted transitions and excitations. High frequency noise is generated in all lossy elements, including the cables and attenuators, according to the Planck formula:

$$S_V(f) = \frac{2Rhf}{1-\exp\left(-\frac{hf}{k_B T}\right)} \tag{5.11}$$

where R is the resistance and I am using the convention where f can be negative (see Chapter 3). The dc lines are the most heavily filtered and therefore have a negligible contribution to the total noise.

The attenuation of the dc lines is summarized in Table 5.1. I note that the rf-SET input line has substantially larger attenuation (40 dB from attenuators plus 20 dB from the directional coupler plus the high frequency attenuation of the stainless steel cables) than either the rf-SET output line or the high-bandwidth gate.

The voltage noise seen at the gate of the CPB can be estimated from the equivalent circuit shown in Fig. 5.9. The power spectrum at the cold end of the high-bandwidth gate is given by:

$$S_V(f) = \frac{S_V(f, 300\,K)}{10^{5.6}} + \frac{S_V(f, 4\,K)}{10^{3.6}} + \frac{S_V(f, 1.6\,K)}{10^{1.6}} + S_V(f, 0.03) \tag{5.12}$$

where $S_V(f,T)$ is evaluated from Eq. 5.11 using $R = 50\Omega$. For the rf-SET output line the

Table 5.1: Attenuation of dc lines at different frequencies.

Frequency (GHz)	Attenuation (300 K – 4 K) (dB)	Attenuation (4 K – 30 mK) (dB)
0.5	13	14
1	18	19
5	40	43
10	> 40	61
20	> 40	87

power spectrum at the cold end is calculated from:

$$S_V(f) = \frac{S_V(f, 4\,K)}{A(f)} + S_V(f, 0.03\,K) \tag{5.13}$$

where $A(f)$ is the measured attenuation of the stainless steel cable connecting the rf-SET to the cryogenic amplifier.

Fig. 5.10a shows a plot of the power spectrum at the output of these lines as calculated from Eqs. 5.12 and 5.13 but without including the last term, $S_V(f, 0.03\ \mathrm{K})$, which is plotted separately to illustrate the frequency range where the total noise could be decreased with increased attenuation or filtering.

I note that the expected excitation and relaxation rates resulting from this noise can be found from:

$$\Gamma_{\uparrow,\downarrow} = \left(\frac{e}{\hbar}\right)^2 \kappa^2 \frac{E_J^2}{(hf_{10})^2} S_V(\pm f_{10}) \tag{5.14}$$

The estimated $T_1 = (\Gamma\uparrow + \Gamma\downarrow)^{-1}$ as a function of n_g is presented in Fig. 5.10b for a CPB with $E_C = 1$ K and $E_J = 0.5$ K, assuming coupling $\kappa = 0.01$. I note that the estimated T_1 (from 3 μs to 42 μs) is substantially larger than measured relaxation times on CPBs with similar parameters and it is also larger than theoretical estimates of the mixing time caused by a coupled SET (see Fig. 4.10b). This implies that my experiment should not be limited by noise from the leads, at least as far as the lifetime of the state is concerned.

5.5 Measurement setup and instrumentation

Figure 5.11 shows a diagram of the setup I used for making dc measurements.

a)

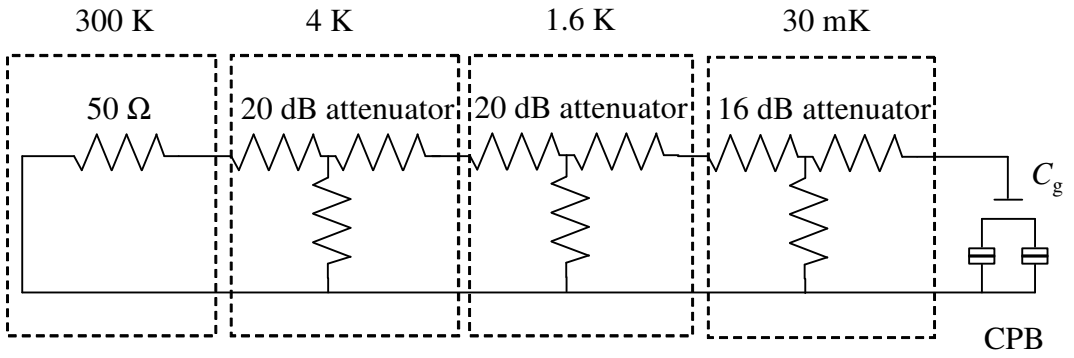

b)

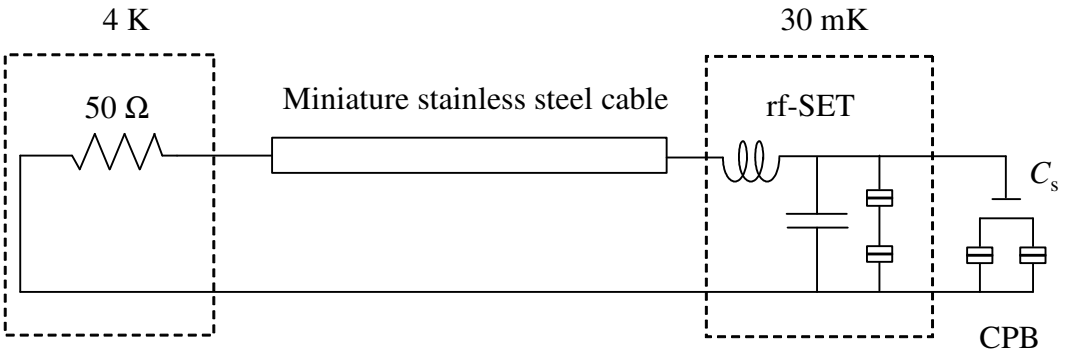

Fig. 5.9: Circuit model used to estimate the voltage noise presented to the CPB by two different lines: (a) High bandwidth gate, (b) rf-SET output line. Note that there is a stray capacitance C_s between the SET leads and the CPB that is not the same as the gate capacitance C_g in (a).

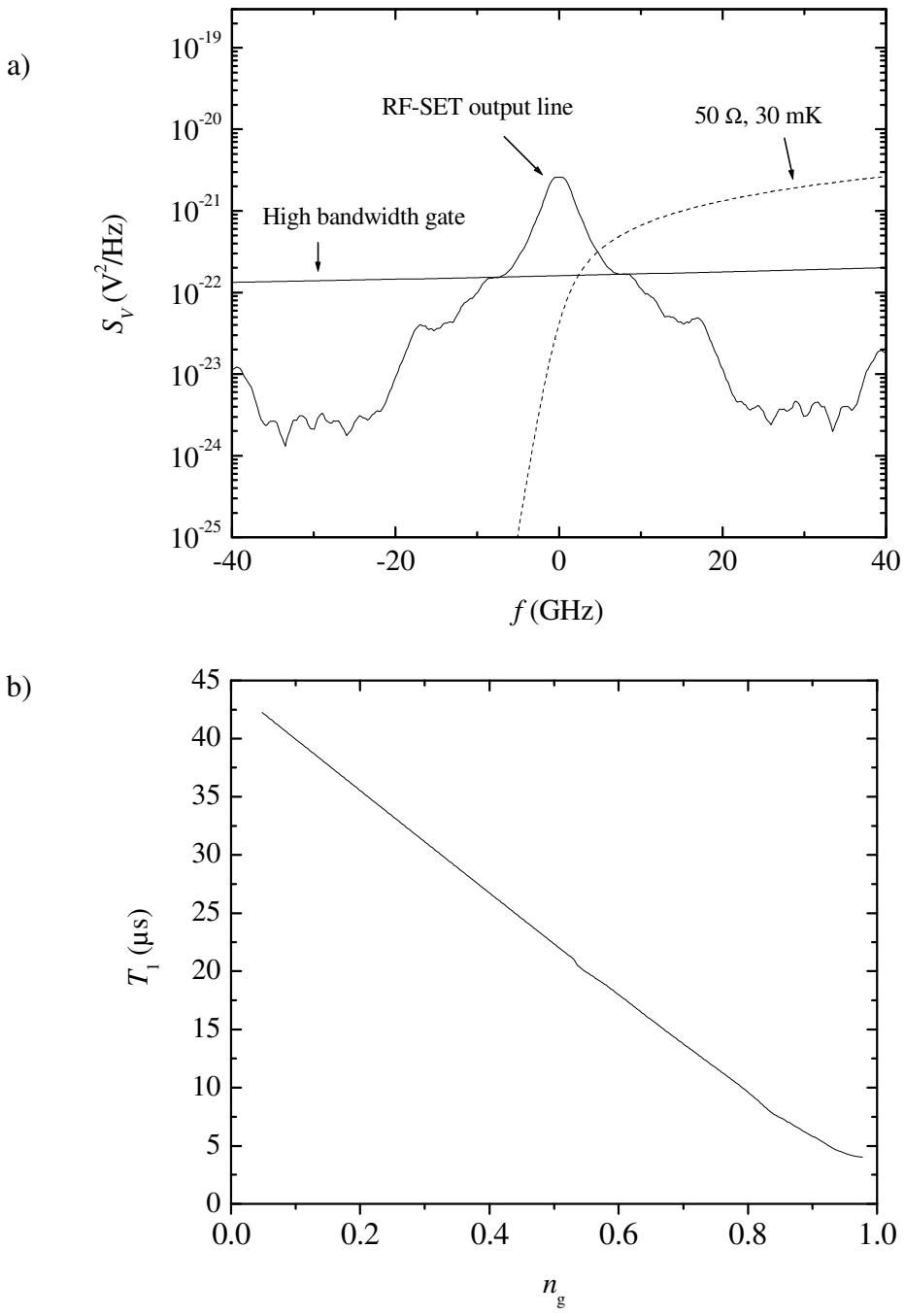

Fig. 5.10: (a) Expected voltage power spectrum at the cold end of the rf lines for the model circuit shown in Fig. 5.9. The solid curve includes only the noise generated at temperatures above 30 mK. The dashed curve shows the noise generated at 30 mK. (b) Estimate for T_1 *vs*. n_g from the total noise coming down the rf lines for a Cooper pair box with E_c=1K, E_J=0.5K and a coupling κ=0.01.

The experiment takes place in an rf-shielded room. Bias voltages V_{DS}, V_{gs}, V_{gb} are computer generated by a National Instruments PCI-4451 DAQ card and fed into the shielded room through optical isolators. The signals at the output of the isolators are scaled down to the mV range by resistive dividers. An Ithaco 1211 current amplifier is connected in series with the SET to measure the dc current. The internal feedback of the amplifier keeps V_{DS} equal to the voltage provided by the resistive divider. The current amplifier is designed to ground the output conductor of the BNC input connector but since the SET source terminal is grounded in the rf-SET configuration, the current amplifier is kept floating and its output measured by a differential amplifier and then fed to the computer through an optical isolator.

Both amplifiers and the optical isolators are battery operated to avoid 60 Hz noise. To characterize the SET, the current is measured as a function of V_{DS} (*IV* measurements) or as a function of V_g (modulation). For measurements of the CPB charge, the SET is biased at a fixed point with large gain ($\partial I/\partial n_g$) and the current is measured as a function of the CPB gate bias parameter n_g. Due to stray capacitances between the box gate and SET island, and between the SET gate and box island, the voltages V_{gs} and V_{gb} have to be swept at the same time to keep the SET operating point fixed during the measurement. Microwave signals are applied to the high-bandwidth gate to cause excitations in the CPB. Pulsed or continuous sinusoidal excitation is provided by an Agilent 83650B, 10 MHz – 50 GHz signal generator. Typically I use a power level of −10 to 0 dBm. Two-level voltage pulses with a 30 ps rise time are produced by an Advantest D3186 pulse pattern generator. The pulse pattern is programmed by a personal computer via GPIB

connections. Table 5.2 summarizes the main equipment used in this setup and the following.

Figure 5.12 shows the setup for rf-SET measurements. Bias voltages are provided through optical isolators. A bias-T is used to add a dc offset to the 500 MHz – 1.5 GHz rf carrier which is generated by an Agilent 83732B signal generator. The reflected wave is amplified first by a cryogenic amplifier with a 30 dB gain and then by two room temperature amplifiers with gains of 35 dB each. Gate signals at frequencies up to 80 MHz can be used to modulate and characterize the rf-SET. For frequency domain measurements the output of the room temperature amplifiers is directly connected to a spectrum analyzer. For time domain measurements the output signal can be demodulated with a mixer and the output displayed in an Agilent Infinium 54855A oscilloscope (0-3 GHz bandwidth).

To measure the charge on the CPB, I first biased the rf-SET on a high sensitivity point (typically in the JQP region) and then swept the gate voltages V_{gb} and V_{gs} by synchronized signal generators at a typical frequency of 1 kHz. The amplitude and phase of the signals are adjusted to account for the stray capacitances and keep the SET bias point fixed.

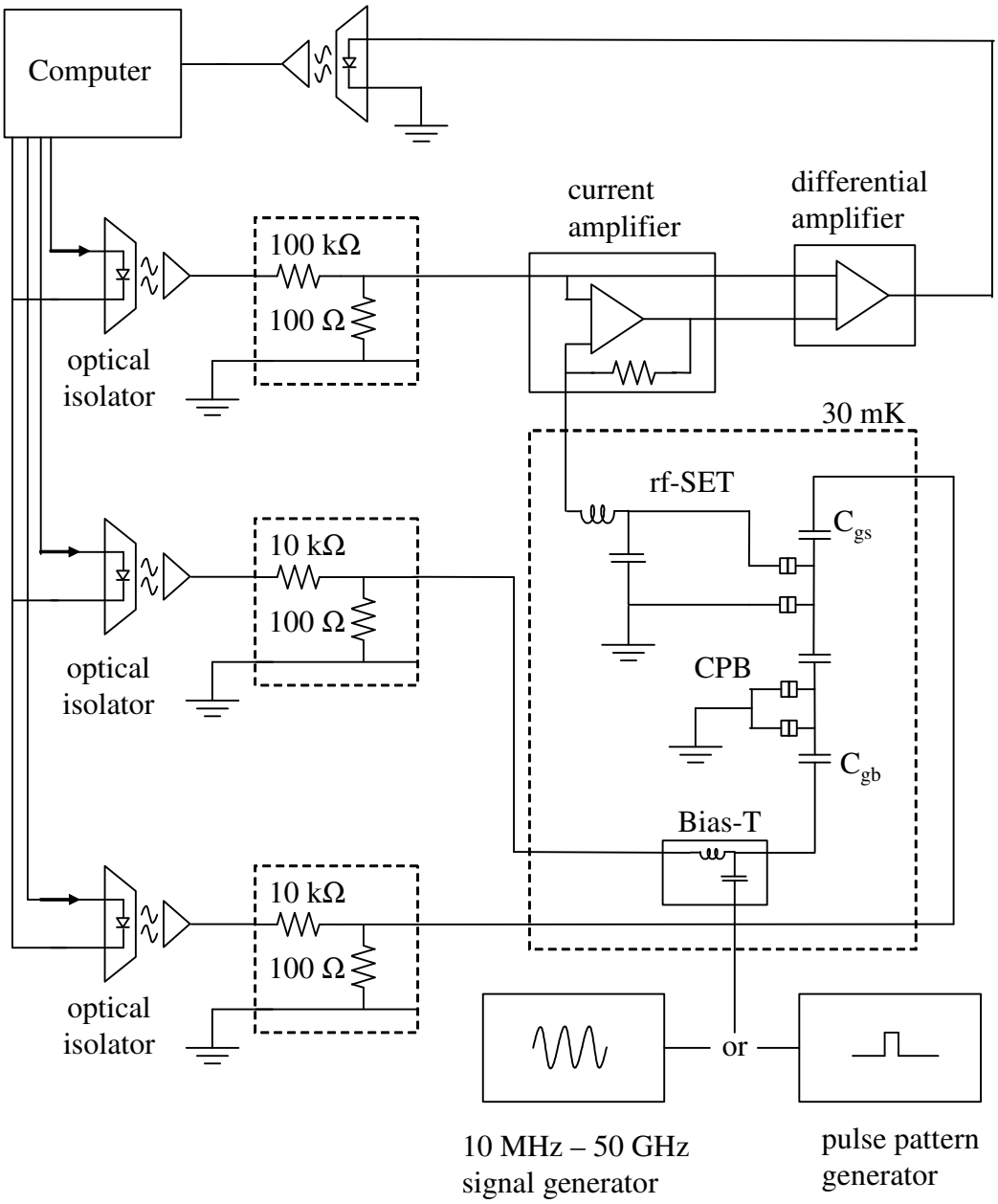

Fig. 5.11: Instrumentation setup for dc measurements on the SET and CPB.

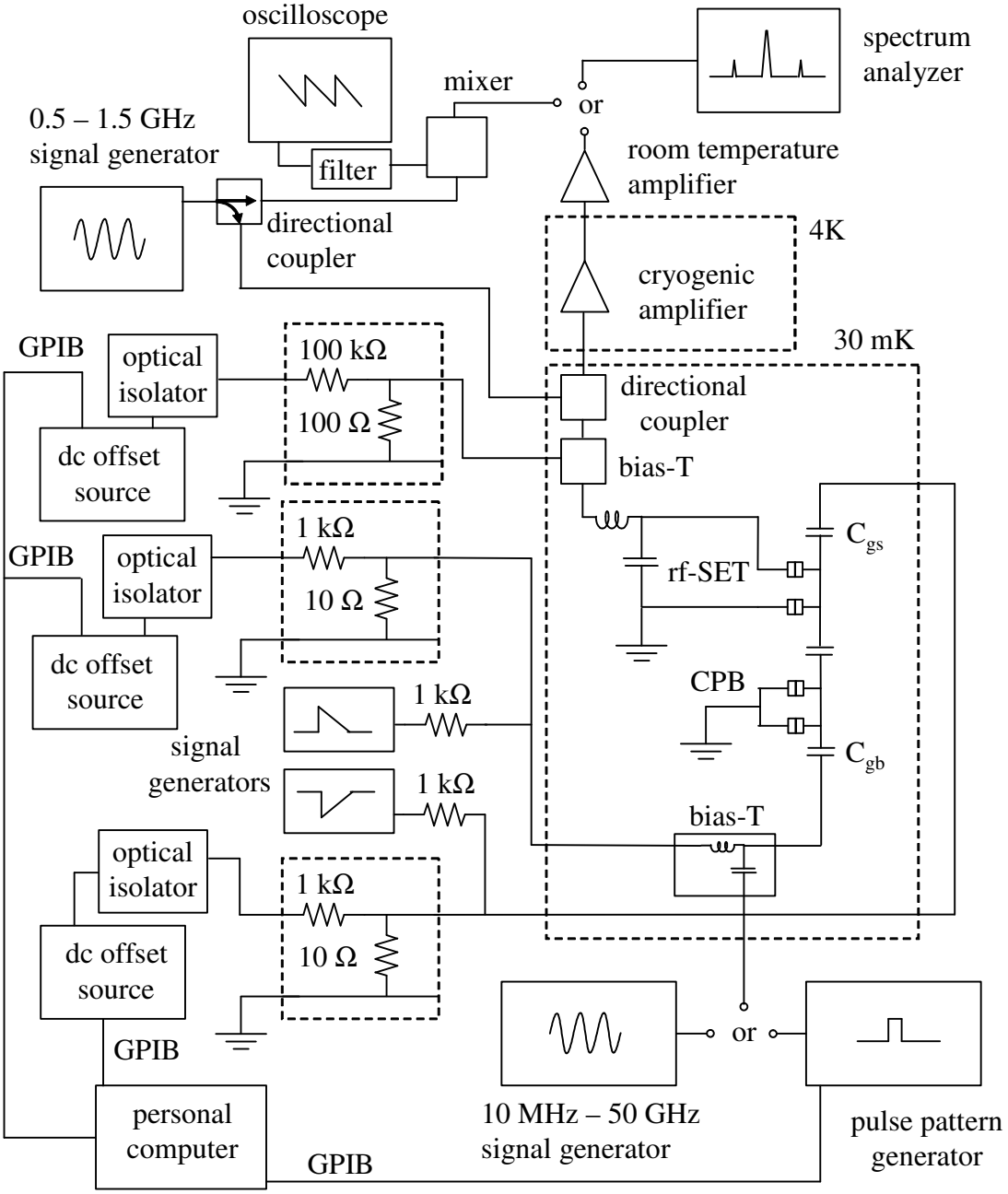

Fig. 5.12: Instrumentation setup for rf-SET measurements of the CPB.

Table 5.2: Main components of the measurement setup

Oscilloscope	Agilent Infinium 54855A
Spectrum analyzer	Agilent E4407B
rf signal generator (0.5 – 1.5 GHz)	Agilent 83732B
rf signal generator (0.1 – 50 GHz)	Agilent 83650B
Signal generators (low frequency)	Agilent 33250 A
Pulse pattern generator	Advantest D3186
Cryogenic amplifier	Berkshire technologies U-650
Directional coupler (rf-SET)	MAC technology C3202
Bias-T (rf-SET)	Mini Circuits ZFBT-4R2GW-FT
Bias-T (high speed line)	Anritsu K-250
Mixer	Mini Circuits ZFM-2000
Current amplifier	Ithaco 1211

Chapter 6: Characterization of devices

In this chapter I describe the measurements I used to characterize SETs and CPBs. Determination of the different device parameters is essential to evaluate theories, quantify sources of decoherence and optimize the CPB qubits. Throughout this thesis, I present data from 8 different samples. Two of the samples were made by Dr. Pierre Echternach [70] at the Jet Propulsion Laboratory (JPL) and are identified as PE1 and PE2. The rest of the samples were fabricated by myself in the cleanroom of the Laboratory for Physical Sciences (LPS), at the University of Maryland and are identified as CS1 to CS6. Table 6.1 summarizes the parameters of all the devices.

6.1 SET *IV* characteristics

Figure 6.1 shows an *IV* characteristic of an SET from sample CS1 measured at 30 mK with no magnetic field applied. Here the dc current through the SET is measured at fixed V_g, while V_{DS} is varied. Each of the curves in the figure corresponds to a different V_g.

The sharp rise of the current at V_{DS} = 886 μV is due to Giaever tunneling [52] and occurs when the voltage across each junction is equal to $\Delta_I+\Delta_L$ or $V_{DS} = 2(\Delta_I+\Delta_L)$, where Δ_I and Δ_L are the energy gaps of the island and leads respectively. As we will see, the two gaps are generally different because the island and the leads are deposited during different evaporations as a result of the two-angle evaporation technique. The energy gap in aluminum films is sensitive to variations in some processing parameters like the film thickness and oxygen content [78,79]. The samples discussed here were made at the base pressure of the evaporator. Therefore, I expect any difference in the gaps to be small and

Table 6.1: Summary of device parameters

Sample	SET parameters			CPB parameters	
	E_c/k_B (K)	R_Σ (kΩ)	Δ/k_B (K)	E_c/k_B (K)	E_J/k_B (K)
CS1	1.14	136	2.57	1.26	-
CS2	1.72	83	2.74	1.64	-
CS3*	1.67	36	2.55	-	-
CS4*	-	51	2.36	-	-
CS5	1.25	62	2.56	1.54	-
CS6	0.92	50	2.82	0.69	-
PE1	1.20	139	2.52	0.794	0.327
PE2	1.03	63	2.48	0.71	0.72

* Samples CS3 and CS4 were fabricated by a different process than the one described in sections 5.2.2 and 5.2.3. Sample CS3 used a trilayer resist system, similar to the one described in section 5.2.1, but with PMMA as the top layer. Sample CS4 used a PMMA/Copolymer bilayer backed at 180 °C for 5 minutes. The Al evaporation for both devices were made from a current-heated tungsten filament.

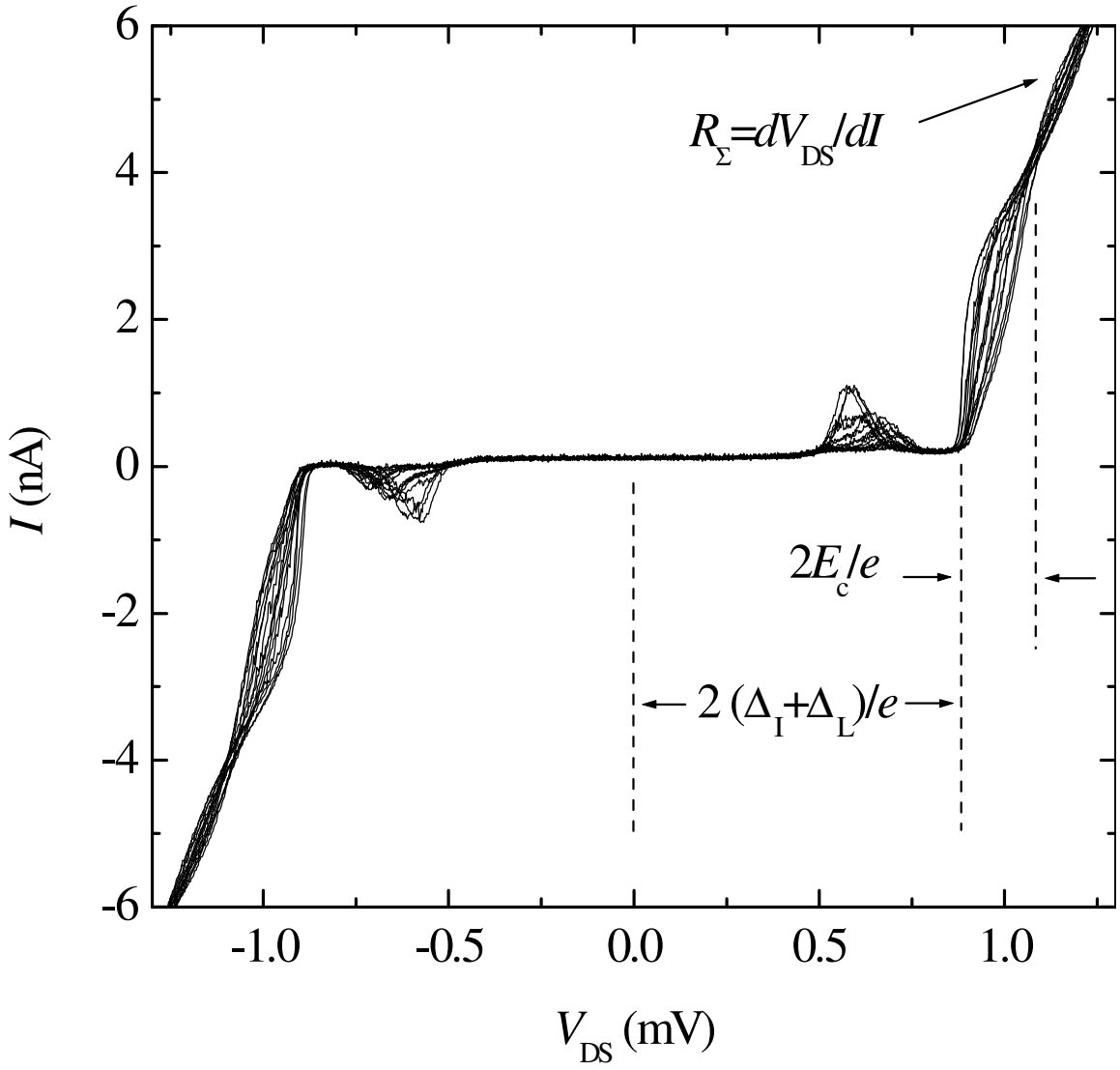

Fig. 6.1: *IV* curves of the Al-AlO_x-Al SET on sample CS1 for different V_g at T=30 mK.

generally I assume $\Delta_1=\Delta_L=\Delta$.

Examination of Fig. 6.1 shows that at large V_{DS} bias, the *IV* characteristic of the SET is linear, with $(\partial I/\partial V)^{-1}=R_\Sigma=R_1+R_2$. For this sample we get $R_\Sigma=136$ kΩ. Modulation of the dc current with gate voltage is apparent for V_{DS} around the JQP and above 4Δ. In the Giaever tunneling range ($V>4\Delta/e$) we can see a nodal structure, *i.e.* V_{DS} values where there is no current modulation (*e.g.* $V_{DS}=1.08$ mV). These nodes are equally spaced by a voltage $\Delta V=2E_c/e$ [53] and thus provide a way to determine $E_c=e^2/C_\Sigma$. For this sample we find $E_c=98$ μeV and $C_\Sigma=0.82$ fF.

For fixed V_{DS} the current is a periodic function of V_g. Figure 6.2 shows the current modulation of Sample CS1 at $V_{DS}=520$ μV, which is near the JQP. Each period corresponds to the average number of electrons on the island changing by one. The gate capacitance is given by $C_g\Delta V=e$ which gives $C_g=7.3$ aF.

Superconductivity in the aluminum films can be suppressed by applying a magnetic field $B\sim1$T. We can obtain additional information from the *IV* curves in the normal state. Figure 6.3 shows the characteristics of sample CS1 in the normal state for different V_g. The most evident feature in these curves is the zero current plateau due to the Coulomb blockade. In principle this feature provides another way to determine E_c, but there are several issues that complicate the interpretation of the curves. According to the orthodox theory [50], at $T=0$ the onset of current happens when $\Delta G(n)$, the change in the free energy of the system after a tunneling event (see Eq. 4.4), is equal to zero. In the actual measurements the current rise is not as sharp as predicted by the orthodox theory, even if one takes into account the temperature of the mixing chamber. Excessive rounding of the *IV* curves is caused by factors like cotunneling [80], noise from the measurement

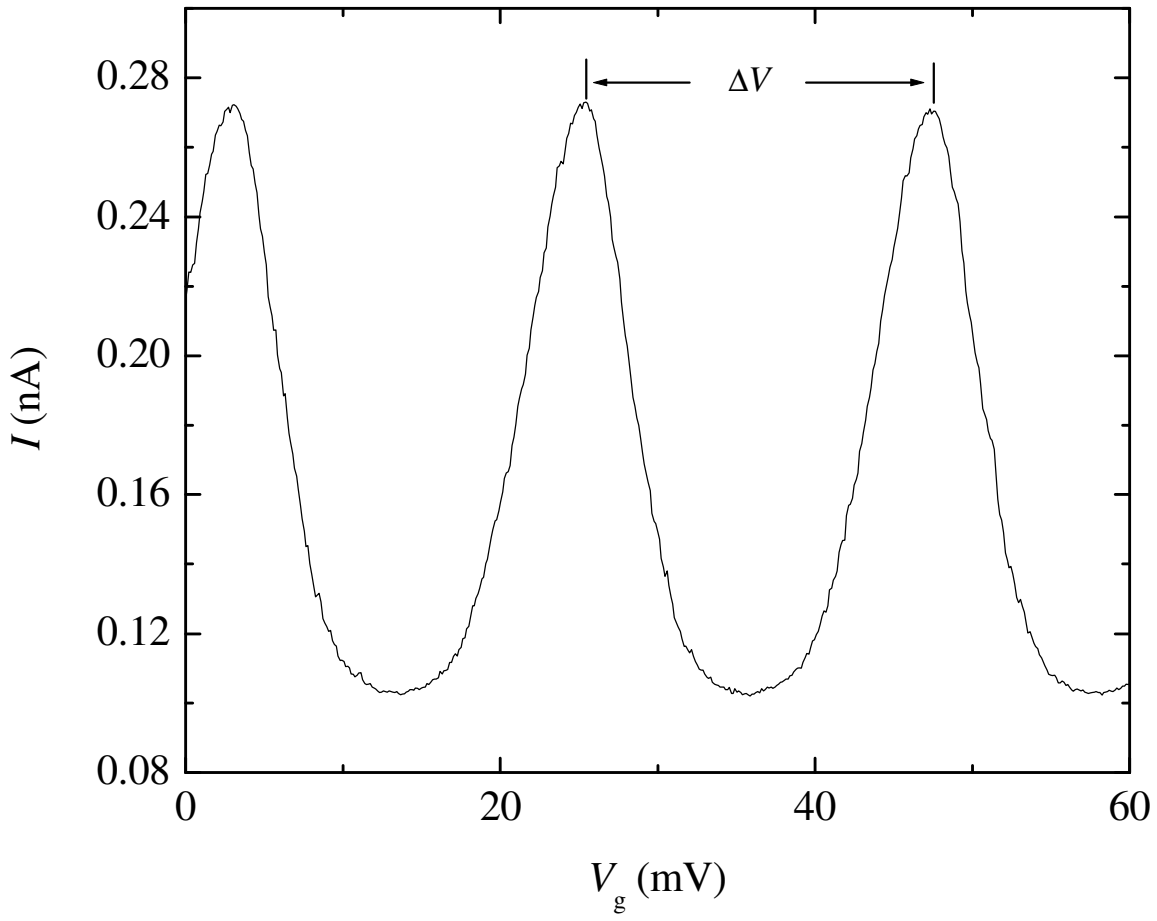

Fig. 6.2: Modulation of the dc current of SET CS1 in the superconducting state for fixed V_{DS}=520 μV.

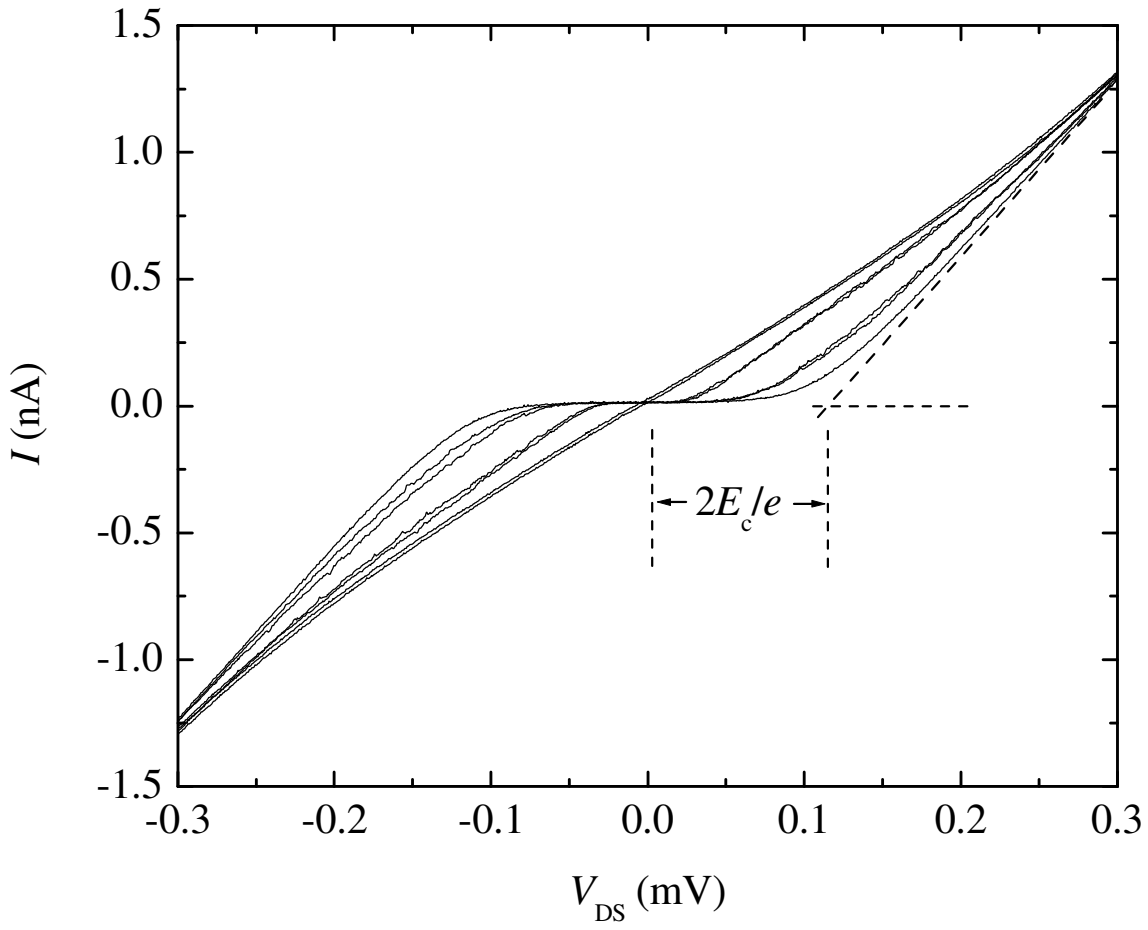

Fig. 6.3: *IV* curves of the SET in sample CS1 in the normal state ($B \approx 1$T) for different V_g.

apparatus and an **e**levated electronic temperature due to self heating.

Cotunneling is the simultaneous tunneling of electrons through both junctions, thereby transferring charge from source to drain without the energy cost specified by Eq. 4.4. For $V_{DS}<E_c/e$ the cotunneling current is on the order of [80]:

$$I \approx \frac{\hbar}{2\pi e R_1 R_2 C_\Sigma} \tag{6.1}$$

or $I\sim 26$ pA for sample CS1, which is small but not negligible.

Low frequency noise from the instrumentation generates rounding when the *IV* characteristic is non-linear. However, since the *IV* curves in the superconducting state show very sharp features I can estimate that the voltage noise must be $V_n \leqslant 5$ μV and conclude that the rounding in Fig. 6.3 is not produced by noise.

A third cause for rounding is self heating, and this is likely the main cause. In a mesoscopic conductor at low temperatures the electron temperature T_e might differ from the phonon temperature T_{ph} due to poor electron-phonon coupling. The electron temperature of the SET island can be found from [81]:

$$T_e = \left(T_{ph}^5 + \frac{P}{\Sigma\Omega} \right)^{1/5} \tag{6.2}$$

where P is the power dissipated in the island, Ω is the volume of the island and Σ is a constant. For sample CS1 at $n_g=0$ and $V_{DS}=100$ μV, we have $I\approx 100$ pA, $P\approx 10^{-14}$ W and $\Omega\approx 0.5\times 10^{-20}$ m^3. Assuming $\Sigma_{Al} \approx 2\times 10^{10}$ Wm^{-3}K^{-5} [82], I find $T_e\approx 160$ mK. Simulated *IV*s (see Fig. 6.4) show considerable rounding for the above conditions $E_c/k_B T_e\approx 7.1$. In fact, these simulated curves look qualitatively very similar to the measured curves, strongly suggesting that self heating effects should be taken into account if the SET

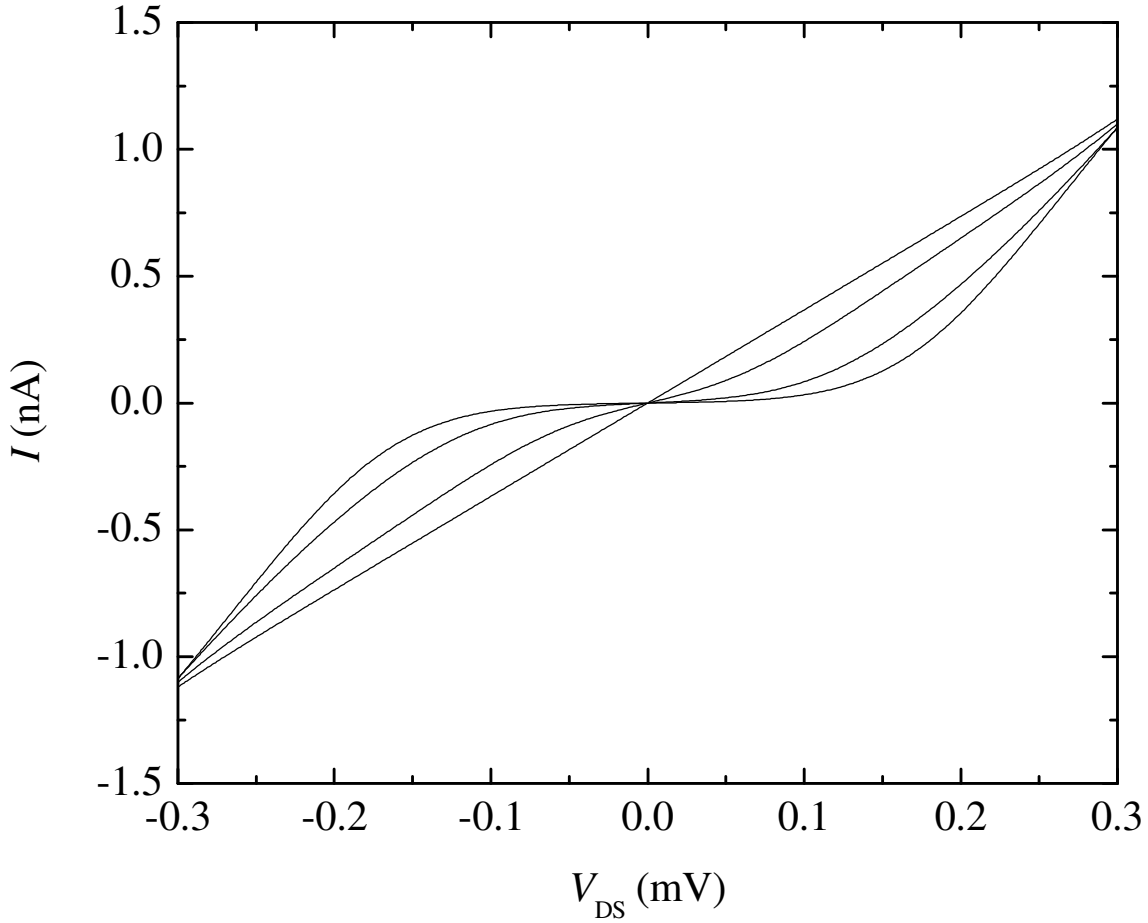

Fig. 6.4: Simulated *IV* curves of a normal metal SET with E_c=1.14 K and R_Σ=136 kΩ at T_e=160 mK.

parameters are to be determined from these curves.

The above analysis shows that an accurate determination of E_c in the normal state requires care since self heating and cotunneling cannot generally be neglected. On the other hand, the *IV* curves in the superconducting state offer sharp features that are to a large extent independent of temperature ($\Delta(T) \approx \Delta(0)$ for $T \ll T_c$) and they provide an easier way to estimate E_c.

Nevertheless, the *IV* curves in the normal state are useful to estimate the ratio of the individual junction capacitances C_1/C_2. The onset of current given by the orthodox theory is found by setting $\Delta G(n)=0$ in Eq. 4.4 [53]. I find:

$$V_g = \frac{e}{C_g}\left[n + \frac{1}{2} + (C_2 + C_g)\frac{V_{DS}}{e} \right] \tag{6.3}$$

and

$$V_g = \frac{e}{C_g}\left[n + \frac{1}{2} - C_1\frac{V_{DS}}{e} \right] \tag{6.4}$$

where n is the number of electrons on the island. These equations (see Fig. 6.5a) define the boundaries of the $I=0$ plateau on the V_g-V_{DS} plane. These boundaries can be identified in a plot of the measured current, shown in Fig. 6.5b as a gray-scale plot for device CS1. The slopes of these boundary lines, $(C_2+C_g)/C_g$ and $-C_1/C_g$, provide an absolute determination of C_1 and C_2 but, as discussed above, the rounding of the *IV* curves makes a precise determination difficult. However, an estimate of C_1/C_2 should be more accurate if a uniform criterion is used to define the $I=0$ boundary. From the plot I estimate $C_1/C_g \approx 100$ and $C_1 \approx C_2$ for the SET on chip CS1.

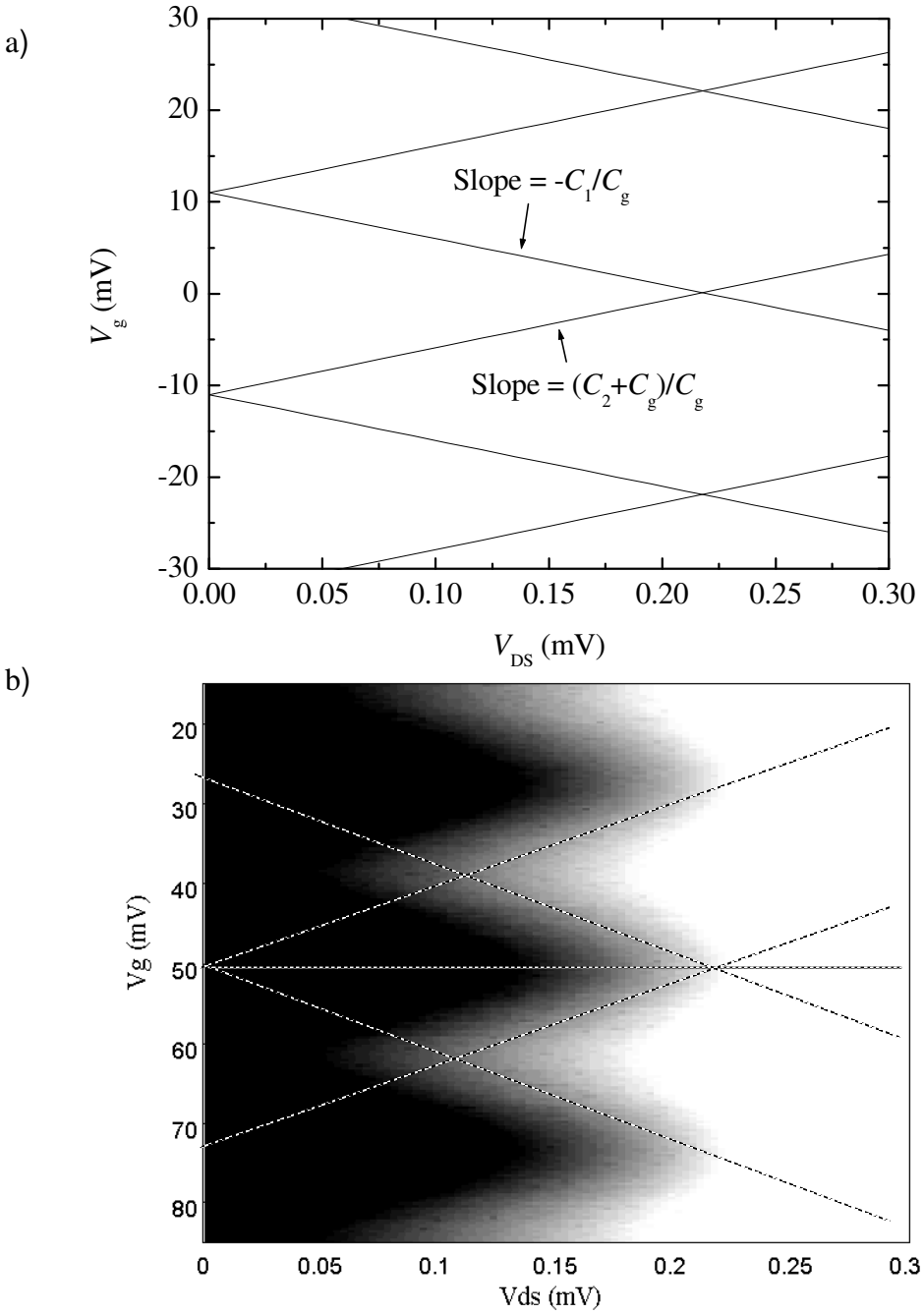

Fig. 6.5: (a) Boundaries of the Coulomb blockade plateau for a sample with C_1=C_2 and C_g=0.02 C_1. (b) Gray-scale plot of the measured current on sample CS1 in the normal state. The slopes of the dotted lines determine the parameters $C_1/C_g \approx 100$ and $C_1 \approx C_2$.

6.2 rf-SET measurements

The sensitivity of the rf-SET depends on the SET characteristics ($R_S=\partial V_{DS}/\partial I$, $\partial R_{SET}/\partial n_g$, E_c, *etc.*) and the impedance matching made by the resonant circuit. As I discussed in Chapter 4, the rf modulation is maximum when the impedance presented to the cable by the tank circuit is 50 Ω, and this requires an unloaded quality factor of $Q=R_S/\omega_o L\approx 30$. Q can be estimated, for example, by biasing the SET with a large dc current and measuring the noise spectrum at the output of the rf amplifier.

Figure 6.6 shows the circuit model I used to calculate the noise. For a large SET bias, the current power spectrum is given by $S_I=2eIF$, with the Fano factor $F=0.5$ arising from correlations between tunneling events [62]. Here S_I is the usual power spectrum, defined for positive frequencies only. This current noise can be modeled as a current source in parallel with a resistance R_S. From a simple circuit analysis, I find the voltage noise V_n at the input of the rf amplifier generated by the SET shot noise I_n:

$$V_n = \frac{Q_L I_n Z_o}{\sqrt{1+\left(2Q_L\frac{\delta\omega}{\omega_o}\right)^2}} \tag{6.5}$$

where $\omega_o=(1/LC)^{1/2}$, $\delta\omega=\omega-\omega_o$, $Z_o=50\ \Omega$ and

$$Q_L = \frac{1}{\frac{\omega_o L}{R_{SET}}+\frac{Z_o}{\omega_o L}} \tag{6.6}$$

is the loaded quality factor.

The output voltage noise measured on sample CS2 with a dc current bias of 400 nA is shown in Fig. 6.7. The maximum in the plot occurs at the resonant frequency $f_o=564$ MHz. I can define the bandwidth as the frequency deviation Δf where the voltage drops

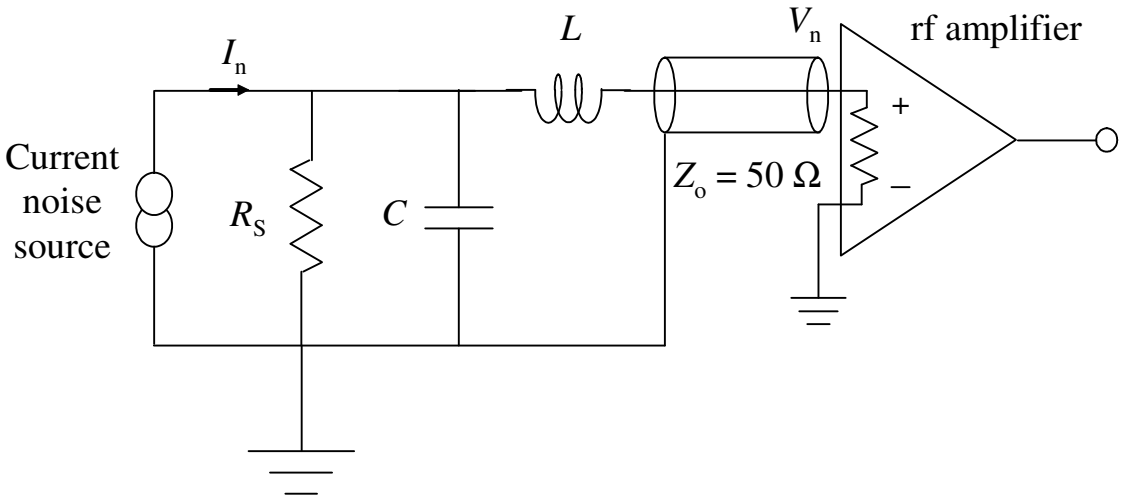

Fig. 6.6: Circuit model used to calculate the voltage noise at the input of the rf amplifier. The LC circuit represents the rf-SET impedance matching network.

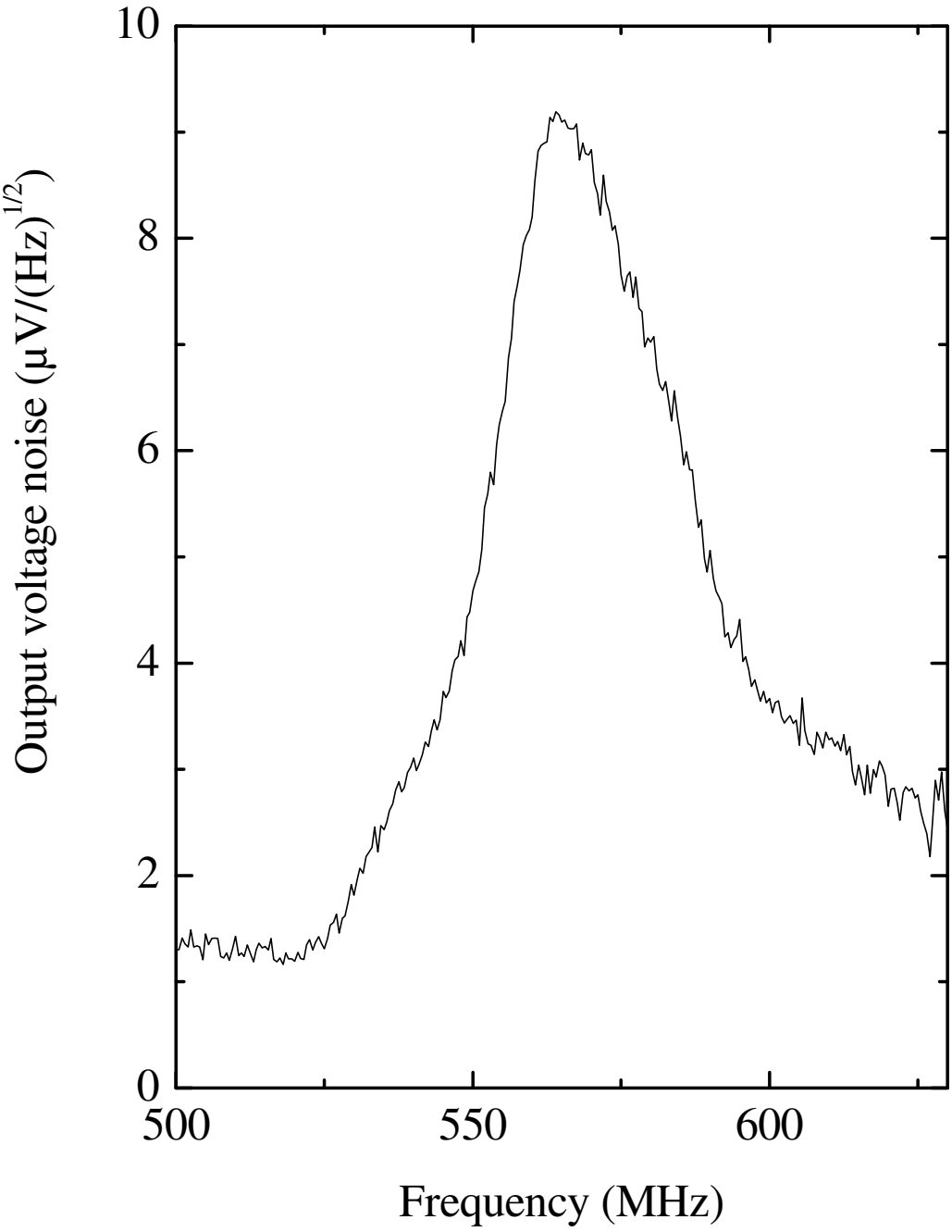

Fig. 6.7: Noise of the rf-SET at the output of the rf amplifier for sample CS2 with a dc current bias of 400 nA at T=30 mK. The noise at the input of the amplifier can be calculated from the circuit model shown in Fig. 6.6.

by $(1/2)^{1/2}$, and find Δf=14.5 MHz. From Eq. 6.5, this gives $Q_L=f_o/2\Delta f$=19.5. I estimated $R_S\equiv(\partial I/\partial V_{DS})^{-1}$=83 kΩ from the *IV* curves of this device and used this value to find the parameters of the resonant circuit, L=493 nH and C=188 fF. These circuit parameters imply that perfect impedance match would be achieved with R_S=61 kΩ, and this device is therefore close to the optimum design.

One can also find the gain of the amplifiers from shot noise measurements. The voltage power spectrum S_V at the output of the amplifiers at f_o is given by:

$$S_V = GS_{V0} + \frac{G}{A}(Q_L Z_o)^2 S_I = GS_{V0} + \frac{G}{A}(Q_L Z_o)^2 eI \tag{6.7}$$

where S_{Vo} is the noise floor referred to the input of the cryogenic amplifier, G is the total power gain between the cryogenic amplifier and the output of the room temperature amplifier and A is the attenuation of the cable connecting the rf-SET to the cryogenic amplifier. Here I am using the classical spectral density, which is defined for positive f only. Fig. 6.8 shows the measured S_V as a function of I. From the slope on this plot, I found G=94.7 dB using the attenuation A=3.3 dB, which was measured at room temperature. Dividing S_V at I=0 by G yields S_{Vo}=(72.5 pV)^2/Hz. I note that the amplifier has a specified noise temperature T_n=0.9 K (V_n=53 pV/(Hz)$^{1/2}$) at 650 MHz and T_n=1.8 K (V_n=70 pV/(Hz)$^{1/2}$) at 550 MHz.

I note that the sensitivity of the rf-SET could be improved by a factor of two by replacing the cable with one that has negligible attenuation and changing the resonant frequency to 650 MHz, where the amplifier noise is lower. In replacing the cable, it would be advisable to introduce a low pass filter to cut off high frequency noise.

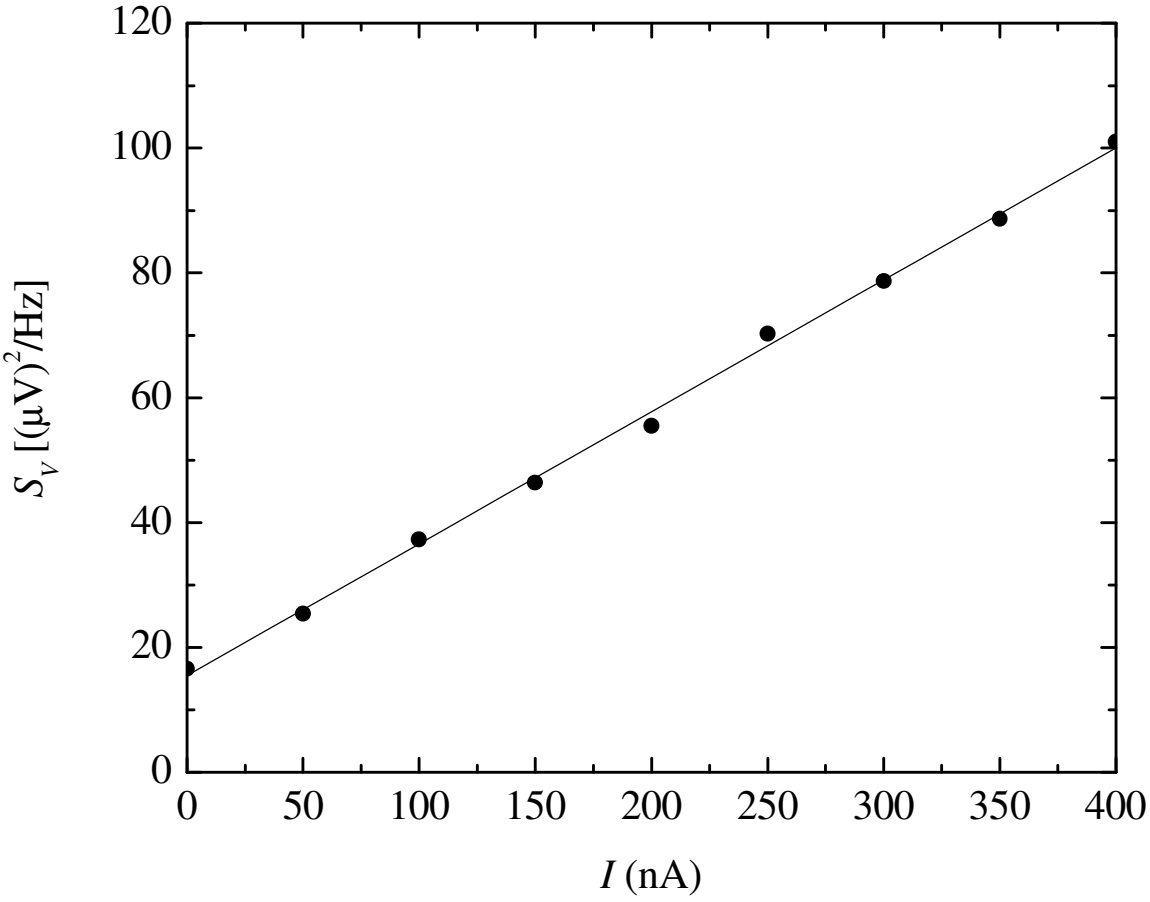

Fig. 6.8: $S_V(f_o)$ at the output of the room temperature rf amplifiers generated by shot noise through the SET of sample CS2.

Figure 6.9 shows a measurement of the reflected wave power for sample CS2 with the SET biased in the JQP region. The reflection coefficient shows a 20 dB modulation by V_g around the resonant frequency. Far away from the resonant frequency the impedance of the tank circuit is almost independent of R_S and therefore the modulation is very small.

Under normal operation a monochromatic rf carrier is sent to the resonant circuit and the reflected wave V_r is monitored to detect changes in the SET n_g. Since R_S is a periodic function of n_g care should be taken to choose a bias point with a linear response in V_r vs. n_g. Also, since the rf-SET response depends on impedance matching it is very sensitive to the bias conditions (V_{DS}, V_g, Carrier power and frequency) and it is necessary to adjust these parameters for optimum operation. The reflected signal can be observed directly in the frequency domain by connecting the output of the rf amplifiers to a spectrum analyzer. Figure 6.10 shows the reflected wave spectrum measured on sample PE1. The center peak corresponds to the carrier frequency f_o=602 MHz. The sidebands are produced by a 200 kHz sine wave applied to the gate of the SET with an rms amplitude corresponding to 0.0184 e.

The reflected power can be demodulated with a mixer or a diode to recover the input signal. Figure 6.11 shows the spectrum of the same signal from Fig. 6.10 after being demodulated with a mixer. The sensitivity of the rf-SET is determined by the noise floor on this graph. We can specify this noise as an equivalent input noise by calibrating the gain of the electrometer (the change in the output voltage for a change in the input charge) and dividing the output noise by this gain. For this sample I found a sensitivity of $2.3\times10^{-5} e_{rms}/(\text{Hz})^{1/2}$ at 1 MHz. I note that the excess noise at low frequency in this measurement is consistent with the noise at audio frequencies determined from dc current

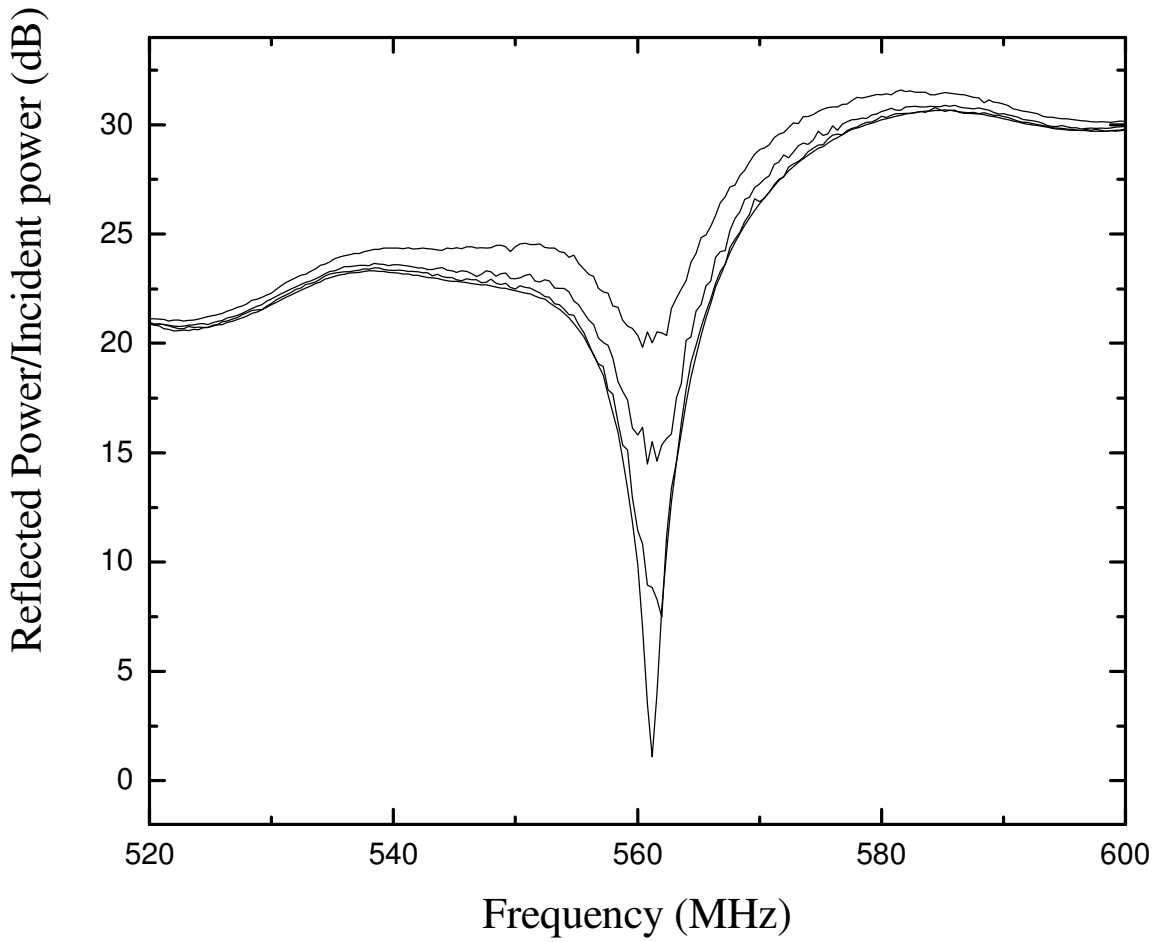

Fig. 6.9: Reflected wave power near the resonance for sample CS2 biased in the JQP for V_g=6.5, 5.8, 5.2 and 4.8 mV, from top to bottom, respectively.

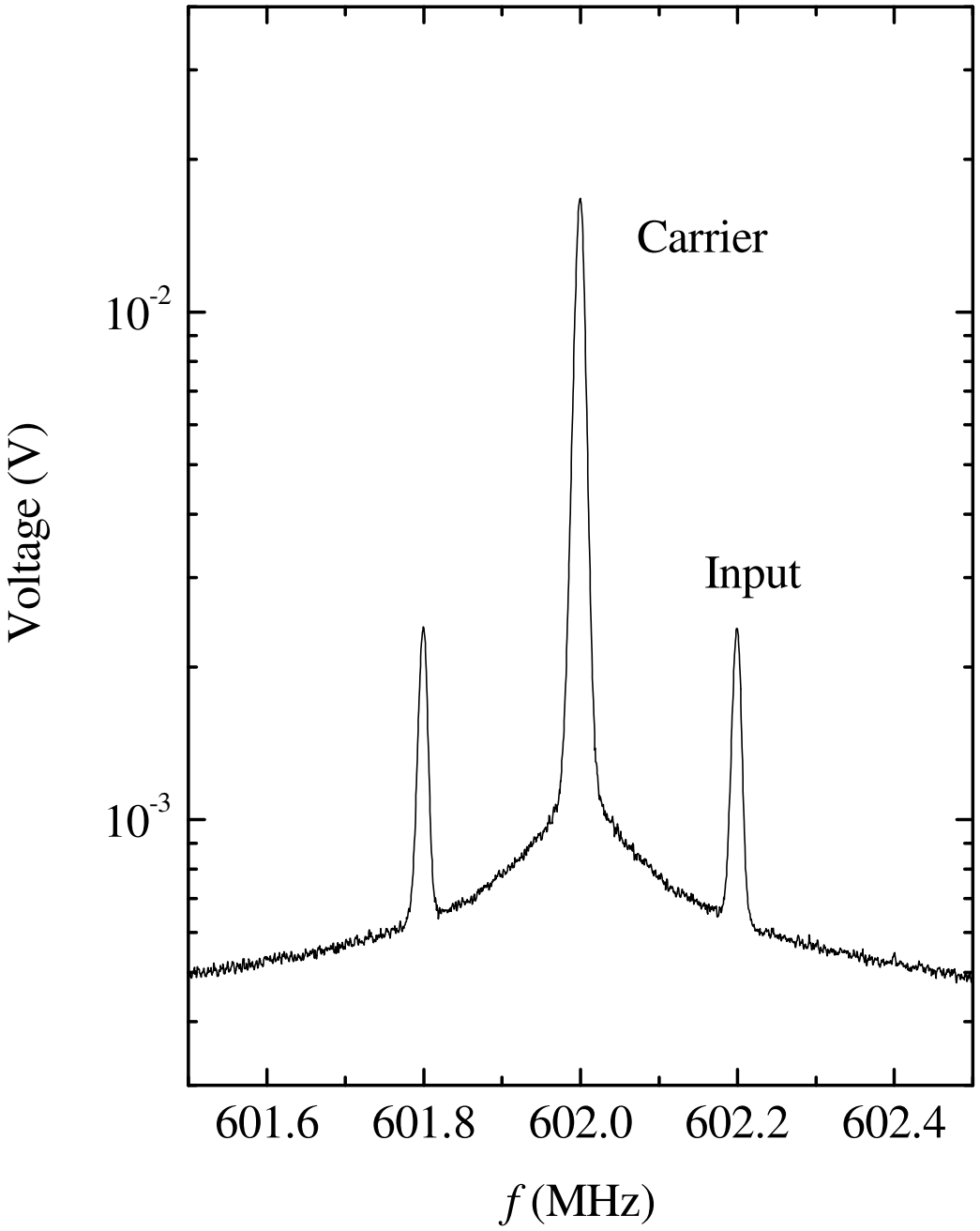

Fig. 6.10: Spectrum of the reflected voltage from the rf-SET of sample PE1 with a 200 kHz sine wave of rms amplitude 0.0184 *e* applied to the gate (see Fig. 5.12 for the circuit schematic). The resolution bandwidth of the spectrum analyzer was 10 kHz.

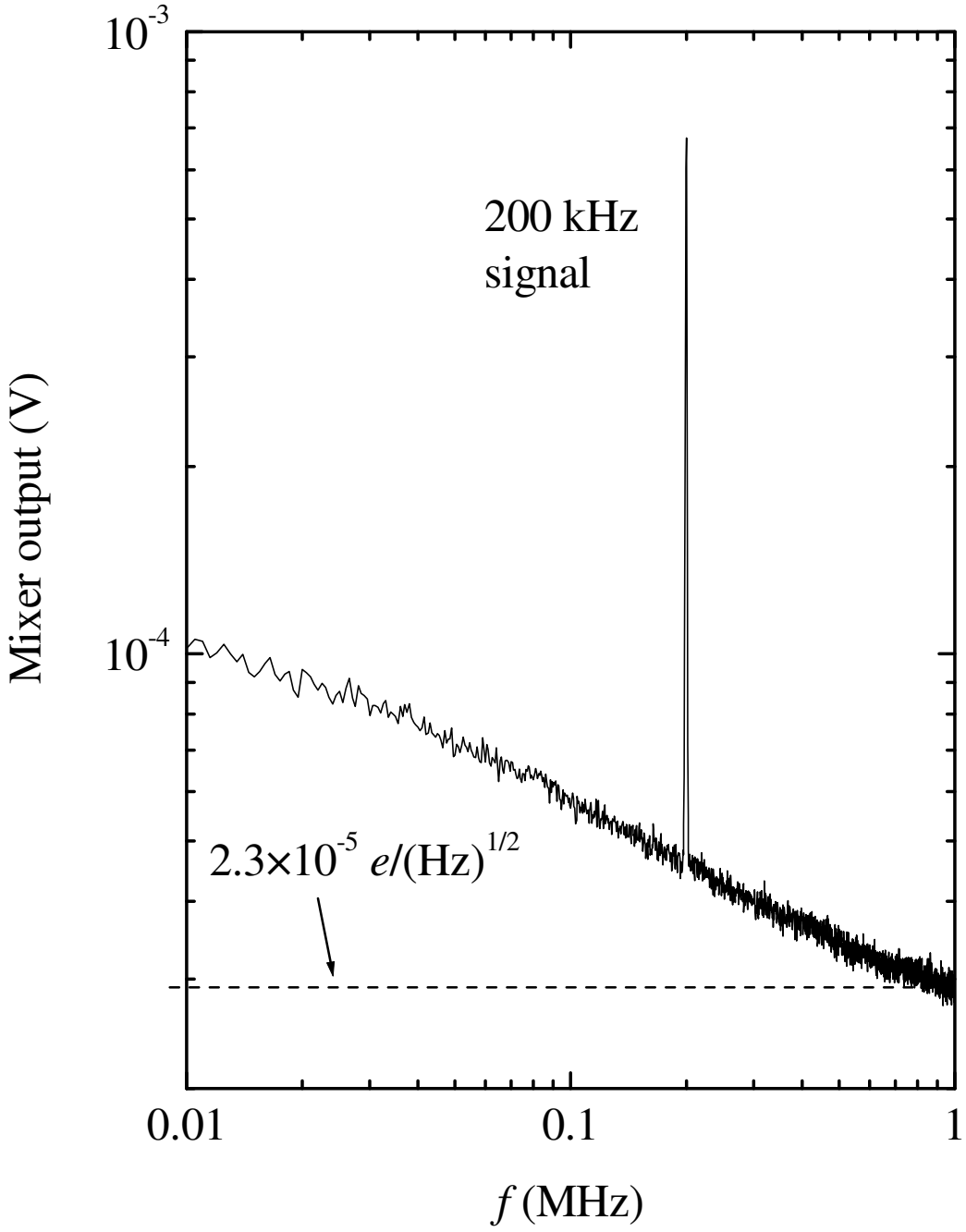

Fig. 6.11: Spectrum of the signal in Fig. 6.10 after being demodulated with a mixer (see Fig. 5.12 for the circuit schematic). The resolution bandwidth of the spectrum analyzer was 1 kHz.

measurements on this sample. Plotting this on a log-log scale shows it scales approximately as 1/*f*. Therefore, I conclude that below 1 MHz the sensitivity of the rf-SET is limited by 1/*f* charge noise. At higher frequencies the sensitivity is limited by the noise of the amplifier and the transfer function $\partial V_r/\partial n_g$.

For small charge variations ($\Delta Q \lesssim 0.1e$) and proper bias conditions, the rf-SET acts like a linear amplifier and the demodulated output signal is proportional to ΔQ. Figure 6.12 shows the rf-SET output for a 100 kHz, 0.1*e* peak-to-peak square wave signal applied to the gate. The bandwidth was limited by a low pass filter with a 1MHz cut-off frequency at the output of the mixer. The standard deviation of the points in a single trace (lower curve) about the average value (upper curve) is equal to 0.035*e*, which is consistent with the noise background in Fig. 6.11 and the measurement bandwidth:

$$\sigma_q^2 \approx \int_{f1}^{f2} S_q(f)\,df \approx 10^6 \left(2.3\times10^{-5} e\right)^2 \ln\left(\frac{1\text{MHz}}{0.1\text{MHz}}\right) = \left(0.0349\,e\right)^2 \tag{6.8}$$

Or σ_q=0.0349 *e*. From these measurements, I can conclude that measurements with a charge resolution as small as 0.035 *e* are possible on a 1.0 μs time scale. A theoretical estimate, shown in Fig. 4.10, predicts a mixing time of about 1 μs for a CPB coupled to an SET with κ=0.02 (Q=0.04*e*), both devices having E_c=1 K and E_J=0.5 K. This suggests that, a single shot measurement of the CPB state is possible with the above quoted charge sensitivity if other sources of noise do not cause the relaxation time to be less than 1 μs.

Devices with higher resonant frequencies were also successfully developed and tested. Figure 6.13 shows the modulation of the reflected wave by the gate voltage as a function of frequency measured on sample CS3. Figure 6.14 shows shot noise data on

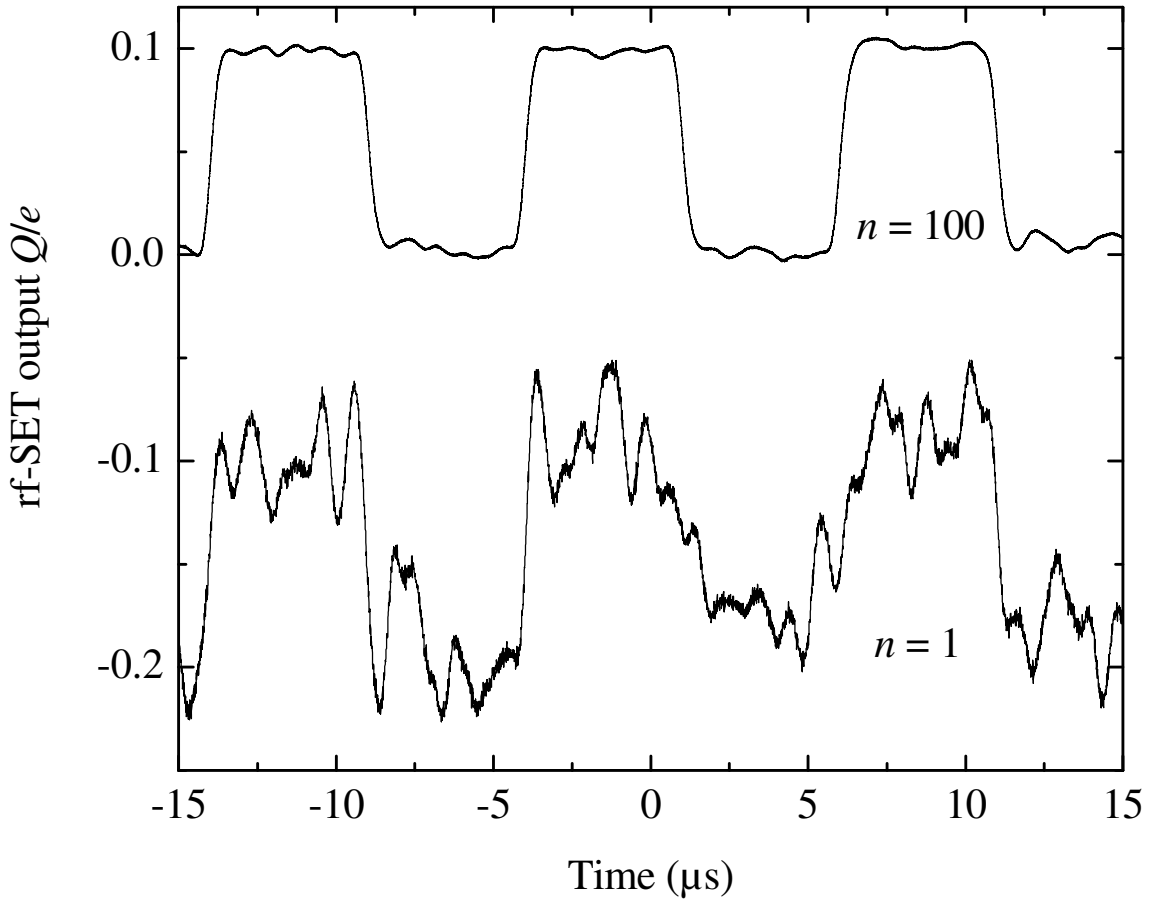

Fig. 6.12: rf-SET response of sample PE1 to a 100 kHz square wave of amplitude 0.1*e* applied to the gate. The output bandwidth was limited to 1MHz. The lower curve corresponds to a single trace and has σ_q=0.035*e*. The upper curve is the average of 100 single measurements.

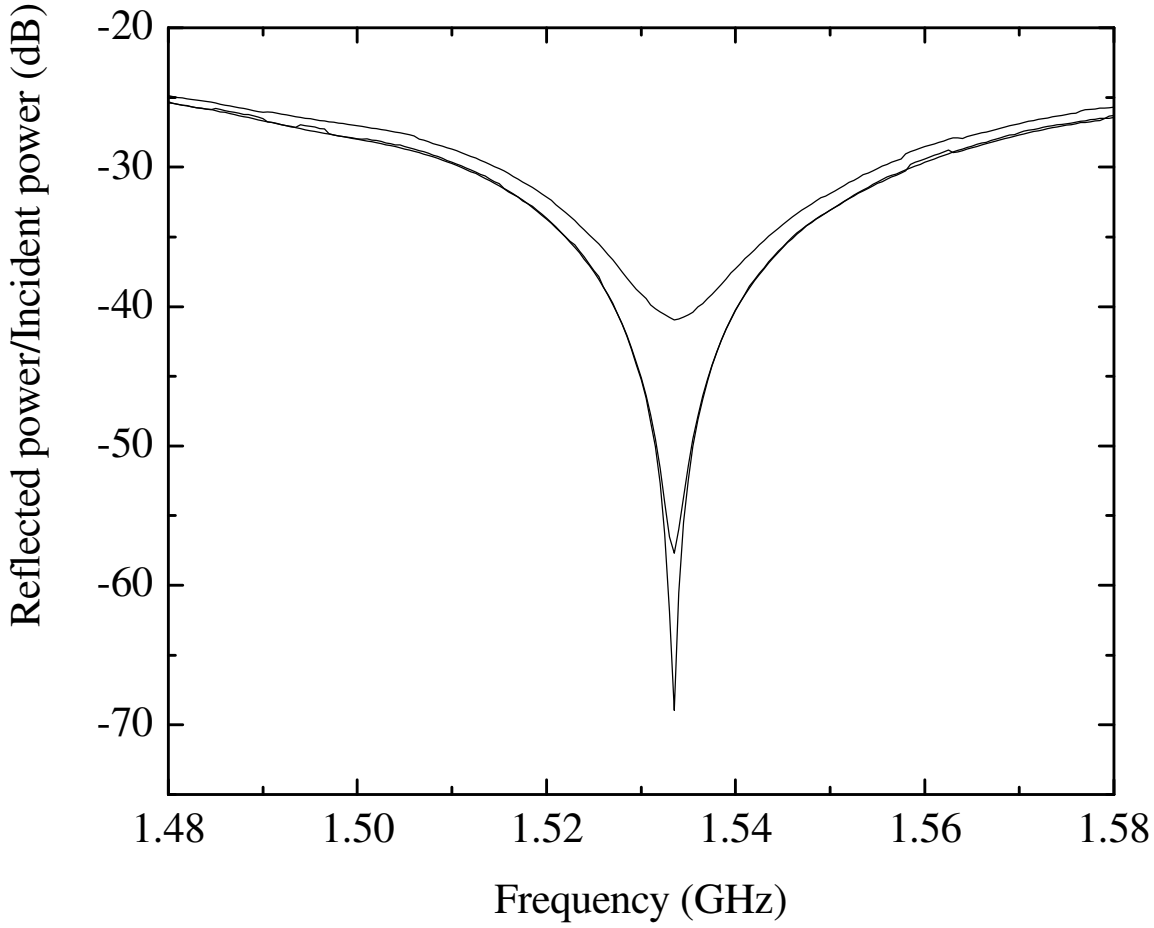

Fig. 6.13: Reflected wave power for the rf-SET of sample CS3 biased at V_{DS}=840 μV, in the Giaever tunneling range for different V_g. Note that the resonance is at higher frequency (1.535 GHz) than that for device CS2 shown in Fig. 6.9.

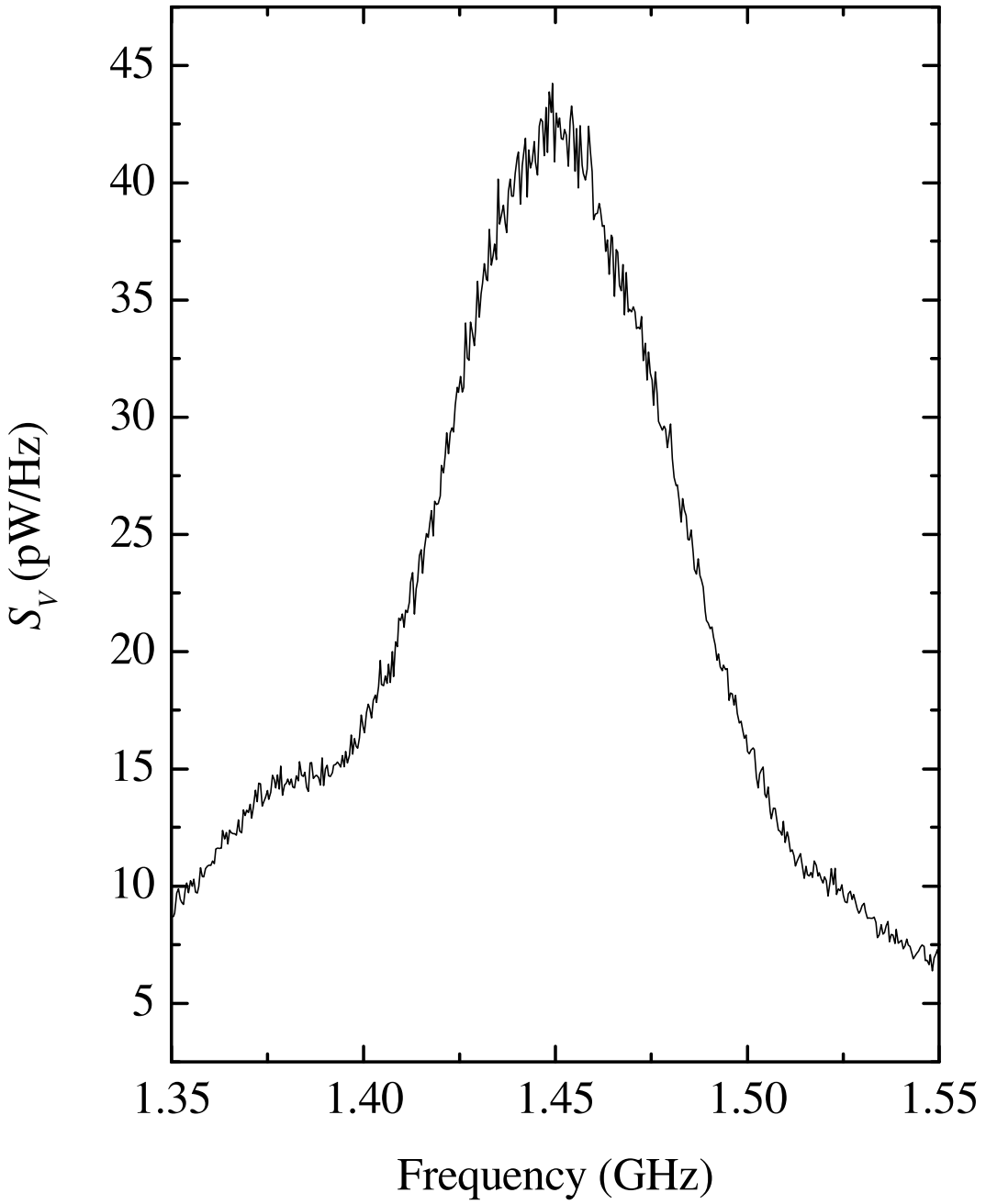

Fig. 6.14: S_V for the rf-SET of sample CS4 generated by shot noise. Q_L=36 was obtained from this measurement.

sample CS4 from which the resonant circuit can be characterized. The obtained Q_L=36 is about a factor of two larger than the optimum value. I note that the best charge sensitivity measured on any of my samples was $q_n=8\times10^{-6}\ e_{rms}/(\mathrm{Hz})^{1/2}$.

6.3 Charge measurements using the CPB

As I discussed in section 6.2, the SET current and dynamic resistance $R_S=\partial I/\partial V_{DS}$ are periodic functions of the SET gate voltage V_g. However, if the SET is properly biased it works like a linear electrometer for small variations of the gate charge and it can be used to measure the charge on the Cooper pair box (CPB).

To measure the charge staircase one needs to sweep the CPB gate voltage V_{gb} while keeping the SET biased in a linear region. Due to cross coupling between the CPB gate and the SET, this requires the SET gate voltage V_{gs} to be swept simultaneously by $\Delta V_{gs}=-\Delta V_{gb}(C_{bs}/C_{gs})$, where C_{bs} is the stray capacitance between the box gate and the SET and C_{gs} is the SET gate capacitance (see Fig. 5.11).

Figure 6.15 shows one such measurement I performed in the normal state (a field B=1 T was applied) on sample CS5 at T=23 mK. The upper curve shows the SET current as a function of V_{gs} with V_{gb}=0. On the bottom curve V_{gs} and V_{gb} were varied simultaneously with their amplitudes adjusted to cancel each other out. The resulting signal is proportional to the potential of the box island and is plotted as a function of V_{gs}. I note that the box gate charge is given by $en_g=C_{gb}V_{gb}-C_{sb}V_{gs}$.The sudden steps in the current are caused by one extra electron entering the box island. The corresponding potential change $\Delta V=-e/C_{\Sigma b}$ shifts the SET bias point by $\Delta Q=-eC_c/C_{\Sigma b}$, where $C_{\Sigma b}$ is the total capacitance of the box and C_c is the coupling capacitance between the box and the SET.

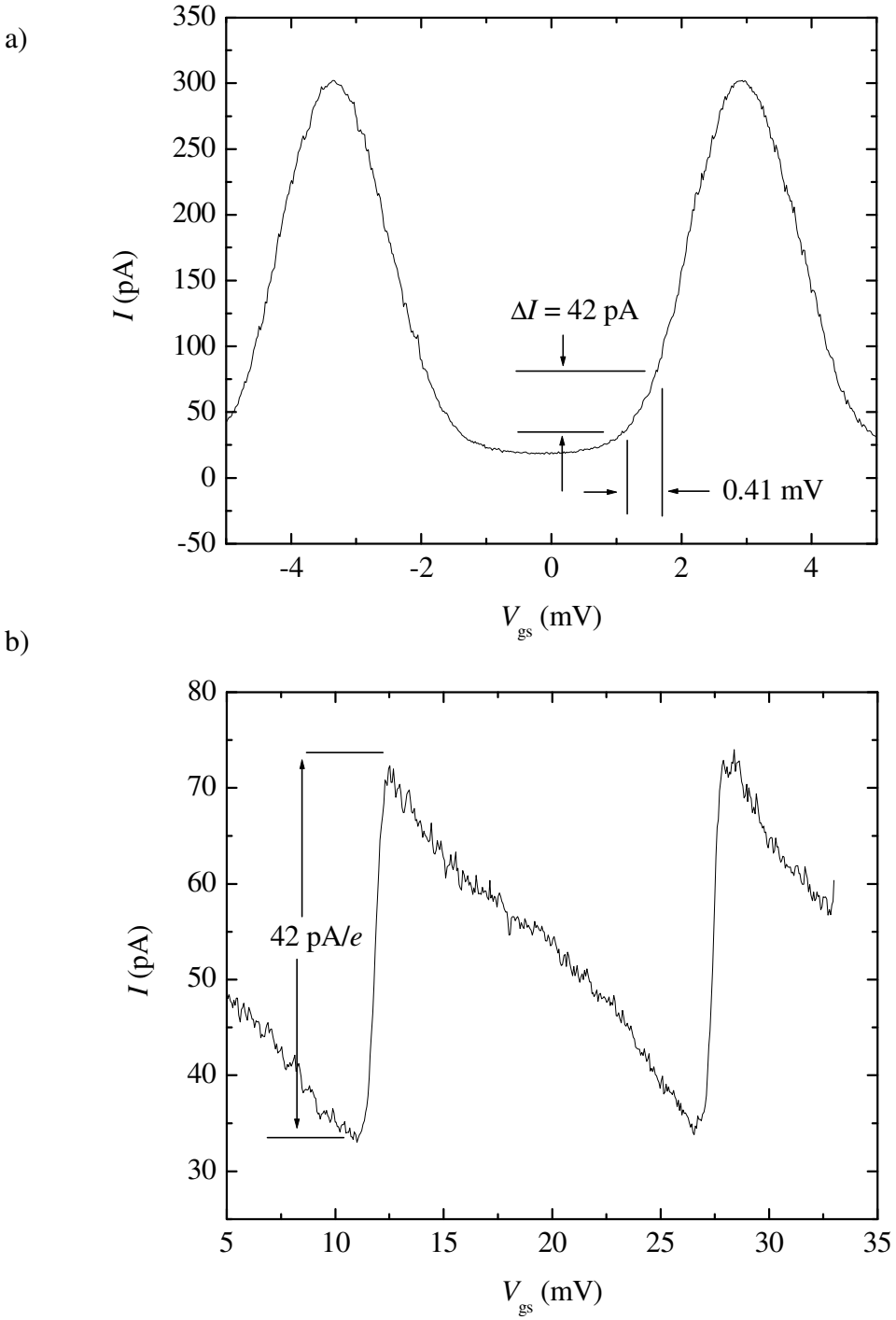

Fig. 6.15: (a) Modulation of the SET current on sample CS5 as a function of V_{gs}. (b) CPB charge signal measured by simultaneously sweeping V_g on both the SET and CPB gates to keep the SET biased in the linear region shown in the upper plot. All measurements were made at T=23 mK.

The coupling factor $\kappa = C_c/C_{\Sigma b}$ determined from these measurements is $\kappa = 0.066$.

The data shown in Fig. 6.15b can be converted to the staircase shape described in Eq. 2.2 by adding a straight line and applying suitable offsets and scaling factors. By fitting the data to the theoretical curve one obtains the ratio E_c/k_BT, besides the correcting factors and offsets. Figure 6.16 shows the best fit obtained by fitting Eq. 2.2 to staircases measured at three different temperatures. I note that some of the small deviations observed in the 45 mK staircase are reproducible and cannot be explained by limited measurement bandwidth or non-linearity of the SET I-V_g characteristic. It is possible that these features are caused by photon assisted tunneling, excited by high frequency noise from the SET [83]. The idea is that the voltage noise V_n generated by the SET scales linearly with E_c [61], which is relatively large ($E_c = 1.3$ K) for this sample. Also the large coupling factor $\kappa = 0.066$ means that the noise is relatively strongly coupled to the box.

Figure 6.17 shows a plot of the best fit values of k_BT/E_c for staircases I measured in device CS5 at different temperatures. I fit a line to the data points and used this to estimate the box charging energy E_{cb} from the slope of that line. For sample CS5, I found $E_{cb}/k_B = 1.54$ K. The plot also shows that the sample temperature follows the temperature of the mixing chamber down to $T \approx 20$ mK. For the measurements used in Fig. 6.17, I took special care to bias the SET at low V_{DS} (50 μV) and low current (60 pA) in order to minimize power dissipation ($P = 3$ fW).

At higher bias the heating of the box by the SET is evident. I also measured the box temperature at three different SET bias points, at a fixed mixing chamber temperature of 29 mK. I found an increase in the box temperature of 8 mK, 28 mK and 38 mK when the power dissipated by the SET was 6 fW, 78 fW and 450 fW respectively (see Fig. 6.17).

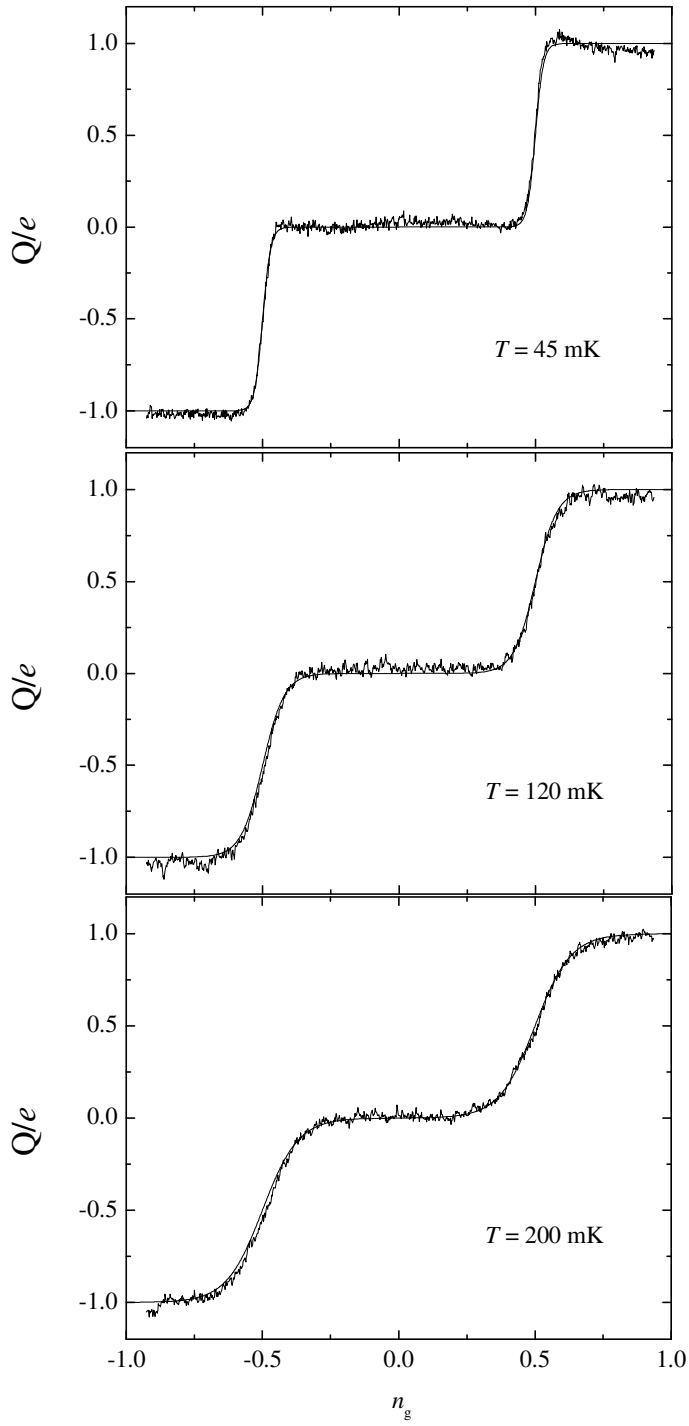

Fig. 6.16: Normal state charge staircase of the CPB on sample CS5 at three different temperatures with an applied field $B \approx 1$ T. Solid curve shows fit to Eq. 2.2 for the best fit parameter E_c/k_BT = 35.2, 12.5 and 7.59 for T=45, 120 and 200 mK, respectively.

Figure 6.18 shows the CPB charge staircase for sample PE2 both in the normal ($B \approx 1$T) and superconducting states ($B=0$T), measured at $T=60$ mK. It is evident that the Coulomb staircase in the superconducting state has charge steps of magnitude $2e$. The staircase in the superconducting state should correspond to the expectation value of the charge in the ground state of the CPB for $k_B T \ll \Delta$ since the density of thermally excited quasiparticles is then very small. In general, a number of issues affect the observation of $2e$ periodicity, as will be discussed in Chapter 7. In particular, because of quasiparticles, the CPB can spend a finite amount of time in the $n=1$ state instead of just the $n=0$ and $n=2$ states. Nevertheless, for sample PE2, the superconducting staircase is clearly 2e periodic and it is well described by the simple theory presented in Chapter 2, ignoring quasiparticles.

For comparison, Fig. 6.19 also shows the fit to the theoretical curve obtained by solving the Hamiltonian (Eq. 2.6) with the parameter $E_J/E_c=0.95$. I note that the values of E_c and E_J that I determined independently on this sample by spectroscopy measurements were $E_J=0.72$ and $E_c=0.71$, or $E_J/E_c=0.95$, in good agreement with the fit.

6.4 Summary

In this Chapter I described measurements I made to characterize SETs and CPBs in the normal and superconducting states. I-V_{DS} and I-V_g measurements were used to obtain SET parameters, such as E_c, R_Σ, C_1, C_2 and C_g. I used rf measurements in time and frequency domain to determine the sensitivity and bandwidth characteristics of rf-SETs.

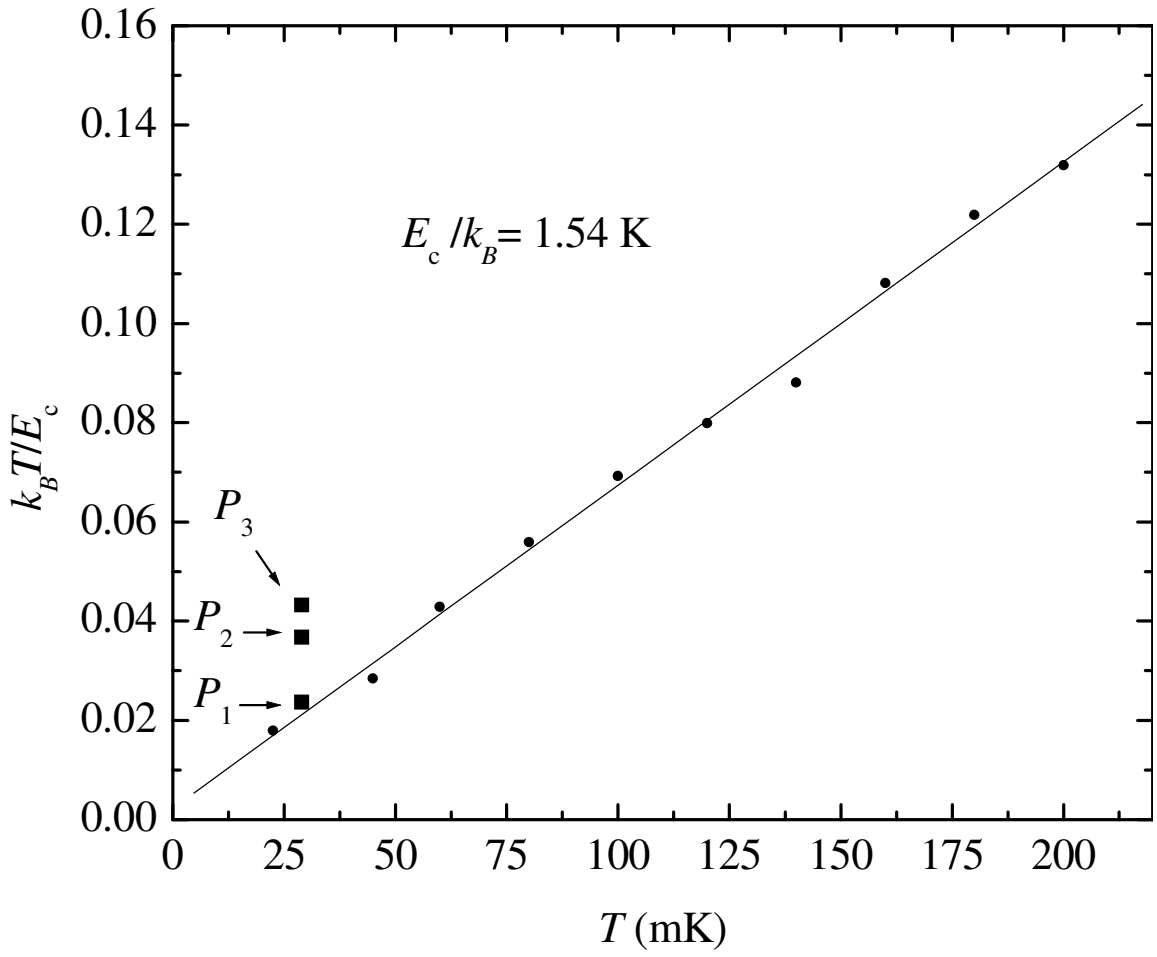

Fig. 6.17: Best fit parameter $k_B T/E_c$ obtained from the staircase measurements of sample CS5 in the normal state plotted versus the mixing chamber temperature T. A straight line was fit to the data points and the value E_c=1.54 K found from the slope, corresponding to C_Σ=0.6 fF. The sample temperatures T_1=37, T_2=57 and T_3=67 mK were measured at T=29 mK for SET power P_1=6, P_2=78 and P_3=450 fW respectively.

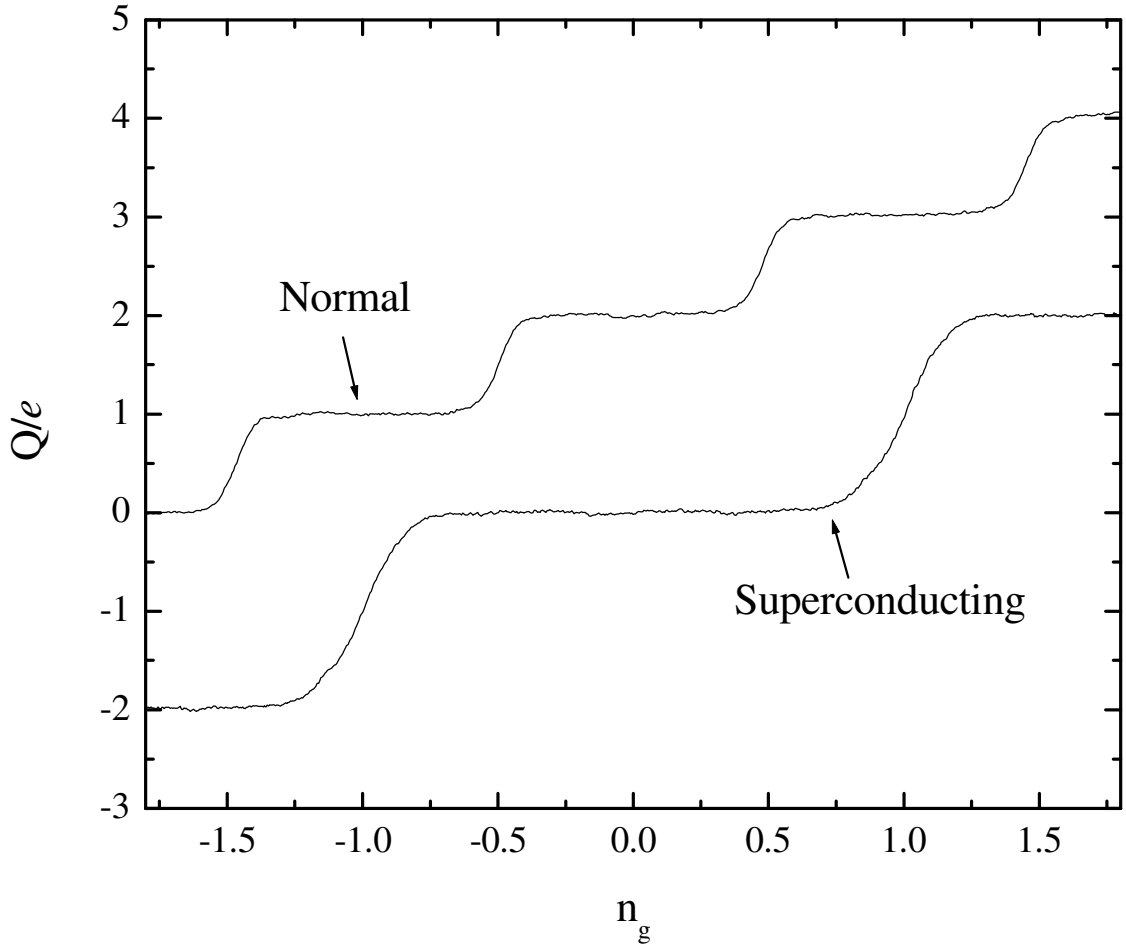

Fig. 6.18 Comparison of the measured box charge in the normal ($B \approx 1$T) and superconducting states ($B = 0$T) for device PE2 at $T = 60$ mK.

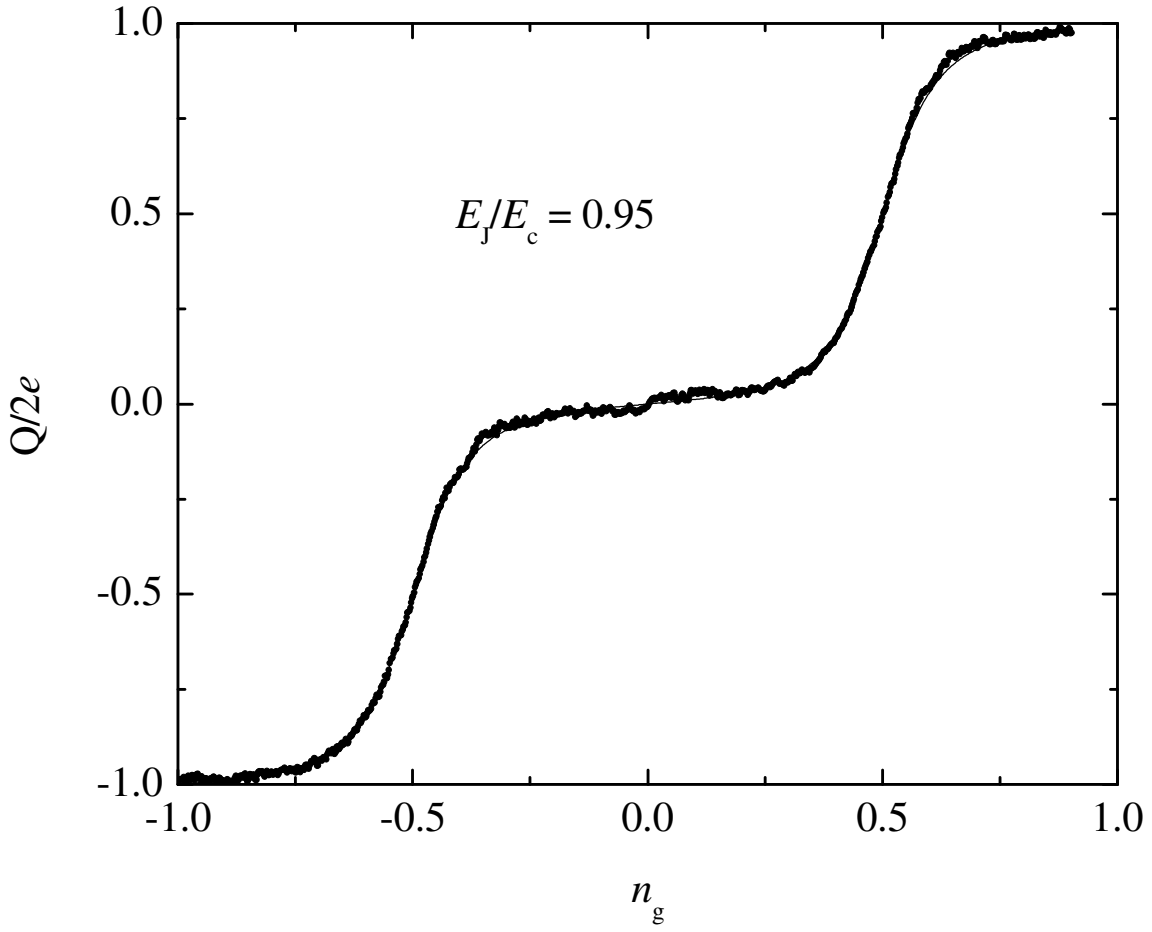

Fig. 6.19 CPB charge staircase measured in the superconducting state of sample PE2 (thick curve), compared with the theoretical curve (thin curve) for the ground state CPB charge with best fit parameter E_J/E_c=0.95.

Measurements of the Coulomb staircase of CPBs provided a way to determine the box parameters E_c and E_J. The results of my devices are summarized in Table 6.1.

Chapter 7 : Quasiparticle poisoning

7.1 Introduction

Figure 7.1 shows the charge staircase of sample PE1 (see Table 6.1) in the superconducting state at 30 mK. The measured charge deviates substantially from the expected ground state charge of the CPB, most notably near the degeneracy point; i.e. the short steps around $n_g=\pm 1$ suggest that the $n=\pm 1$ states are populated around those points. This behavior indicates the presence of quasiparticles in the superconducting electrodes even at very low temperatures, where one would not expect them. This effect is produced by a phenomenon called *quasiparticle poisoning* [84].

I note that, if quasiparticles are present, the short step for $n=1$ would be expected in devices with $E_c>\Delta$ (see Fig. 2.3b). However, short steps have been observed in many devices where E_c is considerably less than Δ [85,86,30], as is the case in sample PE1 which has $E_c/\Delta= 0.34$.

Quasiparticle poisoning has also been observed in superconducting SETs [87,88]. Naively, one would expect that the current in a superconducting SET at low T and low V_{DS} bias would be $2e$ periodic (see Fig. 4.6) and the maximum current would occur at $n_g=1$, where Josephson tunneling is maximum. Quasiparticle poisoning is manifested as a current peak at $n_g=0$ where the Coulomb blockade should be maximum. It is well-known that the current in superconducting SETs becomes e periodic when the thermal energy k_BT is high enough to produce quasiparticles. The crossover from $2e$ to e periodicity was explained by Tuominen *et al*. in terms of the free energy difference between the even and the odd parity states of a small superconducting island [89]:

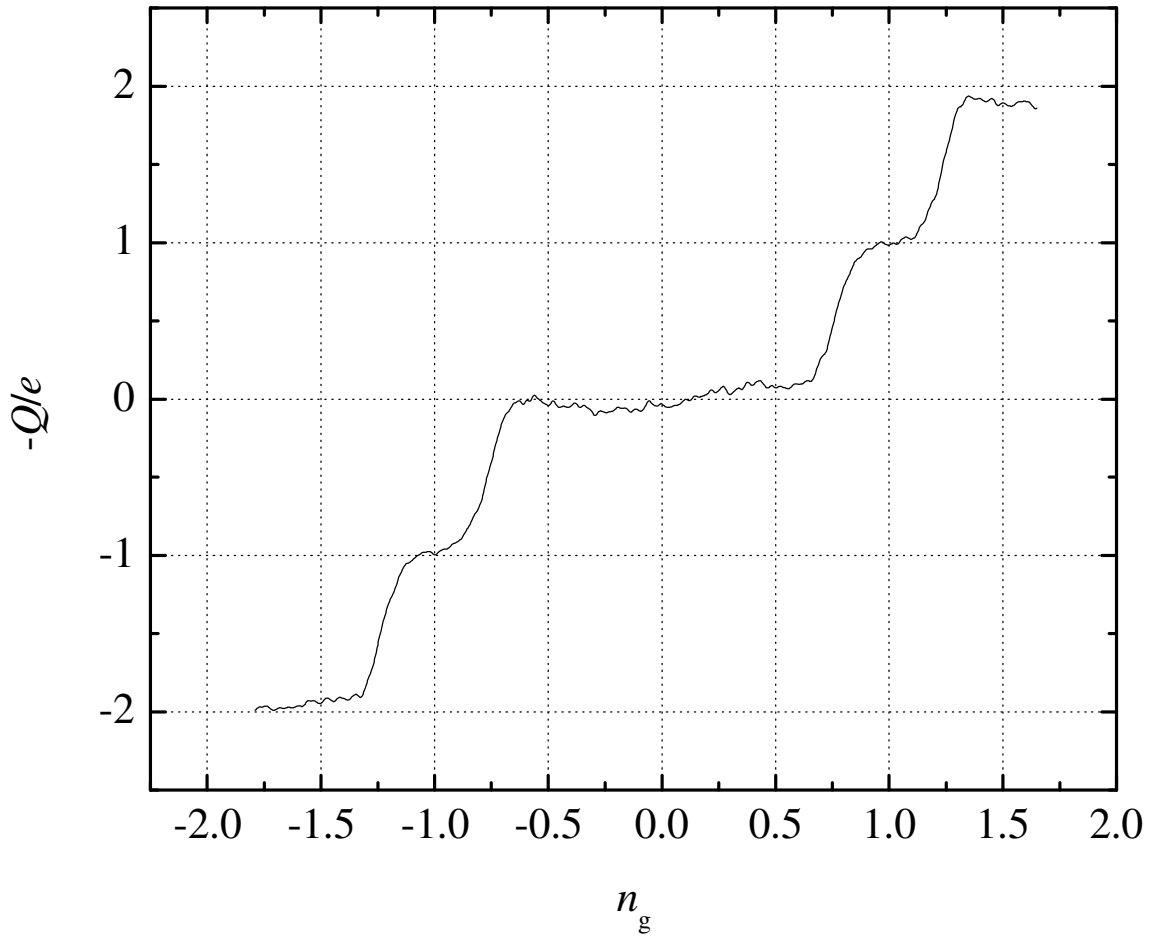

Fig. 7.1: Plot of excess charge Q on the CPB versus gate voltage $V_g=n_g e/C_g$ showing Coulomb staircase for sample PE1 in the superconducting state. The staircase was measured at 30 mK using an SET readout. The coupling strength between the CPB and the SET was $\kappa=0.009$.

$$F_0(T) = \Delta_I - k_B T \ln(N_{eff}) \tag{7.1}$$

where Δ_I is the superconducting gap of the island and N_{eff} is the effective number of quasiparticle states available for excitation. At low temperature N_{eff} is given by [90]:

$$N_{eff}(T) = N_I(0)\Omega_I\sqrt{2\pi\Delta_I k_B T} \tag{7.2}$$

Here $N_I(0)$ is the normal density of states of the island at the Fermi level and Ω_I is the volume of the island. Tuominen *et al*. argued that the crossover temperature is found by setting $F_o=0$ in Eq. 7.1.

Along similar lines, Amar *et al*. [87] and Joyez *et al*. [91] developed a thermodynamic theory that accurately explained the temperature dependence of the current peaks at $n_g=\pm1$ and $n_g=0$ on superconducting SETs with $E_c \ll \Delta$.

However, I note that none of these models predict poisoning at low temperatures. At least two different theories have been proposed to explain quasiparticle poisoning. One possibility is that there might be quasiparticle states at energies $E<\Delta$ [90]. These states can result, for example, from the inclusion of normal metal impurities in the superconductor [92] or from a broadening of Δ because of lifetime effects [93]. A second possibility has been proposed by Aumentado *et al*. [94], that non-equilibrium quasiparticles are responsible for low temperature poisoning. The Aumentado model assumes that quasiparticles with energies $E \geq \Delta_L$ are created in the leads, presumably by a non-thermal source such as high frequency radiation. If quasiparticles are already present in the electrodes and do not recombine then, in certain situations, the system can minimize the electrostatic energy in the range $^1/_2 < n_g < ^3/_2$ by allowing an extra electron onto the island.

The main idea in Aumentado's model is that, in the steady state, the probabilities of finding the system in the even or odd states can be found from a detailed balance condition [94]:

$$\frac{P_{even}}{P_{odd}} = \left(1 + \frac{\Gamma_{l0}}{\Gamma_{0l}}\right) \exp\left(\frac{(\Delta_I - \Delta_L) - \delta E}{k_B T}\right) \tag{7.3}$$

where Γ_{ol} is the generation rate and Γ_{lo} is the loss rate (recombination plus diffusion to the leads) of quasiparticles, $\delta E = E(n_g) - E(n_g+1)$, and $E(n_g)$ is the ground state energy of the system, which depends on E_c and E_J. Equation 7.3 predicts that devices having $\delta E > (\Delta_I - \Delta_L)$ will be in the odd state at $T \approx 0$ for any finite quasiparticle generation rate. At higher temperatures the transition rate from the odd state increases and P_e/P_o can be made very large if the generation of quasiparticles is the bottle neck process to go from the even to the odd state.

In the next section, I discuss a model developed by Schön *et al.* [95] to describe parity effects on small superconducting islands using single electron tunneling rates. I then extend this model to include non-equilibrium quasiparticles in order to calculate poisoning effects over a wide temperature range.

7.2 Tunneling rate formalism

In order to understand the CPB characteristics with quasiparticle poisoning I need to find the probability for the system to be in the even or odd state as n_g is varied. Of course, the true ground state of the CPB is the even state, which can be expressed as a superposition of $n=0$ and $n=2$ in the range $0 \le n_g \le 2$. The odd state has one un-paired electron on the island and can be expressed as a superposition of $n=1$ and $n=3$ in the

range $1 \le n_g \le 3$. I note that changing the CPB charge by e has the same effect on the electrostatic energy of the system as changing n_g by -1. Therefore, the energy eigenstates of the Hamiltonian:

$$H = E_c\left(n - n_g\right)^2 - E_J \cos(\phi) \tag{7.4}$$

in the odd state are the same as those in the even state but shifted in n_g by ± 1 (the sign is not important since the Hamiltonian is $2e$ periodic).

The lowest energy eigenstates of Eq. 7.4 in the even (E_e) and odd (E_o) states are plotted in Fig. 7.2 for a CPB with $E_c/E_J=2$. I note that these energies are just for the Cooper pair condensate in the even and odd states (they do not include the energy of the excitations). I can also define the energy change for the condensate:

$$\delta E \equiv E_e\left(n_g\right) - E_o\left(n_g\right) = E_e\left(n_g\right) - E_e\left(n_g - 1\right) \tag{7.4}$$

When no external drive is applied, the probability P_e of finding the CPB in the even state or in the odd state P_o can found by solving the master equation:

$$\frac{\partial P_e}{\partial t} = P_o \Gamma_{oe} - P_e \Gamma_{eo} \tag{7.5}$$

with the constraint

$$P_e + P_o = 1 \tag{7.6}$$

where Γ_{oe} (Γ_{eo}) is the transition rate from the odd (even) state to the even (odd) state.

In the steady state $\partial P_e/\partial t = 0$ and we find:

$$P_e = \frac{\Gamma_{oe}}{\Gamma_{oe} + \Gamma_{eo}} \tag{7.7}$$

Once these probabilities are known the average CPB charge can be found as:

$$\overline{Q} = P_e Q\left(n_g\right) + P_o\left[Q\left(n_g - 1\right) + e\right] \tag{7.8}$$

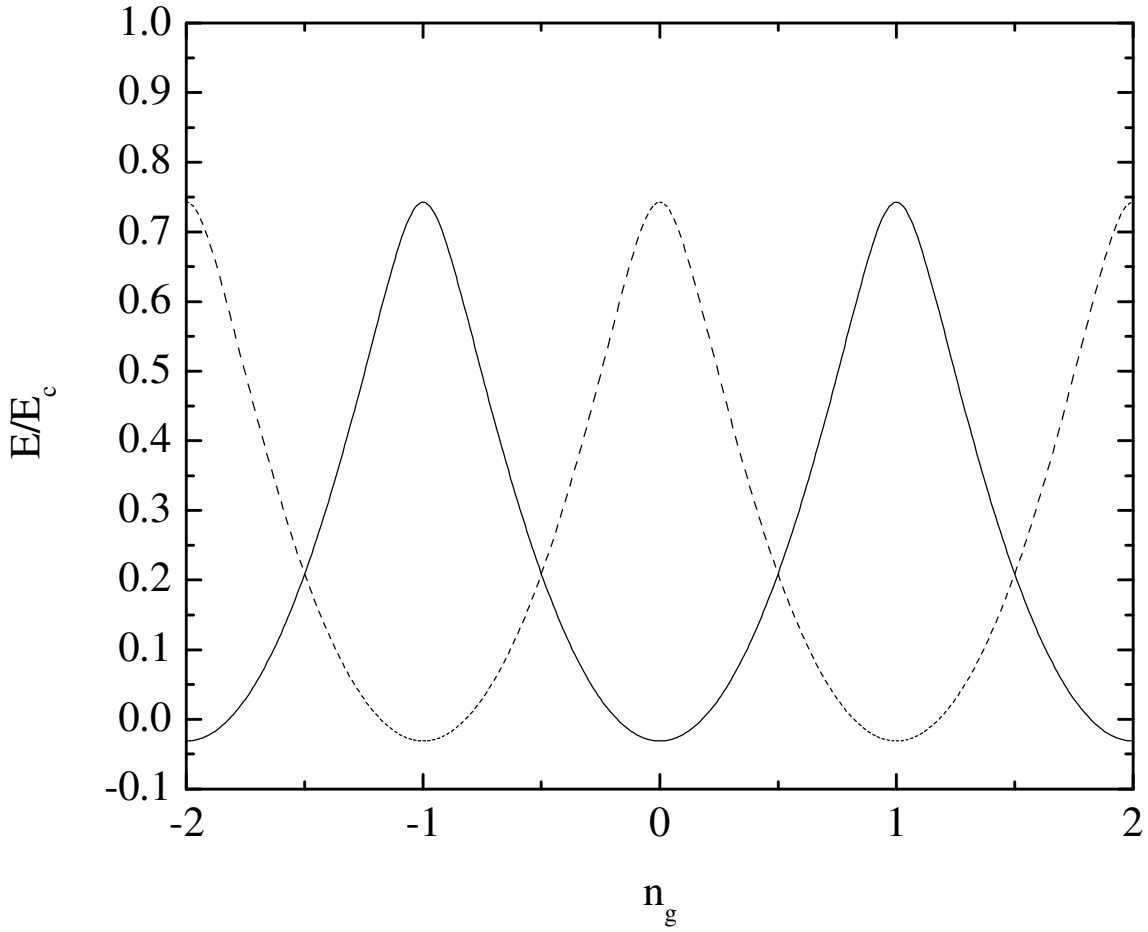

Fig. 7.2: Lowest energy eigenstate of the CPB Hamiltonian in the even state E_e (solid line) and odd state E_o (dashed line) with $E_c/E_J=2$. These energies are just for the Cooper pair condensate and they do not include the energy of excitations in the leads $E \gtrsim \Delta_L$ or in the island $E \gtrsim \Delta_I$ of the CPB.

where $Q(n_g)$ is the expectation value of the charge in the ground state.

Transitions between the even and odd states can occur through different processes. For example, Schön [95] considers one transition type (Γ_{LI}) contributing to Γ_{eo} and two types (Γ_{IL} and γ) contributing to Γ_{oe}. These processes are illustrated in Fig. 7.3. For the Γ_{LI} transition, a quasiparticle excitation is created in the leads by thermal energy and one of the un-paired electrons tunnels onto the island. Γ_{IL} is a similar process in which a quasiparticle is created in the island by thermal energy and one of the un-paired electrons tunnels to the leads. The escape rate γ is the rate for an existing un-paired electron to tunnel off the island, without creating any additional quasiparticles.

Figure 7.3 illustrates these processes for $\Delta_I > \delta E$ and $\delta E > 0$ ($^1/_2 < n_g < ^3/_2$). The figure suggests the limiting forms for the tunneling rates, $\Gamma_{LI} \sim \exp\{-\Delta_L/k_BT\}$, $\Gamma_{IL} \sim \exp\{-(\Delta_L+\delta E)/k_BT\}$ and $\gamma \sim \exp\{-(\Delta_L-\Delta_I+\delta E)/k_BT\}$. Schön found that typically, at low temperature, $\gamma \gg \Gamma_{LI}$ for all n_g. This implies that $P_e \gg P_o$, resulting in negligible poisoning. At high temperatures, $\Gamma_{LI} > \Gamma_{IL} > \gamma$ in the range $^1/_2 < n_g < ^3/_2$ and $\Gamma_{IL} > \Gamma_{LI} > \gamma$ otherwise, which leads to *e* periodicity, with a crossover temperature consistent with Eq. 7.1. I note that this model only has thermally excited quasiparticles and makes a number of simplifying assumptions. Clearly it does not explain poisoning at low temperatures produced by non-equilibrium quasiparticles [94]. One would have to include non-thermal sources of quasiparticles to account for the measured CPB characteristics over the whole temperature range.

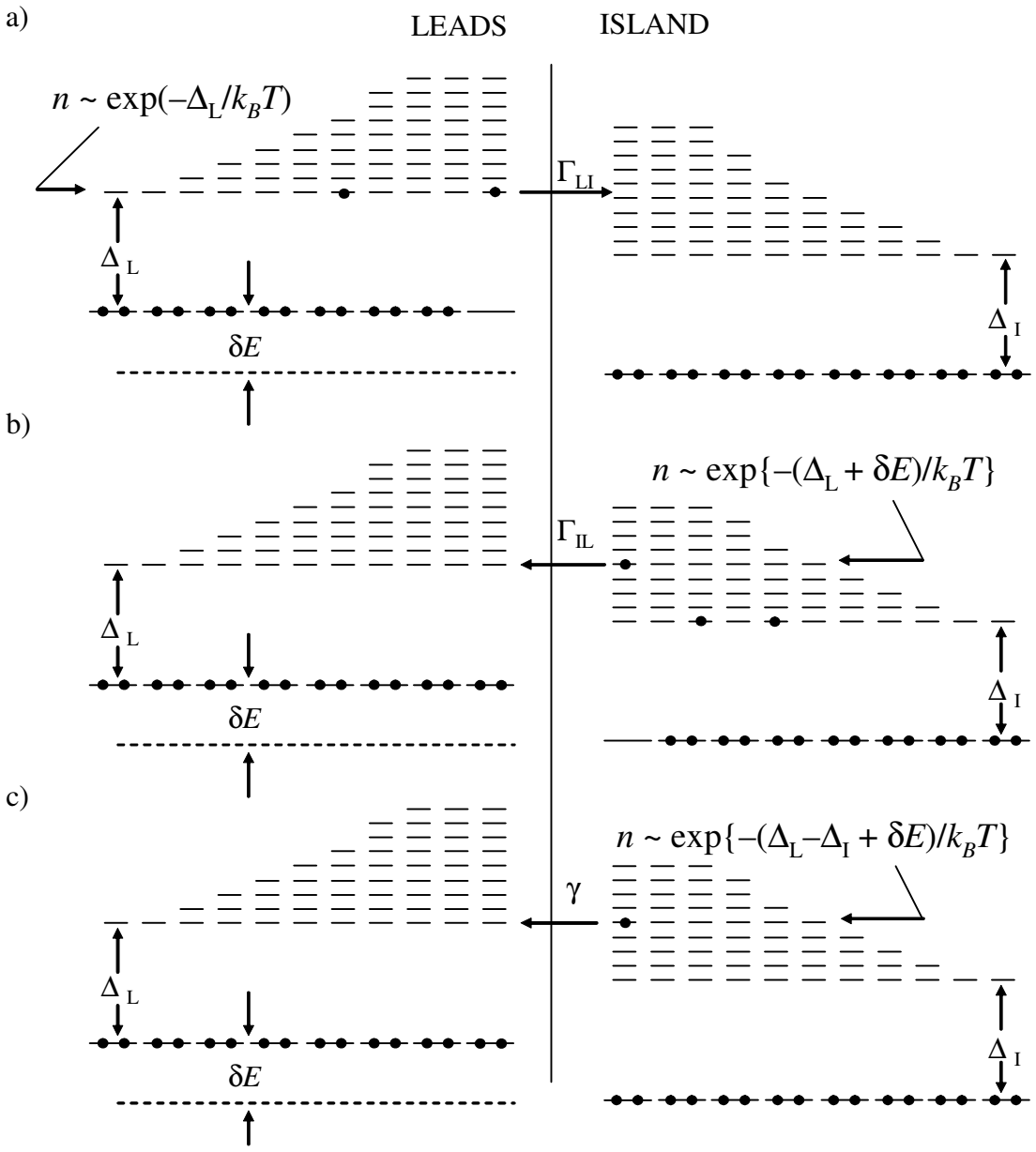

Fig. 7.3: Illustration of three different processes contributing to transitions between the even and odd states of the CPB for $\delta E>0$ and $\Delta_I>\delta E$. (a) a quasiparticle is created by thermal energy and an un-paired electron tunnels from lead to island with rate Γ_{LI}. (b) A thermal quasiparticle is created and an un-paired electron tunnels from island to lead with rate Γ_{IL}. (c) An un-paired electron escapes from the island with rate γ, without creation of new quasiparticles.

7.3 Calculation of tunneling rates

In order to extend Schön's model to the case of non-equilibrium quasiparticles, I now consider the tunneling rates in some detail. The single electron tunneling rates are obtained by treating the tunneling Hamiltonian [33]:

$$H_t = \sum_{L,I,\sigma} T_{L,I} c^+_{L,I} c_{L,I} + h.c. \tag{7.9}$$

in first order perturbation theory. From Fermi's golden rule, the rate for electron tunneling from the leads to the island is given by:

$$\Gamma_{LI} = \frac{4\pi}{\hbar}\Omega_L\Omega_I \times \int_{-\infty}^{\infty} dE \int_{-\infty}^{\infty} dE' \left|T_{LI}(E,E')\right|^2 N_L(E) N_I(E') f_L(E)\left[1 - f_I(E')\right]\delta(E' - E - \delta E) \tag{7.10a}$$

and from the island to the leads:

$$\Gamma_{IL} = \frac{4\pi}{\hbar}\Omega_I\Omega_L \times \int_{-\infty}^{\infty} dE \int_{-\infty}^{\infty} dE' \left|T_{LI}(E,E')\right|^2 N_L(E) N_I(E') f_I(E)\left[1 - f_L(E')\right]\delta(E' - E + \delta E) \tag{7.10b}$$

where $N_L(E)$ is the density of quasiparticle states (per unit energy, per unit volume) in the leads, $N_I(E)$ is the density of states of the quasiparticles in the island, Ω_L is the volume of the leads, Ω_I is the volume of the island and $f(E)$ is the Fermi function (see Fig. 7.4b):

$$f(E) = \frac{1}{1 + \exp\left(\frac{E - \mu}{k_B T}\right)} \tag{7.11}$$

with chemical potential μ. Clearly, this assumes a thermal distribution of quasiparticles.

If the electrodes are non-superconducting δE can be computed classically using charge states, i.e. $E(n,n_g)=E_c(n-n_g)^2$ and $\delta E=E(n=0)-E(n=1)=E_c(2n_g-1)$ for $0<n_g<1$. For normal metal electrodes, Eq. 7.10 can be integrated in closed form (assuming energy independent density of states N and tunneling matrix elements $|T|$). We find [96]:

$$\Gamma_{LI} = \frac{1}{e^2 R_t} \frac{-\delta E}{\exp\left(\frac{\delta E}{k_B T}\right) - 1} \tag{7.12}$$

where the tunneling resistance R_t is given by:

$$\frac{1}{R_t} = \frac{4\pi e^2}{\hbar} N_I(0)\,\Omega_I N_L(0)\,\Omega_L |T|^2 \tag{7.13}$$

Here $N_L(0) \approx 3N_L/2E_{FL}\Omega_L$ and $N_I(0) \approx 3N_I/2E_{FI}\Omega_I$ are the density of states at the Fermi level of the leads (E_{FL}) and island (E_{FI}), respectively.

In an s-wave, BCS superconductor, the quasiparticle density of states is given by (see Fig. 7.4a):

$$N_S \approx \begin{cases} N(0)\dfrac{|E-\mu|}{\sqrt{(E-\mu)^2-\Delta^2}} & for\ |E| < \Delta \\ 0 & otherwise \end{cases} \tag{7.14}$$

The rates Γ_{LI} and Γ_{IL} can be found by substituting Eqs. 7.11, 7.13 and 7.14 into 7.10a and 7.10b:

$$\Gamma_{LI} = \frac{1}{e^2 R_t} \tag{7.15}$$

$$\times \int_{-\infty}^{\infty} \frac{|E|}{\sqrt{E^2-\Delta_L^2}} \frac{|E+\delta E|}{\sqrt{(E+\delta E)^2-\Delta_I^2}} \frac{1}{1+\exp\left(-\frac{E}{k_B T}\right)} \left[1 - \frac{1}{1+\exp\left(-\frac{E+\delta E}{k_B T}\right)}\right] dE$$

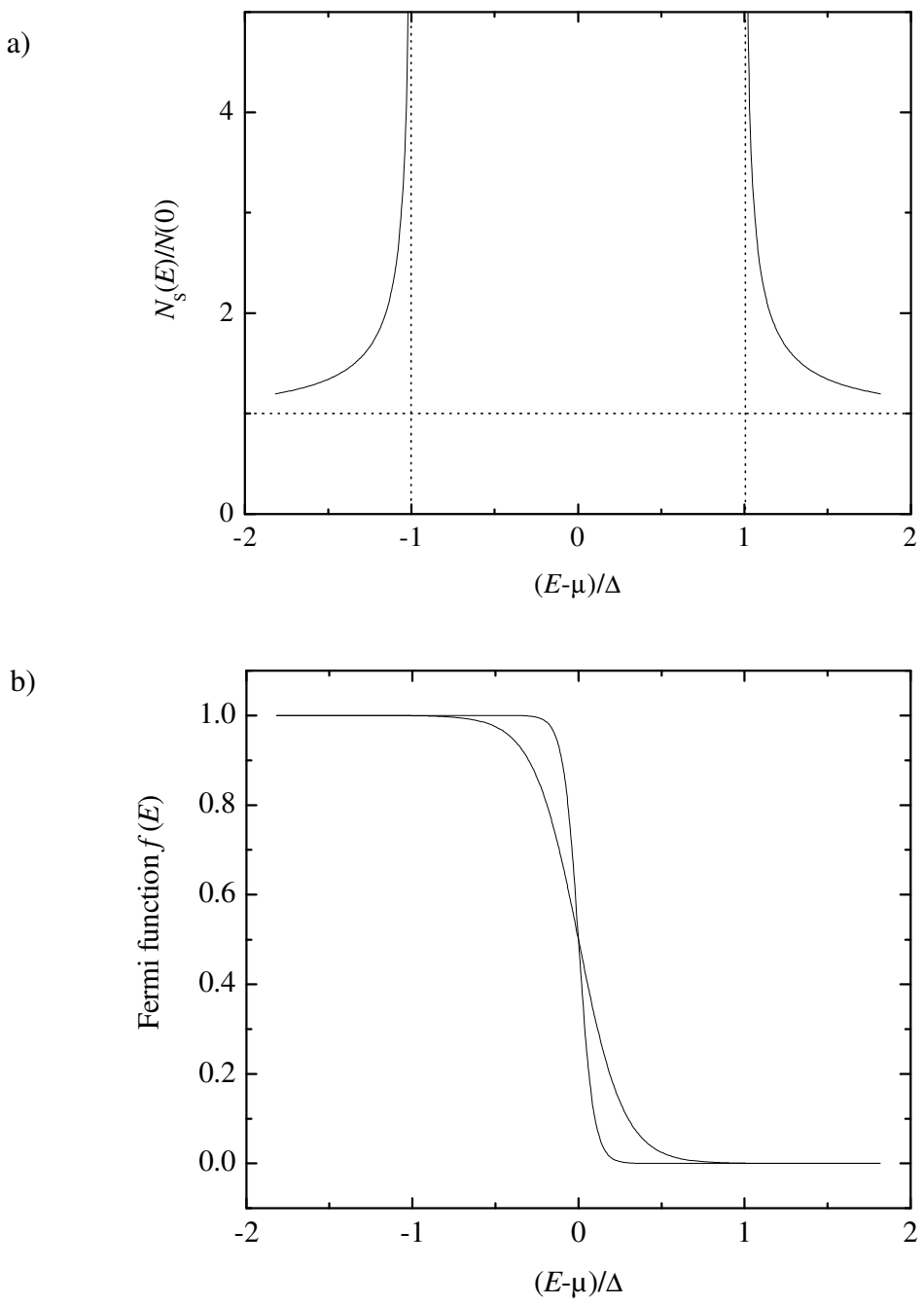

Fig. 7.4: (a) Quasiparticle density of states, (b) Fermi function for T=0.1 K and T=0.3 K.

$$\Gamma_{IL} = \frac{1}{e^2 R_t} \times \int_{-\infty}^{\infty} \frac{|E|}{\sqrt{E^2 - \Delta_I^2}} \frac{|E - \delta E|}{\sqrt{(E - \delta E)^2 - \Delta_L^2}} \frac{1}{1 + \exp\left(-\frac{E}{k_B T}\right)} \left[1 - \frac{1}{1 + \exp\left(-\frac{E - \delta E}{k_B T}\right)}\right] dE \tag{7.16}$$

where the range $-\Delta_{I/L} < E < \Delta_{I/L}$ is excluded from the integrals.

The calculation of the escape rate γ requires special consideration. Equation 7.11, with μ given by the chemical potential of the Cooper pair condensate, gives the probability in thermal equilibrium for a given quasiparticle state with energy $E > \Delta$ to be occupied, and this vanishes as T tends to zero. A different situation takes place in a small isolated superconductor if the total number of electrons is odd. In this case one electron is forced to remain un-paired and therefore the probability that a given quasiparticle state near Δ is occupied remains finite as T goes to zero. Similarly, in the CPB, the island is to some extent isolated by the Coulomb blockade, which suppresses tunneling transitions that raise the electrostatic energy. This is a charge imbalance type of non-equilibrium situation in which the energy distribution of electron-like excitations is different from that of hole-like excitations [15].

This situation can be described by a shift in the chemical potential of the excitations μ_{qp} with respect to the chemical potential of the condensate μ_s. The shift $\delta\mu = \mu_{qp} - \mu_s$ can be found from the condition that there must be exactly one excess electron charge on the island [96]:

$$N_I(0)\Omega_I \int_{-\infty}^{\infty} \frac{|E|}{\sqrt{E^2-\Delta_I^2}} \left[\frac{1}{1+\exp\left(-\frac{E-\delta\mu}{k_B T}\right)} - \frac{1}{1+\exp\left(-\frac{E}{k_B T}\right)} \right] dE = 1 \qquad (7.17)$$

I note that the simple semiconductor model employed to calculate single electron tunneling rates in thermal equilibrium is not valid in this case. Equation 7.17 is obtained by taking into account separately the contributions to single electron tunneling from electron-like and hole-like quasiparticles [97].

At low temperature δμ is approximately equal to [96]:

$$\delta\mu = \Delta_I - k_B T \ln\left(N_{eff}\right) \qquad (7.18)$$

$$N_{eff} = N_I(0)\,\Omega_I \sqrt{2\pi\,\Delta_I k_B T} \qquad (7.19)$$

where N_{eff} is the effective number of quasiparticle states near Δ_I.

Finally, with δμ found from Eq. 7.17, the escape rate γ can be written as:

$$\gamma = \frac{1}{2e^2 R_t} \int_{-\infty}^{\infty} \frac{|E|}{\sqrt{E^2-\Delta_I^2}} \frac{|E-\delta E|}{\sqrt{(E-\delta E)^2-\Delta_L^2}}$$

$$\times \left[\frac{1}{1+\exp\left(-\frac{E-\delta\mu}{k_B T}\right)} - \frac{1}{1+\exp\left(-\frac{E}{k_B T}\right)} \right] \left[1 - \frac{1}{1+\exp\left(-\frac{E-\delta E}{k_B T}\right)} \right] dE \qquad (7.20)$$

I can now extend Schön's model to account for poisoning at low temperatures. First, I assume that there are non-equilibrium quasiparticles generated by a non-thermal source that produces an equal number of electron-like and hole-like excitations [15]. Second, I

assume that non-equilibrium quasiparticles exist on both electrodes and that their generation and recombination rates are only weakly dependent on temperature. This situation can be described by a fixed number of non-equilibrium quasiparticles in the leads N_L^* and island N_I^*. In general, the density of non-equilibrium quasiparticles can be different in the island or leads of the device due to differences in the films but also because quasiparticles in the leads can diffuse to normal metal regions (quasiparticle traps) and relax to lower energy states. Third, I assume that the recombination time for quasiparticles is much longer than the thermalization time and therefore, their energies follow a Fermi distribution with a shifted chemical potential [98].

These assumptions suggest energy distribution functions of the form:

$$f_L(E)=\begin{cases}\dfrac{1}{1+\exp\left(-\dfrac{E-\mu_L}{k_BT}\right)} & \text{for } E>0\\[2ex] \dfrac{1}{1+\exp\left(-\dfrac{E+\mu_L}{k_BT}\right)} & \text{for } E<0\end{cases} \tag{7.21a}$$

$$f_I(E)=\begin{cases}\dfrac{1}{1+\exp\left(-\dfrac{E-\mu_I}{k_BT}\right)} & \text{for } E>0\\[2ex] \dfrac{1}{1+\exp\left(-\dfrac{E+\mu_I}{k_BT}\right)} & \text{for } E<0\end{cases} \tag{7.21b}$$

The chemical potential of the leads μ_L and island μ_I are determined from:

$$N_L^* = 2N_L(0)\Omega_L \int_0^\infty \frac{E}{\sqrt{E^2-\Delta_L^2}} \frac{1}{1+\exp\left(-\frac{E-\mu_L}{k_B T}\right)} dE \tag{7.22a}$$

$$N_I^* = 2N_I(0)\Omega_I \int_0^\infty \frac{E}{\sqrt{E^2-\Delta_I^2}} \frac{1}{1+\exp\left(-\frac{E-\mu_I}{k_B T}\right)} dE \tag{7.22b}$$

where the factor of 2 is due to the two spin orientations. With these assumptions, the tunneling rates due to non-equilibrium quasiparticles are given by:

$$\Gamma_{LI}^* = \frac{1}{e^2 R_t} \times \int_{-\infty}^\infty \frac{|E|}{\sqrt{E^2-\Delta_L^2}} \frac{|E+\delta E|}{\sqrt{(E+\delta E)^2-\Delta_I^2}} f_L(E)\left[1-f_I(E+\delta E)\right] dE \tag{7.23}$$

$$\Gamma_{IL}^* = \frac{1}{e^2 R_t} \times \int_{-\infty}^\infty \frac{|E|}{\sqrt{E^2-\Delta_I^2}} \frac{|E-\delta E|}{\sqrt{(E-\delta E)^2-\Delta_L^2}} f_I(E)\left[1-f_L(E-\delta E)\right] dE \tag{7.24}$$

The total transition rates between the even and odd states can now be written as:

$$\Gamma_{eo} = \Gamma_{LI} + \Gamma_{LI}^* \tag{7.25}$$

and

$$\Gamma_{oe} = \Gamma_{IL} + \Gamma_{IL}^* + \gamma \tag{7.26}$$

Here I have simply added the rates due to non-equilibrium quasiparticles to the rates previously considered by Schön.

I note that, If I assume an equal density of non-equilibrium quasiparticles on both electrodes and $N_I(0)=N_L(0)$, then only two free parameters (*e.g.* $N_I(0)\Omega_I$ and N_I^*) are

necessary to calculate all the rates, besides the device parameters E_c, E_J, R_t, Δ_I and Δ_L that can be measured as explained in Chapter 6.

I evaluated these rates numerically for the parameters of device CS1 in order to compare measured characteristics with the predictions of the model. These rates are plotted in Figs. 7.5 and 7.6 as a function of δE for three different temperatures and in Fig. 7.7 as a function of temperature for δE=0.5 K. In these calculations I used E_c=1.26 K, E_J=0.24 K, R_t=34 kΩ, Δ_I=Δ_L=2.57 K, $N_I(0)\Omega_I$=2500 K^{-1} and N_I^*=0.0016, and I assumed equal density of non-equilibrium quasiparticles for leads and island and $N_I(0)$=$N_L(0)$.

I note that the range $\delta E>0$ ($^1/_2<n_g<^3/_2$) is more prone to poisoning since $E_o<E_e$. Figure 7.5a shows that at T=50 mK, γ is the largest rate for $\delta E<0.32$ K, whereas $\Gamma_{LI}^*>\gamma$ otherwise. This means there will be significant poisoning for $\delta E>0.32$ K due to non-equilibrium quasiparticles. Clearly this depends on my choice of N_I^*. At larger temperatures γ increases with respect to Γ_{LI}^* and at 100 mK and 150 mK the crossover points shift to higher energies (0.62 K and 0.94 K respectively). As T is further increased the rates Γ_{LI} and Γ_{IL} grow faster than γ, moving the crossover point to lower energies until above 300 mK one finds $\Gamma_{LI}>\gamma$ for $\delta E>0$ and $\Gamma_{IL}>\gamma$ for $\delta E<0$ resulting in e periodicity. The explicit temperature dependence of these rates is shown in Fig. 7.7 for δE=0.5 K.

I can now identify some of the factors affecting quasiparticle poisoning and discuss some simple guidelines to minimize their effect. At low temperature the escape of the un-paired electron, $\gamma \sim \exp[(\Delta_I-\Delta_L-\delta E)/k_BT]$ (see Fig. 7.3), is the dominant mechanism to

restore the system to the even state. From the dependence of γ on $\Delta_I-\Delta_L$ it is easy to see that one can decrease poisoning by engineering the device so that $\Delta_I>\Delta_L$. One possibility to achieve this condition in aluminum devices is to introduce a small amount of oxygen in the chamber during the evaporation of the island in order to increase Δ_I [94,99,100]. The escape rate γ also increases with decreasing δE. In the CPB, δE takes the maximum value $\delta E_{max}\approx E_c-E_J/2$ at $n_g=1$ and thus, poisoning is much less important in devices with small E_c and/or large E_J, provided Δ_I is not much smaller than Δ_L.

Another approach to reducing poisoning involves the idea that the transition from the even to the odd state is dominated by non-equilibrium quasiparticles at low temperature. Quasiparticles can be extracted efficiently from the leads by attaching quasiparticle traps to them. These traps consist of either a normal metal electrode or a superconductor with a smaller energy gap. In both cases, the traps have low energy quasiparticle states so quasiparticles that diffuse into the traps relax to one of the lower energy states and are subsequently prevented from reentering the leads.

7.4 Comparison to measurements

I have used the above approach to model the average charge on the CPB of sample CS1. The sample parameters were previously estimated using measurements described in Chapter 6 (see Table 6.1). $E_c=1.26$ K was determined from the slope of the staircase in the normal state at different temperatures (see Fig. 6.16). The sum of the energy gaps $\Delta_I+\Delta_L$ was measured from the SET *IV* characteristics (see Fig. 6.1) and I have further assumed that $\Delta_I=\Delta_L=2.57$ K. The SET tunneling resistance $R_\Sigma=136$ kΩ and charging

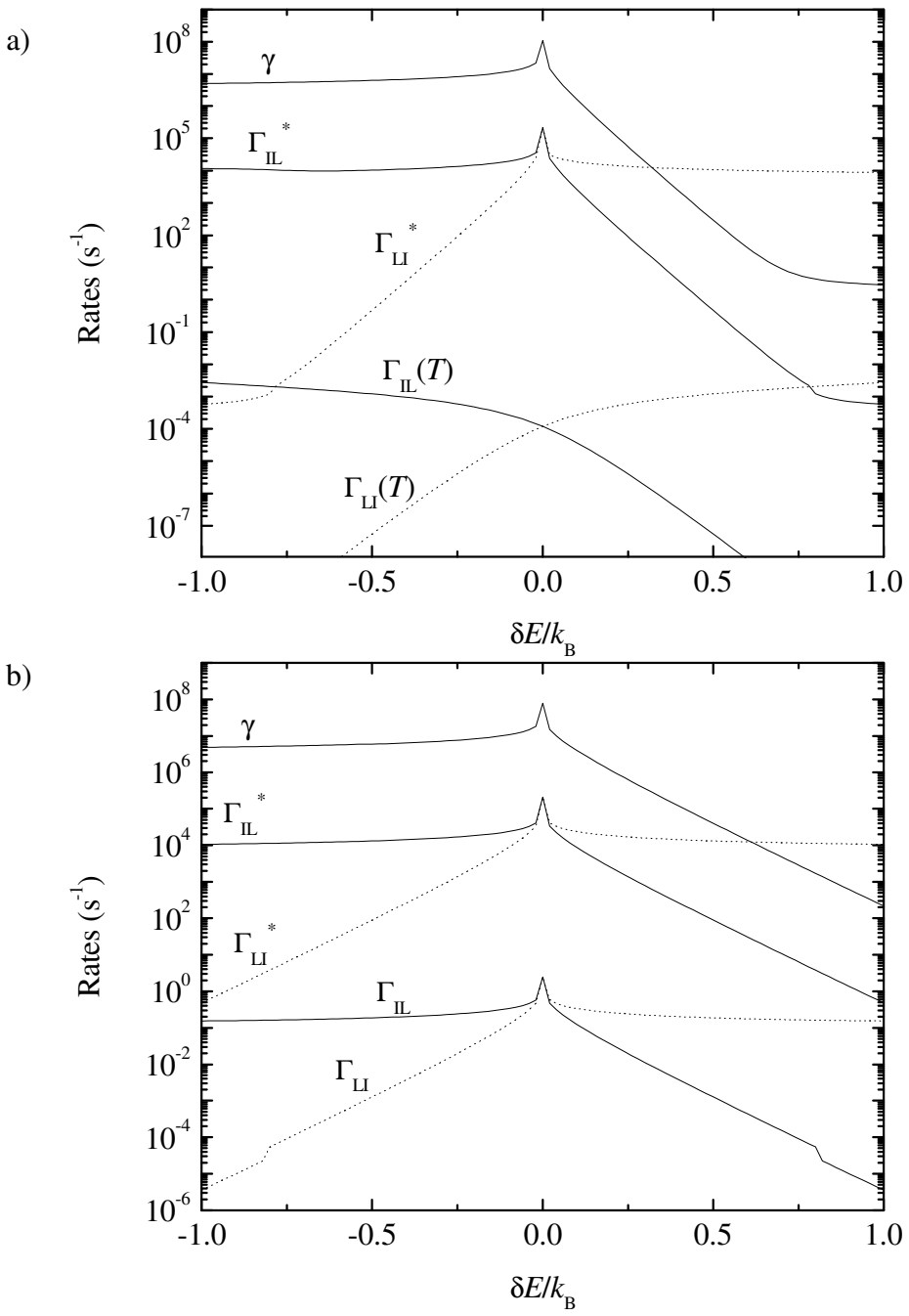

Fig 7.5: Tunneling rates as a function of δE at temperatures of (a) 50 mK and (b) 100 mK. The rates were computed for R_t=34 kΩ, $\Delta_I=\Delta_L$=2.57 K, $N_I(0)\Omega_I$=2500 K^{-1}, N_I^*=0.0016 and $\mu_L=\mu_I$. Transitions contributing to Γ_{eo} are plotted using dotted curves.

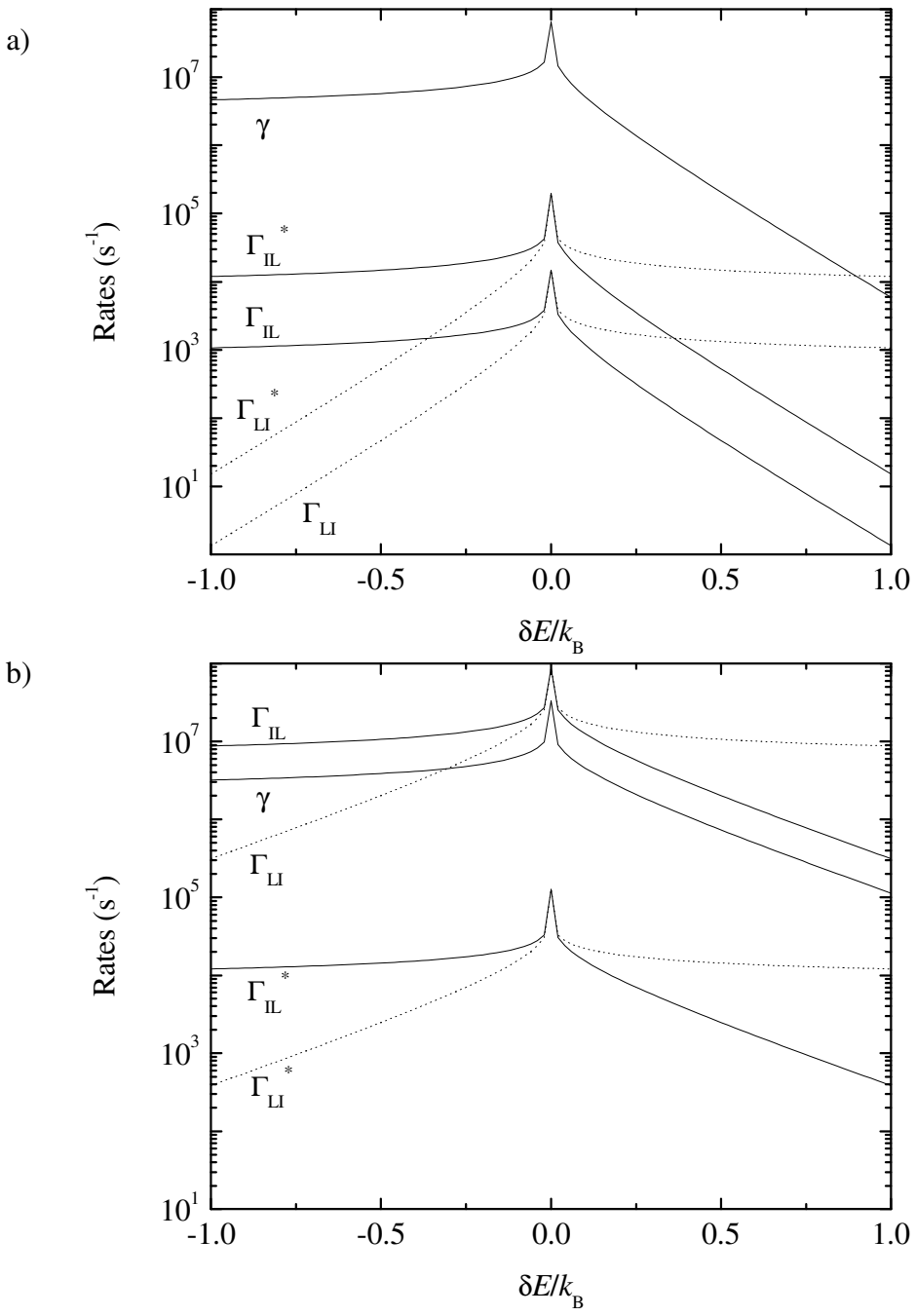

Fig. 7.6: Tunneling rates as a function of δE at temperatures of (a) 150 mK and (b) 300 mK. The rates were computed for R_t=34 kΩ, $\Delta_I=\Delta_L$=2.57 K, $N_I(0)\Omega_I$=2500 K^{-1}, N_I^*=0.0016 and $\mu_L=\mu_I$. Transitions contributing to Γ_{eo} are plotted as dotted curves.

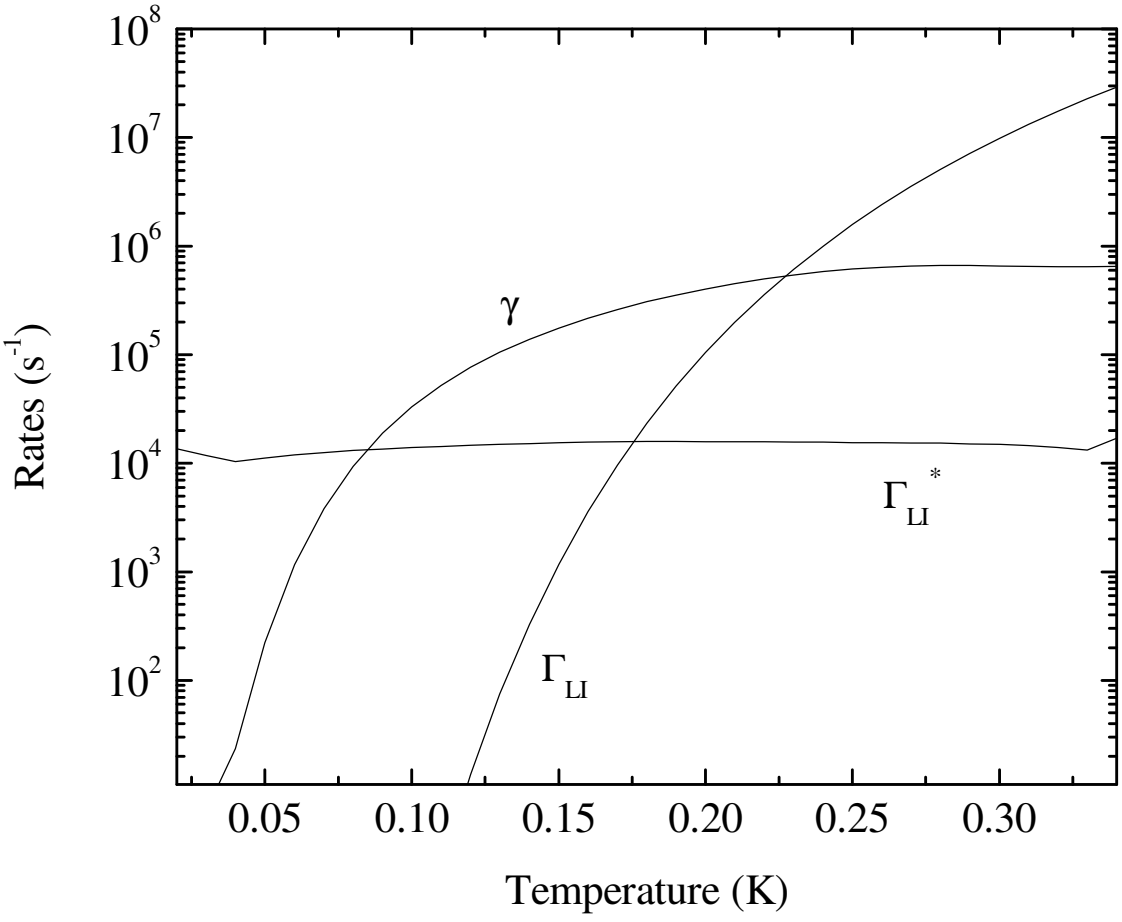

Fig. 7.7: Tunneling rates Γ_{LI}, γ and Γ_{LI}^{*} as a function of temperature for δE =0.5 K. The rates were computed for R_t=34 kΩ, $\Delta_I=\Delta_L$=2.57 K, $N_I(0)\Omega_I$=2500 K^{-1}, N_I^{*}=0.0016 and $\mu_L=\mu_I$.

energy E_c=1.14 K were also determined from the *IV* characteristics. The CPB tunnel resistances were not determined for this sample but, since all the junctions were nominally identical and the charging energies of both devices are similar, I assume that their tunneling resistances are equal and therefore, I used $R_t=R_\Sigma/4$=34 kΩ for the CPB.

Figures 7.8 and 7.9 show a comparison between the simulated CPB charge and staircase for device CS1. I would like to acknowledge that the data was measured by Ben Palmer. For the model, I assumed $N_I(0)=N_L(0)$ and $\mu_L=\mu_I$ and then varied the parameters $N_I(0)\Omega_I$ and N_I^* to obtain a good fit. Examination of the figures shows I found excellent agreement with $N_I(0)\Omega_I$=2500 K^{-1} and N_I^*=0.0016 over the full temperature range from 60 mK to 300 mK, and that over this range the device goes from *e* to 2*e* and then back to *e* periodicity. I note that these parameters can be determined independently since N_I^* is not important in the high temperature limit. The most significant deviation between theory and data, which happens at *T*=60 mK, could be due to insufficient knowledge of the device parameters or an actual inaccuracy of the model. However, it is also possible that the CPB was heated by the SET. These measurements were done with the SET biased on JQP ($V_{DS}\approx$500μV, $I\approx$100 pA or $P\approx5\times10^{-14}$ W). As mentioned in Chapter 6, a temperature change from 29 mK to 57 mK was measured in sample CS5 in the normal state for an SET power dissipation of 8×10^{-14} W.

I have also attempted to use my model to describe the temperature dependence of the SET current at low V_{DS} bias (see Fig. 7.10a). It was shown by Amar *et al*. [87] that, in the absence of quasiparticle poisoning, the 2*e* periodic SET current consists of a series of peaks at $n_g=\pm1, \pm3$, etc, where Josephson tunneling is maximum. Quasiparticle poisoning causes a current peak at n_g=0 and a decrease of the peak amplitude at n_g=1 (see Fig.

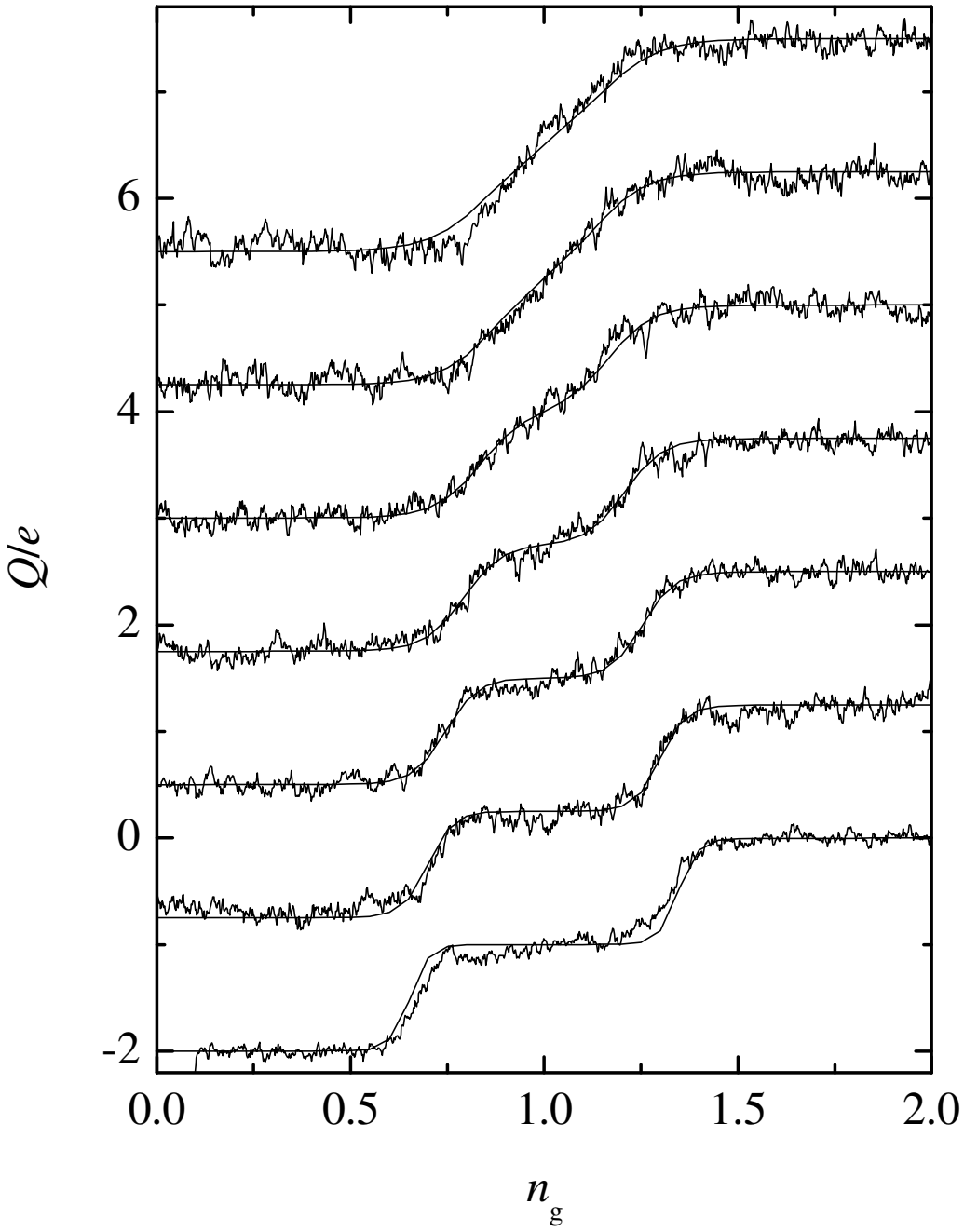

Fig. 7.8: Comparison between measured and calculated CPB charge of sample CS1 at different temperatures: (from bottom to top) 60 mK, 80 mK, 100 mK, 120 mK, 140 mK, 160 mK and 180 mK. The parameters $N_I(0)\Omega_I$=2500 K^{-1}, N_I^*=0.0016 and $\mu_L=\mu_I$ were used to obtain the best fit.

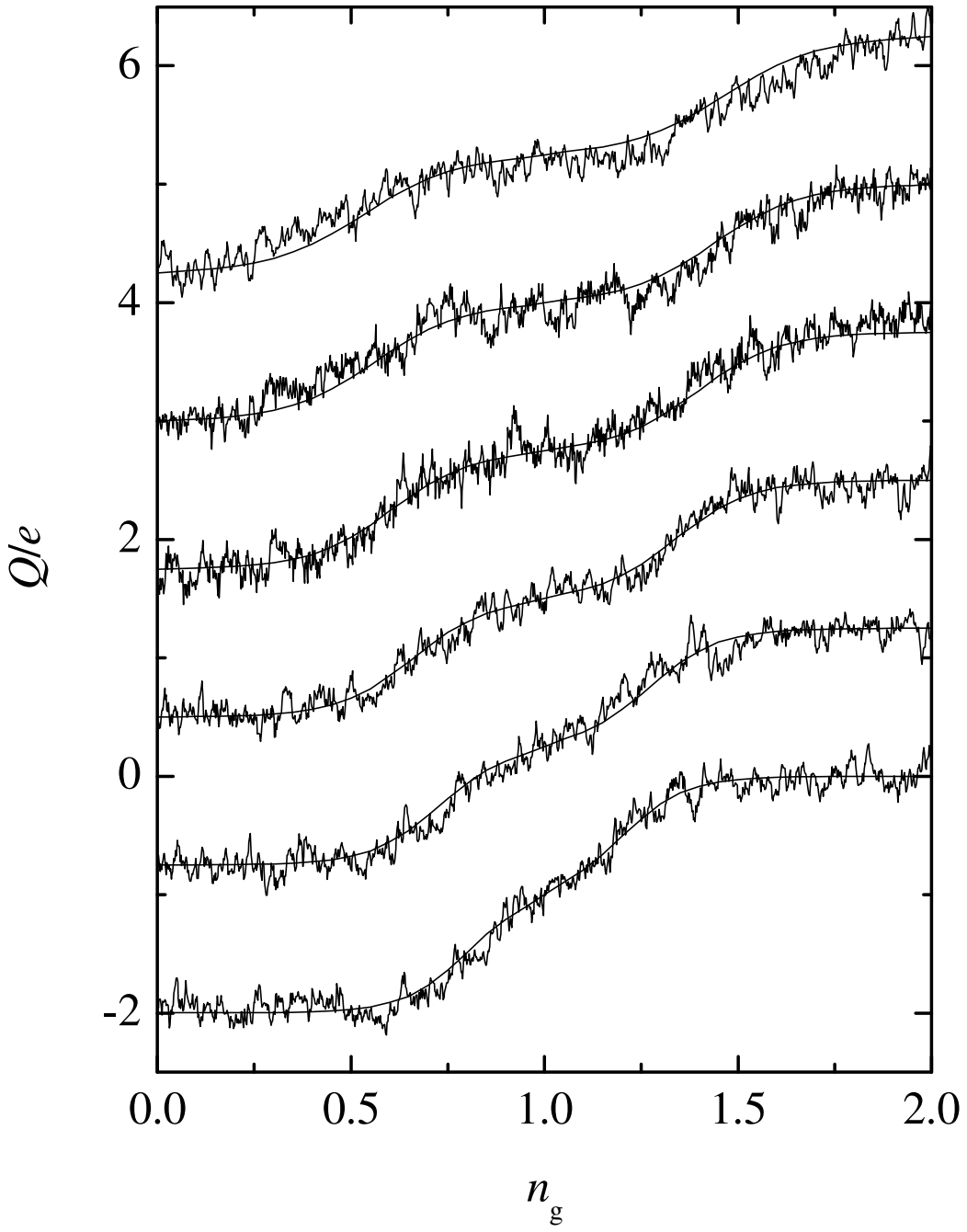

Fig. 7.9: Comparison between measured and calculated CPB charge of sample CS1 at different temperatures: (from bottom to top) 200 mK, 220 mK, 240 mK, 260 mK, 280 mK and 300 mK. The parameters $N_I(0)\Omega_I$=2500 K^{-1}, N_I^*=0.0016 and $\mu_L=\mu_I$ were used to obtain the best fit.

7.10a). Amar *et al.* [87] interpreted the current peak at $n_g=1$ as being proportional to $P_e(n_g=1)$ and the current peak at $n_g=0$ as being proportional to $P_o(n_g=0)$.

However, this interpretation does not seem to be adequate for the measurements on sample CS1 shown in Fig. 7.10a. In Fig. 7.10b, the peak amplitudes measured at different temperatures are compared with the theoretical calculations for $P_e(n_g=1)$ and $P_o(n_g=0)$. Here I used $\mu_L=\mu_I$ and $N_I(0)\Omega_I=2500\ K^{-1}$ as before, but the best fit was now obtained with $N_I^*=0.008$. There are significant deviations at low temperatures between the model and the data and clearly a deeper understanding of the mechanisms responsible for this current is necessary to interpret these results.

The behavior of a superconducting SET at low bias current has been analyzed by Maassen van den Brink *et al*. [57] and Siewert *et al*. [56]. The dominant current generating cycle starts with coherent Cooper pair tunneling, which mixes charge states of the same parity, followed by an energy dissipating transition that returns the system to the initial state. Two different mechanisms exist to absorb the power IV_{DS} supplied by the voltage source, these are quasiparticle tunneling and exchange of energy with the environment. The current produced by the first mechanism can be expected to follow the temperature dependence predicted by the above theory since the tunneling rates temperature behavior is accounted for. On the other hand, the environment impedance causes transitions between the SET eigenstates with the transition rates given by [57]:

$$\Gamma_{i\to f}^{env}=\frac{\left|\left\langle \psi_f\left|\overline{Q}/2\right|\psi_i\right\rangle\right|^2}{\hbar^2}S_V(\omega) \tag{7.27}$$

where $\overline{Q}\equiv Q_1+Q_2$ is the total that has passed through the whole system. The spectral density $S_V(f)$ is given by [38]:

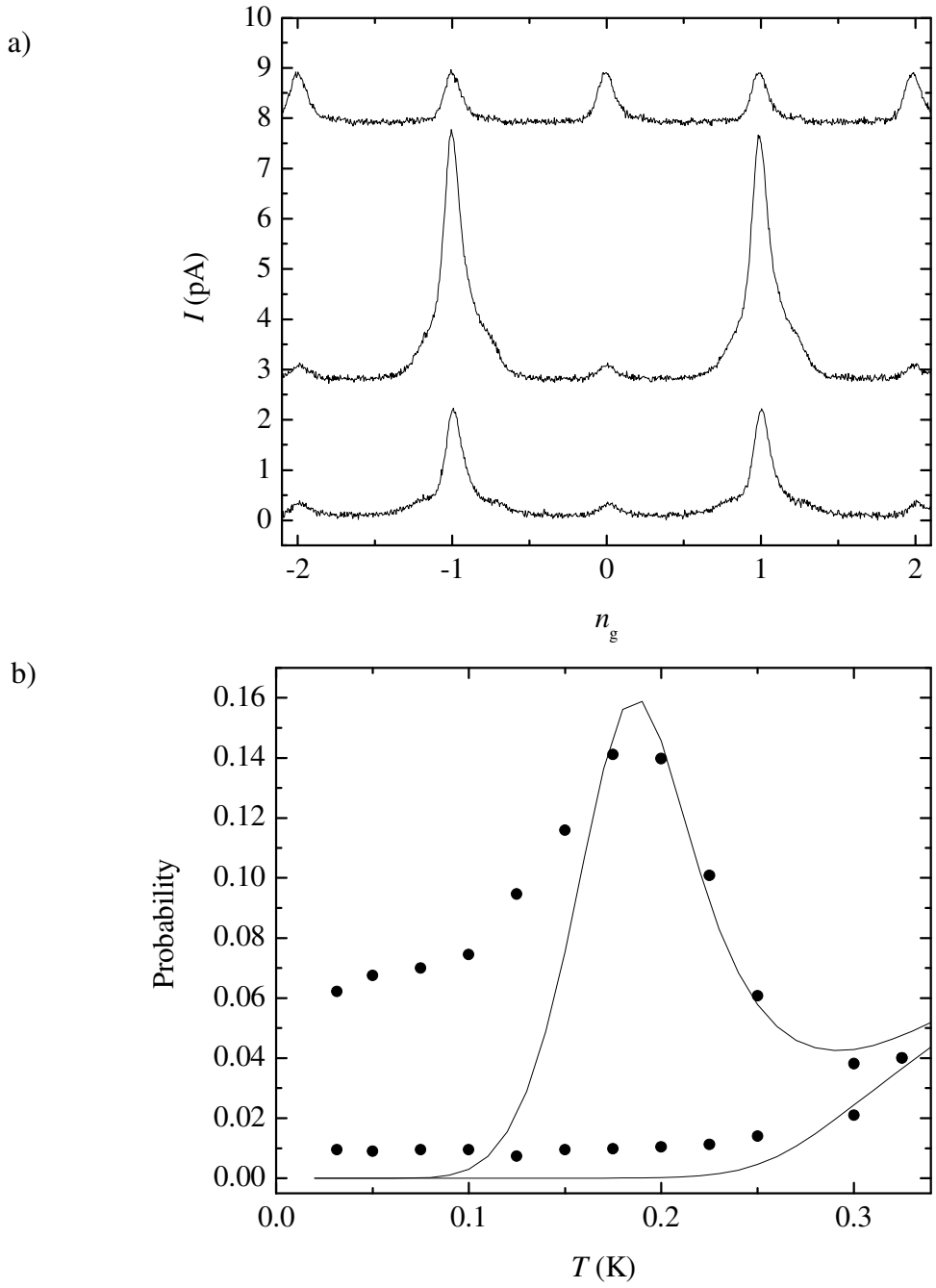

Fig. 7.10: (a) SET current for sample CS1 with V_{DS}=30μV at 32 mK (bottom), 175 mK (middle) and 325 mK (up). Curves have been shifted vertically for clarity. (b) Calculated probabilities (solid lines) $P_e(n_g=1)$ (upper curve) and $P_o(n_g=0)$ (bottom curve). The data points are proportional to the current peak at n_g=1 (upper curve) and n_g=0 (bottom curve).

$$S_V(f) = 2\mathrm{Re}\{Z\}\frac{hf}{1-\exp\left(-\frac{hf}{k_B T}\right)} \tag{7.28}$$

and Z is the impedance of the environment.

At low temperatures ($k_B T \ll hf$) $S_V(f)$ is approximately given by:

$$S_V(f) = \begin{cases} 2\mathrm{Re}\{Z\}hf & for\ f > 0 \\ 0 & for\ f < 0 \end{cases} \tag{7.29}$$

which states that, in this limit, the environment can absorb energy but not emit energy and the relaxation rate to the environment is temperature independent. Maassen van den Brink *et al*. [57] also note that the presence of both dissipation mechanisms produces features in the *IV* characteristics that cannot be generated by either mechanism alone. Therefore, I believe that the residual low temperature current in Fig. 7.10 cannot be explained by quasiparticle tunneling only.

The effect of the environment could be much smaller under certain conditions. For example, the environment impedance can be decreased at high frequencies by having bonding pads with large capacitances. Also, the current due to quasiparticle tunneling increases with increasing ratio E_J/E_c [56] and therefore, environmental effects could be difficult to see on devices with low R and large E_c.

I note that the current peak at $n_g=0$ and the reduction of the peak at $n_g=1$ can also be caused by high frequency radiation if the bias leads are insufficiently filtered [87,47]. In order to test for inadequate filtering I extended the length of the thermocoax cables on

one of my devices by 30 cm to provide for additional attenuation at base temperature (see Chapter 5 for the filtering characteristics of this cable). The device characteristics showed no change after the additional filtering was inserted and therefore I conclude that the filtering was sufficient.

7.5 Magnetic field effects

Turek *et al*. [86] reported the reduction of quasiparticle poisoning in a CPB upon application of a magnetic field on the order of 20 mT. The island of the CPB consisted of a narrow aluminum film (~100 nm wide). The leads were also narrow close to the Josephson junctions but became much wider about 1 μm away from the junctions. The application of a small magnetic field strongly reduces the energy gap on the wide parts of the leads while having little effect on the narrow regions. Turek *et al*. interpreted the reduction in quasiparticle poisoning as being caused by a decrease of the energy gap of the leads, which makes it more difficult for a quasiparticle in the leads to enter the island.

In order to test this hypothesis I designed the device (sample CS6) shown in Fig. 7.11a. The idea was to look for quasiparticle poisoning in the 2*e* periodic SET current. By making the SET leads wide, one would expect to see the periodicity in the current depend on the magnetic field. Furthermore, one can directly measure the average energy gap $(\Delta_I+\Delta_L)/2$ from the *IV* characteristics. The results are shown in Figs. 7.11b and 7.12.

Figure 7.11b shows I versus n_g measurements on sample CS6 at T=30 mK and V_{DS}=17 μV under different applied fields. The reduction in quasiparticle poisoning is evident from the increase in the current. Figure 7.12a shows the peak amplitude versus field whereas Fig. 7.12b shows the average gap for the same magnetic fields. It can be

a)

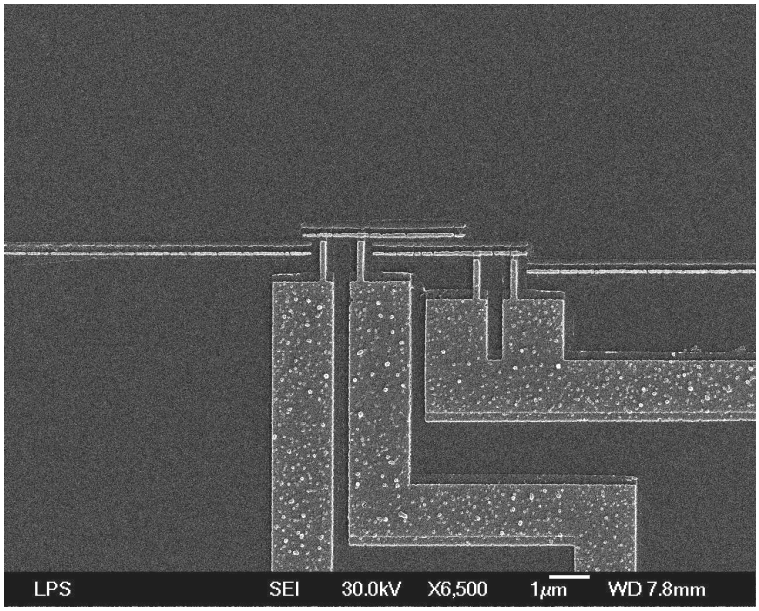

b)

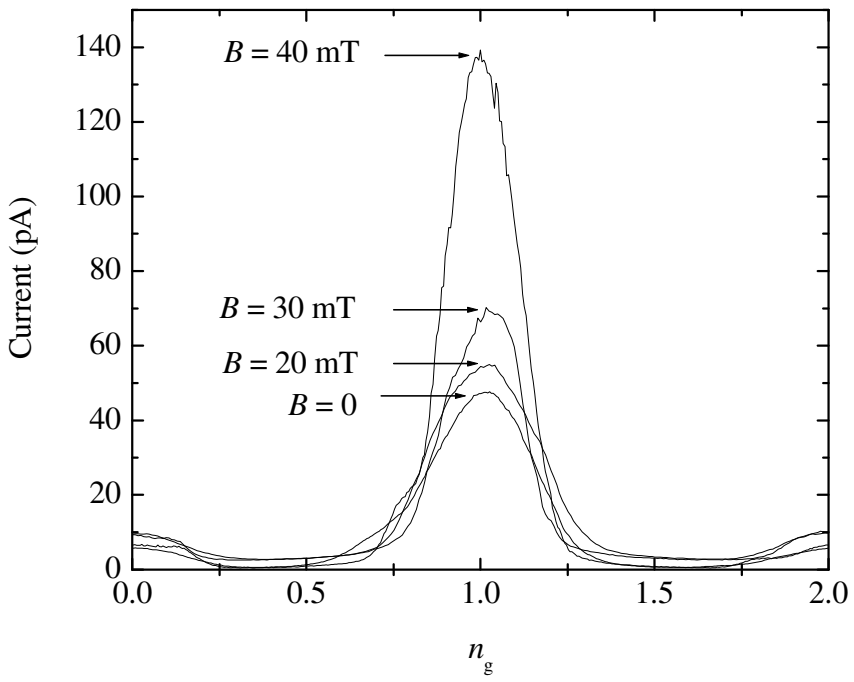

Fig. 7.11: (a) SEM picture of sample CS6 showing wide leads going to an SET (left) and a CPB (right). (b) SET current at T=30 mK and V_{DS}=17 μV for different magnetic fields.

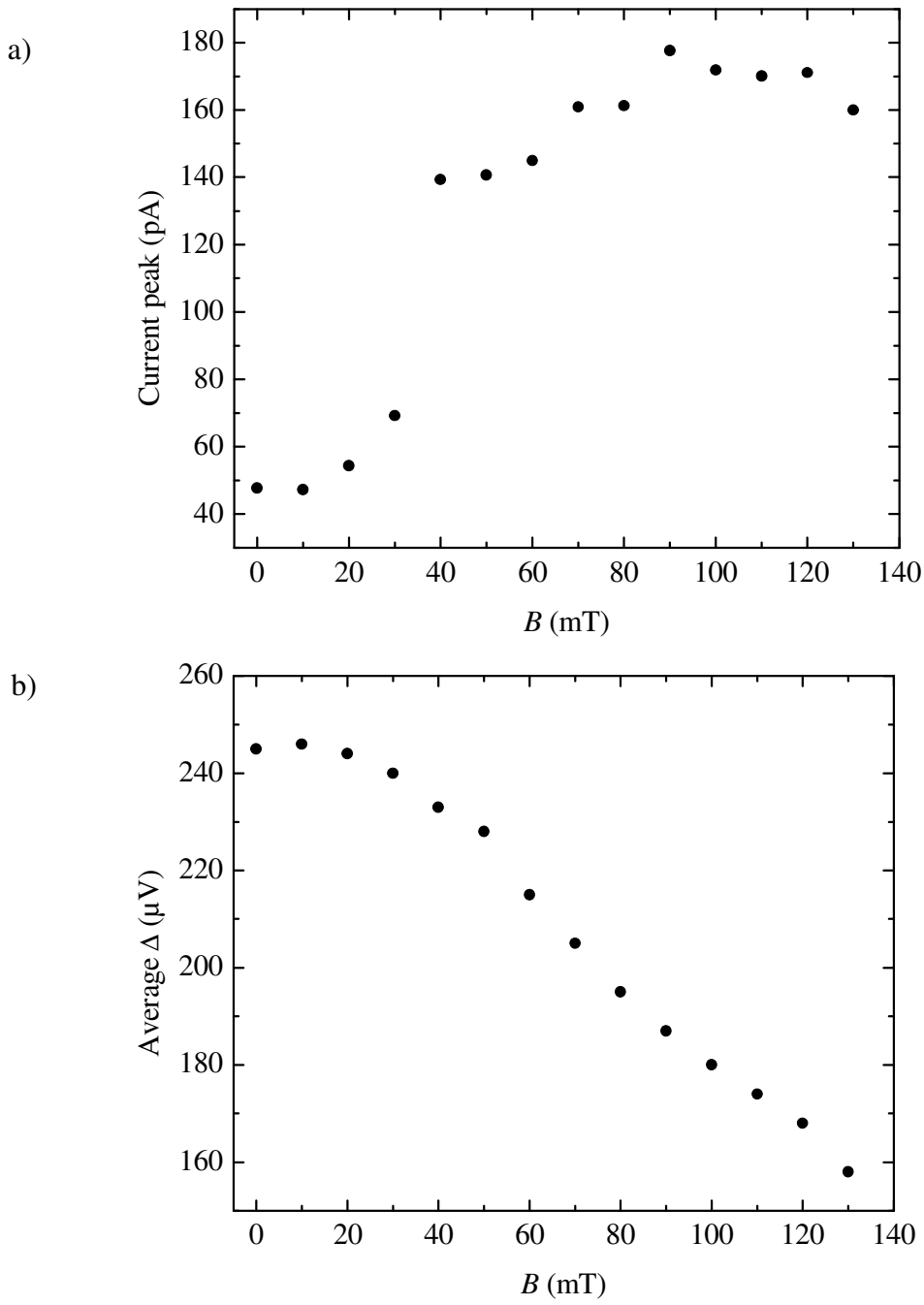

Fig. 7.12: (a) Low bias SET current peak at $n_g=1$ versus magnetic field for sample CS6. (b) Average energy gap Δ/e versus magnetic field.

appreciated that, while the field has a dramatic effect on the current between 20 mT and 40 mT, it has only a modest effect on the energy gap.

If we assume that the change in the average gap is entirely due to the change in Δ_L then at B=40 mT one would have $\delta\Delta_L = \Delta_L(0) - \Delta_L(40\,\mathrm{mT}) \approx 13\ \mu\mathrm{eV}$, which corresponds to 0.15 K. From the *IV* characteristics I estimated E_c=0.92 K, R_Σ=50 kΩ and from the Ambegaokar-Baratoff relation E_J=0.72 K, resulting in $\delta E \approx 0.61$ K at n_g=1.

Using these parameters, I computed the escape rate $\gamma \approx 2\times10^3\ \mathrm{s}^{-1}$ at B=40mT. I also estimated that one would need N_I^*=0.00032 and N_L^*=0.00032(Ω_L/Ω_I) in order to make $\Gamma_{LI}^* = \gamma$. This number is much smaller than the one I previously found on sample CS1 and it suggests that the reduction in quasiparticle poisoning is probably not caused by the change in the energy gap only. However, a reduction in N_L^* would be possible if the wide leads act as quasiparticle traps. I note that the critical field for pure bulk aluminum is about 10 mT and therefore, it is reasonable to assume that the wide regions are normal at B=40 mT.

7.6 Quasiparticle poisoning of the CPB by the SET

Figure 7.13 shows measurements of the average CPB charge on sample PE1. Here the SET was biased at a different point for each of the curves. At low bias, the Coulomb staircase is 2*e* periodic and shows evidence of quasiparticle poisoning only around $n_g = \pm 1$. As the SET bias is increased the staircase develops new features in the vicinity of $n_g = \pm 0.5$, until finally at large bias the staircase shows *e* periodicity. These observations are consistent with the measurements by Männik *et al*. [101] on a system of capacitively coupled superconducting SETs. Männik *et al*. investigated poisoning on one of the SETs

(simulating a CPB) by measuring its switching current while the other SET was carrying a quasiparticle current (simulating an SET electrometer). He found that the quasiparticle current through the electrometer induces a quasiparticle population in the CPB and that the induced population is proportional to the electrometer current. The mechanism producing this effect was not determined but it was speculated that recombination of quasiparticles in the electrometer leads could produce phonons and/or photons that could in turn break pairs in the CPB.

It is also possible that the peaks around $n_g=\pm 0.5$ are produced in part by the excited states of the CPB (even states), which can be significantly populated if the transition rates produced by SET back-action are comparable to the intrinsic relaxation time of the CPB. However, spectroscopy measurements (see Chapter 8) show that the odd state is populated around those peaks. Figure 7.14 shows the Coulomb staircase of sample PE1 measured with the rf-SET at high bias while applying a microwave signal at 24, 28 and 32 GHz to the gate of the CPB.

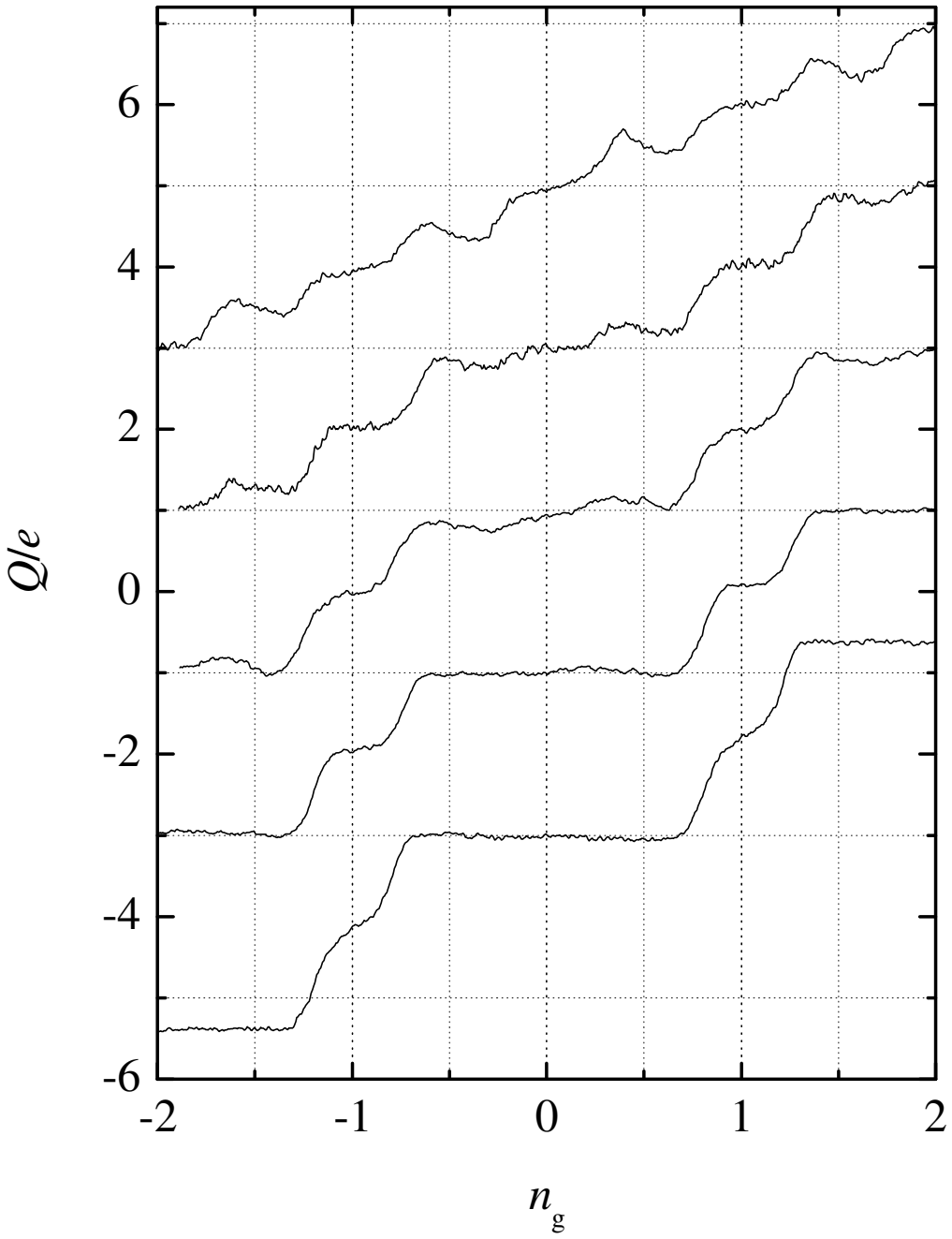

Fig. 7.13: Average charge on the CPB of sample PE1 measured at different SET bias points. From bottom to top (a) V_{DS}=290 μV, I=3 pA (b) 540 μV, 70 pA, (c) 660 μV, 240 pA, (d) 880 μV, 320 pA, and (e) 920 μV, 900 pA. The curves have been shifted vertically for clarity.

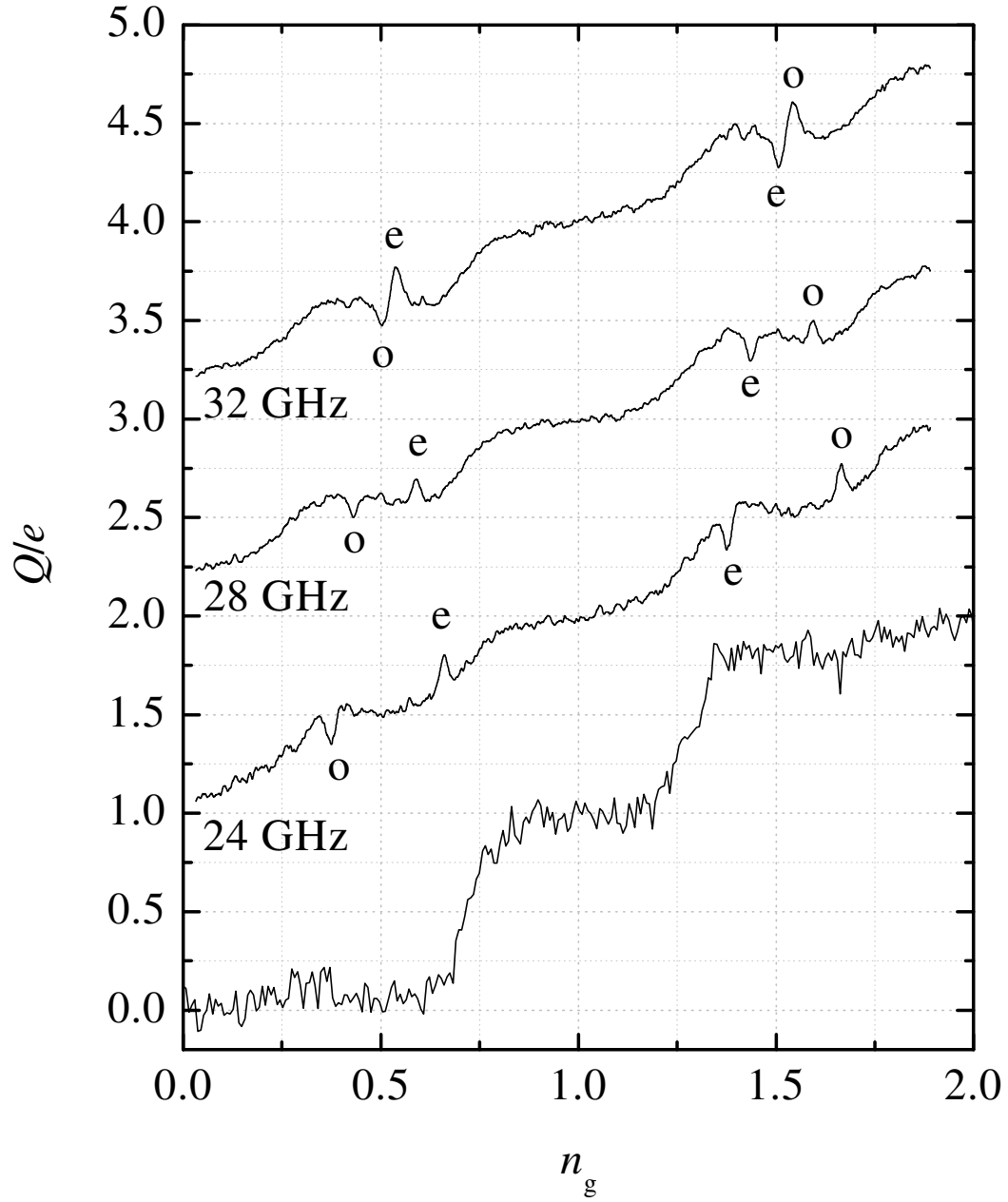

Fig. 7.14: Average charge on the CPB of sample PE1 measured with the rf-SET while applying a microwave signal to the gate of the CPB at three different frequencies. The SET was biased at V_{DS}=540 μV for the bottom curve (no microwaves applied) and V_{DS}=660 μV for the curves with microwaves at 24, 28 and 32 GHz applied. The two different set of resonant peaks ("e" and "o") correspond to the CPB being in the even or odd state.

The bottom curve in the figure was measured with a relatively low SET bias (V_{DS}=540 μV) and no microwaves applied. The other curves were measured with V_{DS}=660 μV, where the features induced by the SET are more prominent. Microwaves induce narrow peaks at the resonant points $\Delta E_{10}(n_g)=hf$, where $\Delta E_{10}(n_g)$ is the energy difference between the ground state and the first excited state of the CPB. In the even state, only the points marked with a letter "e" are resonant. The second set of resonant peaks observed in the figure (marked with an "o") are shifted with respect to the first set by $\Delta n_g=1$. I interpret the second set of peaks as being the result of the microwaves causing transitions between odd states (e.g. between $|1\rangle$ and $|3\rangle$ or between $|-1\rangle$ and $|1\rangle$).

I have attempted to simulate the measurements shown in Fig. 7.13 using the theory developed in sections 7.2 and 7.3. The results of the simulation are shown in Fig. 7.15. I previously determined the parameters E_c=0.794 K and E_J=0.327 K from spectroscopy measurements (see Chapter 8) and the average energy gap $(\Delta_I+\Delta_L)/2$=2.515 K from the *IV* characteristics of the SET. The rest of the parameters were unknown and I explored combinations of them to try to reproduce the experimental features. I found that the peaks in the staircase around $n_g=\pm 0.5$ ($\delta E=0$) can be produced in my model if there is a difference between Δ_I and Δ_L. The peaks in the simulation are produced at $\delta E=\pm(\Delta_I-\Delta_L)$, when the discontinuities in the density of states are aligned on both sides of the tunnel junction. The tunneling rate Γ_{LI}^* for Δ_I=2.6 K and Δ_L=2.43 K is shown in Fig. 7.16 to illustrate this point.

Although the model seems to explain the general qualitative structure in the Coulomb staircase of the CPB induced by the SET current, my choice of parameters is somewhat arbitrary and more work needs to be done to verify the validity of the assumptions.

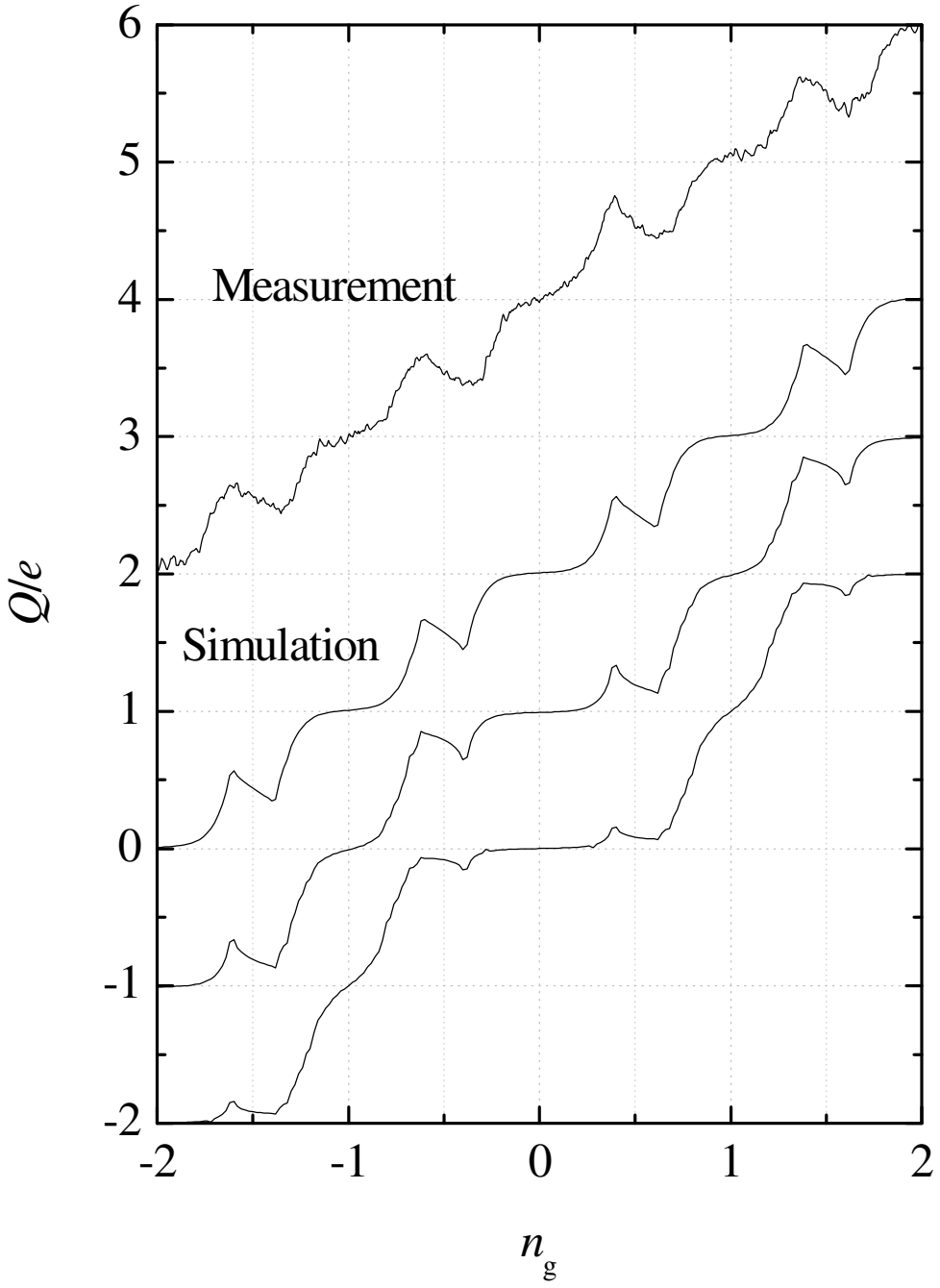

Fig. 7.15: Measured (top) and simulated (3 bottom curves) charge on the CPB of device PE1 with Δ_I=2.6 K, Δ_L=2.43 K, $N_I(0)\Omega_I$=2500 K^{-1}, T=0.1 K and N_I^*=0.03, N_L^*=0.01(Ω_L/Ω_I) (bottom), N_I^*=0.12, N_L^*=0.04(Ω_L/Ω_I) (middle), and N_I^*=1.2, N_L^*=0.4(Ω_L/Ω_I) (top).

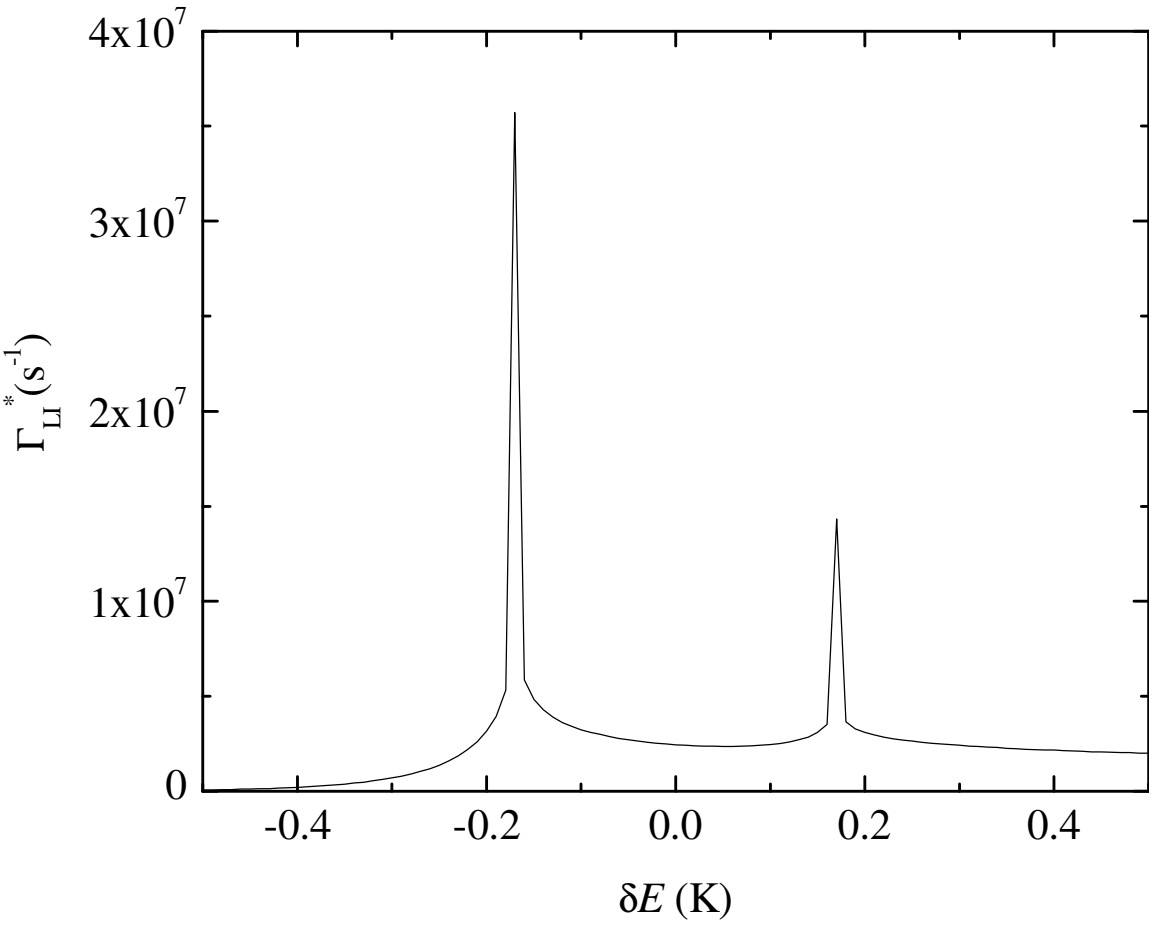

Fig. 7.16: Tunneling rate Γ_{LI}^{*} for Δ_I=2.6 K and Δ_L=2.43 K, T=0.1 K, N_I^{*}=0.12 and N_L^{*}=0.04(Ω_L/Ω_I). The peaks at $\delta E=\pm(\Delta_I-\Delta_L)$ are due to the discontinuities in the quasiparticle density of states.

7.7 Fabrication and materials issues

The samples discussed in this chapter were fabricated using the PMMA/Copolymer bilayer resist system described in Chapter 5. However, before I adopted this fabrication process, I made and tested several SETs and CPBs using the PMMA/Ge/PMGI trilayer system, also described in Chapter 5. Only one of these samples showed 2*e* periodicity (sample CS7), the rest were *e* periodic, including one sample with normal metal leads and superconducting island (CS8). It was this problem that caused me to change my fabrication process along the lines of Dr. Echternach's techniques. Since the normal metal leads provide a very effective trap for quasiparticles, the results on sample CS8 strongly suggest that quasiparticle poisoning in the samples made with the trilayer process was not caused by non-equilibrium quasiparticles, but rather by the presence of quasiparticle states within the gap.

It is possible that the trilayer system introduces contaminants in the aluminum films which lead to sub gap states. I observed, for example, that the tunneling resistance of samples fabricated with the bilayer process increased by about ten percent over a few days after they were first made, while stored at room temperature. I believe this can be caused by annealing of the aluminum films at room temperature with subsequent grain growth. On the other hand, the tunneling resistance does not change in devices fabricated with the trilayer process. This may be due to small differences in the impurity content of the films. It is known that the addition of silicon or copper in aluminum films can inhibit the formation of holes and hillocks in narrow wires if the doping atoms segregate in the aluminum grain boundaries [102].

Another difference I found is that the energy gap obtained in the trilayer samples is smaller (~190 μV) than that of the bilayer samples (~220 μV). This suggests that the bilayer samples are dirtier, since Al tends to increase its T_c in the presence of disorder [99,100], but it would also be consistent with the idea that the trilayer samples might have metallic or magnetic contaminants.

The effect of quasiparticle states inside the gap on the periodicity of the CPB can be simulated, for instance, by using a broadened BCS density of states [93]:

$$N_S(E,\Gamma) = N(0)\mathrm{Re}\left\{\frac{E - i\Gamma}{\sqrt{(E - i\Gamma)^2 - \Delta^2}}\right\} \tag{7.30}$$

Figure 7.17a shows the *IV* characteristics of a Josephson junction obtained by using Eq. 7.30 to calculate the tunneling rates (Eq. 7.15) for three different broadening parameters: Γ=0.01 K, Γ=0.001 K, and Γ=0.0001 K.

Figure 7.17b shows the calculated charge of a CPB with E_c=0.8 K, E_J=0.325 K and $\Delta_I=\Delta_L$=2.5 K at T=50 mK using the same broadened density of states. Even though I did not include non-equilibrium quasiparticles in this simulation, poisoning is evident in the middle curve, despite the fact that the onset of current in the *IV* looks fairly sharp. These simulations suggest that the purity of the superconducting films is important to obtain 2*e* periodicity in SETs and CPBs and that even relatively few states below the gap can cause significant poisoning.

The broadening parameter Γ would be difficult to determine using the *IV* characteristics of SETs because heating and charging effects can have significant effects

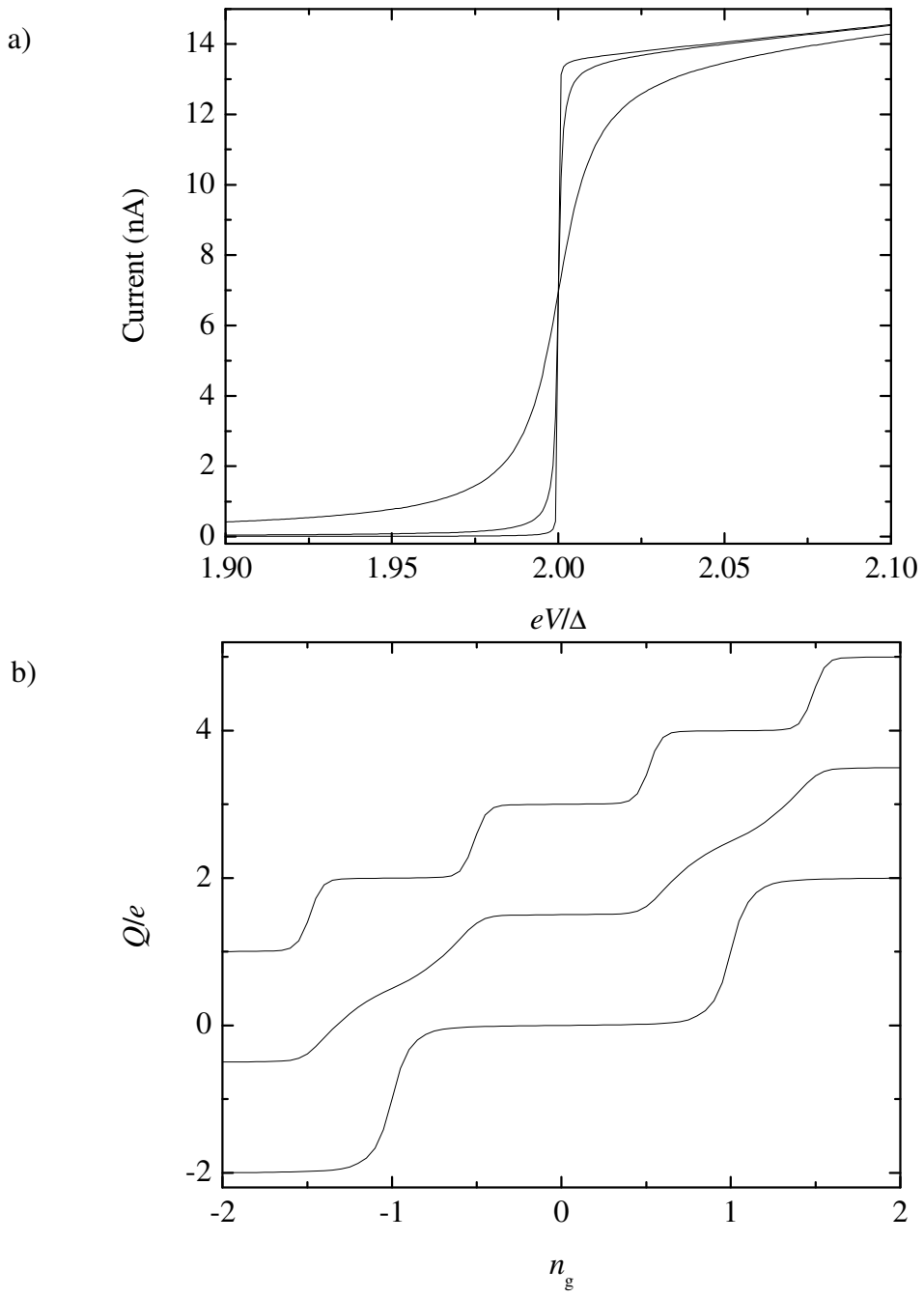

Fig. 17: (a) Calculated *IV* characteristics near the gap voltage of a Josephson junction at T=50 mK using a broadened BCS density of states with broadening parameters: Γ=0.01 K, Γ=0.001 K and Γ=0.0001 K. (b) Calculated charge of a CPB with E_c=0.8 K, E_J=0.325 K and $\Delta_I=\Delta_L$=2.5 K at T=50 mK using the same density of states as above. Non-equilibrium quasiparticles were not included.

on the slope $(\partial I/\partial V)^{-1}$ [53]. However, one could fabricate a single Josephson junction and an SET/CPB device on the same chip and then use the *IV* characteristics of the single junction to measure Γ and subsequently use this parameter to simulate quasiparticle poisoning effects in the SET and CPB devices.

7.8 Summary

In this Chapter, I have extended previous theories of quasiparticle poisoning to try to explain parity effects in SETs and CPBs. I used my model to simulate different experiments. I found excellent agreement between the theory and experiment on the measured average charge of a CPB in the temperature range from 60 mK to 300 mK. However, my model does not reproduce the behavior of the $2e$ periodic current on SETs with large E_c at low temperature, which suggests that processes producing the current in this range are not accounted for in my model. This theory provides an explanation for the features induced in the CPB around $n_g=\pm 0.5$ for large SET bias. Finally, I discussed a number of fabrication and materials issues that can produce quasiparticle poisoning in SETs and CPBs, and presented the strong effects produced by the broadening of the density of states.

Chapter 8: Quantum state manipulation of the CPB qubit

8.1 Spectroscopy

The first excited state of the CPB can be populated by applying high frequency voltage signals to the gate. For a sinusoidal gate signal $V_{\mathrm{rf}}\cos(\omega_{\mathrm{rf}}t)$ the CPB Hamiltonian takes the form:

$$H = E_c\left(n - n_g\right)^2 - E_J\cos(\phi) + 2E_c n n_g^{rf}\cos\left(\omega_{rf}t\right) \tag{8.1}$$

where $n_{\mathrm{g}}^{\mathrm{rf}} = C_{\mathrm{g}}V_{\mathrm{rf}}/e$. For small $n_{\mathrm{g}}^{\mathrm{rf}}$ and assuming a two-level system, the Hamiltonian can be written in matrix form as:

$$H = \begin{pmatrix} E_0 & \hbar\Omega\cos\left(\omega_{rf}t\right) \\ \hbar\Omega\cos\left(\omega_{rf}t\right) & E_1 \end{pmatrix} \tag{8.2}$$

where the basis states $|\psi_{\mathrm{o}}\rangle$ and $|\psi_1\rangle$ are the ground and excited states of the CPB without microwaves, E_0 and E_1 are the corresponding energies and $\Omega \equiv 2E_{\mathrm{c}}n_{\mathrm{g}}^{\mathrm{rf}}\left|\langle\psi_{\mathrm{o}}|n|\psi_1\rangle\right|$ is the bare Rabi frequency. In the range $0<n_{\mathrm{g}}<2$ the eigenstates and energies of the CPB with $E_{\mathrm{c}} \gtrsim E_{\mathrm{J}}$ are well approximated by Eqs. 2.8 – 2.12 and we can explicitly evaluate Ω:

$$\Omega = \frac{2E_c n_g^{rf}}{\hbar}\frac{E_J}{\Delta E_{10}} \tag{8.3}$$

The quantum behavior of the CPB is described by the density matrix [103] which evolves according to:

$$i\hbar\frac{\partial\rho}{\partial t} = [H, \rho] \tag{8.4}$$

The Hamiltonian in Eq. 8.4 should include the coupling of the CPB to a dissipative environment in order to fully account for the qubit state dynamics. Using the harmonic oscillator bath model [104] or merely introducing ad hoc terms to account for loss and decoherence [105], one can obtain:

$$\frac{\partial \rho_{00}}{\partial t} = -i\Omega(\rho_{10} - \rho_{01})\cos(\omega_{rf} t) + \frac{\rho_{11}}{T_1} \tag{8.5a}$$

$$\frac{\partial \rho_{01}}{\partial t} = -i\left\{\Omega(\rho_{11} - \rho_{00})\cos(\omega_{rf} t) - \frac{\Delta E_{10}}{\hbar}\rho_{01}\right\} - \frac{\rho_{01}}{T_2} \tag{8.5b}$$

$$\frac{\partial \rho_{10}}{\partial t} = i\left\{\Omega(\rho_{11} - \rho_{00})\cos(\omega_{rf} t) - \frac{\Delta E_{10}}{\hbar}\rho_{10}\right\} - \frac{\rho_{10}}{T_2} \tag{8.5c}$$

$$\frac{\partial \rho_{11}}{\partial t} = i\Omega(\rho_{10} - \rho_{01})\cos(\omega_{rf} t) - \frac{\rho_{11}}{T_1} \tag{8.5d}$$

Here T_1 and T_2 correspond to the energy relaxation and dephasing times introduced in Chapter 3.

Equations 8.5a - 8.5d can be simplified by noting that a linearly polarized signal can be expressed as the sum of two circularly polarized waves, $\cos(\omega_{rf} t) = (^1/_2)\{\exp(i\omega_{rf} t)+\exp(-i\omega_{rf} t)\}$, rotating in opposite directions. Near resonance, i.e. $\hbar\omega_{rf} \approx \Delta E_{10}$, the wave rotating in the same direction as the precession of the fictitious spin associated with the two-level system will have a significant effect, whereas the wave rotating in the opposite direction can be neglected. This is known as the rotating wave approximation. With this approximation, equations 8.5a-8.5d are exactly analog to the original Bloch equations [104] used in nuclear magnetic resonance (NMR) to describe the magnetization of an ensemble of spins under a static magnetic field in the z direction and

a circularly polarized rf magnetic field in the x-y plane [106]. The steady state solution to the Bloch equations can be used to find the probability for the CPB to be found in the excited state [105]:

$$\rho_{11} = \frac{\Omega^2 T_1 T_2 / 2}{1 + T_2^2 \left(\frac{\Delta E_{10}}{\hbar} - \omega_{rf} \right)^2 + \Omega^2 T_1 T_2} \tag{8.6}$$

Figure 8.1 illustrates the calculated effect of 28 GHz microwave radiation on the average charge of a CPB with E_c=0.794 K and E_J=0.327 K, Ω=3.16 GHz, T_1=143 ns and T_2=250 ps. Figure 8.1a shows $\Delta E_{10}/h$ ranging from 6.8 GHz at the degeneracy point to 66 GHz at n_g=0. The resonant condition $\Delta E_{10}/h$=28 GHz occurs at n_g=±0.59 and n_g=±1.41, and the excited state becomes populated around those points. Since the expectation value of the charge in the ground state $\langle Q \rangle_g$ is different from that in the excited state $\langle Q \rangle_e$, the average charge, shown in Fig. 8.1b, is given by $Q_{avg}=P_g\langle Q \rangle_g + P_e\langle Q \rangle_e$, where P_g and P_e are the probabilities for the CPB to be in the ground and excited states respectively.

Figure 8.2 shows a comparison of theory to the measured CPB charge on sample PE1 under 28 GHz microwave excitation. The theoretical curve used the previously determined parameters E_c=0.794 K, E_J=0.327 K and T_1=143 ns, as well as free parameters T_2=250 ps and n_g^{rf}=0.003 that were adjusted to reproduce the shape of the peaks. The deviation between the theoretical curve and the data around n_g=1 is probably due to quasiparticle poisoning; a short step around the degeneracy point was present on this sample at 35 mK (see Fig. 7.1). The data shown in Fig. 8.2 was taken at 100 mK to reduce the occupation probability of the odd state, as explained in Chapter 7, but some

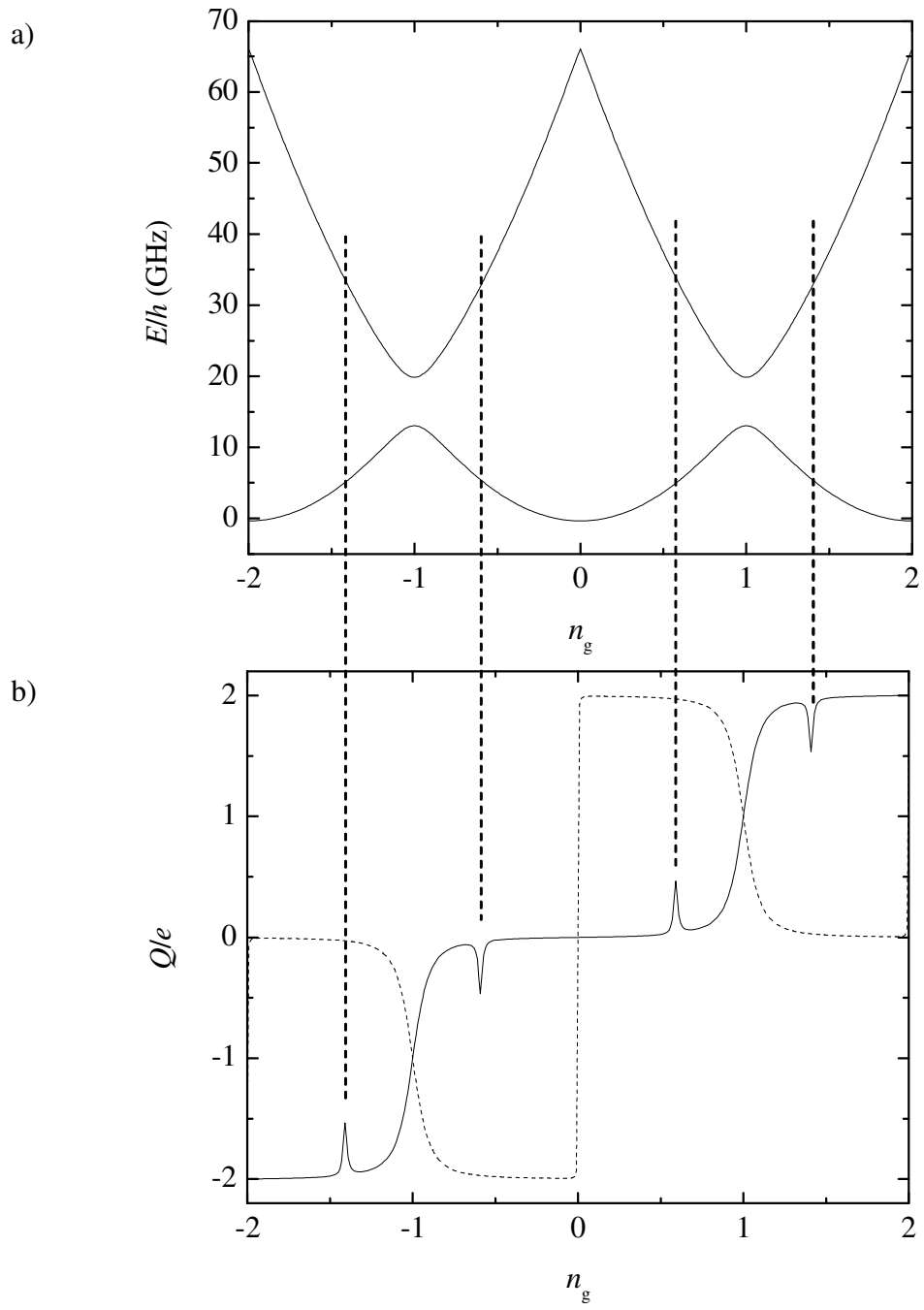

Fig. 8.1: Effect of 28 GHz radiation on a CPB with E_c=0.794 K and E_J=0.327 K. (a) Ground state and excited state energies vs n_g. (b) Average CPB charge (solid line). The dashed line is the expectation value of the charge in the excited state. Around the resonant points the average charge lies between the ground state and the excited state expectations.

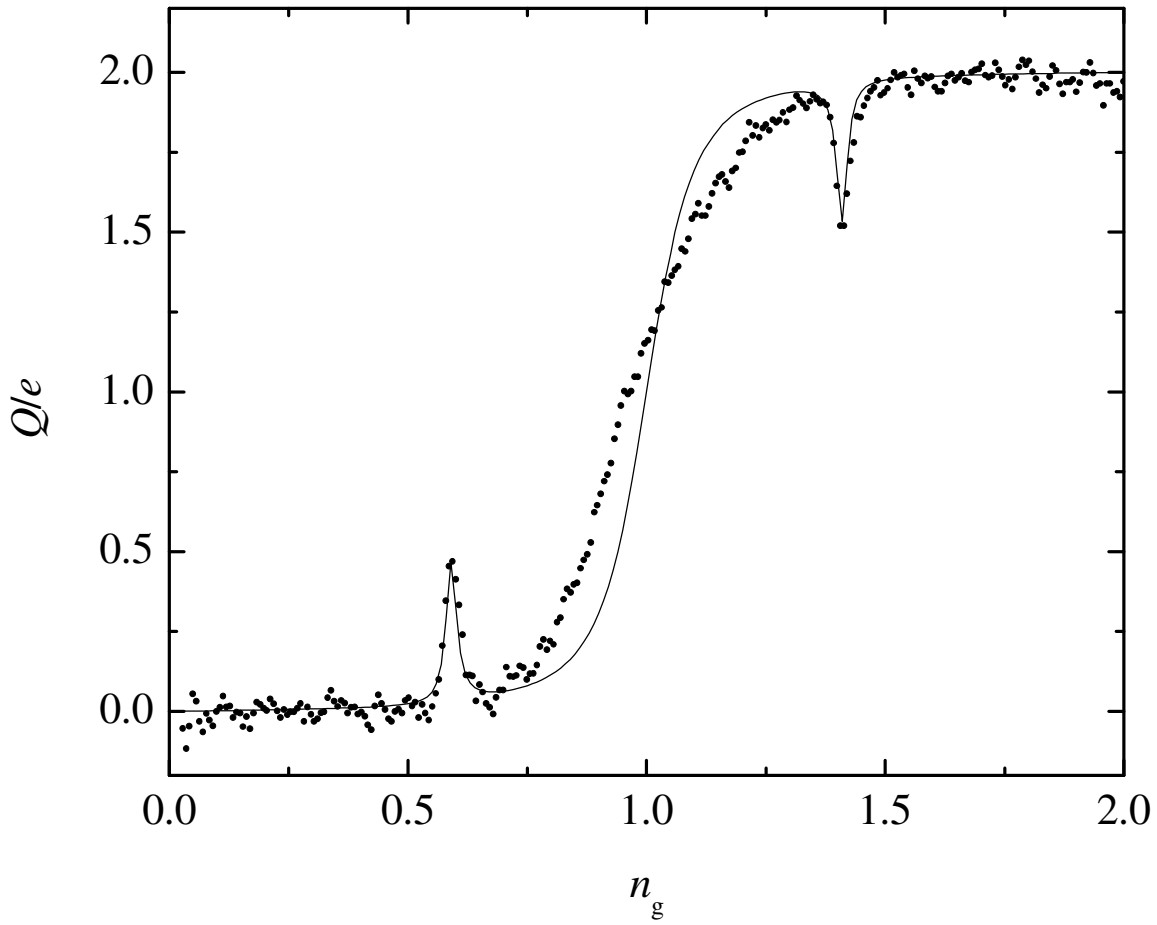

Fig. 8.2: Comparison of measured CPB charge of sample PE1 at T=100 mK under 28 GHz radiation (points) with theoretical curve (solid line). The parameters E_c=0.794 K, E_J=0.327 K and T_1=143 ns were determined from previous measurements. T_2=250 ps and n_g^{rf}=0.003 were adjusted to fit the data.

poisoning effects are still present at that temperature. The dephasing time T_2=250 ps inferred from this measurement is consistent with that due to typical 1/*f* charge noise, as shown in Chapter 3. T_2 is expected to be larger at n_g=1 since $\partial\Delta E_{10}/\partial n_g$=0 at that point and therefore ΔE_{10} is immune to first order charge fluctuations. Unfortunately, charge read-out cannot be used at the degeneracy point since the ground state and the first excited state have the same expectation value of the charge, i.e. $\langle\psi_o|Q|\psi_o\rangle=\langle\psi_1|Q|\psi_1\rangle$.

I also used spectroscopy to determine the energy splitting of the CPB by means of the resonant condition $\Delta E(n_g^{peak})=hf_{rf}$, where n_g^{peak} is the location of the peak maximum and f_{rf} is the excitation frequency. Figure 8.3 shows the peak locations n_g^{peak} for different frequencies measured on sample PE1. ΔE depends on the CPB parameters E_c and E_J according to Eq. 2.13:

$$\Delta E = \sqrt{\left[4E_c\left(1-n_g\right)\right]^2 + E_J^2} \tag{8.7}$$

This equation is also plotted in Fig. 8.3 using the best fit estimates for E_c and E_J, E_c=0.794 K and E_J=0.327 K. I note that there is excellent agreement between the theory and experiment.

8.2 Coherent oscillations

Quantum state control of the CPB was first demonstrated by Nakamura *et al*. [26] and subsequently by other groups [29,30]. Rabi oscillations induced by a sinusoidal rf gate signal have been demonstrated as a quantum state manipulation technique [107]. However, this method is difficult to implement in devices with small decoherence times since the rf signal has to be turned on and off in a time short compared to T_1 and T_2.

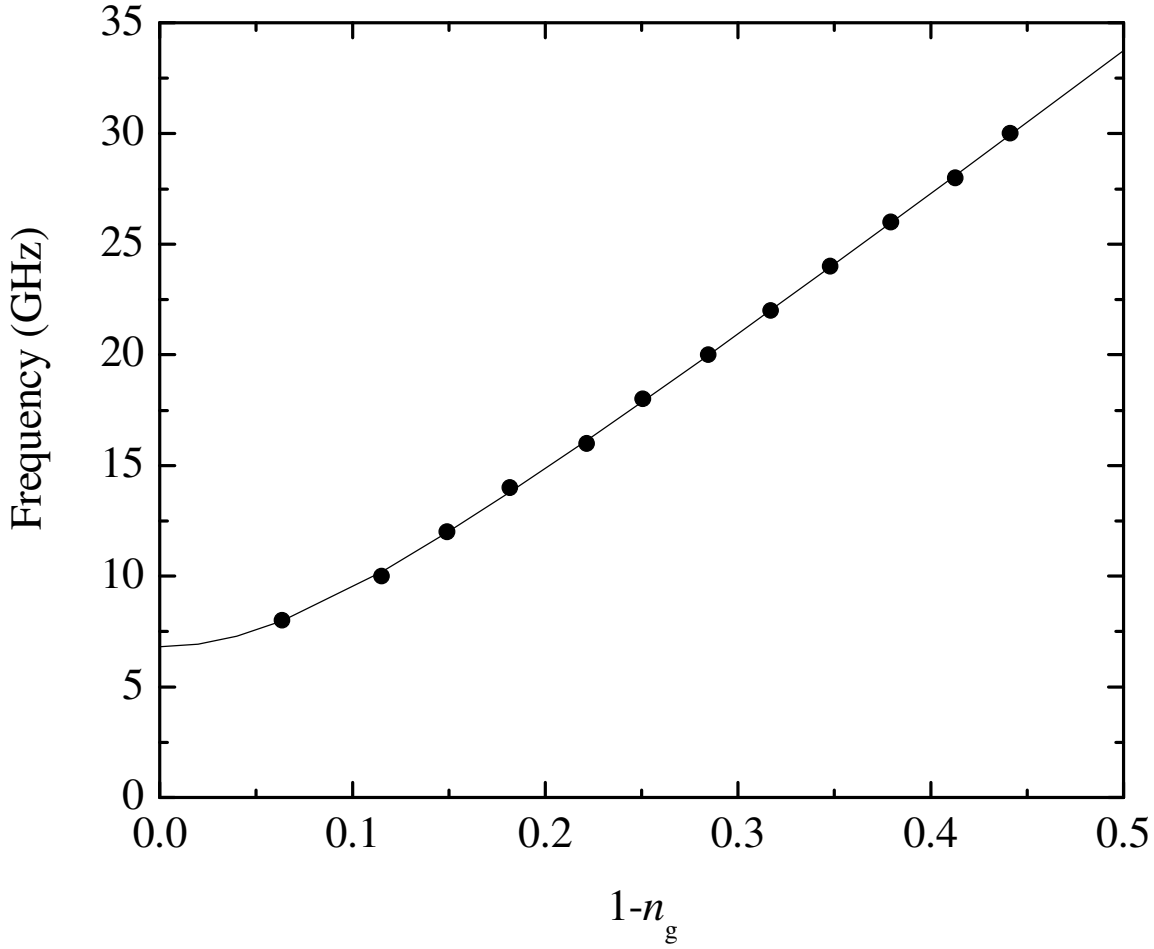

Fig. 8.3: Spectroscopy data for sample PE1. The data points map the peak location for a given excitation frequency. The solid line is the theoretical energy splitting with the best fit parameters E_c=0.794 K and E_J=0.327 K.

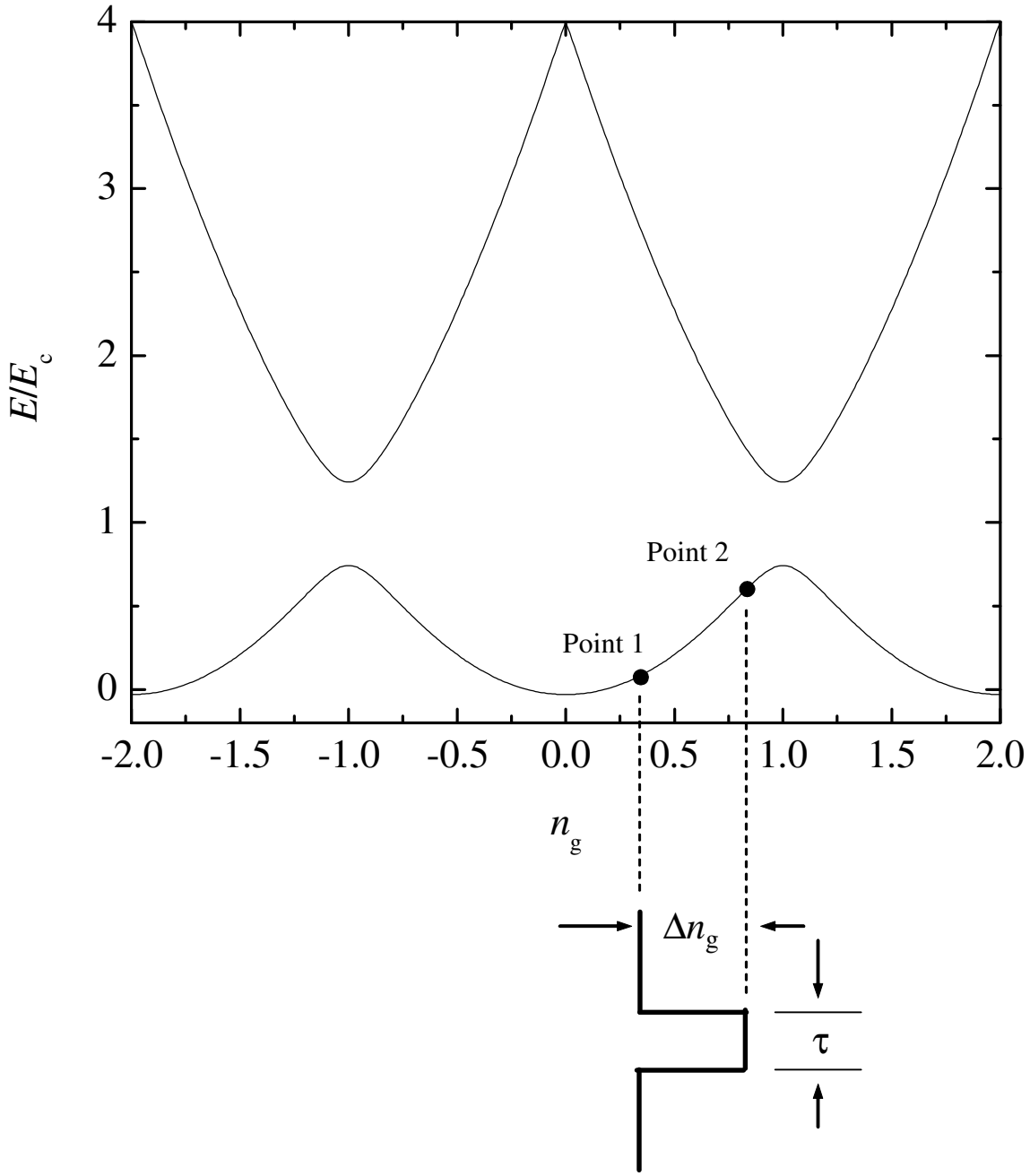

Fig. 8.4: Fast voltage pulse technique used for quantum state control of a CPB. The CPB bias is quickly shifted from point 1 to point 2 where the energy splitting and eigenstates are different. After a time τ, the gate voltage is returned to point 1 and the CPB is left in a superposition of the ground and excited states.

An alternative and arguably better technique for state control involves applying a fast voltage pulse to the gate of the CPB. This approach is illustrated in Fig. 8.4. The qubit is assumed to be initially in the ground state $|\psi_o\rangle_1$ at bias point 1 [22]:

$$|\psi_0\rangle_1 = \cos\left(\frac{\theta_1}{2}\right)|0\rangle + \sin\left(\frac{\theta_1}{2}\right)|1\rangle \tag{8.8}$$

where

$$\tan(\theta_1) = \frac{E_J}{4E_c(1-n_{g1})} \tag{8.9}$$

I note that if point 1 lies in the $|n=0\rangle$ plateau of the staircase then $\cos(\theta_1/2)\approx 1$, $\sin(\theta_1/2)\approx 0$ and the initial state is almost equal to the charge state $|0\rangle$.

For this technique to work, the gate pulse with amplitude Δn_g must suddenly change the CPB bias to point 2. If the pulse rise time is short compared to T_1 and to the evolution time $\hbar/\Delta E_{10}$, the state immediately after the bias change is almost the same as the initial state and can be expressed as a superposition of the energy eigenstates at point 2:

$$|\psi(t=0)\rangle = A_2|\psi_0\rangle_1 = a|\psi_o\rangle_2 + b|\psi_1\rangle_2 \tag{8.10}$$

The matrix A_2 can be found using Eqs. 2.10 and 2.11:

$$A_2 = \begin{pmatrix} \cos\left(\frac{\theta_2}{2}\right) & \sin\left(\frac{\theta_2}{2}\right) \\ -\sin\left(\frac{\theta_2}{2}\right) & \cos\left(\frac{\theta_2}{2}\right) \end{pmatrix} \tag{8.11}$$

with the corresponding parameter:

$$\tan(\theta_2) = \frac{E_J}{4E_c(1-n_{g2})} \tag{8.12}$$

If the CPB is kept at point 2 for a time τ, then it will evolve to the state:

$$\left|\psi(t=\tau)\right\rangle = a\left|\psi_o\right\rangle_2 + e^{-i\phi} b\left|\psi_1\right\rangle_2 \tag{8.13}$$

where the phase ϕ is given by:

$$\phi = \frac{\Delta E_{10}\left(n_{g1}\right)\tau}{\hbar} \tag{8.14}$$

The vector 8.13 can then be multiplied by the matrix A_2^{-1} to obtain the final state in the charge state basis:

$$\left|\psi(\tau)\right\rangle_{in\ charge\ basis} = A_2^{-1}\left[a\left|\psi_o\right\rangle_2 + e^{-i\phi} b\left|\psi_1\right\rangle_2\right] = c\left|0\right\rangle + d\left|2\right\rangle \tag{8.15}$$

From Eq. 8.15, we can see that the probability P_2 of finding the CPB in the state $|2\rangle$ immediately after the pulse has an oscillatory dependence on the pulse duration τ due to the $e^{-i\phi}$ factor. The state 8.15 keeps evolving at point 1 into a different superposition of $|0\rangle$ and $|2\rangle$. However, if point 1 is such that $4E_c(1-n_g) \gg E_J$ then $\cos(\theta_1/2)\approx 1$, $\sin(\theta_1/2)\approx 0$ and $[H,n]\approx 0$. In this case $P_2|_{t>\tau} \approx P_2|_{t=\tau}$. In the special case where point 2 is the degeneracy point this probability is given by [26]:

$$P_2 = \left|d\right|^2 = \sin^2\left(\frac{E_J\tau}{2\hbar}\right) \tag{8.16}$$

Thus this state control technique prepares the CPB into a superposition of charge states and the coefficients c and d of the superposition are determined by the pulse duration τ. A measurement of the island charge after a state preparation pulse should result in measured charge $Q=2e$ with probability P_2. However the excited state of the CPB relaxes to the ground state in a typical time T_1 and therefore, a single shot measurement of the CPB state would need to be completed in a time $t_m \ll T_1$ after the pulse.

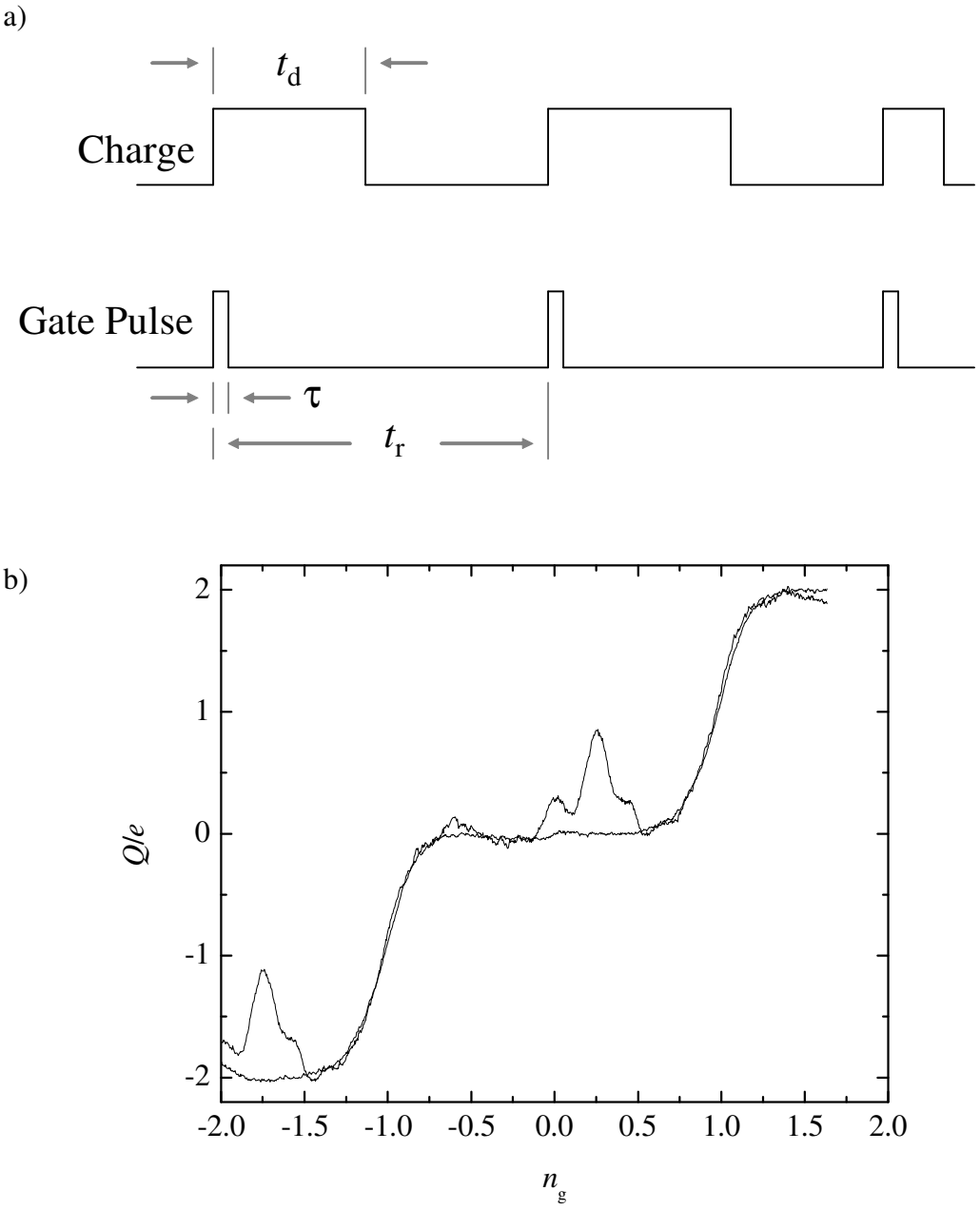

Fig. 8.5: (a) Train of pulses technique used to repeatedly populate the excited state of the CPB. (b) Measured charge staircase on sample PE2 with and without fast gate pulses.

The sensitivity and bandwidth requirements for a single shot measurement are not easy to accomplish, as will be discussed in Section 8.4. Instead, one can determine the CPB state by measuring the average charge over a large number of single events. This is illustrated in Fig. 8.5a. A train of fast pulses with pulse duration τ and repetition rate t_r is applied to the gate of the CPB while otherwise keeping it dc biased at fixed n_g (point 1). After the pulse, the CPB is found in the excited state with probability $P(\psi_1)$ depending on the choice of point 1, point 2 and τ. The charge in the excited state differs from that in the ground state. The difference $\Delta Q=\langle\psi_1|Q|\psi_1\rangle-\langle\psi_o|Q|\psi_o\rangle$ is equal to $2e$ close to $n_g=0$ and goes to zero at $n_g=1$. The excited state decays after a random time t_d following a Poisson distribution function, i.e. the probability that the system remains in the excited state at time t is given by:

$$P_e(t)=\exp\left(-\frac{t}{T_1}\right) \tag{8.17}$$

If $t_r \gg T_1$ we can assume that the CPB is in the ground state before each pulse. In this case the average charge induced by the train of pulses is given by:

$$\overline{\delta Q}=P(\psi_1)\Delta Q\frac{1}{t_r}\int_0^{tr}\exp\left(-\frac{t}{T_1}\right)dt=P(\psi_1)\Delta Q\frac{T_1}{t_r}\left[1-\exp\left(-\frac{t_r}{T_1}\right)\right] \tag{8.18}$$

Figure 8.5b shows the charge staircase measured on sample PE2 while applying a train of pulses with $t_r=100$ ns and $\tau=100$ ps nominally (the pulse rise time was estimated to be about 70 ps at the end of a 3 meter long cable). The exact pulse amplitude was not determined but it was roughly equal to $\Delta n_g \approx 1.7$. The measurement was done by slowly sweeping the dc gate of the box at a rate of about $dn_g/dt=1\ s^{-1}$ while measuring the dc current through the SET. The measured staircase without pulses is also shown in the

graph for comparison. I note that the excess charge induced by the pulses is maximum when point 2 lies in the vicinity of n_g=1. At that point the Hamiltonian is Josephson dominated and therefore, considerable mixing occurs between $|0\rangle$ and $|2\rangle$.

Figure 8.6b shows the measured charge on sample PE2 while applying a train of pulses with τ varying from 85 ps to 200 ps in 5 ps steps, measured using the setup shown in Fig. 5.11. The curves have been displaced vertically for clarity. Figure 8.6a shows the calculated CPB charge using equations 8.8 to 8.15. The parameters E_c=0.715 K and E_J=0.722 K, determined for sample PE2 through spectroscopy measurements, were used in the calculations. The theoretical curves show the charge to be an oscillating function of τ. The period of the oscillations $T=h/\Delta E_{10}$ is determined by the energy splitting of point 2 (see equations 8.13 and 8.14) and is maximum when the evolution takes place at the degeneracy point, in which case:

$$T_{\max} = \frac{h}{E_J} \tag{8.19}$$

This data also shows that the local charge maxima move in the n_g-τ plane. The oscillations and the trend in the local maxima can be seen in the data of Fig. 8.6b for short evolution times. For larger τ the oscillations are not well defined due to decoherence. I note that the oscillations on the measured data are lost close to n_g=0. There are two possible explanations for this. First, it was noted by Duty *et al*. [29] that the maximum probability P_2 for the state $|2\rangle$ is reduced as a consequence of a large E_J/E_c ratio and a finite pulse rise time. However, when point 2 is past the degeneracy point the state $|2\rangle$ can be prepared with higher probability and therefore, the right side part of the coherent oscillations would be more prominent in this case. A second problem is that the

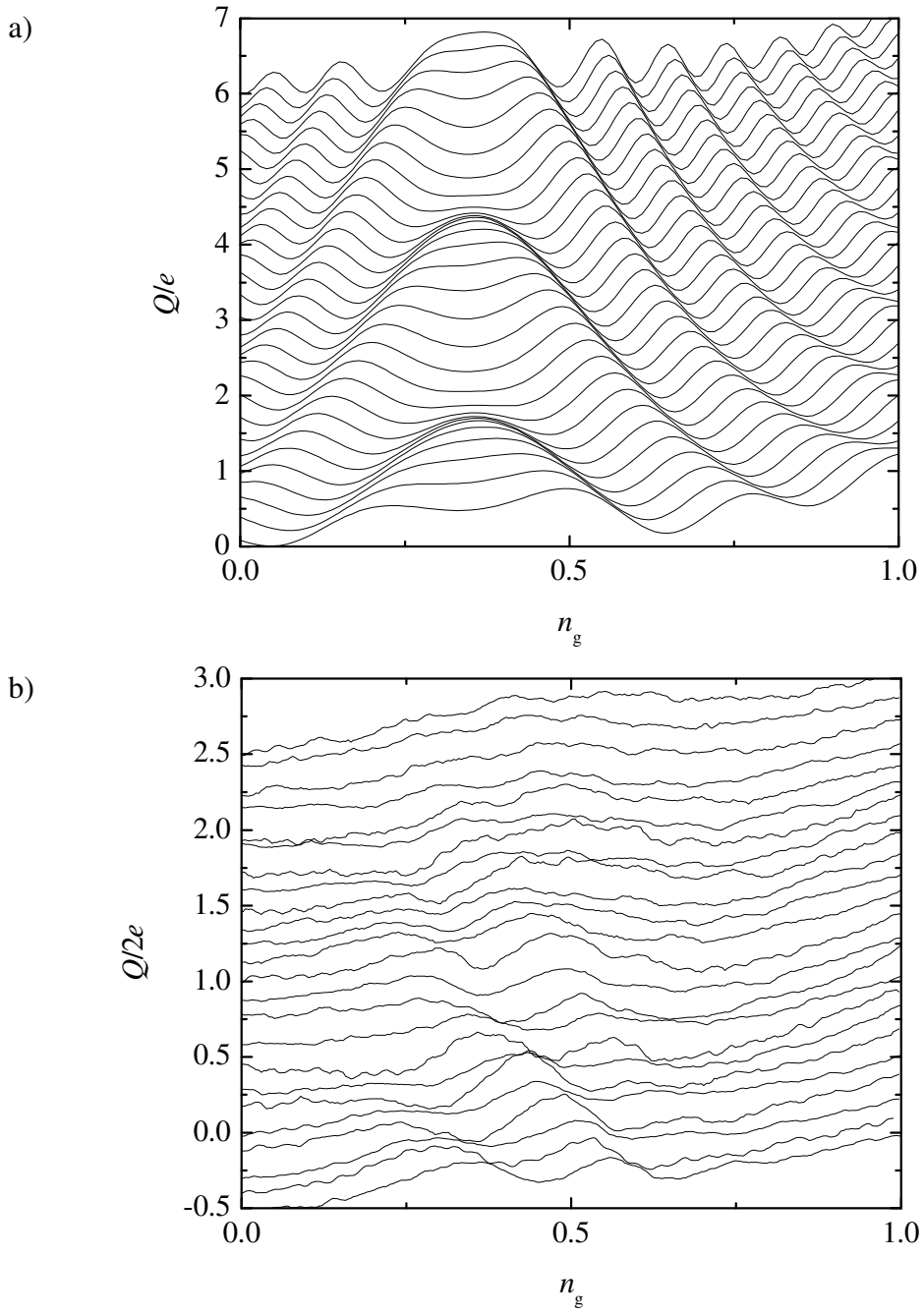

Fig. 8.6: (a) Calculated CPB charge vs. n_{g1} of sample PE2 with applied gate pulses of amplitude Δn_g=0.65 and τ varying between 85 ps (bottom trace) and 200 ps (upper trace) (b) Measured CPB charge vs. n_{g1} of sample PE2 with fast gate pulses. τ was varied from 85 ps (bottom trace) to 200 ps (upper trace) in steps 5 ps steps. The pulse amplitude was not determined.

two-level approximation is not valid in this region. In particular, at n_g=0 the excited state of the CPB is equal to $|\psi_1\rangle \approx (|-2\rangle - |2\rangle)/(2)^{1/2}$. Since the state $|2\rangle$ is not close to an energy eigenstate in the vicinity of this point, it evolves fast into a superposition of $|2\rangle$ and $|-2\rangle$ and the average charge tends to zero. This implies that the useful range for the observation of coherent oscillations is $0<n_g<1$ and one should limit the pulse amplitude to about $\Delta n_g \leqslant 0.7$ to be able to see the whole picture shown in Fig. 8.6a.

Figure 8.7 shows the excess charge as a function of pulse time τ, obtained by taking a cross section of Fig. 8.6b for fixed n_g=0.23 (point 1). A best fit to the equation:

$$\Delta Q = Q_0 + Q_1 \sin^2\left(\frac{\Delta E_{10}}{2\hbar}\tau + \varphi\right)\exp\left(-\frac{\tau}{T_2}\right) \tag{8.20}$$

produced the parameters $\Delta E_{10}/h$=19 GHz, T_2=212 ps, Q_1=0.72e, φ=−0.29π and Q_o=0.035e. This energy splitting for point 2 corresponds to $n_g \approx 1.19$ from which I can deduce the pulse amplitude $\Delta n_g \approx 0.96$.

The estimated dephasing time of 212 ps in sample PE2 is much shorter than $T_2 \approx 4$ ns, obtained by Duty *et al*. [108] and $T_2 \approx 5.8$ ns obtained by Astafiev *et al*. [32] in similar experiments. In Chapter 3, I presented theoretical estimates for the dephasing time caused by 1/*f* charge noise. Rewriting Eq. 3.14, T_2 is approximately given at n_g=1 by:

$$T_2 \approx \frac{1}{8}\hbar\left(\frac{E_J}{E_c^2}\right)\left(\frac{e}{\sigma_q}\right)^2 \tag{8.21}$$

where σ_q is the rms charge noise. The dephasing times found by Duty *et al*. and Astafiev *et al*. are consistent with typical levels of low frequency charge noise measured in SETs. However, some devices can have two-level fluctuators strongly coupled to the CPB, and this may be the case with device PE2.

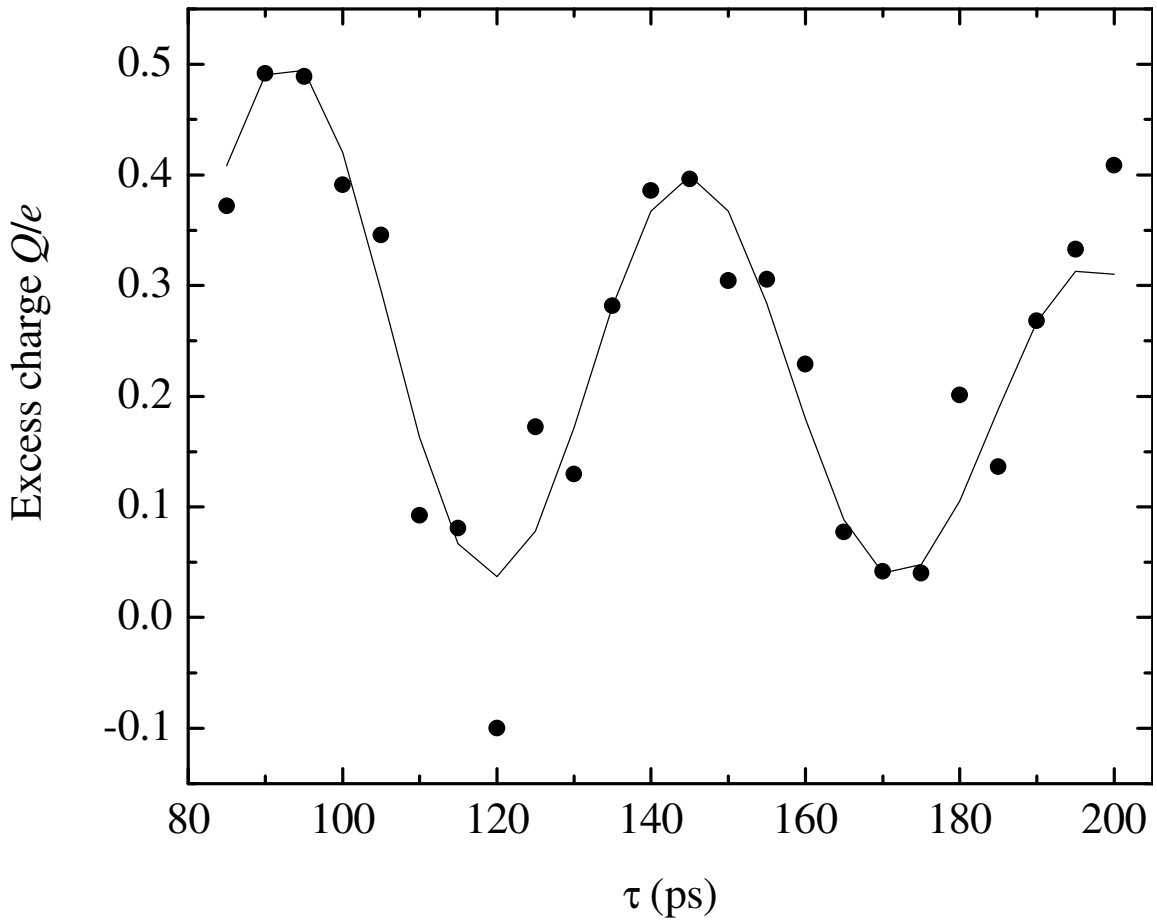

Fig. 8.7: Excess charge in Fig. 8.6b for fixed n_g=0.23 as a function of τ. The solid curve is a fit to Eq. 8.20 with T_2=212 ps.

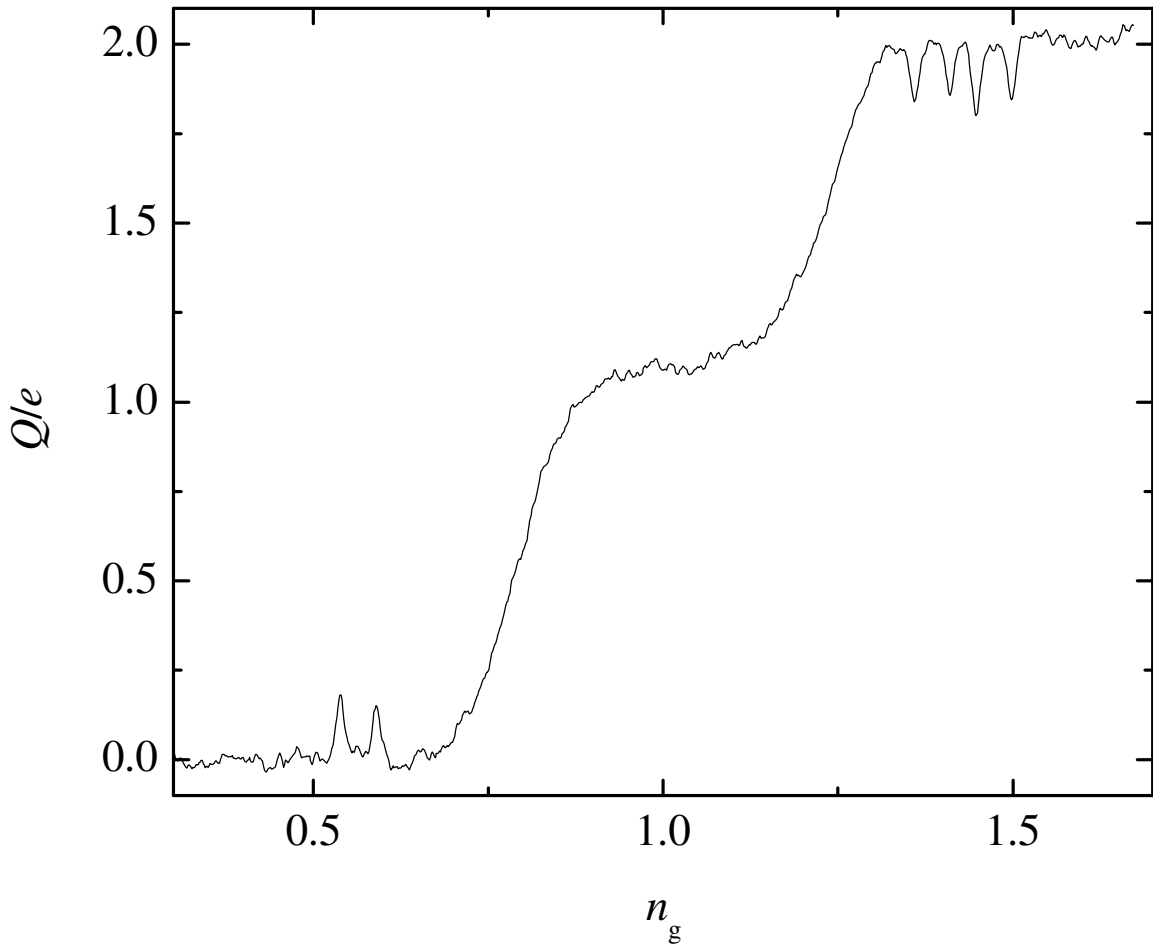

Fig. 8.8 Measurement of the average charge of the CPB in sample PE1 under 30 GHz microwave radiation, revealing two-level fluctuations. The fluctuators cause changes in the offset charge of the CPB and shift the staircase horizontally.

Two-level fluctuators in the CPB are revealed, for example, by spectroscopy measurements. Figure 8.8 shows the Coulomb staircase measured in sample PE1 under 30 GHz microwave radiation. The fluctuators change the offset charge around the CPB that shift the staircase horizontally. The resonant peak provides a clear marker for the states of the fluctuators. The plot suggests that at least two fluctuators are strongly coupled to the CPB and that the charge fluctuation is about 0.05 e. For sample PE2, Eq. 8.21 gives $T_2 \approx (0.5\ \text{ps}) \times (\sigma_q/e)^{-2}$. A dephasing time $T_2 \approx 200$ ps could be explained by charge fluctuators with an rms amplitude $\sigma_q = 0.05e$. Unfortunately, I was not aware of this problem when I performed the measurements on sample PE2 and therefore, I could not measure the charge fluctuators in that sample.

8.3 Relaxation measurements

The measurements presented in this section make use of the large rf-SET bandwidth to observe the decay of the excited state of the CPB. The charge measurements discussed in the previous section were done by measuring the dc current through the SET. This has the advantage that the SET can be operated at low V_{DS} (~50 μV) and low current (~15 pA) to minimize quasiparticle poisoning on the CPB, although it has the disadvantage that the measurement bandwidth is limited to about 1kHz. On the other hand, the sensitivity of the rf-SET depends on impedance matching as explained in Chapter 4. The resonant circuit is usually designed for the SET resistance range $R_S = (\partial I/\partial V_{DS})^{-1} \sim 50$ kΩ which is attainable on the JQP region. For low V_{DS} bias, R_S is usually much larger, which results in a very small RF modulation and poor rf-SET sensitivity.

Figure 8.9 shows the effects of the rf-SET bias conditions on the CPB. In Fig. 8.9b the SET was biased in the middle of the JQP (V_{DS}=640 μV), which is the point were the rf-SET had the best charge sensitivity of 3×10^{-5} $e_{rms}/(\text{Hz})^{1/2}$. Unfortunately, operation of the rf-SET at this point results in significant quasiparticle poisoning. Figure 8.9a shows that a weaker but still significant perturbation results in the range $0.3 \leqslant n_g \leqslant 0.7$ when the SET is biased at the onset of the JQP (V_{DS}=640 μV) with a reduced charge sensitivity of 7×10^{-5} $e_{rms}/(\text{Hz})^{1/2}$. The measurement of the relaxation time T_1 to be discussed next was made with these bias conditions (Fig. 8.9a), which were the best I could obtain.

Figure 8.10b shows the staircase (time averaged charge) of sample PE1 measured with the rf-SET while the rf signal shown in Fig. 8.10a was applied to the gate of the CPB. The sinusoidal excitation signal with f_{RF}=30 GHz was turned on for a time t_{on}=20 ns and then off for a variable time. For Fig. 8.10b the repetition time was t_r=50 ns. The microwave pulses induce an excess charge on the CPB only close to the resonant points $hf_{RF}=\Delta E_{10}$ (e.g. points A and C in Fig. 8.10b), while there is no appreciable effect on the staircase away from resonance (e.g. point B). The induced charge on point A is positive since the excited state $|\psi_1\rangle \approx |2\rangle$. On point C $|\psi_1\rangle \approx |-2\rangle$ and therefore the induced charge is negative.

When the rf signal is turned off, the CPB is found in the excited state with probability given by Eq. 8.6. The excited state decays to the ground state in a time t_d following the distribution function 8.17. Figure 8.11a shows the output of the rf-SET for device PE1 when the CPB bias is fixed on points A, B and C respectively. These curves were obtained by averaging 40,000 individual oscilloscope traces. A 70 MHz low pass filter was used at the output of the mixer to cut-off higher frequency noise from the amplifiers.

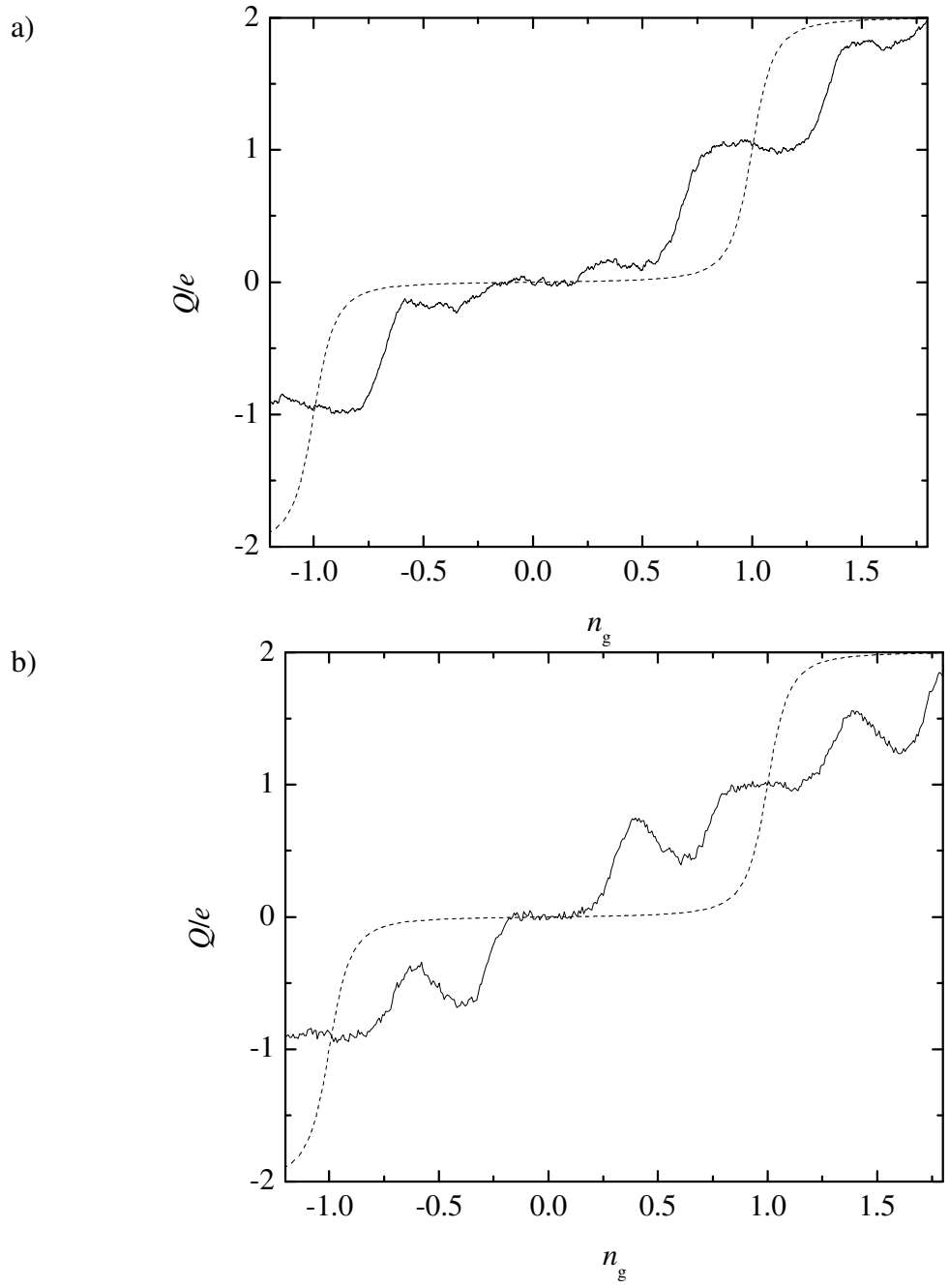

Fig. 8.9: Staircase measured for sample PE1 at 30 mK with the rf-SET biased on two different points: (a) V_{DS}=540 μV, I_{DC}≈120 pA, and (b) V_{DS}=640 μV, I_{DC}≈430 pA. The dashed line is the theoretical staircase neglecting any back-action or quasiparticles produced by the SET.

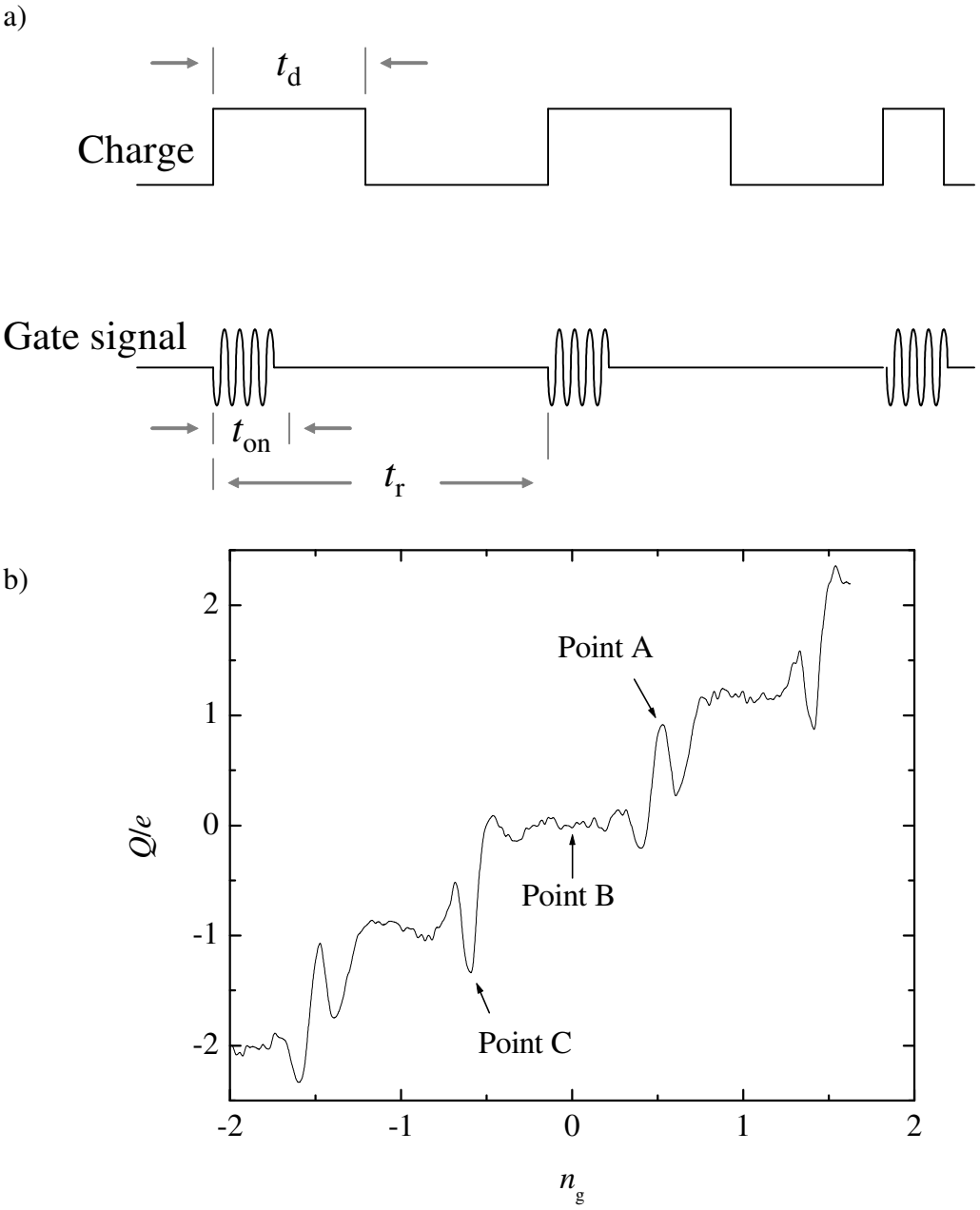

Fig. 8.10: (a) Pulsed microwave gate signal with f=30 GHz, t_{on}=20 ns and t_r=50 ns. (b) Staircase found when the above excitation signal was applied to device PE1 at 30 mK.

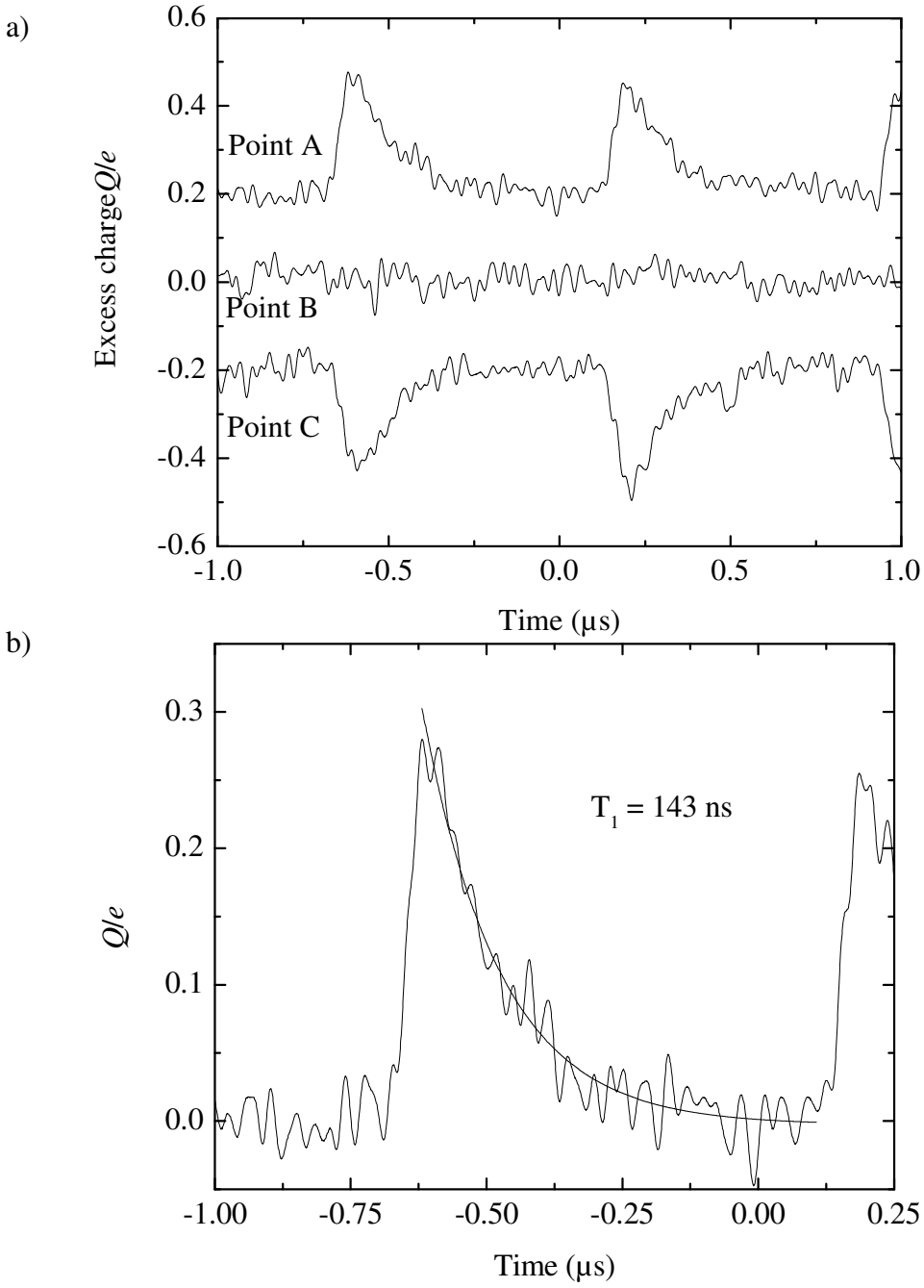

Fig. 8.11: (a) Induced CPB charge at each of the bias points indicated in Fig. 8.10a for device PE1 at 30 mK using f=30 GHz radiation found by averaging 40,000 individual traces. (b) Solid line shows exponential charge decay with best fit parameter T_1=143 ns at point A.

The rf-SET bandwidth however, which is set by the Q of the resonant circuit, was not determined for this sample but from the design it was expected to be on the order of 40 MHz. Figure 8.11b shows an exponential excited state decay with a best fit estimate T_1=143 ns.

The relaxation time T_1 can also be estimated from time averaged measurements (Fig. 8.10b). Assuming an induced charge given by:

$$\Delta Q = \begin{cases} \Delta Q_0 & \text{for} \quad -t_{on} < t < 0 \\ \Delta Q_0 \exp\left(-\frac{t}{T_1}\right) & \text{for} \quad 0 > t > t_{off} \end{cases} \tag{8.22}$$

the peak height can be approximated as:

$$\Delta Q = \frac{\Delta Q_0}{t_r}\left\{t_{on} + \int_0^{t_{off}} \exp\left(-\frac{t}{T_1}\right)dt\right\} = \frac{\Delta Q_0}{t_r}\left\{t_{on} + T_1\left[1 - \exp\left(-\frac{t_{off}}{T_1}\right)\right]\right\} \tag{8.23}$$

where ΔQ_o is the peak height for continuous microwave radiation and can be readily determined. For high microwave power ΔQ_o tends to e as the probability of the excited state equals the probability of the ground state (see Eq. 8.6). Equation 8.23 shows that one can obtain T_1 by measuring the peak height as a function of repetition rate t_r. This measurement is shown in Fig. 8.12. By fitting the data to Eq. 8.22, I find T_1=128 ns, which is close to that found using the first technique.

One can also use a train of fast pulses to populate the excited state of the CPB and determine T_1 from the dependence of the induced charge on the repetition rate (*i.e.* no microwaves are applied, just fast pulses). This technique has the added difficulty that one must know the effect of the pulse on the states $|0\rangle$ and $|1\rangle$ in order to calculate the average

charge for $t_r \ll T_1$. If one assumes a π-pulse (i.e. a pulse that evolves the state $|0\rangle$ into $|1\rangle$ and vice versa) then the induced charge is given by [29]:

$$\Delta Q = 2\Delta Q_0 \frac{T_1}{t_r}\left[\frac{1-\exp\left(-\frac{t_r}{T_1}\right)}{1+\exp\left(-\frac{t_r}{T_1}\right)}\right] \tag{8.24}$$

where ΔQ_o is the maximum induced charge which depends on the pulse rise time. However, I did not try this technique on device PE1.

I note that my estimates for T_1 on sample PE1 are consistent with relaxation times measured on CPBs with similar parameters by other groups [39,29,30]. The physical mechanism responsible for such short relaxation times is currently a subject of investigation. Out of the possible mechanisms discussed in Chapter 3, noise coming from the electromagnetic environment (lead impedance at different temperatures) seems unlikely to be the cause, as suggested by the calculations in Chapters 3 and 7. The SET noise can be roughly estimated from Eqs. 4.27 and 4.28. Substituting the SET parameters E_c=112 μeV and R_Σ=123 kΩ for this device we find $S_V(30\text{GHz})=2.3\times10^{-20}$ $(\text{nV})^2/\text{Hz}$. Using the box parameters E_c=0.794 K, E_J=0.327 K and $\kappa \equiv C_c/C_\Sigma$=0.009 in Eqs. 3.2 and 3.3 we find the mixing rate $\Gamma_{mix}=\Gamma_\uparrow+\Gamma_\downarrow=(4.4\ \mu\text{s})^{-1}$. Although this is not an accurate estimate, it suggests that the SET is not responsible for the measured T_1. However, I note that using the same equations one would estimate $T_1 \approx 176$ ns if κ and E_J were larger by a factor of 2.5 and 2 respectively. These are not extreme values for these experimental parameters and therefore many experiments could be affected by SET back-action.

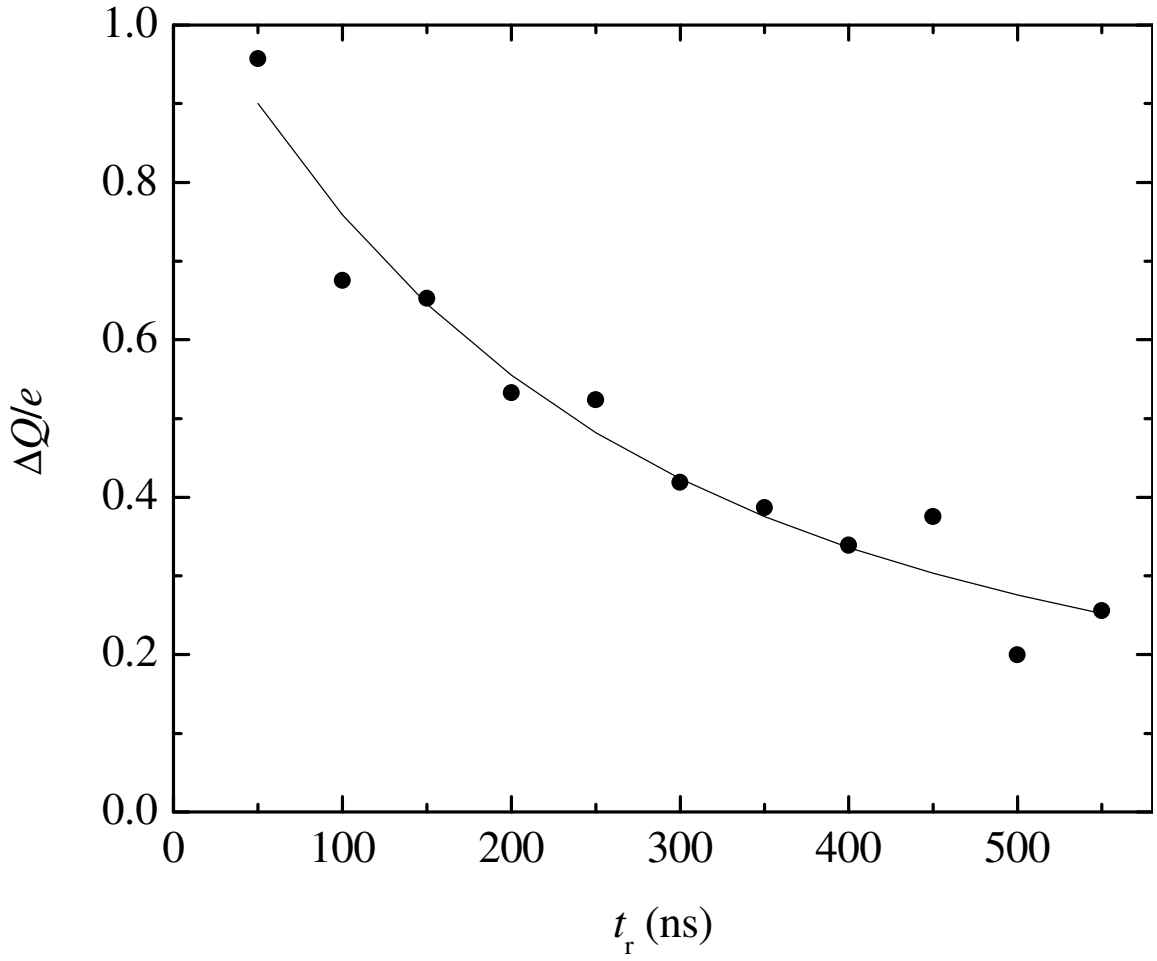

Fig. 8.12: Peak height induced by the pulsed microwave signal with repetition rate t_r for device PE1. A fit to Eq. 8.21 yields T_1=128 ns.

Other possible causes include dielectric loss (see Chapter 3), which could also be the source of charge noise. At this point more work needs to be done to account for the experimental relaxation times and hopefully increase them substantially.

8.4 Fidelity of single shot measurements

In previous sections I've discussed the design factors affecting the rf-SET sensitivity, the possible physical origins of relaxation and how signal and measurement back-action are affected by the coupling strength between the CPB and the SET. Here I present an analysis of the quality of single shot measurements given the above mentioned factors.

A single shot measurement consists in measuring the charge in the CPB after a state manipulation pulse and determining from the measurement whether the state $|0\rangle$ ("0") or $|2\rangle$ ("1") was produced by the pulse. The upper trace in Fig. 8.13 shows the measured CPB charge induced by a fast voltage pulse applied at t=0 in device PE1 of duration τ=200 ps at n_g=0.39. This curve is not a single shot measurement but the average of 4×10^4 individual measurements taken with a 30 MHz low pass filter inserted on the rf-SET output signal and its presented here to compare to a single shot signal resulting from the 1-state. The bottom curve is just the 4×10^4 times averaged baseline of the rf-SET output under the same conditions except without a pulse applied and represents the signal from the 0-state.

The decision to interpret the measurement as a 0 or a 1 can be made by integrating the output signal and comparing the outcome to some discrimination level. In the absence of noise the result of the integration would be:

$$B_Q = \int_0^{tm} Q(t)dt = 2e\kappa t_d = \Delta Q\, t_d \tag{8.25}$$

for the 1-state (assuming $t_m > t_d$) and $B_Q = 0$ for the 0-state. Here t_m is the measurement time, $\kappa \equiv C_c/C_{\Sigma box}$ is the coupling strength and t_d is the decay time which is a random variable with the probability density function:

$$P_d = \frac{1}{T_1}\exp\left(-\frac{t_d}{T_1}\right) \tag{8.26}$$

Due to charge noise B_Q has a random component characterized by the variance:

$$\sigma_B^2 = \left\langle \left[\int_{-tm/2}^{tm/2} Q(t)dt\right]^2 \right\rangle = \int_0^{tm} dt_1 \int_0^{tm} dt_2 \langle Q(t_1)Q(t_2)\rangle = \int_0^{\infty} S_Q \frac{\sin^2(\pi f\, t_m)}{(\pi f)^2} df = \frac{S_Q\, t_m}{2} \tag{8.27}$$

whereas the signal for the 1-state is proportional to t_d, with an average value of $B_{Q\,avg} = 2e\kappa T_1$. If we know T_1, we can choose the measurement time $t_m = T_1$ and define the signal-to-noise ratio for this situation as:

$$SNR \equiv \left(\frac{B_{Q\,avg}}{\sigma_B}\right)^2 = 8(e\kappa)^2 \frac{T_1}{S_Q} \tag{8.28}$$

I now assume that the charge noise follows a Normal distribution. The probability distribution for B_Q in the 0-state is just:

$$P_o = \frac{1}{\sigma_B\sqrt{2\pi}}\exp\left(-\frac{x^2}{2\sigma_B^2}\right) \tag{8.29}$$

In the 1-state, B_Q is the sum of two terms. The probability density for the sum is given by the convolution of the probability densities of the terms:

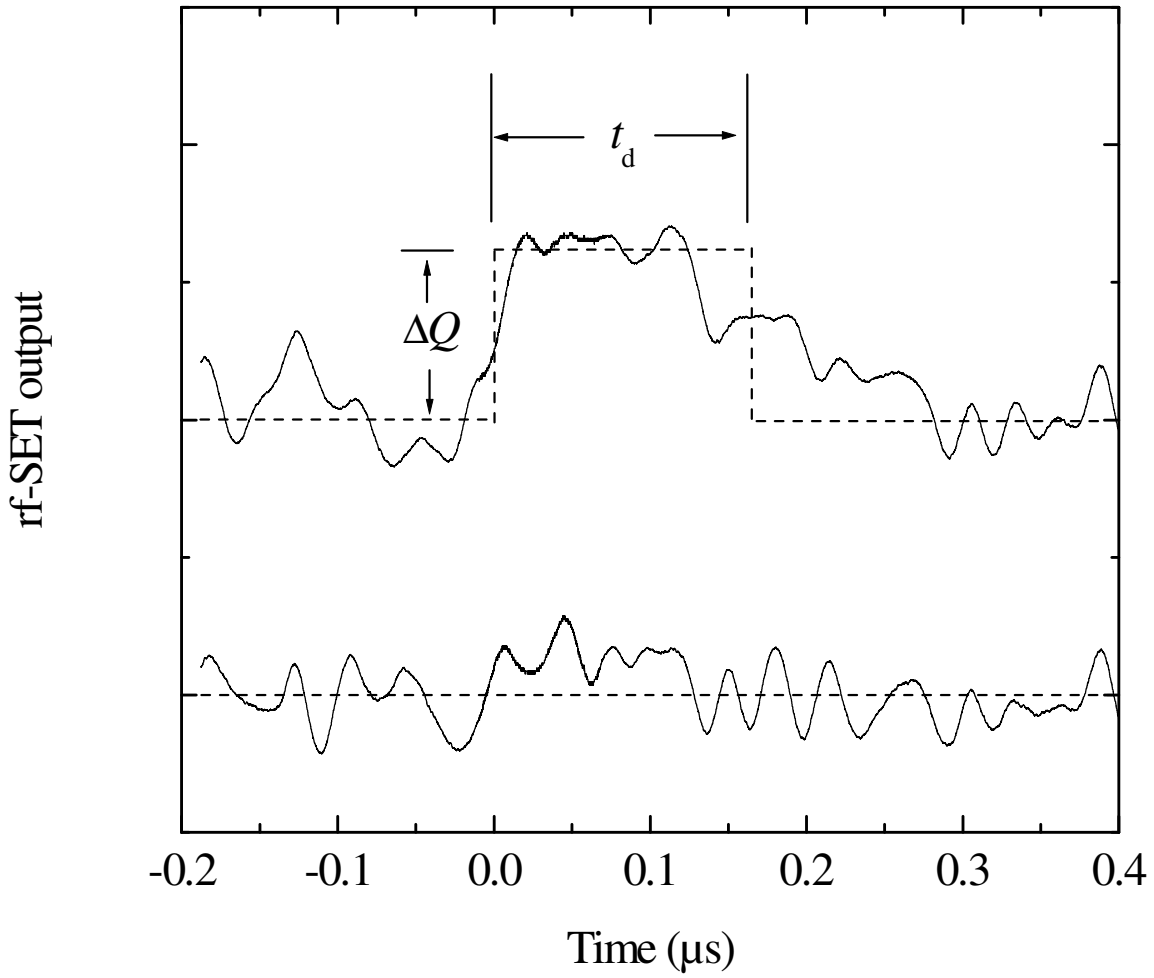

Fig. 8.13: Average of 4×10^4 rf-SET measurements of the CPB charge induced by fast voltage pulses (upper curve) and noise baseline (bottom curve).

$$P_1 = \int_{-\infty}^{\infty} P_0(x')P_d(x-x')dx' \tag{8.30}$$

For comparison the probability densities are shown in Fig. 8.14 for SNR=1 and SNR=25. The fidelity is defined for a particular state as the fraction of measurements of that state that are interpreted correctly. One can see from Fig. 8.14 that the fidelities of the 0 and 1 states are not independent. They both depend on the choice of discrimination level and in particular, shifting this level improves the measurement of one state while worsening the other. If we set the discrimination level to σ, such that the fidelity of the 0-state measurement is fixed at 0.841, then the fidelity of the 1-state is calculated by integrating P_1 from σ to infinity. The result is shown in Fig. 8.15 as a function of SNR.

For sample PE1, I find $\text{SNR} \approx 8(0.009e)^2(143\times10^{-9})/(7\times10^{-5}e)^2 \approx 0.019$. This implies that I would need to make about 53 measurements to detect the 1-state with a 46 % fidelity.

a)

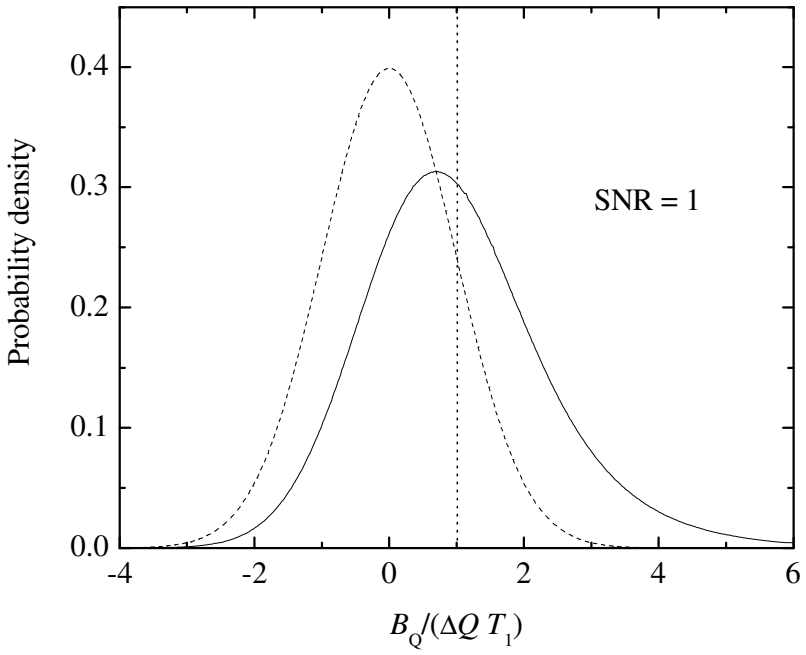

b)

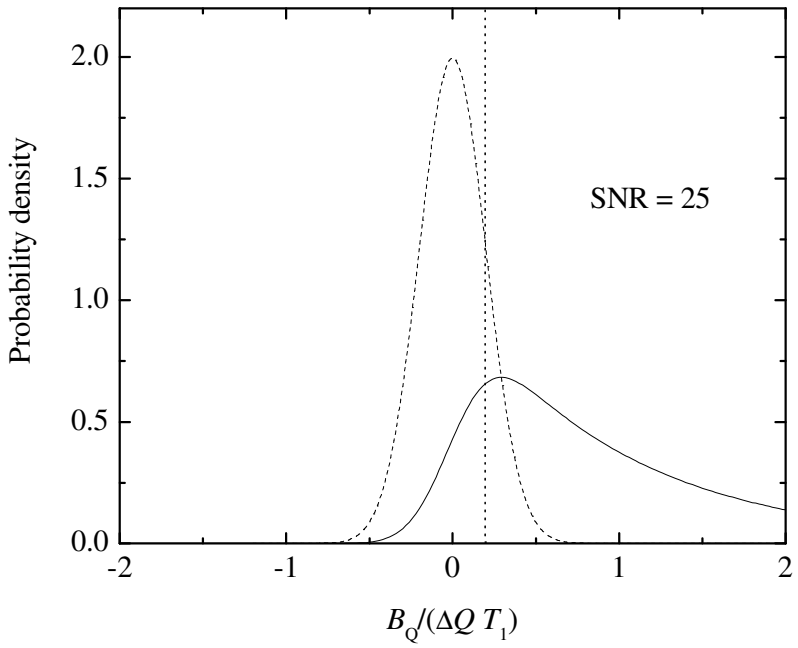

Fig. 8.14: Probability density of B_Q for a 1-state (dashed line) and for a 0-state (solid line) for (a) SNR=1 and (b) SNR=25. The dotted vertical line indicates the discrimination level.

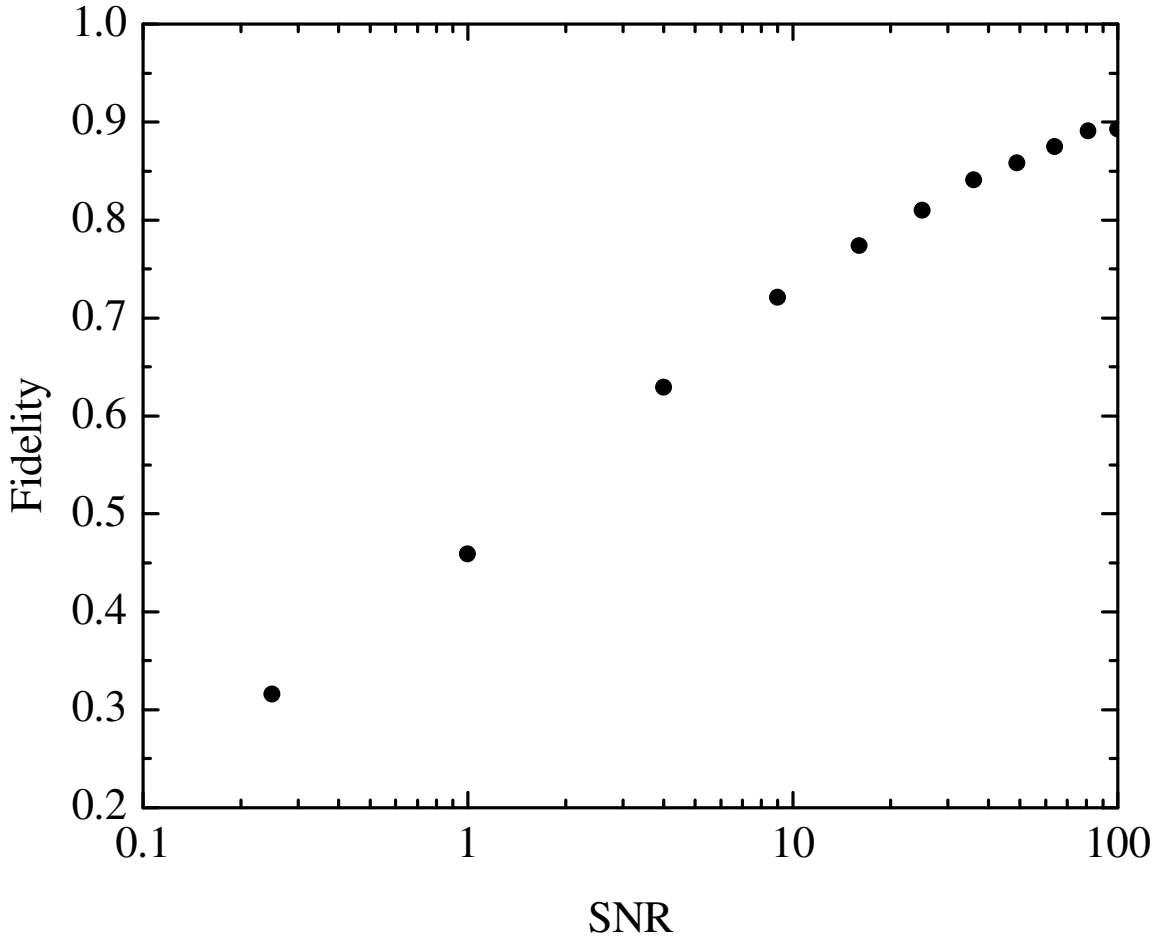

Fig. 8.15: Fidelity for the 1-state measurement when the discrimination level is set to fix the 0-state measurement fidelity to 0.841.

Chapter 9: Conclusions and suggestions for future work

9.1 Conclusions

In this thesis, I presented measurements on Cooper pair boxes and SETs and discussed results I achieved towards making single-shot measurements of a CPB using an rf-SET. I designed and fabricated devices that integrated CPBs, SETs, impedance matching components and high frequency transmission lines to carry out the measurements. I achieved good control of device parameters and this allowed me to optimize the performance of CPBs and rf-SETs. As part of this work, I characterized several rf-SETs and CPBs. Data from 8 different devices are shown throughout the thesis and summarized in Table 6.1. The best obtained sensitivity on any of my rf-SETs was $q_n = 8\times10^{-6}\ e_{rms}/(\mathrm{Hz})^{1/2}$ with a bandwidth of about 30 MHz.

Concerning the fabrication, I found that a specific process employing a trilayer resist system resulted in devices displaying e periodicity, which made them unsuitable for quantum computing. A different process (bilayer resist system) produced devices with $2e$ periodicity, but they were still not completely free of quasiparticle poisoning effects. To understand my results, I extended previously existing theories of parity effects (in the temperature range from $T\approx0$ to $T\approx350$ mK) and compared the theory with my measurements. I found good agreement between the theory and the data on my CPB. Comparison of the theory to my measurements of the $2e$ periodic SET current show significant discrepancies, possibly due to the effect of the electromagnetic environment, which also affects the current at low temperatures.

In Chapter 8, I described my experiments in quantum state control of the CPB using fast voltage pulses. I observed coherent oscillations of charge states, but phase coherence could be observed only for a short time. The dephasing time inferred from the envelope of the oscillations was $T_2 \approx 200$ ps in device PE2, consistent with theoretical expectations away from the degeneracy point due to charge noise. A larger dephasing time would be expected at $n_g = 1$ but was not seen in the experiments. Data analysis of the measurements suggested that the pulse amplitude used in these measurements might have been too large to observe oscillations at $n_g = 1$. The measurements could also have been affected by two-level fluctuators coupled to the CPB. On device PE1 the dephasing time determined from the width of spectroscopy resonance was $T_2 \approx 250$ ps.

I also measured the relaxation time of a CPB by looking at the time decay of the charge signal with an rf-SET and found $T_1 = 143$ ns in device PE1. I did not determine whether SET back-action was responsible for the relaxation time; further measurements are necessary to investigate this question. A crude theoretical estimate suggests that the mixing time due to SET noise should have been ~4 μs for this measurement and therefore, other mechanisms are likely causing the short relaxation time.

Given the charge sensitivity for this measurement ($q_n = 7 \times 10^{-5}\ e_{rms}/(\mathrm{Hz})^{1/2}$) and the coupling strength between the CPB and the SET for this device ($\kappa = 0.009$) the signal-to-noise ratio for a single-shot measurement was estimated at $\mathrm{SNR} \approx 0.019$. A statistical analysis shows that even a $\mathrm{SNR} = 1$ would result in a measurement fidelity of only 46 % for the excited state and therefore, substantial improvements need to be accomplished in order to make single-shot rf-SET read-out feasible.

Examination of my results shows that there is still room for improvement both on the detection side and on the qubit side. Currently the sensitivity of rf-SETs is limited by the noise level of the rf preamplifier and is typically about ten times above the shot noise limit. It is not clear whether an increase of the rf-SET signal through larger charging energy or smaller resistance would improve qubit read-out. For example, I found that the CPB undergoes substantial quasiparticle poisoning if the SET current is too large (~1nA) and this compromises the sensitivity of the measurement since one is forced to use a low SET bias in order to minimize perturbation of the CPB.

An improvement in the coherence time of the CPB with rf-SET read-out is necessary, not only to make single-shot measurements possible, but also for this to be a viable scheme for quantum computing. It is possible that such an improvement can be attained through new ideas, and better materials or processing.

9.2 Suggestions for future work

More experiments are necessary to understand the sources of relaxation in the CPB. Presumably, relaxation should be dominated by SET back-action in the limit of strong coupling. In this case, it should be possible to turn on the rf-SET excitation some time after producing the excited state of the CPB. By measuring charge decay under varying delay time one could find out if other sources of relaxation are present. Measurements of relaxation at different SET bias points would also be illuminating.

Since relaxation times scale linearly with the spectral density S_V of the source, SET back-action should have a square dependence on the SET charging energy. Previous research has focused on SETs with large E_c in order to improve their charge sensitivity

and hopefully achieve single-shot detection, but it is also possible to improve the rf-SET sensitivity by using a SQUID preamplifier [109].

The above remarks imply that an SET with smaller E_c should be better suited to study decoherence mechanisms in the CPB. In particular, it might be interesting to exploit the $2e$ periodic SET current for rf-SET operation. For an SET with $R_\Sigma \approx 40$ kΩ and $E_c \approx 0.4$ K, the current at low V_{DS} bias (~10 μV) in excess of 100 pA can be expected [53]. This dynamic resistance $(\partial I/\partial V)^{-1} \sim 10^5$ is optimum for rf-SET impedance matching. This mode of operation would have low power dissipation and also a large gain since the current is peaked around $n_g = 1$ and therefore, the circuit can be brought from impedance match to mismatch with a small change in n_g.

I also note that the effects of quasiparticle poisoning in CPBs could be decreased through an understanding of the sources of non-equilibrium quasiparticles at low temperatures and by engineering devices with quasiparticle traps, clean materials and with islands having an increased energy gap.

Finally, it is worth exploring other read-out schemes for a CPB. One recently demonstrated idea for a dispersive and direct read-out [110,111] consists in using the quantum capacitance of the CPB to change the resonant frequency of an LC circuit.

APPENDIX A

MatLab subroutines

QPpoison

```
global DI; global DL; global T; global V; global NV; global R; global DI;
global DL; global mu2; global ML; global NL; global MI; global NI;
DI=2.6; DL=2.43; % Energy gap of the island and leads
T=0.1; R=24890; NL=0.4; NI=1.2; % non-equilibrium quasiparticles
NV=2500; %Density of states times volume of island
Ec=0.794; EJ=((DI+DL)/2)*(26000/(8*R));
ng=[0:0.02:2]; PE=ng; Q=ng;
mu2=mu; %Finds the chemical potential for the escape rate
ML=muL; %Finds the chemical potential of the leads
MI=muI; %Finds the chemical potential of the island
for k=1:length(ng)
   V=Ec*(E0(EJ/Ec,ng(k))-E0(EJ/Ec,ng(k)-1));
   Roe=RG+RIL+RIL2;
   V=-V;
   Reo=RLI+RLI2;
   PE(k)=Roe/(Roe+Reo);
   Q(k)=PE(k)*SuperStair(EJ/Ec,ng(k))+(1-PE(k))*(1+Superstair(EJ/Ec,ng(k)-1));
   k
```

```
end
plot(ng,Q);

function s = Fermi(E,T); % Fermi distribution.
s=1./(1+exp(E./T));

function s = SupDenSt(E,D) % quasiparticle density of states
gama=1e-12;
s=abs(real((E-i*gama)./sqrt((E-i*gama).^2-D^2)));

function s=RLI; %Finds the tunneling rate LI for thermal equilibrium quasiparticles.
global DI; global DL; global T; global V; global R;
s=quad(@integrand,-10,10,1e-16);
s=(s*(1.38E-23))/(R*(2.56E-38));

function s = Integrand(E) % called by RLI
global DI; global DL; global T; global V; global TL;
s=E;
for k=1:length(E)
s(k)=SupDenSt(E(k),DL)*(Fermi(E(k),T))*SupDenSt((E(k)-V),DI)*(1-Fermi((E(k)-
V),T));
end
```

```
function s=RIL; % Tunneling rate IL for thermal equilibrium quasiparticles.
global DI; global DL; global T; global V; global R;
s=quad(@intIL,-10,10,1e-16);
s=(s*(1.38E-23))/(R*(2.56E-38));

function s = IntIL(E) % called by RIL
global DI; global DL; global T; global V; global TL;
for k=1:length(E)
s(k)=SupDenSt(E(k),DI)*(Fermi(E(k),T))*SupDenSt((E(k)-V),DL)*(1-Fermi((E(k)-
V),T));
end

function s=RG; % Escape rate
global DI; global DL; global T; global V; global R;
s=quad8(@intG,-10,10);
s=(s*(1.38E-23))/(2*R*(2.56E-38));

function s = IntG(E) % called by RG
global DI; global DL; global T; global V; global mu2;
for k=1:length(E)
s(k)=SupDenSt(E(k),DI)*(Fermi(E(k)-mu2,T)-Fermi(E(k),T))*SupDenSt((E(k)-
V),DL)*(1-Fermi((E(k)-V),T));
end
```

```
function s=RLI2; % Rate LI for non-equilibrium quasiparticles
global DI; global DL; global T; global V; global R;
s=quad(@intLI2,-10,10,1e-16);
s=(s*(1.38E-23))/(R*(2.56E-38));

function s = IntLI2(E) %  called by RLI2
global DI; global DL; global T; global V; global DL; global DI; global ML; global MI;
s=E;
for k=1:length(E)
s(k)=Fermi(E(k)-sign(E(k))*ML,T)*(1-Fermi(E(k)-V-
sign(E(k))*MI,T))*SupDenSt(E(k)-V,DI);
s(k)=s(k)*SupDenSt(E(k),DL);
end

function s=RIL2; % Tunneling rate IL for non-equilibrium quasiparticles
global DI; global DL; global T; global V; global R;
s=quad(@intIL2,-10,10,1e-16);
s=(s*(1.38E-23))/(R*(2.56E-38));

function s = IntIL2(E) % called by RIL2
global DI; global DL; global T; global V; global DL; global DI; global ML; global MI;
s=E;
for k=1:length(E)
```

```
s(k)=Fermi(E(k)-sign(E(k))*MI,T)*(1-Fermi(E(k)-V-
sign(E(k))*ML,T))*SupDenSt(E(k)-V,DL);
s(k)=s(k)*SupDenSt(E(k),DI);
end
```

```
function s=mu; % Finds the chemical potential for the escape rate
global DI; global DL; global NV; global mu2; global pres;
mu2=DI*(1.1); % Initial value for the chemical potential
inc=0.1*DI; N1=100; s=0;
for k=1:20      % Accuracy of 1 part in 10
   mu2=mu2-inc;
    Nest=NV*quad8(@Nf,-10,10);
    if abs(Nest-1)<abs(N1-1)
    N1=Nest;
    Mu2Est=mu2;
   end
end
mu2=Mu2Est+inc;
inc=0.1*inc;
s=0;
for k=1:20      % Accuracy of 1 part in 100
   mu2=mu2-inc;
   Nest=NV*quad8(@Nf,-10,10);
```

```
    if abs(Nest-1)<abs(N1-1)
        N1=Nest;
        Mu2Est=mu2;
    end
end
mu2=Mu2Est+inc;
inc=0.1*inc;
s=0;
for k=1:20       %  Accuracy of 1 part in 1000
    mu2=mu2-inc;
    Nest=NV*quad8(@Nf,-10,10);
    if abs(Nest-1)<abs(N1-1)
        N1=Nest;
        Mu2Est=mu2;
    end
end
mu2=Mu2Est;
s=Mu2Est;

function s = Nf(E)  % called by mu
global DI; global T; global mu2;
s=SupDenSt(E,DI).*(Fermi(E-mu2,T)-Fermi(E,T));
```

```
function s=muI;  % Finds the chemical potential of the island
global DI; global DL; global NV; global MI; global NI;
MI=DI*(1.1); % Initial valud
inc=0.1*DI;
N1=1000000;
s=0;
for k=1:20       %  Accuracy of 1 part in 10
   MI=MI-inc;
   Nest=NV*quad8(@NfI,0,10);
   if abs(Nest-NI)<abs(N1-NI)
      N1=Nest;
      MuEst=MI;
   end
end
MI=MuEst+inc;
inc=0.1*inc;
s=0;
for k=1:20       %  Accuracy of 1 part in 100
   MI=MI-inc;
   Nest=NV*quad8(@NfI,0,10);
   if abs(Nest-NI)<abs(N1-NI)
      N1=Nest;
      MuEst=MI;
```

```
   end
end
MI=MuEst+inc;
inc=0.1*inc;
s=0;
for k=1:20      % Accuracy of 1 part in 1000
   MI=MI-inc;
   Nest=NV*quad8(@NfI,0,10);
   if abs(Nest-NI)<abs(N1-NI)
      N1=Nest;
      MuEst=MI;
   end
end
s=MuEst;
```

```
function s = NfI(E)  % called by muI
global DI; global T; global MI;
s=SupDenSt(E,DI).*Fermi(E-MI,T);
```

```
function s=muL; % Finds the chemical potential of the leads
global DI; global DL; global NV; global ML; global NL;
ML=DL*(1.1); % Initial value
inc=0.1*DL; N1=1000000; s=0;
```

```
for k=1:20      %      Accuracy 1 part in 10
   ML=ML-inc;
   Nest=NV*quad8(@NfL,0,10);
   if abs(Nest-NL)<abs(N1-NL)
      N1=Nest;
      MuEst=ML;
   end
end
ML=MuEst+inc;
inc=0.1*inc;
s=0;
for k=1:20      %      Accuracy 1 part in 100
   ML=ML-inc;
   Nest=NV*quad8(@NfL,0,10);
   if abs(Nest-NL)<abs(N1-NL)
      N1=Nest;
      MuEst=ML;
   end
end
ML=MuEst+inc;
inc=0.1*inc;
s=0;
for k=1:20      %      Accuracy 1 part in 1000
```

```
    ML=ML-inc;
    Nest=NV*quad8(@NfL,0,10);
    if abs(Nest-NL)<abs(N1-NL)
        N1=Nest;
        MuEst=ML;
    end
end
s=MuEst;
```

function s = NfL(E) % called by muL

```
global DL; global T; global ML;
s=SupDenSt(E,DL).*Fermi(E-ML,T);
```

function s = E0(p,n) % Ground state energy of the CPB

```
% p=Ej/Ec
n=n/2;
Number=[-2 0 0 0 0; 0 -1 0 0 0; 0 0 0 0 0; 0 0 0 1 0; 0 0 0 0 2];
for k=1:length(n)
a=[4*(n(k)+2)^2 -p/2 0 0 0
   -p/2 4*(n(k)+1)^2 -p/2 0 0
   0 -p/2 4*n(k)^2 -p/2 0
   0 0 -p/2 4*(1-n(k))^2 -p/2
   0 0 0 -p/2 4*(2-n(k))^2];
```

```
b=eig(a);
ss(k)=b(1);
end
s=ss';
```

function s = E1(p,n) % Excited state energy of the CPB

```
% p=Ej/Ec
n=n/2;
Number=[-2 0 0 0 0; 0 -1 0 0 0; 0 0 0 0 0; 0 0 0 1 0; 0 0 0 0 2];
for k=1:length(n)
a=[4*(n(k)+2)^2 -p/2 0 0 0
   -p/2 4*(n(k)+1)^2 -p/2 0 0
   0 -p/2 4*n(k)^2 -p/2 0
   0 0 -p/2 4*(1-n(k))^2 -p/2
   0 0 0 -p/2 4*(2-n(k))^2];
b=eig(a);
ss(k)=b(2);
end
s=ss';
```

function s = SuperStair(p,n) % Expectation value of the charge in the ground state.

```
%p=Ej/Ec
n=n/2;
```

```
Number=[-2 0 0 0 0; 0 -1 0 0 0; 0 0 0 0 0; 0 0 0 1 0; 0 0 0 0 2];
for k=1:length(n)
a=[4*(n(k)+2)^2 -p/2 0 0 0
   -p/2 4*(n(k)+1)^2 -p/2 0 0
   0 -p/2 4*n(k)^2 -p/2 0
   0 0 -p/2 4*(1-n(k))^2 -p/2
   0 0 0 -p/2 4*(2-n(k))^2];
[v,b]=eig(a);
ss(k)=v(:,1)'*Number*v(:,1);
end
s=2*ss';
```

function s = SuperStair1(p,n) % Expectation value of the charge in the excited state.

```
%p=Ej/Ec
n=n/2;
Number=[-2 0 0 0 0; 0 -1 0 0 0; 0 0 0 0 0; 0 0 0 1 0; 0 0 0 0 2];
for k=1:length(n)
a=[4*(n(k)+2)^2 -p/2 0 0 0
   -p/2 4*(n(k)+1)^2 -p/2 0 0
   0 -p/2 4*n(k)^2 -p/2 0
   0 0 -p/2 4*(1-n(k))^2 -p/2
   0 0 0 -p/2 4*(2-n(k))^2];
[v,b]=eig(a);
```

```
ss(k)=v(:,2)'*Number*v(:,2);

end

s=2*ss';
```

NormSET % Calculates IVs for the symmetric normal SET

```
global R; global Ec; global T;

Ec=0.93; % Charging energy in Kelvin

R=1e5/2; % Total resistance divided by 2

VDS=1; % Vds = 1 corresponds to 100 microVolts

%ng=0.5;

T=0.1; % Temperature in Kelvin

ng=[-1:0.01:1];

I=ng;

%VDS=[-3:0.01:3];

C1=0.5; C2=0.49; Cg=0.01;

for k=1 : length(ng)

I(k)=I_NSET(ng(k),VDS);

end

plot(ng,I)
```

function s=I_NSET(ng,VDS); % Calculates the current for the normal SET

```
global R; global T;

   Den=det([R1(-2,-1,ng,VDS,T)+R2(-2,-1,ng,VDS,T) -R1(-1,-2,ng,VDS,T)-R2(-1,-

2,ng,VDS,T) 0 0 0
```

```
  0  R1(-1,0,ng,VDS,T)+R2(-1,0,ng,VDS,T) -R1(0,-1,ng,VDS,T)-R2(0,-1,ng,VDS,T) 0 0
  0 0 R1(0,1,ng,VDS,T)+R2(0,1,ng,VDS,T) -R1(1,0,ng,VDS,T)-R2(1,0,ng,VDS,T) 0
  0 0 0 R1(1,2,ng,VDS,T)+R2(1,2,ng,VDS,T) -R1(2,1,ng,VDS,T)-R2(2,1,ng,VDS,T)
  1 1 1 1 1]);
Num=det([0 -R1(-1,-2,ng,VDS,T)-R2(-1,-2,ng,VDS,T) 0 0 0
  0  R1(-1,0,ng,VDS,T)+R2(-1,0,ng,VDS,T) -R1(0,-1,ng,VDS,T)-R2(0,-1,ng,VDS,T) 0 0
  0 0 R1(0,1,ng,VDS,T)+R2(0,1,ng,VDS,T) -R1(1,0,ng,VDS,T)-R2(1,0,ng,VDS,T) 0
  0 0 0 R1(1,2,ng,VDS,T)+R2(1,2,ng,VDS,T) -R1(2,1,ng,VDS,T)-R2(2,1,ng,VDS,T)
  1 1 1 1 1]);
Pm2=Num/Den;
Num=det([R1(-2,-1,ng,VDS,T)+R2(-2,-1,ng,VDS,T) 0 0 0 0
  0  0 -R1(0,-1,ng,VDS,T)-R2(0,-1,ng,VDS,T) 0 0
  0 0 R1(0,1,ng,VDS,T)+R2(0,1,ng,VDS,T) -R1(1,0,ng,VDS,T)-R2(1,0,ng,VDS,T) 0
  0 0 0 R1(1,2,ng,VDS,T)+R2(1,2,ng,VDS,T) -R1(2,1,ng,VDS,T)-R2(2,1,ng,VDS,T)
  1 1 1 1 1]);
Pm1=Num/Den;
Num=det([R1(-2,-1,ng,VDS,T)+R2(-2,-1,ng,VDS,T) -R1(-1,-2,ng,VDS,T)-R2(-1,-
2,ng,VDS,T) 0 0 0
  0  R1(-1,0,ng,VDS,T)+R2(-1,0,ng,VDS,T) 0 0 0
  0 0 0 -R1(1,0,ng,VDS,T)-R2(1,0,ng,VDS,T) 0
  0 0 0 R1(1,2,ng,VDS,T)+R2(1,2,ng,VDS,T) -R1(2,1,ng,VDS,T)-R2(2,1,ng,VDS,T)
  1 1 1 1 1]);
P0=Num/Den;
```

```
Num=det([R1(-2,-1,ng,VDS,T)+R2(-2,-1,ng,VDS,T) -R1(-1,-2,ng,VDS,T)-R2(-1,-
2,ng,VDS,T) 0 0 0
  0  R1(-1,0,ng,VDS,T)+R2(-1,0,ng,VDS,T) -R1(0,-1,ng,VDS,T)-R2(0,-1,ng,VDS,T) 0 0
  0 0 R1(0,1,ng,VDS,T)+R2(0,1,ng,VDS,T) 0 0
  0 0 0 0 -R1(2,1,ng,VDS,T)-R2(2,1,ng,VDS,T)
  1 1 1 1 1]);
P1=Num/Den;
Num=det([R1(-2,-1,ng,VDS,T)+R2(-2,-1,ng,VDS,T) -R1(-1,-2,ng,VDS,T)-R2(-1,-
2,ng,VDS,T) 0 0 0
  0  R1(-1,0,ng,VDS,T)+R2(-1,0,ng,VDS,T) -R1(0,-1,ng,VDS,T)-R2(0,-1,ng,VDS,T) 0 0
  0 0 R1(0,1,ng,VDS,T)+R2(0,1,ng,VDS,T) -R1(1,0,ng,VDS,T)-R2(1,0,ng,VDS,T) 0
  0 0 0 R1(1,2,ng,VDS,T)+R2(1,2,ng,VDS,T) 0
  1 1 1 1 1]);
P2=Num/Den;
   s=Pm2*R1(-2,-1,ng,VDS,T);
   s=s+Pm1*(R1(-1,0,ng,VDS,T)-R1(-1,-2,ng,VDS,T));
   s=s+P0*(R1(0,1,ng,VDS,T)-R1(0,-1,ng,VDS,T));
   s=s+P1*(R1(1,2,ng,VDS,T)-R1(1,0,ng,VDS,T));
   s=s+P2*(-R1(2,1,ng,VDS,T));
   s=-(1.38e5)*s/(1.6*R);
```

function s=G1(n1,n2,ng,VDS); % Calculates free energy differences for junction 1

```
global Ec;
```

```
if n1<n2
ss=Ec*(2*(n1-ng)+1)+0.5*VDS/0.8625;
else ss=Ec*(-2*(n2-ng)-1)-0.5*VDS/0.8625;
end
s=ss;
```

function s=G2(n1,n2,ng,VDS); % Calculates free energy differences for junction 2

```
global Ec;
if n1<n2
ss=Ec*(2*(n1-ng)+1)-0.5*VDS/0.8625;
else ss=Ec*(-2*(n2-ng)-1)+0.5*VDS/0.8625;
end
s=ss;
```

function s=R1(n1,n2,ng,VDS,T); % Tunneling rate through junction 1

```
G=G1(n1,n2,ng,VDS);
s=-G/(1-exp(G/T));
```

function s=R2(n1,n2,ng,VDS,T); % Tunneling rate through junction 2

```
G=G2(n1,n2,ng,VDS);
s=-G/(1-exp(G/T));
```

Coherent Oscillations % Generates staircases with pulses

```
ng=[0:0.01:2];
Ec=0.715; % in Kelvin
EJ=0.722; % in Kelvin
Dng=0.65;
Dt=0.100; %Delta t in nanoseconds
RelFac=0.4;
DE=Ec*(E1(EJ/Ec,ng+Dng)-E0(EJ/Ec,ng+Dng))';
S0_N=[0
      0];
A2=[1 1
    1 1];
P2=ng;
for k=1 : length(ng)
    S0_N(2)=sqrt(superstair(EJ/Ec,ng(k))/2);
    S0_N(1)=sqrt(1-S0_N(2)^2);
    A2(1,2)=sqrt(superstair(EJ/Ec,ng(k)+Dng)/2);
    A2(1,1)=sqrt(1-(A2(1,2))^2);
    A2(2,2)=sqrt(superstair1(EJ/Ec,ng(k)+Dng)/2);
    A2(2,1)=-sqrt(1-(A2(2,2))^2);
    S0_E=A2*S0_N;
    Ph=130.8*DE(k)*Dt;
    S0_E(2)=exp(-i*Ph)*S0_E(2);
    SF_N=inv(A2)*S0_E;
```

```
   P2(k)=abs(SF_N(2))^2;
end
P2=2*P2-superstair(EJ/Ec,ng)';
P2=RelFac*P2+superstair(EJ/Ec,ng)';
plot(ng,P2);
```

Spectroscopy

```
% Generates staircases with microwaves
ng=[-2:0.01:2];
Ec=0.794; % in Kelvin
EJ=0.327; % in Kelvin
ngm=0.003;
Wm=2*pi*28; % 2pi f_microwaves in GHz
T1=143; % in nanoseconds
T2=0.25; % in nanoseconds
DE=Ec*(E1(EJ/Ec,ng)-E0(EJ/Ec,ng))';
RabiF=131*2*Ec*ngm*EJ./DE; % Rabi frequency in GHz
Num=(T1/(2*T2))*(RabiF).^2;
Den=((131*DE)-Wm).^2;
Den=Den+(1/T2)^2;
Den=Den+(T1/T2)*(RabiF).^2;
P1=Num./Den;
Q=(1-P1)'.*SuperStair(EJ/Ec,ng)+P1'.*SuperStair1(EJ/Ec,ng);
plot(ng,Q);
```

REFERENCES

[1] D. Deutsch, Proceedings of the Royal Society of London: Series A – Mathematical and Physical Sciences **A400**, 97 (1985).

[2] M. A. Nielsen and I. L. Chuang, *Quantum Computation and Quantum Information*, 2001 ed. (Cambridge Univ. Press, Cambridge, 2001).

[3] P. Shor, Proceedings of the 35th Annual Symposium on the Foundations of Computer Science, IEEE Computer Society, Los Alamos, CA, 1994, p. 124.

[4] L. K. Grover, in *Proc. 28th Annual ACM Symposium on the Theory of Computing* (STOC), ACM Press, New York (1996), p. 212.

[5] C. H. Bennett and G. Brassard, "Quantum Crptography: Public Key Distribution and Coin Tossing" in *Proceedings of the IEEE International Conference on Computers, Systems and Signal Processing, Bangalore, India* (IEEE, New York, 1984), p.175.

[6] A. M. Steane and B. Ibinson, Fault-tolerant logical gate networks for css codes, (4-Nov-03) preprint *quant-ph*/0311014.

[7] D. P. DiVincenzo, "The Physical Implementation of Quantum Computation", quant-ph/0002077.

[8] J. I. Cirac and P. Zoller, Phys. Rev. Lett. **74**, 4091 (1995).

[9] D. G. Cory, A. F. Fahmy and T. F. Havel, Proceedings of the National Academy of Science (USA) **94**, 1634 (1997).

[10] A. Blais, R.-S. Huang, A. Wallraff, S. M. Girvin and R. J. Schoelkopf, Phys. Rev. A **69**, 062320 (2004).

[11] B. Kane, Nature **393**, 133 (1998).

[12] F. Schmidt-Kaler, H. Häffner, M. Riebe, S. Gulde, G. P. T. Lancaster, T. Deuschle, C. Becher, C. F. Roos, J. Eschner and R. Blatt, Nature **422**, 408 (2003).

[13] L. M. K. Vandersypen, M. Steffen, G. Breyta, C. S. Yannoni, M. H. Sherwood and I. L. Chuang, Nature **414**, 883 (2001).

[14] B. D. Josephson, Phys. Lett. **1**, 251 (1962).

[15] Michael Tinkham, *Introduction to superconductivity*, 2nd edition, (McGraw-Hill,1996).

[16] J. E. Mooij, T. P. Orlando, L. Levitov, L. Tian, C. H. van der Wal and S. Lloyd, Science **285**, 1036 (1999).

[17] I. Chiorescu, Y. Nakamura, C. J. P. M. Harmans and J. E. Mooij, Science **299**, 1869 (2003).

[18] R. C. Ramos, M. A. Gubrud, A. J. Berkley, J. R. Anderson, C. J. Lobb and F. C. Wellstood, IEEE Trans. on Appl. Supercond. **11**, 998 (2001).

[19] J. M. Martinis, K. B. Cooper, R. McDermott, M. Steffen, M. Ansmann, K. Osborn, K. Cicak, S. Oh, D. P. Pappas, R. W. Simmonds and Clare C. Yu, "Decoherence in Josephson Qubits from Dielectric Loss", cond-mat/0507622.

[20] A. J. Berkley, H. Xu, R. C. Ramos, M. A. Gubrud, F. W. Strauch, P. R. Johnson, J. R. Anderson, A. J. Dragt, C. J. Lobb and F. C. Wellstood, Science **300**, 1548 (2003).

[21] H. Xu, F. W. Strauch, S. K. Dutta, P. R. Johnson, R. C. Ramos, A. J. Berkley, H. Paik, J .R. Anderson, A. J. Dragt, C. J. Lobb and F. C. Wellstood, Phys. Rev. Lett. **94**, 027003 (2005).

[22] Y. Makhlin, G. Schön, A. Shnirman, Rev. Mod. Phys. **73**, 357 (2001).

[23] M. Büttiker, Phys. Rev. B **36**, 3548 (1987).

[24] A. Shnirman, G. Schön, and Z. Hermon, Phys. Rev. Lett. **79**, 2371 (1997).

[25] V. Bouchiat, V. Vion-D, P. Joyez, D. Esteve and M. H. Devoret, Physica Scripta**T76**, 165 (1998).

[26] Y. Nakamura, Y. A. Pashkin, and J. S. Tsai, Nature **398**, 786 (1999).

[27] R. J. Schoelkopf, P. Wahlgren, A. A. Kozhevnikov and P. Delsing, Science **280**, 1238 (1998).

[28] K. W. Lehnert, K. Bladh, L. F. Spietz, D. Gunnarsson, D. I. Schuster, P. Delsing and R. J. Schoelkopf, Phys. Rev. Lett. **90**, 027002 (2003).

[29] T. Duty, D. Gunnarsson, K. Bladh and P. Delsing, Phys. Rev. B **69**, 140503 (2004).

[30] A. Guillaume, J. F. Schneiderman, P. Delsing, H. M. Bozler and P. M. Echternach, Phys. Rev. B **69**, 132504 (2004).

[31] D. Vion, A. Aassime, A. Cottet, P. Joyez, H. Pothier, C. Urbina, D. Esteve, and M. H. Devoret, Science **296**, 886 (2002).

[32] O. Astafiev, Y. A. Pashkin, T. Yamamoto and Y. Nakamura, Phys. Rev. B **69**, 180507 (2004).

[33] *Single charge tunneling*, edited by H. Grabert and M. H. Devoret (Plenum, NewYork, 1992).

[34] D. V. Averin and Yu. V. Nazarov, Phys. Rev. Lett. **69**, 1993 (1992).

[35] V. Ambegaokar and A. Baratoff, Phys. Rev. Lett. **10**, 486 (1963).

[36] M. H. Devoret, A. Wallraff and J. M. Martinis, "Superconducting Qubits: A Short Review", cond-mat/0411174v1.

[37] D. Vion in "*Quantum entanglement and information processing*", Edited by D. Esteve, J. M. Raimond et J. Dalibard, (2004).

[38] Schoelkopf, A. A. Clerk, S. M. Girvin, K. W. Lehnert and M. H. Devoret in *Quantum noise*, chapter *Qubits as Spectrometers of Quantum Noise*, R. J., Kluwer Academic, Dordrecht (2003). Cond-mat/0210247.

[39] O. Astafiev, Yu. A. Pashkin, Y. Nakamura, T. Yamamoto, and J. S. Tsai, Phys. Rev. Lett. **93**, 267007 (2004).

[40] G. Zimmerli, T. M. Eiles, R. L. Kautz and J. M. Martinis, Appl. Phys. Lett. **61**,237 (1992).

[41] M. Kenyon, C. J. Lobb and F. C. Wellstood, J. Appl. Phys. **88**, 6536 (2000).

[42] A. Shnirman, G. Schön, I. Martin and Y. Makhlin, Phys. Rev. Lett. **94**, 127002 (2005).

[43] M. v. Schickfus, S. Hunklinger, Physics Letters, **64A**, 144 (1977).

[44] A. A. Clerk, S. M. Girvin, A. K. Nguyen and A. D. Stone, Phys. Rev. Lett. **89**, 176804 (2002).

[45] J. M. Martinis, S. Nam, J. Aumentado, and K. M. Lang, Phys. Rev. B **67**, 094510 (2003).

[46] Y. Nakamura, Y. A. Pashkin, T. Yamamoto, and J. S. Tsai, Phys. Rev. Lett. **88**, 047901 (2002).

[47] J. M. Hergenrother, J. G. Lu, M. T. Tuominen, D. C. Ralph and M. Tinkham, Phys. Rev. B **51**, 9407 (1995).

[48] V. A. Krupenin, D. E. Presnov, and M. N. Savvateev, H. Scherer, A. B. Zorin and J. Niemeyer, J. Appl. Phys. **84**, 3212 (1998).

[49] A. Korotkov, Appl. Phys. Lett. **69**, 2593 (1996).

[50] D. V. Averin and K. K. Likharev, J. Low Temp. Phys. **62**, 345 (1986).

[51] Oxford Instruments, Carteret, NJ, Tel. (732) 541-1300.

[52] H. R. Zeller and I. Giaever, Phys. Rev. **181**, 789 (1969).

[53] D. Song, *Properties of Coulomb-blockade electrometers in the superconducting state*, Thesis, University of Maryland (1997).

[54] T. A. Fulton, P. L. Gammel, D. J. Bishop and L. N. Dunkleburger, Phys. Rev.Lett. **63**, 1307 (1989).

[55] Y. Nakamura, C. D. Chen, and J. S. Tai, Phys. Rev. B **53**, 8234 (1996).

[56] J. Siewert and G. Schön, Phys. Rev. B **54**, 7421 (1996).

[57] A. Maassen van den Brink, A. A. Odintsov, P. A. Bobbert and G. Schön, Z. Phys. B **85**, 459 (1991).

[58] M-S. Choi, F. Plastina and R. Fazio, Phys. Rev. B **67**, 045105 (2003).

[59] M. Kenyon, *Behavior of Single Electron Transistors and their use in scanning microscopy*, Thesis, University of Maryland (2001).

[60] A. Aassime, D. Gunnarsson, K. Bladh, P. Delsing and R. J. Schoelkopf, App. Phys. Lett, **79**, 4031 (2001).

[61] A. Kack, G. Wendin, G. Johansson, Phys. Rev. B **67**, 35301 (2003).

[62] A. N. Korotkov, Phys. Rev. B **49**, 10381 (1994).

[63] A. Aassime, G. Johansson, G. Wendin, R. J. Schoelkopf and P. Delsing, Phys. Rev. Lett, **86**, 3376 (2001).

[64] S. S. Mohan, M. Hershenson, S. P. Boyd and T. H. Lee, IEEE J. Solid-State Circuits **34**, 1419 (1999).

[65] K. C. Gupta, R. Garg, I. J. Bahl, and P. Bhartia, *Microstriip Lines and Slotlines*, 2nd ed. Artech House, Inc., 1996.

[66] Universitywafer.com, Tel. (800) 713-9375.

[67] MicroChem Corp., Newton, MA, Tel. (617) 965-5511.

[68] Futurrex, Inc., Franklin, NJ, Tel. (973) 209-1563.

[69] P. M. Echternach, H. G. LeDuc, A. Skalare and W. R. McGrath, Tenth International Symposium on Space Terahertz Technology, Charlottesville, Virginia, 1999, p.261.

[70] Pierre M. Echternach, Jet Propulsion Laboratory, California Institute of Technology, Pasadena, CA, 91109-8099, Private communication.

[71] JC Nabity Lithography Systems, Bozeman, MT, Tel. (406) 587-0848.

[72] T. A. Fulton and G. J. Dolan, Phys. Rev. Lett. **59**, 109 (1987).

[73] MDC Vacuum Products Corp., Hayward, CA, Tel. (510) 265-3500.

[74] Coax Co. LTD., 461-1 Eda-cho Aoba-ku, Yokohama-shi, Kanagawa-ken 225-0013 Japan, Tel +81-45-913-7101.

[75] Lakeshore cryotronics Inc., Westerville, OH, Tel. (614) 891-2244.

[76] QuinStar Technology, Inc. Torrance, CA, Tel. (310) 320-1111.

[77] Micro-Coax, Pottstown, PA, Tel. (610) 495-0110.

[78] C. C. Chi and J. Clarke, Phys. Rev. B **20**, 4465 (1979).

[79] J. Aumentado, M. W. Keller, L. M. Martinis, and M. H. Devoret, Phys. Rev. Lett. **92**, 066802 (2004).

[80] L. J. Geerligs, D. V. Averin, and J. E. Mooiji, Phys. Rev. Lett. **65**, 3037 (1990).

[81] F. C. Wellstood, C. Urbina, and J. Clarke, Phys. Rev. B **49**, 5942 (1993).

[82] R. L. Kautz, G. Zimmerli, and J. M. Martinis, J. Appl. Phys. **73**, 2386 (1993).

[83] A. Hädicke and W. Krech, Physica B **210**, 439 (1995).

[84] P. Joyez, P. Lafarge, A. Filipe, D. Esteve and M. H. Devoret, Phys. Rev. Lett. **72**, 2458 (1994).

[85] D. Gunnarsson, T. Duty, K. Bladh, R. Schoelkopf and P. Delsing, Physica E **18**, 27 (2003).

[86] B. Turek, J. Majer, A. Clerk, S. Girvin, A. Wallraff, K. Bladh, D. Gunnarsson, T. Duty, P. Delsing and R. Schoelkopf, IEEE Trans. on App. Superconductivity **15**, 880 (2005).

[87] A. Amar, D. Song, C. Lobb and F. C. Wellstood, Phys. Rev. Lett. **72**, 3234 (1994).

[88] J. M. Hergenrother, J. G. Lu and M. Tinkham, IEEE Trans. on App. Superconductivity **5**, 2604 (1995).

[89] M. T. Tuominen, J. M. Hergenrother, T. S. Tighe and M. Tinkham, Phys. Rev. Lett. **69**, 1997 (1992).

[90] P. Lafarge, P. Joyez, D. Esteve, C. Urbina and M. H. Devoret, Phys. Rev. Lett. **70**, 994 (1993).

[91] P. Joyez, P. Lafarge, A. Filipe, D. Esteve and M. H. Devoret, Phys. Rev. Lett. **72**, 2458 (1994).

[92] D. V. Averin and Yu. V. Nazarov, Phys. Rev. Lett. **69**, 1993 (1992).

[93] R. C. Dynes, J. P. Garno, G. B Hertel and T. P. Orlando, Phys. Rev. Lett. **53**, 2437 (1984).

[94] J. Aumentado, M. W. Keller, J. M. Martinis and M. H. Devoret, Phys. Rev. Lett. **92**, 066802 (2004).

[95] G. Schön and A. D. Zaikin, Europhysics Lett. **26**, 695 (1994).

[96] *Quantum transport and dissipation*, chapter *single electron tunneling*, T. Dittrich, P. Hänggi, G. Ingold, B. Kramer, G. Schön and W. Zwerger, (Wiley-VHC, Weinheim, 1998).

[97] M. Tinkham, Phys. Rev. B **6**, 1747 (1972).

[98] C. S. Owen and D. J. Scalapino, Phys. Rev. Lett. **28**, 1559 (1972).

[99] C. C. Chi and J. Clarke, Phys. Rev. B **20**, 4465 (1979).

[100] B. Abeles, R. W. Cohen and G. W. Cullen, Phys Rev. Lett. **17**, 632 (1966).

[101] J. Männik and J. E. Lukens, Phys. Rev. Lett. **92**, 057004 (2004).

[102] R. K. Waits, J. Vac. Sci. Technol. A **18**, 1736 (2000).

[103] C. Cohen-Tannoudji, B. Diu and F. Laloë, *Quantum Mechanics, Vol. 1*, New York, Wiley (1997).

[104] H. Xu, *Quantum Computing with Josephson Junction Circuits*, Thesis, University of Maryland (2004).

[105] R. A. Smith, Proc. Roy. Soc. London **A362**, 1 (1978).

[106] F. Bloch, Phys. Rev. **70**, 460 (1946).

[107] Y. Nakamura, Yu. A. Pashkin and J. S. Tsai, Phys. Rev. Lett. **87**, 246601 (2001).

[108] T. Duty, K. Bladh, D. Gunnarsson and P. Delsing, J. Low Temp. Phys. **136**, 453 (2004).

[109] L. Roschier, P. Hakonen, K. Bladh and P. Delsing, Journal of App. Phys. **95**, 1274 (2004).

[110] T. Duty, G. Johansson, K. Bladh, D. Gunnarsson, C. Wilson and P. Delsing, "Observation of quantum capacitance in the Cooper-pair transistor", cond-mat/0503531.

[111] M. A. Sillanpaa, T. Lehtinen, A. Paila, Yu. Makhlin, L. Roschier and P. J. Hakonen, "Direct observation of macroscopic quantum renormalization of capacitance", cond-mat/0504517.